Université de Montréal

Construction ascendante d'assemblages moléculaires cristallins dérivés du motif 1,2,4,5-benzènetétramine

Par

Johann Sosoe

Département de chimie, Université de Montréal, Faculté des arts et des sciences

Thèse présenté(e) en vue de l'obtention du grade de *Philosophiae Doctor* (Ph.D.) en chimie

Août 2023

Université de Montréal

Unité académique : Chimie, Faculté des arts et des sciences

Cette thèse intitulée

Construction ascendante d'assemblages moléculaires cristallins dérivés du motif 1,2,4,5-benzènetétramine

Présenté par

Johann Sosoe

A été évalué(e) par un jury composé des personnes suivantes

William Skene
Président-rapporteur

James Wuest
Directeur de recherche

Frank Schaper
Membre du jury

Xavier Ottenwaelder
Examinateur externe

Résumé

Le XXIe siècle est une ère de progrès technologique sans précédent : jamais auparavant il ne nous n'a été possible de se déplacer et de communiquer aussi vite et loin. La démocratisation des transports et des appareils de communication modernes réduisent cependant la disponibilité de ressources naturelles causant des problématiques socio-économiques et sanitaires globales comme la pollution ou des conflits politiques. Le contenu de cette thèse tente proposer des façons dont la conception rationnelle de matériaux organiques aux propriétés programmées pourrait améliorer la durabilité et les performances des cathodes de batteries Li-ion. Dans un premier temps, des stratégies permettant la construction contrôlée et ascendante d'assemblages cristallins organiques (essentiellement faits de carbone, hydrogène, oxygène et azote) seront présentées. Ensuite, différentes manières dont ces stratégies de constructions sont mises à contribution du développement de batteries Li-ion plus vertes seront exposées. Finalement, un projet de recherche reposant sur une expertise en chimie organique et en ingénierie cristalline pour la génération de matériaux aux propriétés pertinentes à de telles applications sera détaillé.

Mots-clés : chimie supramoléculaire, ingénierie cristalline, composés rédox, quinones

Abstract

The 21st century marks an unprecedented era of technological advancement. Never before have we been able to travel and communicate as swiftly and extensively as we can now. While the accessibility of modern transportation and communication devices democratizes these capabilities, it also diminishes the availability of natural resources, giving rise to global socio-economic and health-related challenges such as pollution and political conflicts. The objective of this thesis is to propose methods by which the rational design of organic materials with programmed properties could improve both durability and sustainability of Li-ion batteries. Initially, the thesis outlines strategies for the controlled and bottom-up construction of organic crystalline assemblies primarily composed of carbon, hydrogen, oxygen, and nitrogen. Subsequently, various ways in which these construction strategies contribute to the development of more environmentally friendly Li-ion batteries are discussed. Finally, a research project is presented, centered around expertise in organic chemistry and crystal engineering for generating materials with properties relevant to such applications.

Keywords: supramolecular chemistry, crystal engineering, redox compounds, quinones

Table des matières

Liste des tableaux

Liste des figures

Liste des schémas

Liste des sigles et abréviations

°C	Degré Celsius
AA	Acide aminé
1,2,4,5-BTA	Benzène-1,2,4,5-tétramine
Bu	Butyl
CCDC	*Cambridge Crystallographic Data Centre*
C_{spe}	Capacité spécifique
C_{th}	Capacité théorique
COF	*Covalent Organic Framework*
CPMAS	*Cross-Polarization Magic Angle Spinning NMR Spectroscopy*
2D	Bidimensionnel
3D	Tridimensionnel
DAHQ	2,5-Diamino-*p*-hydroquinone
DAR	4,6-Diamino-résorcinol
DAT	4,6-Diamino-1,3,5-triazin-2-yl
DHHQ	2,5-Dihydroxy-*p*-hydroquinone
DMC	Carbonate de diméthyle
DME	Méthoxyméthane
DOL	1,3-Dioxolane
EC	Carbonate de diéthyle
E_{dens}	Densité d'énergie
Équiv.	Équivalent
E_{spe}	Énergie spécifique
FTIR	Spectroscopie infrarouge à transformée de Fourier

H_2BDC	Acide téréphtalique
HMRS	*High Resolution Mass Spectrometry*
HOFs	*Hydrogen Bonded Organic Frameworks*
I_{pa}	Courant de pic anodique
I_{pc}	Courant de pic cathodique
LCO	Oxide de cobalt lithié
MeCN	Acétonitrile
MEO	Matériau d'électrode organique
MOFs	*Metal-organic frameworks*
o	*Ortho*
ODEL	Diode organique électroluminescente
p	*Para*
SCXRD	*Single Crystal X-Ray Diffraction*
TEGDME	1-Méthoxy-2-[2-[2-(2-méthoxyéthoxy)éthoxy]éthoxy]éthane
v	Vitesse de balayage

Remerciements

Mon passage à l'Université de Montréal (B.Sc. 2014-2017, M.Sc. 2017-2019, PhD 2019-2023) m'a inculqué la discipline et insufflé l'amour pour le travail acharné. Cela m'a permis de matérialiser mes idées, vivre pleinement mes projets et explorer le monde. Je tiens donc à remercier toutes les personnes qui ont rendu cette aventure possible.

Je tiens d'abord à remercier chaleureusement toutes les personnes qui ont contribué à ma formation de scientifique que j'ai côtoyées de jour comme de nuit au cours de cette dernière décennie : corps professoral, camarades, personnel administratif, personnel des ateliers mécaniques, la Direction de la prévention et de la sécurité et les préposés au ménage. Je salue tout particulièrement : mon comité de thèse **James Wuest**, **Hélène Lebel**, **William Skene**, **Franck Schaper** et **Xavier Ottenwaelder**. Je vous remercie profondément pour l'encadrement et les conseils que vous m'avez prodigués durant mon doctorat. Je tâcherai de mettre à profit les compétences que vous m'avez permis de développer. **Dominic Rochefort**, **Mickaël Dollé** et leurs groupes de recherche respectifs pour les discussions et les travaux entrepris conjointement qui m'ont fait découvrir l'univers des batteries. **Thierry Maris** et **Daniel Chartrand** pour la qualité exceptionnelle de leur service au Laboratoire de diffraction de rayons X ainsi que leur implication dans les activités du groupe Wuest. Je vous remercie particulièrement de m'avoir guidé à travers le monde passionnant de la cristallographie et d'avoir pris le temps de répondre à mes innombrables questions. **Alexandra Furtos**, **Karine Gilbert**, **Louiza Mahrouche**, **Marie-Christine Tang** et **Marc-Antoine Vaudreuil** du Centre régional de spectrométrie de Masse, **Pedro Aguiar**, **Cédric Malveau** du Centre régional de résonance magnétique nucléaire, **Éric Dione** du *Montreal area platform for electrochemical systems* et **Nicolas Macia** du Laboratoire de caractérisation des matériaux, pour leur patience, leurs recommandations avisées et l'accompagnement dont j'ai bénéficié auprès d'eux pour la caractérisation de mes composés. J'ai grandement apprécié votre engouement contagieux pour les défis qui se sont présentés à nous ainsi que votre support indéfectible. J'espère sincèrement pouvoir continuer à travailler et apprendre à vos côtés dans le futur. **Donald Provost**, **Benoît Gaudette** et **Naouel Ougouti** parce qu'on ne ferait pas de chimie sans matériel adéquat, je vous remercie chaleureusement, non seulement pour votre efficacité mais également pour les tranches de rires et les agréables discussions qui ont animées chacune de nos rencontres. **Audrey Morin** sans qui je n'aurais pas pu assurer efficacement l'approvisionnement du groupe Wuest en produits chimiques et équipements essentiels à nos recherches !

Cher **Groupe Wuest 2019-2023**, de ma courte vie je n'avais encore jamais rencontré d'individus aussi originaux et bizarres que vous. Pourtant, je ne m'étais non plus jamais autant senti à a place. Ma curiosité, ma créativité et mon émerveillement des sciences n'auront jamais été autant stimulés qu'auprès de vous. Je garde tendrement en mémoire nos discussions animées, nos sorties, nos délires, nos somptueux repas, nos shifts au Café-In ainsi que nos séances studio. **Sophie Langis-Barsetti**, **Alice Heskia** et **Nino Georgiev**, nous ne nous sommes pas côtoyés longtemps dans les laboratoires mais votre influence se fait encore sentir dans nos rangs. Vous avez été pour moi des modèles d'exception dans ma formation et j'espère sincèrement que mes travaux actuels en témoignent. **Alexandre Lévesque**, en plus d'être un cuisinier hors pair, j'estime que tu es un des expérimentalistes les plus talentueux et les plus téméraires que j'ai rencontré jusqu'à maintenant. J'espère que tes talents t'apporteront tout ce dont tu as besoin et que l'on gardera contact pour de moins sérieuses affaires. **Tina Khadivjam**, ton français devrait désormais être suffisamment bon pour te permettre de comprendre que je « te kiff de ouf ! ». D'abord je salue le périple que tu as parcouru entre l'Iran et le Canada en parallèle de tes études que tu as réussies avec brio dans une région dont tu ne connaissais même pas la langue ! Même exilée à Toronto tu as toujours su prendre le temps de veiller sur moi et pour cela je te suis éternellement reconnaissant. J'espère pouvoir te remercier encore longtemps pour tout ce que tu auras fait pour moi. **Norbert Villeneuve**, tu es l'un des êtres les plus brillants et « flamboyant » que j'ai rencontré. Je t'ai regardé sortir de ton cocon et t'ouvrir le monde avec beaucoup de compassion et de tendresse. Ta minutie est exemplaire : tu réalises chaque étape de ton travail avec une patience et un soin qui m'ont beaucoup inspiré. J'espère que ta force tranquille ne cessera de se raffermir et te permettra de révéler ces fabuleuses choses dont tu es capable. **Abdel el Hamad**, j'ai un profond respect pour ta persévérance. Ton évolution me surprend encore : je t'ai vu écouter, changer, te remettre en question et constater avec admiration les efforts que tu as investis à devenir un bon chimiste mais aussi un bon père. Avec un père qui essaye sans cesse, tes enfants sont entre de bonnes mains. Nos discussions philosophiques m'ont également beaucoup inspiré. Si j'en ai la chance, j'aimerais moi aussi pouvoir m'épanouir aux côtés de ma famille dans un monde rempli de compassion. **Patrick Chartier**, un sacré personnage cultivant une ouverture d'esprit peu commune. J'ai toujours été fasciné par ta culture, tes lectures originales ainsi que les discussions philosophiques que nous avons eues. Un véritable penseur des sciences comme on en fait plus animé d'un sens de la fête bestial ! Je te souhaite beaucoup de réussite dans tes projets les plus sérieux comme les plus farfelus. On se reverra l'ami. **Aaron Gabriel Nunez Avila**, l'enfant prodige. Avec des jeunes comme toi je suis convaincu que l'avenir est entre de bonnes mains. Tu es talentueux, créatif et même en silence, les choses se passent dans ton sillage. Je rejoins tes nombreux amis qui t'ont témoigné leur affection de manière spectaculaire à de nombreuses reprises pour te dire que tu es une personne exceptionnelle. Reste en mouvement **Chetna Mohanty** : la fougue. J'ai rarement vu autant d'énergie dans un si petit corps ! Tu as une capacité incroyable à réunir les gens, les faire se sentir bien mais aussi à faire bouger les choses et avancer les projets. Je t'admire et t'apprécie comme une sœur. Avec une force pareille et un esprit aussi vif que le tien, rien ne t'arrêtera et tu pourras t'adapter à toutes les situations de la vie. **Jessica Patel** : la tendresse. De pair avec Chetna je te remercie infiniment

pour m'avoir exposé à la culture indienne qu'il me tarde de découvrir en personne. J'admire sincèrement ta douceur ta bonne humeur, ton ouverture d'esprit et ta générosité. J'ai maintenant une nouvelle grande sœur dont les pas guident les miens. **Puzhen Li**, chaque échange que l'on a eu m'ont beaucoup appris. J'ai beaucoup de respect pour ton parcours et la détermination dont tu as fait preuve. J'ai beaucoup apprécié ton altruisme et ta bienveillance. Merci particulièrement pour m'avoir encouragé à concourir pour la seule bourse d'étude que j'ai obtenue ! **Ilies Seddiki** le charboneur. J'ai énormément de respect pour ton parcours et ta ferveur. Je souhaite sincèrement que tes efforts paient (dans tous les sens du termes). Force kho. **Zachary Leduc** Je ressens beaucoup de talent et de bon sens à discuter avec toi. Je te souhaite beaucoup de réussite big Z ! **Érika Younk** merci pour ton implication autant dans le groupe et la vie du Départ' : il en faut plus comme toi ! Drôle, espiègle et vive d'esprit t'as bien souvent des perspectives pertinentes sur les choses et les gens. Hâte de voir ce que tu nous réserves ! **Loïc Carrier**, je m'estime privilégié d'avoir bénéficier de ton aide, ton dynamisme, ta générosité et ta motivation. Surtout reste aussi (si ce n'est plus) curieux, enthousiaste et travaillant que tu l'es déjà. Je regarde avec beaucoup d'intérêt ce que tu deviens, certain que beaucoup d'autres chanceux en bénéficieront car tu as énormément d'énergie à revendre ainsi que la capacité et l'envie de faire bouger les choses pour que tout le monde en profite. **Kisseline Romain**, le diamant brut. J'admire sincèrement ta persévérance, ton sens de l'observation et ton esprit critique. Peu de gens que j'ai rencontrés se remettent en question, cherchent à comprendre les choses en profondeur et envisager des perspectives comme tu le fais. Cultive ces qualités uniques, le reste suivra et de belles réalisations en découleront. **A-Jay Khanmohamed** Merci du fond du cœur pour m'avoir permis de prouver l'intérêt pratique de mes travaux à l'extrême dernière minute. Cela n'aura pas été possible sans ta détermination et le soin que tu mets dans ton travail. Je ressens beaucoup de sérieux et d'ambition chaque fois que nous discutons et j'espère qu'ils continueront d'accompagner tes projets. **Jim**, plus qu'un mentor scientifique, j'ai trouvé en toi un véritable ami, modèle et figure paternelle inestimable. Je respecte et admire profondément le personnage hors du commun que tu es. Je reconnais et m'inspire chaque jour du soin, de la patience, de la passion et de l'enthousiasme dont tu fais preuve dans chacune des choses que tu réalises : de la simple écoute de tes proches à tes prises de décisions avisées. C'était un honneur que de travailler avec toi. Je débute maintenant mon parcours autonome avec la certitude d'avoir reçu un bagage intellectuel et humain d'une grande qualité à tes côtés. Salutations affectueuses à **Mary** et **Spencer**.

Groupe Collins, je n'oublie pas d'où je viens et ne te remercierai jamais assez pour m'avoir pris sous ton aile à une époque où je doutais de moi-même. J'ai vécu de précieux moments auprès de tes membres passés et présents avec lesquels j'ai ri autant que j'ai pleuré et dont je chéris les souvenirs partagés. J'ai notamment eu l'immense privilège d'y côtoyer **Shawn Collins**, **Jeffrey Santandrea**, **Shawn Parisien Colette**, **Antoine Caron**, **Émilie Morin**, **Éric Godin**, **Sacha Nguyen**, **Florian D'ambra**, **Charlotte Cave**, **Bastien Rey**, **Noémie Beaucage**, **William Niderer**, **Cédric Bertin** et **Oliver Bleton**, **Guillaume Roland**, **Nicolas Dowe**. Mention spéciale à mon partenaire de *Whiskemistry* **Corentin Cruché**, auprès duquel le projet de doctorat

tel qu'il est écrit ici s'est matérialisé. Un grand merci également à **Christina Gagnon** ! Merci de continuer à veiller sur moi et pour toutes les belles soirées passées ensemble. Je sais que je peux toujours compter sur vous tous et inversement. Je suis particulièrement fier et heureux qu'on soit resté si complices avec les années. Je vous souhaite sincèrement de continuer à matérialiser ce potentiel et cette passion immenses que vous détenez. Merci au groupe **Schmitzer** et plus particulièrement à **Andreea** dont le cours de chimie supramoléculaire a profondément inspiré les premiers pas de mes travaux de doctorat. Un grand merci aussi au fraté **Guillaume Lefrançois** pour tous nos délires mais aussi tes conseils et pour les séances de natation que je n'aurais clairement pas repris sans tes encouragements. Un chaleureux et profond merci à toi aussi **Margaux Lecluse** que j'ai eu la chance d'apprendre à mieux connaître et dont j'ai apprécié chaque moment passé ensemble. Je ne te remercierai jamais assez pour ta participation à mon opération. Merci également au frérot **Pierre Maas** dont je salue respectueusement la somptueuse cuisine et la présence inconditionnelle et indispensable aux apéros. Un grand merci à **Julie Vatté** dont j'admire tout particulièrement la créativité en matière d'organisation de jeux et de soirées hors du commun, largement appréciés durant la pandémie. Je te remercie pour tout ça ainsi que pour les merveilleuses (bien arrosées)! Salutations amicales aux autres membres du groupe : **Alexandra Doré**, **Samy Faraj**, **Sigrid Lacaille**, **Julien Desloges**, **Philippe Beauclair** et **Maud Petit**. Je remercie chaleureusement les groupes **Charette**, **Lebel**, **Lubel**, **Hanessian, Dollé**, **Sauvé**, **Pellerin** et **Skene** pour nos soirées mémorables, les moments forts vécus ensemble ainsi que nos échanges enrichissants. Mention spéciale à **Céphas Amoah**, **Scarlett Kiyeleko**, **Claire Deilhes**, **Cédric Barcha**, **Gary Mathieu**, **Léa Thai-Savard**, **Léa Caradant**, **Yann Pauvert**, **Julien Mimeault**, **Olivier Schott**, **Yousra Hamdane**, **Nassim Maarouf**, **Darince Truong**, **Kévin Saint-Jacques**, **Arnaud Laramée**, **Agathe Le Moing** et **Justine Fontaine**. Un merci particulier à **Manon Faral** dont les paroles et le chemin sont d'or. Le silence également, qui démontre d'ailleurs encore une fois à quel point on se comprend. Merci pour tes si précieux conseils, écoute, aide, confiance et présence. BIIIG UP à l'**équipe du Café-In**, de l'**AEDCUM** et tous ceux avec qui j'ai passé des moments formidables durant ma dernière année : **Nicolas Leclainche**, **Laurence Pelletier**, **Megan McGeehan**, **Nahel Blanc**, **Diana Djurdjevic**, **Louis Hamlet**, **Élise Napolitano**, **Érica Tomassi**, **Nora Chelfouh**, **Ariane Caron**, **Alix Genieyz**, **Clémentine Troncy**, **Inès Mary**, **Mélina Fabe**, **Mick Vaillancourt**, **Rayan Zarrouky**, **Alexy Sanseigne**, **Michael Kuakuvi** et **Olivier Roy**. Merci pour les efforts incroyables que vous avez investis pour garder vivant le campus malgré la pandémie et le déménagement au campus MIL. J'ai rarement vu des personnes aussi déterminées, pleine de ressources et infatigables. Cette dernière année était magique, je vous adore !

J'ai l'immense privilège d'être encore étroitement lié aux amis avec lesquels j'ai grandi en France mais aussi ceux que j'ai rencontré lors de mes voyages. Tous m'ont toujours accueilli à bras ouverts, soutenu et encouragé chaleureusement et leurs interrogations pertinentes m'ont aidé à me remettre en question et grandir. Nous avons traversé beaucoup ensemble et j'espère encore vous avoir encore longtemps à mes côtés. Merci à **Paul Hoffmann**, **Claire Porecca**, **Julie Claude**, **Linda Delia**, **Antoine Bel**, **Victor Girardin**, **Alice Biondini**, **Johan Grünenwald**, **Fanny Marriet**, **Thomas Manuelli**, **Corentin Voegtlin**, **Martin Muhar**, **Kévin Nicolas**, **Lucas Schreiner**, **Coralie Lebrun**, **Sophie Du Boutiez**, **Mina Roussset**, **Laurine Vibert** et **Lucie Lagard**. Merci également à mes amis de Montréal, pour me sortir du labo et de mes pensées pour vivre des moments incroyables. Sans vous je serais passé à côté de beaucoup d'expériences qui font que la vie vaut la peine d'être vécu. Vous êtes un pilier essentiel à mon équilibre. Je veux parler bien sûr de **Jacques Courtès**, **Simon Delorme**, **Pierre Longpré**, **Adam Lazar**, **Thomas Guy**, **Mathieu Fonderflick**, **Jules Dube**, **OG Mike**, **Ephrem**, **Chloé Raffier**, **Caro** et **Stro**. **Mehdi**, **Sébastien**, **Amélie**, **Samy** et **Iliana** vous êtes la famille que j'ai à Montréal. Merci pour votre support inconditionnel. J'ai vécu de grands moments grâce à vous et été exposé à des cultures qui ont façonné ma personnalité. Notre amitié m'accompagnera longtemps.

Chers Oncles et tantes qui ont littéralement bercé ma vie: **Aimée**, **Marc**, **Omer**, **Géraldine**, **Sylvie**, **Clément**, **Yao**, **Sarah**, **Steven**, **Redempta**, **Lukas**, **Jeannine**, **Gilles**, **Varus**, **Barthy**, **Brigitte**, **Kodjo**, **Béthel**, **Barbara** et **Philippe** je vous remercie profondément pour l'amour et les enseignements que vous m'avez prodigués. On m'a dit un jour que la réussite d'un Homme pouvait être évaluée à son nombre d'oncles et de tantes. Si tel est le cas, alors je suis le plus fortuné d'entre eux ! Salutations chaleureuses aux amis de la famille également. **Les cousins et cousines** : On est ensemble. **Papa** et **Maman**, vous êtes des parents exemplaires. Vos recommandations et enseignements sont à la base de tout ce que j'entreprends et de mes relations. Les valeurs que vous m'avez transmises et les expériences que vous m'avez permis de vivre me font aujourd'hui d'apprécier une vie belle et libre. C'est le présent pour lequel je vous suis le plus reconnaissant. J'espère profiter encore longtemps de votre présence et réaliser des projets conjoints à l'aide de mes nouvelles ressources. Avoir l'honneur de savourer les fruits d'un labeur commun serait pour moi l'une des plus prestigieuses et agréables réalisations qui me serait donner d'accomplir. **Olivier**, je suis si fier de toi. Tu es l'être le plus attachant que je connaisse et dont je me sens le plus proche. Ta bienveillance et ta joie de vivre m'inspire. Le monde se porterait mieux avec plus de gens comme toi. Profite de chaque journée comme si c'était la dernière, mais veille à préparer convenablement la suivante, juste au cas où. **Ambre**, grâce à toi l'idiot du village que je suis est devenu plus attentif, conciliant, structuré et pragmatique. Plusieurs de mes projets fous se sont matérialisés par le simple fait de te les avoir exposés. J'ai littéralement appris à franchir des étapes et me servir de mon esprit chaotique à tes côtés. De plus, tu m'as convié à vivre des aventures formidables à travers le monde qui m'ont profondément marqué. Bien que j'aie toutes les raisons imaginables de t'aimer un peu plus chaque jour, je ne sais toujours pas ce qui me vaut en retour l'immense privilège de tes tendresses. Toutefois, je compte bien offrir tout ce que je peux pour continuer de grandir auprès de toi et de ta famille que je salue et remercie bien affectueusement.

Chapitre 1. Introduction

Pigments et colorants rythment silencieusement rites et coutumes des civilisations humaines depuis des millénaires. Les fresques pariétales du monde entier témoignent d'initiatives universelles de transmission de connaissances ainsi que d'une compréhension intime du monde naturel (Figure 1.1). En effet, le pigment rouge de plusieurs de ces œuvres, l'hématite (Fe_2O_3), a été préparée en chauffant la goethite (FeOOH) de couleur jaune.[1] L'hématite ainsi préparée par la main humaine est dite synthétique, du grec *σύνθεσις/súnthesis* « action de composer ». C'est donc depuis la nuit des temps que l'Homme étudie la matière qui l'entoure, ses propriétés et ses transformations : discipline aujourd'hui appelée chimie. Ce chapitre introductif décrira comment l'étude des matières colorantes a influencé la conception de matériaux modernes.

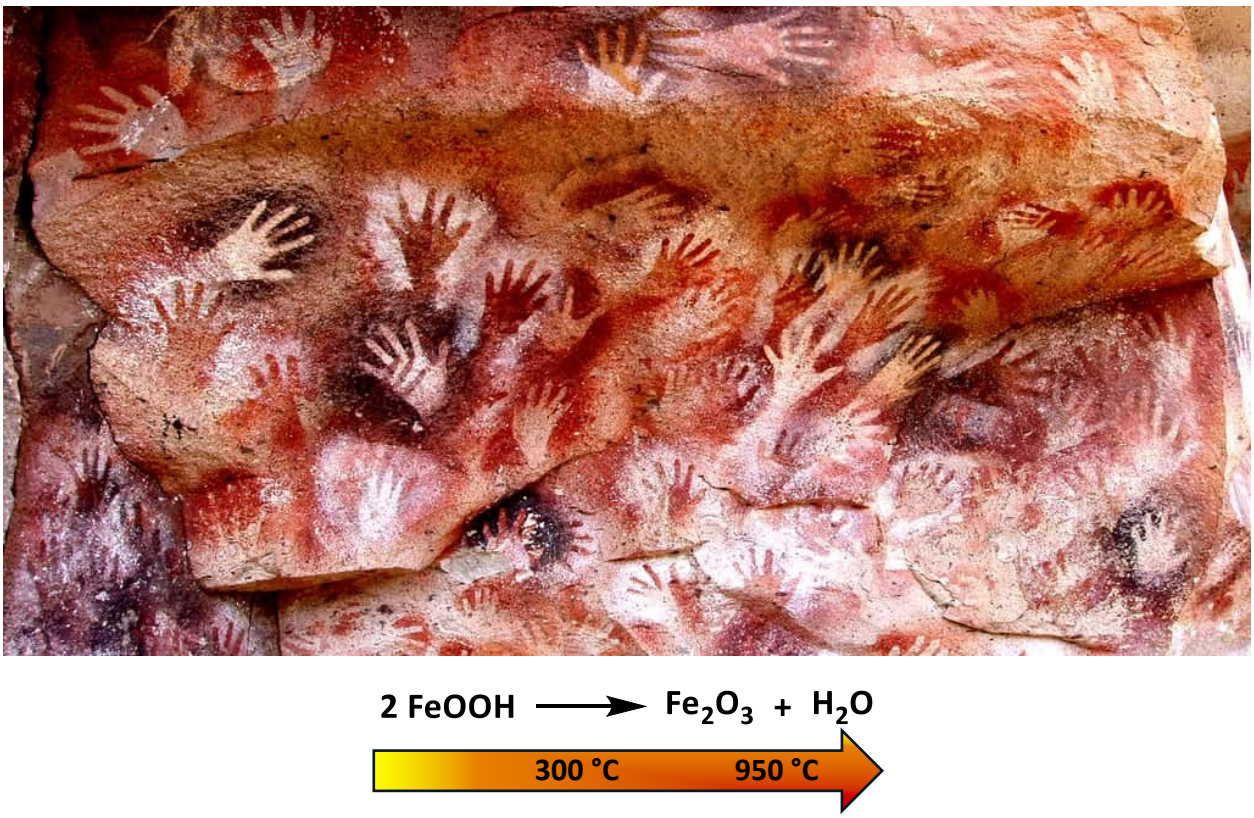

Figure 1.1 Photographie de peintures rupestres réalisées entre 52 et 40 000 ans avant notre ère sur l'île de Bornéo et transformation de la goethite en hématite.[1,2] ©Mariano, CC by-sa 3.0.

1.1. Une histoire haute en couleur !

Au XIXe siècle, la houille, minéral riche en matières carbonées fossilisée, était extraite pour produire le gaz d'éclairage dont la combustion illuminait les nuits de plusieurs villes européennes.[3] La distillation pyrogénée de la houille générait également un goudron duquel étaient isolés le benzène, l'aniline, le phénol et plusieurs de leurs dérivés. Les chimistes de ce temps utilisaient ces substances pour préparer des matières colorantes telles que la mauvéine (**1**), l'alizarine (**2**) ou l'indigo (**3**, Figure 1.2). L'élucidation de la constitution atomique et le développement de méthodes de synthèse de ces matières contribueront aux fondements de la chimie organique moderne dédiée à l'étude des substances essentiellement constituées de carbone, hydrogène, oxygène et azote (C, H, O et N).

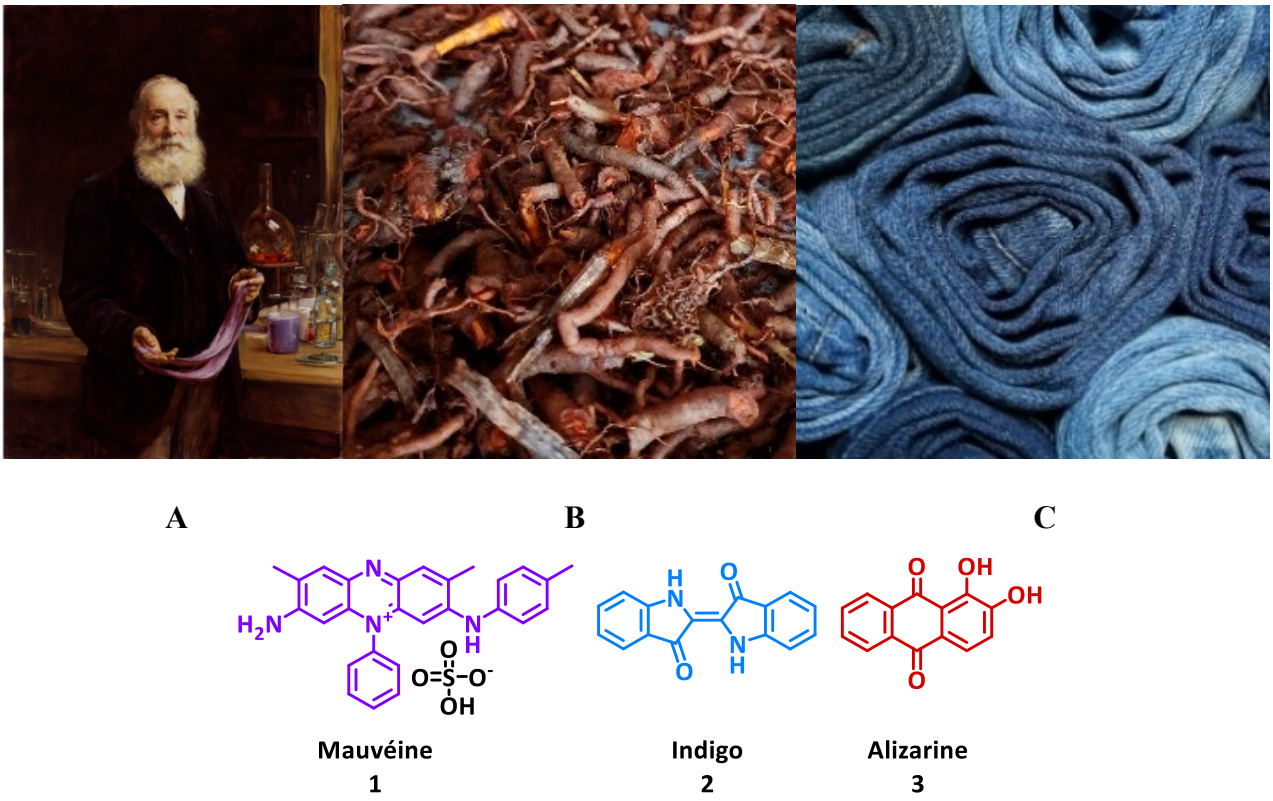

Figure 1.2 (**A**) Portrait de Sir William Perkin qui découvrit accidentellement la mauvéine (**1**) en 1856.[4] Par Sir Arthur Stockdale Cope ©*National Portrait Gallery*. (**B**) Racines de la garance des teinturier (*Rubia tinctorum*) du Québec. Source d'alizarine (**2**), produite industriellement dès 1869. ©Dahlia Milon.[5,6] (**C**) *Blue jeans* teints à l'indigo (**3**) dont la première synthèse totale est

publiée par Viggo Drewsen et le lauréat Nobel Adolph von Baeyer.[7] ©Kranich17, *Content licence*.

Alors que les noms Liebig, Kekulé ou Bayer sont passés à la postérité, d'éminents chimistes dont l'impact des travaux est encore retentissant demeurent méconnus. Parmi eux figure Rudolf Hugo Nietzki (1847-1917), chimiste prussien à l'influence considérable sur la recherche fondamentale et industrielle sur les matières colorantes organiques (Figure 1.3).[8–10] L'élogieuse notice nécrologique d'Emilio Noelting détaille en français l'étendue des travaux de Nietzki qui y apparait comme un prolifique et entreprenant chercheur au parcours atypique.[9] Féru de botanique et de littérature, il est successivement pharmacien, prisonnier de guerre et chimiste indépendant avant d'obtenir un doctorat de l'Université de Göttingen sous la supervision d'August W. von Hofmann en 1874. Devenu professeur à l'Université de Bâle en 1884, il y enseignera et travaillera en laboratoire jusqu'à 64 ans avant de décéder 6 ans plus tard, affaibli par l'artériosclérose.

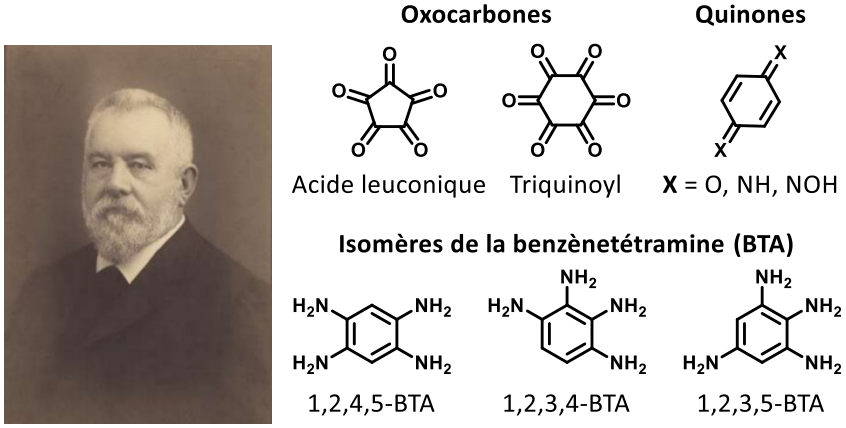

Figure 1.3 Photographie de Rudolf Hugo Nietzki en 1910. ©Conrad Ruf. Composés étudiés par son groupe de recherche, pertinents aux matériaux moléculaires conçus au XXIe siècle.

Nietzki est reconnu par ses pairs pour la rédaction d'un ouvrage de référence sur les matières colorantes organiques traduit dans plusieurs langues et utilisé plusieurs décennies après sa mort.[3] Il a également élucidé la constitution et synthétisé de nombreuses molécules organiques

de type oxocarbones, quinones et arylamines.[9,10] Son groupe de recherche étudia notamment les isomères de la benzènetétramine (BTA), motif central du projet de recherche résumé dans la thèse. La plupart de ces composés sont aujourd'hui intensivement étudiés pour le développement d'électrodes de batteries organiques (Chapitre 1.3.).

1.2. Matériaux moléculaires

Les matériaux organiques (majoritairement faits de C, H, O et N) sont essentiels à la vie humaine. Les protéines en sont un exemple saisissant constituant, entre autres, os, peau et poils sous forme de collagène, d'élastine et de kératine respectivement.[11] Étonnamment, leur diversité structurelle et fonctionnelle émane de leur point commun : les acides aminés (AA) qui les composent (**Schéma 1.1**). En effet, l'ensemble de nos protéines sont assemblées à partir d'une vingtaine de différents AA formant des polypeptides (structure primaire) variant en nombre et en type d'AA intégrés. Ces polypeptides flexibles peuvent se replier sur eux-mêmes pour former des hélices ou des feuillets (structures secondaires) consolidés des liens covalents et/ou électrostatiques intramoléculaires. L'ensemble des structures primaires et secondaires est qualifié de protéine (structure tertiaire), dont forme et réactivité sont dictées par la disposition relative et la nature des AA qui la constituent. Les protéines peuvent à leur tour s'agréger en de plus larges structures (dites quaternaires) comme l'hémoglobine par exemple, qui transporte l'oxygène dans le sang.

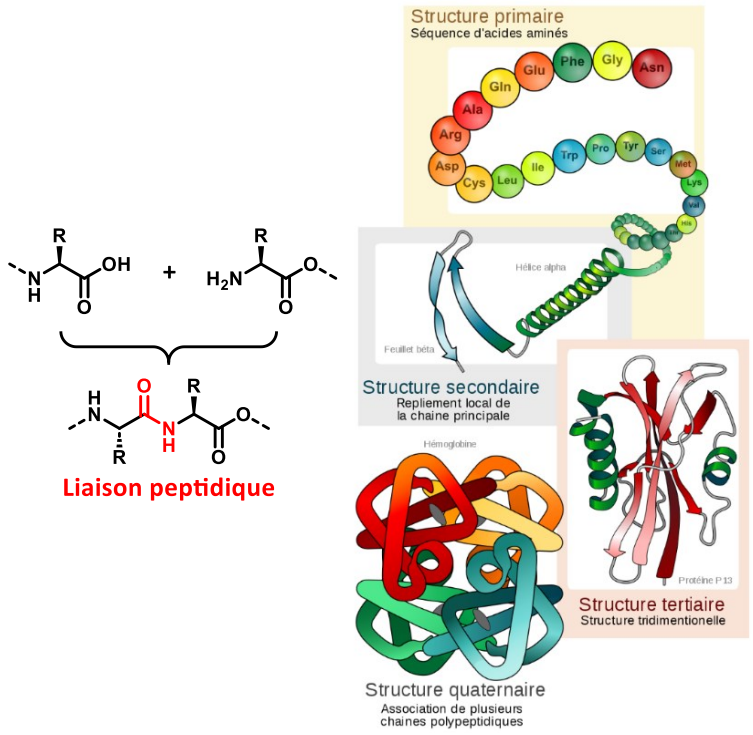

Schéma 1.1 Peptides et structures d'organisation protéique. ©LadyofHats, WikimediaCommons.

L'étude des matériaux biologiques révèle qu'un contrôle précis de la nature et de la disposition relative de leurs constituants, ainsi que des paramètres de leur milieu (température, pH ou présence de sels), régit leurs propriétés structurales et physicochimiques. L'évolution des connaissances synthétiques et des méthodes d'analyse nous permettent aujourd'hui de concevoir des molécules qui, à l'instar des AA, sont capables de s'agréger de manière relativement prédictible pour générer des matériaux aux propriétés programmées.

1.2.1. Le cristal : la supramolécule par excellence

La chimie supramoléculaire est l'étude des assemblages moléculaires.[12] Lorsque ceux-ci sont suffisamment ordonnées dans une ou plusieurs dimensions de façon régulière et périodique, il arrive qu'ils cristallisent (Figure 1.4). L'organisation intrinsèque des cristaux est si régulière qu'elle peut être modélisée à partir de patrons de diffraction de rayons X incidents. Le réseau cristallin ainsi modélisé est souvent décrit par sa maille élémentaire : le plus petit motif détenant suffisamment d'informations structurelles pour reproduire l'ensemble de l'assemblage. Les

cristaux sont utilisés comme pigments, en pharmacologie, en catalyse et pour le stockage de gaz et d'énergie parmi pléthore d'applications.[13–17] Il est donc enviable de développer des stratégies ascendantes pour bâtir des matériaux cristallins aux propriétés programmées dont les contraintes et enjeux seront discutés.

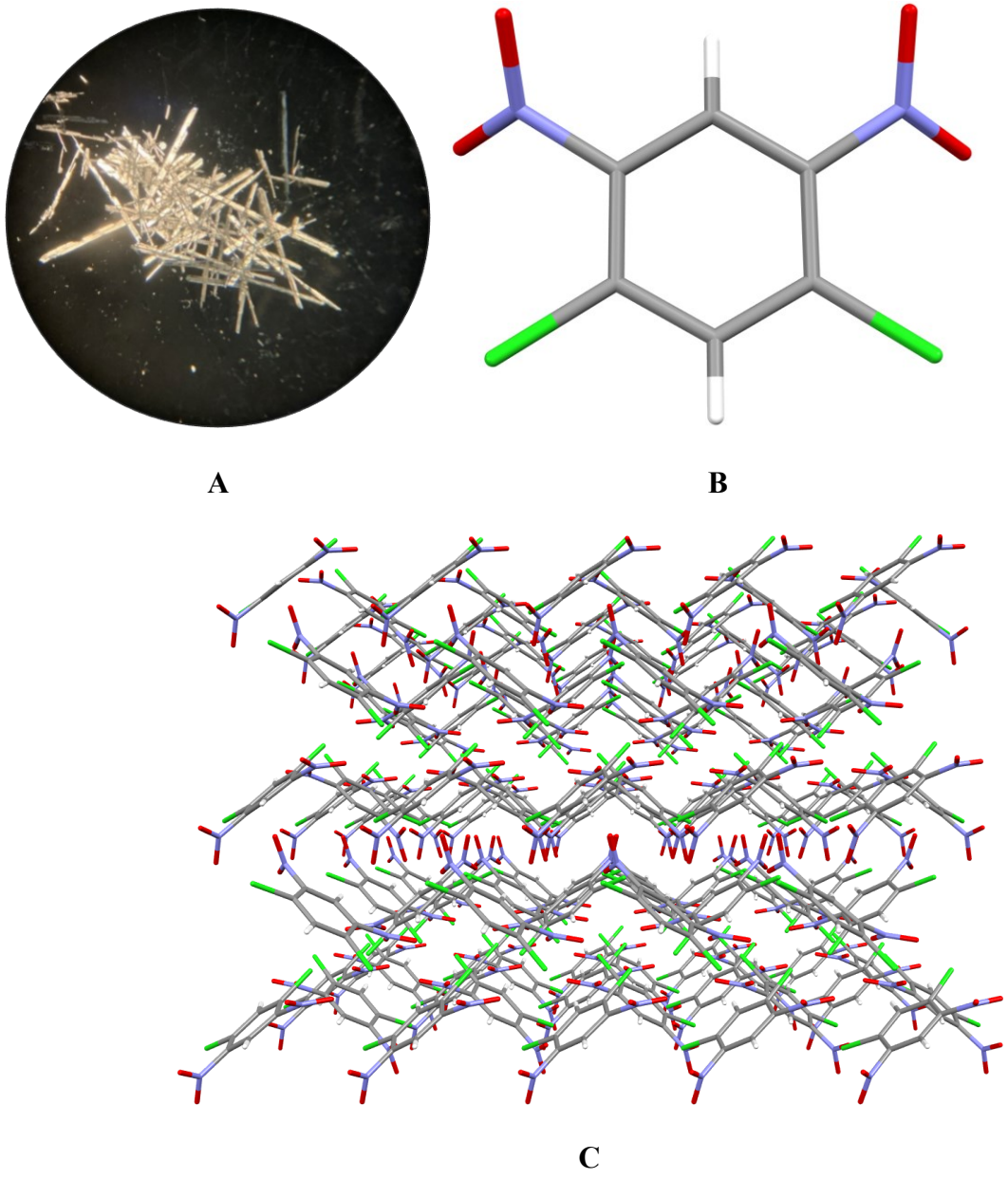

Figure 1.4 (**A**) Micrographe optique de monocristaux de 2 à 3 cm de long du 1,5-dichloro-2,4-dinitrobenzène éclairés sous lumière polarisée. (**B**) Structure et (**C**) maille cristallines résolues par diffraction de rayons X. Code couleur : O, rouge; N, bleu; Cl, vert; C, gris; H, blanc.

1.2.2. Le processus de cristallisation

Les molécules constituant un cristal sont ordonnées de manière périodique sur une distance plusieurs fois supérieure à leurs tailles individuelles. Dans leur forme cristalline la plus stable, elles adoptent une configuration dans laquelle l'intensité et le nombre d'interactions intermoléculaires attractives sont maximisées. En effet, la cristallisation est alimentée par une force motrice enthalpique qui compense la perte de degrés de liberté de translation, rotations et vibrations des molécules impliquées.[12] *A priori*, la conception judicieuse des unités à cristalliser devrait permettre de prédire sans équivoque l'arrangement du réseau. Dans les faits, l'issue du processus demeure incertaine en partie à cause de son amorce : la nucléation (Schéma 1.2).[18,19]

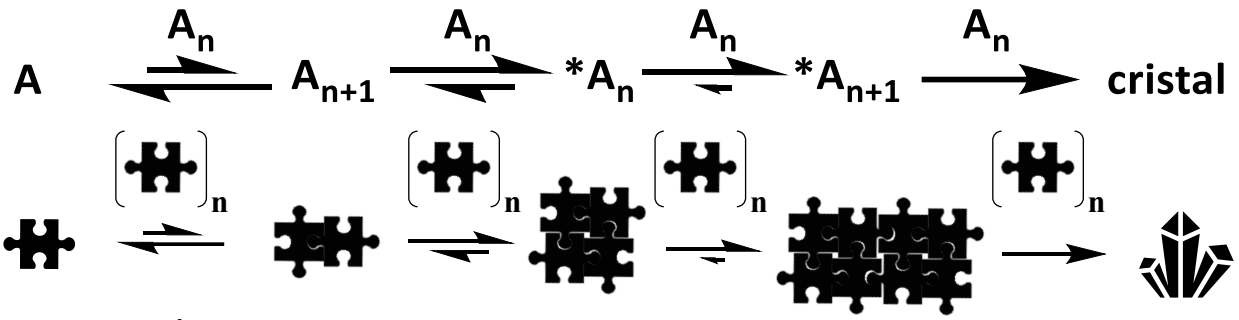

Schéma 1.2 Étapes de cristallisation d'une molécule A en solution saturée ou pure et fondue avec n = 1, 2, 3, … et An* un noyau stable de taille critique.

Considérons la formation d'un cristal généré à partir d'une solution saturée en une molécule **A**, ou de la substance **A** pure et fondue.[12,18] La cristallisation débute par la reconnaissance des molécules **A** en solution qui s'agrègent étroitement pour maximiser leurs interactions attractives et minimiser les interactions répulsives ainsi que le vide entre elles.[20] Les agrégats dissous ($\mathbf{A_{n+1}}$) vont alors réversiblement s'assembler jusqu'à former un noyau stable ($\mathbf{*A_n}$) autour duquel le cristal se forme. En dessous de la taille critique de $\mathbf{*A_n}$, le facteur entropique prédomine et l'équilibre penche vers la dissolution. Cette taille critique est inversement proportionnelle à la concentration de monomères **A** disponibles pour agrégation. De multiples paramètres dirigent la nucléation : la diffusion des monomères dans le liquide, leurs propriétés stéréoélectroniques intrinsèques, leur cage de solvatation, la pureté du milieu, ainsi que

le temps et l'énergie thermique alloués à leur formation.[19] En effet, le coût d'énergie libre payé par le système pour générer l'interface liquide-agrégats doit être compensé par la libération d'énergie issue de la cristallisation. De surcroit, il est difficile de déterminer comment, où et à quelle fréquence la nucléation opère, à quel point les noyaux critiques sont ordonnés et dans quelle mesure les interactions solvant-noyaux influencent leurs structures. Ainsi, même en contrôlant les paramètres de cristallisation ainsi que la nature et la position des éléments de reconnaissance moléculaires, la manière dont les molécules vont s'agréger durant la nucléation ne peut pas être déterminée avec certitude. Une branche de la chimie supramoléculaire s'intéresse toutefois aux façons de contrôler la cristallisation : l'ingénierie cristalline.[19]

1.2.3. L'ingénierie cristalline

L'aspect, la couleur, le point de fusion, ou encore la réactivité des cristaux sont des propriétés en partie régies par la nature et l'arrangement des molécules les constituant. L'ingénierie cristalline tente d'établir des méthodes pour contrôler la formation des réseaux cristallins malgré les incertitudes inhérentes à l'issue de la cristallisation (Chapitre 1.2.2).[19,20] Il est généralement plus facile d'orienter des molécules rigides dont la forme défavorise l'empilement compact : tel est le cas des composés aromatiques notamment dérivés du triptycène (**4**), du tétraphénylméthane (**5**) ou du spirobifluorène (**6**, Schéma 1.3).[17,21] Ces motifs sont souvent munis de fonctions chimiques qui se lient les unes aux autres de manière directionnelle, covalente et/ou électrostatiques, suffisamment fort pour diriger l'orientation des motifs d'attache (Chapitre 1.2.4). Une fois les modules de construction conçus et synthétisés, les conditions expérimentales de cristallisation menant à l'arrangement escompté sont criblées (étape requérant beaucoup de patience et une pincée de chance). Ce criblage peut être assisté par ordinateur en réalisant des prédictions statistiques à partir des bases de données cristallographiques et de calculs (dynamique moléculaire et/ou densité fonctionnelle théorique).

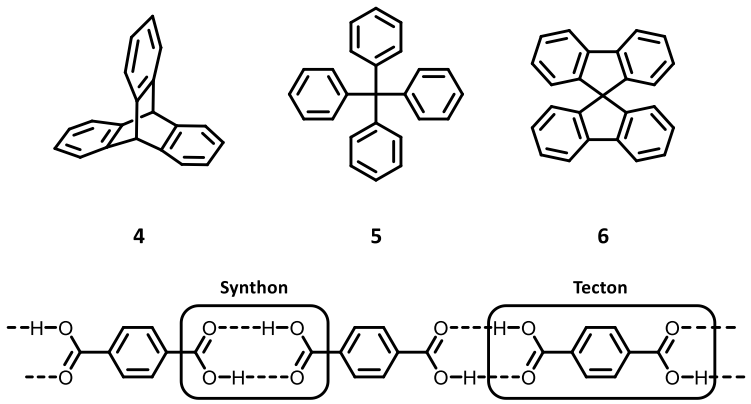

Schéma 1.3 Motifs, synthons et tectons récurrents en ingénierie cristalline.[17,20,21]

Les bases de données cristallographiques regorgent également de précieuses informations. Le *Cambridge Crystallographic Data Centre* (CCDC), par exemple, créé en 1965 par Olga Kennard, compte aujourd'hui plus d'un million d'entrées d'un support inestimable pour l'ingénierie et l'étude des structures cristallines.[22] Des motifs de reconnaissance appelés parfois synthons ou tectons peuvent y être dénichés. Ce terme désigne les fonctions chimiques non-covalentes impliquées dans la reconnaissance.[23] Le mot tecton désigne « toute molécule dont les interactions sont dominées par des forces associatives particulières qui induisent l'autoassemblage d'un réseau organisé avec une architecture spécifique ou des propriétés fonctionnelles. ».[24] Différents exemples de matériaux cristallins ingénieusement conçus selon ces concepts seront maintenant présentés.

1.2.4. Matériaux cristallins poreux : HOFs, COFs et MOFs

Il est généralement plus facile de synthétiser des molécules organiques à la constitution et configuration atomique désirées que de les faire cristalliser de manière contrôlée. En effet, plus ces molécules arborent de fonctions chimiques différentes, plus elles disposent de façons de s'agréger. Tout cela combiné aux incertitudes inhérentes au processus de cristallisation (chapitre 1.2.2) amène les ingénieurs de cristaux à exploiter des phénomènes de reconnaissance fiables et versatiles. En ce sens, la formation de ponts hydrogène a grandement été exploitée, notamment grâce aux motifs recensés par la Prof. Margaret Etter.[25] En l'occurrence, les fonctions 2,3-diaminotriazine (DAT) et carboxyles greffés à des molécules rigides génèrent souvent des

réseaux cristallins poreux : les *Hydrogen-bonded Organic Frameworks* (HOFs).[17,21,26] Leurs pores sont souvent accessibles à des molécules invitées de solvant ou de gaz. La flexibilité des ponts hydrogène rend les HOFs généralement plus flexibles que les matériaux consolidés par des liens covalents ou ioniques et donc plus accommodables au gonflement. Ils sont en revanche plus susceptibles de s'effondrer lors de l'excrétion des molécules invitées. Ceux qui résistent à l'effondrement sont dits à porosité permanente (Figure 1.5).[27,28] Certains HOFs peuvent être dissous pour récupérer les tectons intacts et régénérer le matériau par recristallisation.

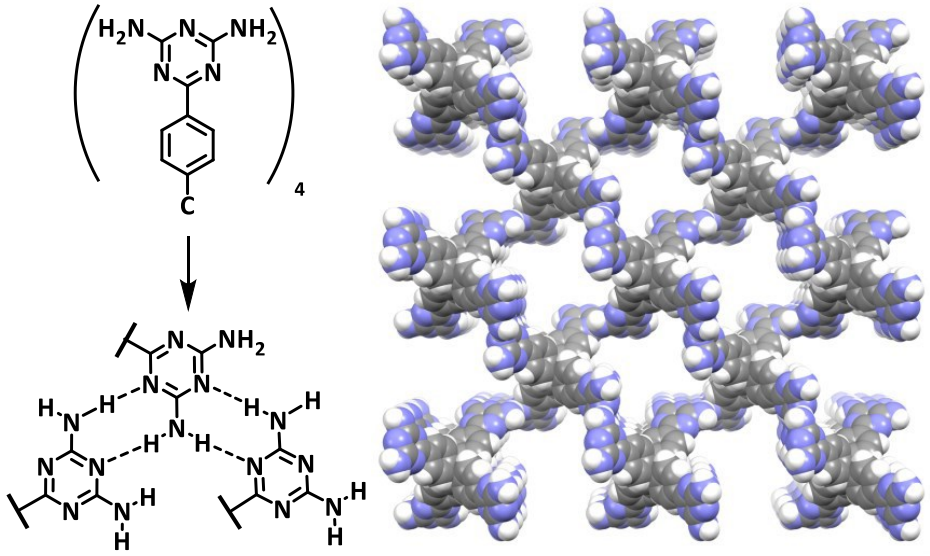

A **B**

Figure 1.5 (**A**) Schéma structurel d'un tecton dérivé du tétraphénylméthane fonctionalisé avec des unités DAT capable de s'assembler via des ponts hydrogène. (**B**) Structure cristalline du réseau formé par ce tecton. Code couleur : C, gris; N, bleu; H, gris.[27,28]

Bâtir des assemblages cristallins à 1, 2 ou 3 dimensions à partir de liens covalents C-C simples ou insaturés avec un haut degré de précision est un défi de taille.[17,29] En effet, la plupart des réactions de polymérisation forment des solides insolubles et peu cristallins. Il est alors difficile de briser ces liens pour corriger les défauts du réseau sans nuire à l'intégrité de sa structure. Pour pallier ces limitations, des réactions réversibles dans les conditions expérimentales de cristallisation sont exploitées comme des condensations (formation d'imines)

ou la polymérisation des acides boroniques, composés nitroso et nitriles (Figure 1.6).[30,31] De larges cristaux dont les pores sont accessibles à des molécules invitées ont ainsi été produits. Les réseaux construits avec des liens réversibles sont parfois sensibles à l'extrusion de molécules invitées, au pH et à la présence de nucléophile/électrophiles. De par la potentialité de former des matériaux cristallins aux surfaces π étendues, les réseaux covalents organiques (COFs) sont particulièrement intéressants en vue d'applications électroniques.[32–34]

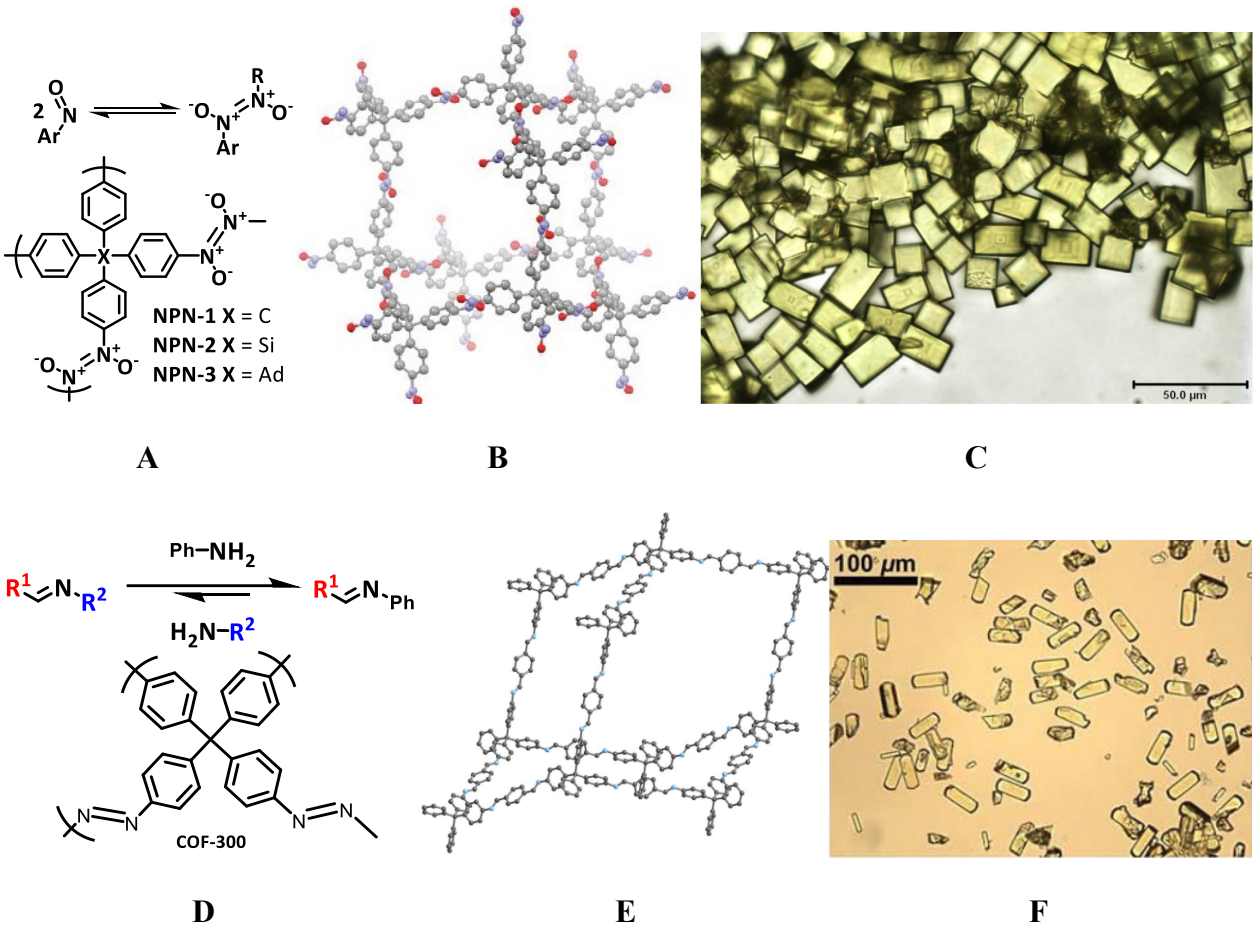

Figure 1.6 (**A**) Schéma de l'équilibre nitrosoarènes-azodioxydes et structures des matériaux obtenus grâce à ce principe. (**B**) Structure cristalline diamantoïde de **NPN-1**. Code couleur : O, rouge; C, gris; N, bleu. (**C**) Micrographe optique de monocristaux de **NPN-1**. (**D**) Schéma de l'échange d'imine utilisé pour construire **COF-300** en présence d'un excès d'aniline. (**E**) Structure cristalline diamantoïde de **COF-300**. Code couleur : C, gris; N, bleu. (**F**) Micrographe optique de monocristaux de **COF-300**. Les figures **B** et **C** sont reproduites avec permission de la

référence 30, © 2013 *Springer Nature Limited* ; les figures **E** et **F** avec celle de la référence 31, © 2018 *The American Association for the Advancement of Science*.[30,31]

Les composés cristallins de coordination forment un autre type de matériaux utilisés, entre autres, pour la séparation, en électronique ou pour la délivrance de principes actifs médicamenteux.[16, 36-39] Ils sont souvent formés à partir de ligands ditopiques rigides liés à des métaux de transition.[38,39] La forme des ligands et la géométrie du centre métallique (tétra/octaédrique ou encore plan carré) déterminent l'architecture du réseau cristallin. Les polymères de coordination, linéaires, plan ou 3D, sont souvent distingués des *Metal-Organic Frameworks* (MOFs) tridimensionnels à porosité permanente.[40] Les MOFs dérivés de Zn^{2+}, Zr^{2+}, Co^{2+} et de polyacides carboxyliques aromatiques sont peut-être les composés les plus emblématiques de cette famille (Figure 1.7). Ils sont souvent caractérisés par leur porosité leur conférant des surfaces de l'ordre de 1 000 $m^2 \cdot g^{-1}$ (évaluée par adsorption de gaz) et la versatilité de leurs structures. Les MOFs peuvent être synthétisés par voie autoclave, assistée par micro-ondes ou électrochimique parmi d'autres.[41] La voie autoclave consiste souvent à faire réagir un sel du cation d'intérêt et ses ligands dissous en solution à haute pression et température durant plusieurs jours. Ce procédé génère souvent de larges cristaux mais requiert des conditions drastiques, et de longs temps de réaction. La méthode est donc difficile à mettre à l'échelle.

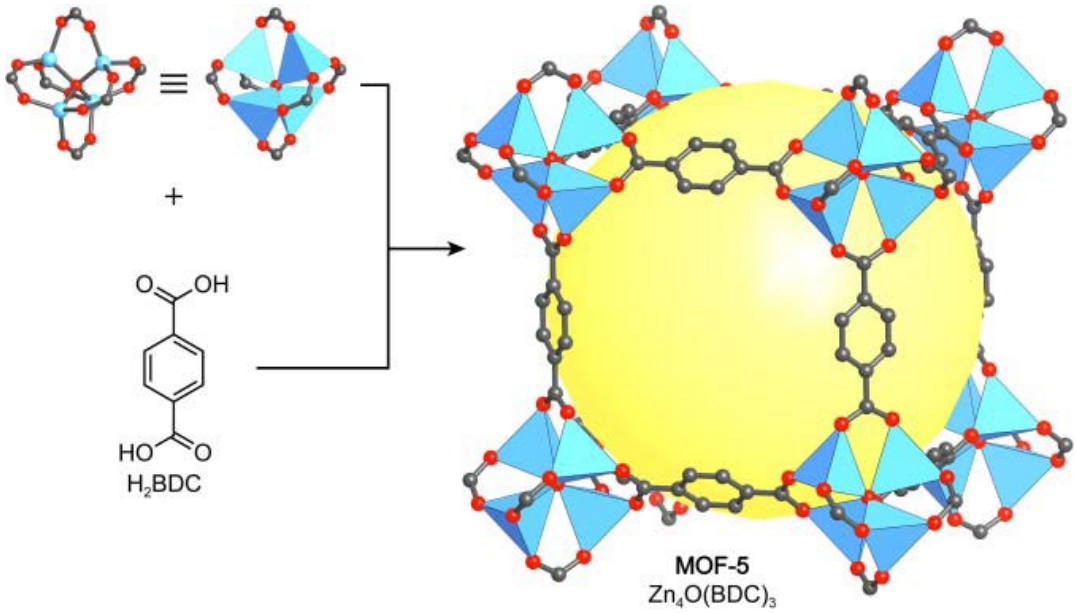

Figure 1.7 Structure cristalline de **MOF-5** construit à partir $Zn_4O(CO_2)_6$ et du ligand ditopique **H_2BDC**. La sphère jaune représente le plus grand volume pouvant être mis à l'intérieur du pore sans pénétrer les rayons de van der Waals des atomes le constituant. Les hydrogènes ont été omis par soucis de clarté. Code couleur : Zn, bleu; C, gris; O, rouge. Figure reproduite avec la permission de la référence 38, © 2019 *Wiley-VCH Verlag GmbH & Co. KGaA*.[38,42]

Ultimement, l'ingénierie cristalline tend à établir des stratégies ascendantes et fiables pour bâtir des cristaux aux propriétés programmées par la conception rationnelle d'unités de construction moléculaires. Le Chapitre 2 présentera des façons dont l'ingénierie cristalline peut être utilisée pour pallier les défis énergétiques contemporains.

1.3. Le défi contemporain du stockage d'énergie

Le XXIe siècle est une ère de progrès technologique sans précédent : jamais il n'a été aussi facile de se déplacer et de communiquer aussi vite et loin. L'électrification des transports et la démocratisation des appareils électroniques nomades (téléphones, ordinateurs et montres intelligentes) ont toutefois un coût énergétique et écologique important. En effet, leurs composantes contiennent souvent des métaux précieux (généralement lithium, cobalt ou tantale) isolés par des procédés énergivores et polluants. Dans certaines régions du monde, ces appareils sont alimentés par

des sources d'électricité hautement émettrices de gaz à effet de serre. Dans un contexte de demande énergétique mondiale croissante, ces problématiques stimulent de nombreux projets visant à durablement faire bénéficier le grand public du confort des technologies modernes. En ce sens, les énergies renouvelables (solaire, hydroélectrique ou géothermique) sont attractives. Elles sont toutefois intermittentes et réparties inégalement sur Terre. Pour être exploitées efficacement, elles doivent être collectées et stockées au moment où elles sont le plus affluentes.

1.3.1. Les batteries

Les batteries sont des dispositifs capables de convertir sur demande l'énergie électrique en liens chimiques et inversement.[43] Elles offrent donc une solution séduisante pour stocker les énergies renouvelables lorsqu'affluentes. Trois composantes sont essentielles à leur fonctionnement : un électrolyte et deux électrodes (anode et cathode) formant ensemble une cellule électrochimique (Schéma 1.4).[44] Durant la décharge, l'oxydation de l'anode libère des électrons conduits à travers le circuit électrique à alimenter et dirigés à la cathode qui est alors réduite. Si la batterie est rechargeable, l'application d'un potentiel force le processus inverse. Les électrodes sont en contact constant avec un électrolyte (fluide ou solide), faisant office de medium où les ions se déplacent pour équilibrer les charges dans la cellule. Une membrane poreuse, perméable aux ions mais pas aux électrons, sépare les électrodes et empêche les courts-circuits.

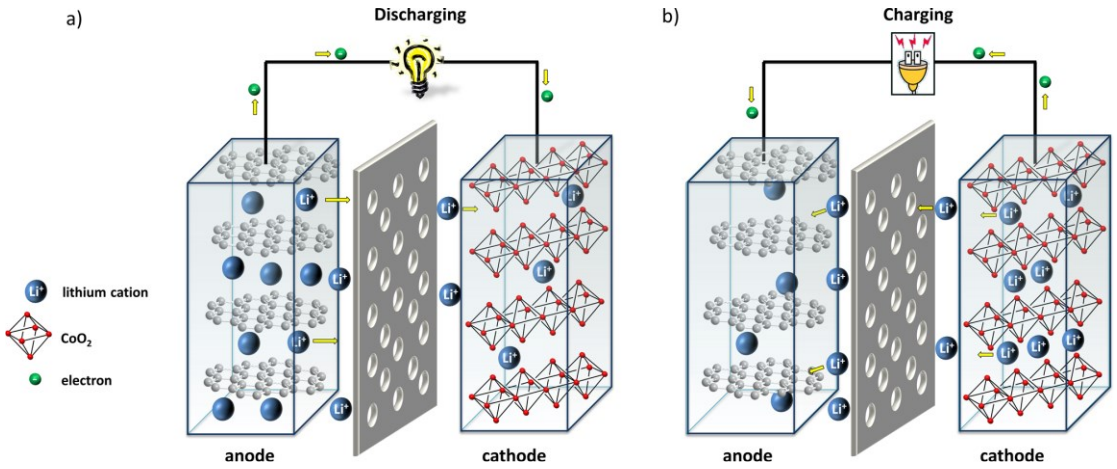

Schéma 1.4 Décharge et charge d'une cellule électrochimique de type LCO/graphite. Figure reproduite avec la permission de la référence 44, © 2016 *American Chemical Society*.[43,44]

On distingue les cellules électrochimiques primaires (non rechargeables) des cellules secondaires (rechargeables).[43] Le terme batterie désigne l'ensemble des cellules électrochimiques secondaires, reliées en parallèle ou en série, qui composent le pack de batterie d'un appareil nomade. Le principe de fonctionnement des cellules électrochimiques est universel mais leur conception et composition peuvent différer. Le reste de la discussion sera porté sur la technologie Li-ion, l'une des plus établies en termes de performances et de sécurité.[16,43,45] Leur ubiquité est telle que les batteries Li-ion dépassent bien souvent le nombre de personnes (munies de téléphones et de montres intelligents) dans une pièce !

1.3.2. Enjeux liés aux électrodes solides

Le lithium est l'élément le plus électropositif du tableau périodique et l'un des plus légers. Pour ces raisons, il est utilisé pour la fabrication de dispositifs à haute énergie spécifique (E_{spe}, $kW \cdot h \cdot kg^{-1}$) et haute densité d'énergie (E_{dens}, $kW \cdot h \cdot L^{-1}$). Les cellules électrochimique Li-ion commerciales sont en général constituées d'une anode graphitique, d'un sel de lithium, d'un électrolyte (fluide ou solide) et d'une cathode métallique (Figure 1.8).[17,44] Les carbones graphitiques sont fréquemment utilisés dans les appareils commerciaux. Ils sont conducteurs, plus légers que la plupart des métaux de transition, souples et organisés en feuillets perméables aux ions Li^+. Le lithium y est réversiblement désinséré sans former de dendrites. Une capacité spécifique (C_{spe}, $mA \cdot h \cdot g^{-1}$) de l'ordre de 350 $mA \cdot h \cdot g^{-1}$ peut en être extraite. Cette grandeur représente l'énergie emmagasinée dans l'électrode et est proportionnelle au nombre d'électrons expérimentalement échangés par sa matière active durant un cycle de charge ou de décharge. Dans l'idéal, une cellule secondaire est assemblée avec des électrodes dont les capacités spécifiques de décharge et de recharge sont stables sur un grand nombre de cycles (C_{spe}(anode) = C_{spe}(cathode) et C_{spe}(décharge) = C_{spe}(recharge)). Cependant, les valeurs de C_{spe} des matériaux cathodiques d'usage sont deux fois moins élevées que ceux des anodes graphitiques. Les performances de la cathode limitent donc celles de la cellule.

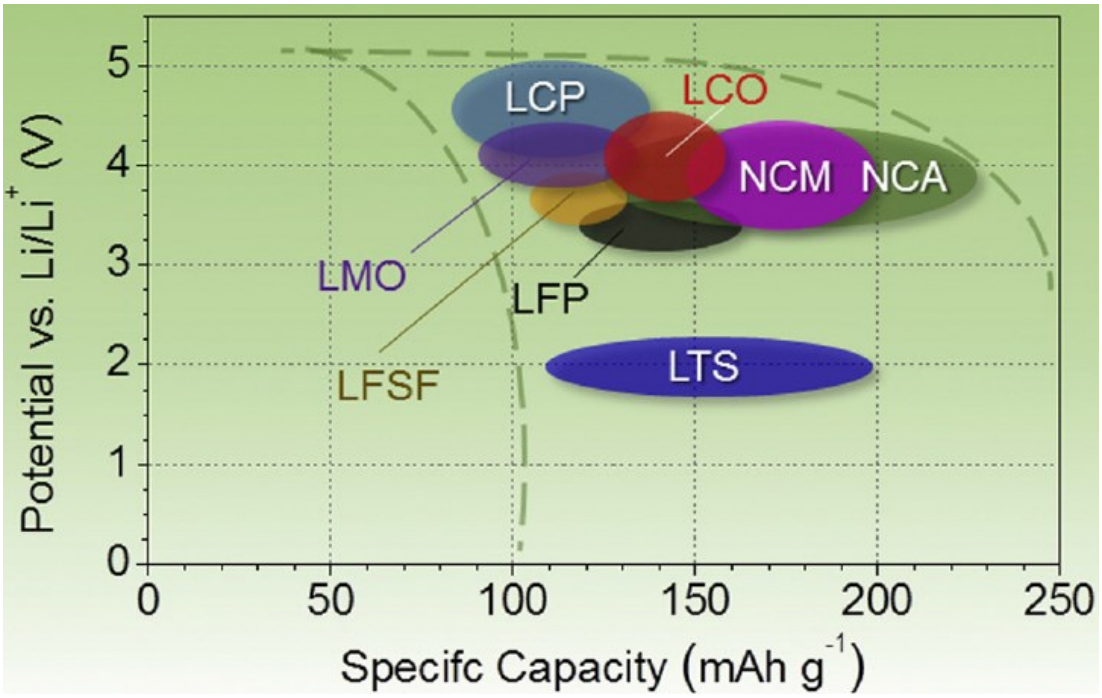

Figure 1.8 Tension de décharge en fonction de la C_{spe} de matériaux cathodiques commerciaux. LCP = $LiCoPO_4$; LMO = $LiMnO_2$; LFSF = $LiFeSO_4F$, LFP = $LiFePO_4$; LCO = $LiCoO_2$; NCM = $LiNi_xCo_yMn_zO_2$; NCA = $LiNi_{0.8}Co_{0.15}Al_{0.05}O_2$; LTS = $LiTiS_2$. Figure reproduite avec la permission de la référence 47, © 2014 *Elsevier Ltd*.[47]

Les matériaux cathodiques usuels des cellules Li-ion commerciales sont des oxydes, phosphates ou sulfides de métaux de transition.[16,47,48] Ils sont qualifiés de matériaux d'intercalation car les ions Li^+ y diffusent, *via* des sites de coordination vacants. L'oxyde de cobalt lithié $LiCoO_2$ (LCO), introduit en 1990 par le lauréat du prix Nobel de 2019, John B. Goodenough, est un des plus vendu.[49,50] Dans les appareils électroniques grand public, la capacité spécifique de LCO avoisine 140 $mA{\cdot}h{\cdot}g^{-1}$, soit la moitié de sa valeur théorique (C_{th} = 274 $mA{\cdot}h{\cdot}g^{-1}$).[47,48] La tension d'utilisation commerciale de LCO est en effet bridée à un maximum de 4.2 V pour inhiber la libération exothermique d'oxygène à haute tension et/ou température, pouvant causé l'emballement de la batterie ou simplement le déclin de sa C_{spe}. Le prix, les conditions préoccupantes d'extraction du cobalt ainsi que sa toxicité sont également limitants.[51]

Les performances des batteries commerciales sont aujourd'hui limitées, entre autres, par la capacité spécifique, le coût et la disponibilité des matériaux cathodiques, qui en affectent le prix, l'autonomie et la puissance.[16,44,45,47,48] Ces paramètres sont intrinsèquement liés à la composition des électrodes et à la quantité d'énergie (E_{spe} et E_{dens}) qu'elles emmagasinent. S'ajoutent à cela les contraintes météorologiques, comme les extrêmes de températures, qui affectent grandement certaines composantes. Des efforts sont donc tournés vers l'optimisation de :

- La composition des électrodes : évoluant vers des matériaux composites ou polymétalliques.
- Leur porosité : qui tend vers l'échelle macroscopique.
- L'optimisation des interfaces électrodes/électrolyte.
- La formulation de l'électrolyte.

En l'occurrence, de nombreux efforts sont tournés vers l'usage de composantes organiques faites de matières abondantes, biodégradables et/ou recyclables.[46,52] Pour rivaliser avec les matériaux cathodiques solides actuels, ces derniers devraient idéalement être rédox-actifs, conducteurs, perméables aux ions et insolubles dans les électrolytes liquides.

1.3.3. La contribution des composés organiques

Les matériaux organiques, incluant les composés de coordination, inondent progressivement le marché électronique mondial. Des dispositifs comme les diiodes électroluminescentes (ODEL) et les semi-conducteurs organiques ont rapidement évolué de simples curiosités de laboratoire, aux technologies d'affichage et photovoltaïques modernes. L'inclusion de tels matériaux peut offrir de nombreux avantages aux systèmes de stockage d'énergie. En l'occurrence, leurs constituants (surtout H, C, O et N) sont souvent plus légers, abondants et biodégradés que les matériaux cathodiques inorganiques d'usage (Chapitre 1.3.2). Ils sont aussi généralement transformés et purifiés en conditions plus douces que les procédés métallurgiques. Tout cela pourrait réduire le cout, l'énergie consommée et les émissions de CO_2 liés à la production des batteries. [46,52]

1.3.4. Motifs organiques rédox-actifs récurrents

Pour être incorporé dans une électrode à titre de matière active, un matériau d'électrode organique (MEO) doit avant tout pouvoir participer à des réactions rédox (Schéma 1.5).[45,46,52] Ces échanges d'électrons sont réversibles dans les cellules électrochimiques secondaires et non-réversibles dans les cellules primaires. Les MEO actuels sont distingués en trois types :

- Les matériaux de type-n sont réduits durant la décharge de la cellule électrochimique et passent généralement d'un état initial neutre (N) à un état chargé négativement (N^-)
- Les matériaux de type-p sont oxydés durant la décharge de la cellule et passent généralement d'un état initial neutre (P) à un état chargé positivement (P^+)
- Les matériaux de type-b dits bipolaires, depuis un état souvent neutre (B), peuvent être oxydés (B^+) ou réduits (B^-) dépendamment de l'usage d'intérêt. Lorsqu'un seul des couples B/B^+ ou B/B^- est exploité, ils sont généralement considérés comme des matériaux de type-p ou n respectivement.

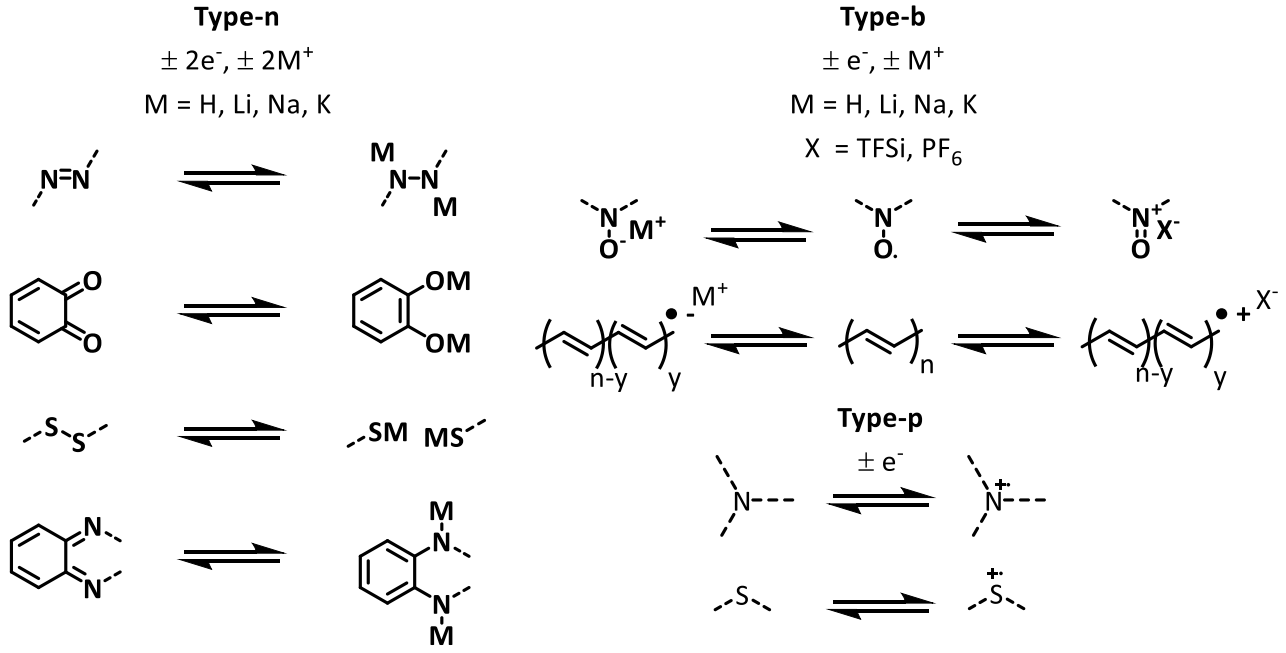

Schéma 1.5 Fonctions chimiques rédox-actives utilisées dans les MEO de types n, b et p.[45,46,52]

Certains motifs moléculaires sont récurrents dans les articles sur les MOE.[45-47,53] Parmi les fonctions rédox-actives des matériaux de type-n figurent les liens doubles (C=C, C=O ou C=N), pouvant être réduits en présence de cations M^{n+} (avec M^{n+} = Li^+, Na^+, K^+, H^+, Mg^{2+} ou Zn^{2+}). Certains liens simples peuvent également être réduits réversiblement, notamment le couple disulfide/thiol impliquant 2 électrons. Les fonctions chimiques des matériaux organiques de type-b doivent pouvoir générer des espèces peu réactives qu'elles soient oxydées ou réduites. Ainsi, les radicaux *N*-oxy stables sont souvent utilisés dans des réactions d'échanges d'un électron. Lorsqu'oxydés, ils génèrent des espèces cationiques de type oxoammonium, dont la charge positive est équilibrée par des anions de l'électrolyte qui diffusent à proximité. Des polymères conjugués et conducteurs de type polyaniline, polythiophène, polypyrrole ou encore polypropylène dopé sont également utilisés comme matériau de type b. Parmi les matériaux de type-p sont retrouvées les amines tertiaires, utilisées comme réducteurs dans des processus rédox à 1 ou 2 électrons si elles sont conjuguées. Les amines tertiaires portant des fonctions aryles sont particulièrement prisées pour la stabilité des espèces rédox ainsi que pour leur adhésion aux additifs de l'électrode facilités par des interactions d'empilement-π.

La capacité théorique des matériaux moléculaires peut être finement ajustée par l'inclusion de multiples fonctions rédox dans les MEO. Leur potentiel rédox peut également être modulé par la présence de groupements électroattracteurs ou donneurs. L'une des principales limitations des MEO est la faible conductivité électrique des molécules organiques, généralement compensée par une quantité importante d'additif conducteur intégré à la cathode. Plusieurs molécules organiques sont également solubles dans les électrolytes développés pour les cellules Li-ion commerciales (Schéma 1.6). Diverses stratégies permettent de surmonter cette limitation comme l'utilisation d'électrolytes non-traditionnels (tels les polymères, les gels, les solution super saturées ou les liquides ioniques) ou encore l'ajustement fin de la composition de l'électrode (nature de la matière active et usage d'additifs). L'ensemble de ces paramètres, combinés à l'utilisation d'une anode adéquate, sont interdépendants et déterminent les performances de la cellule électrochimique. Il sera maintenant montré comment l'ingénierie cristalline peut répondre à différentes problématiques pour favoriser l'usage des MEO.

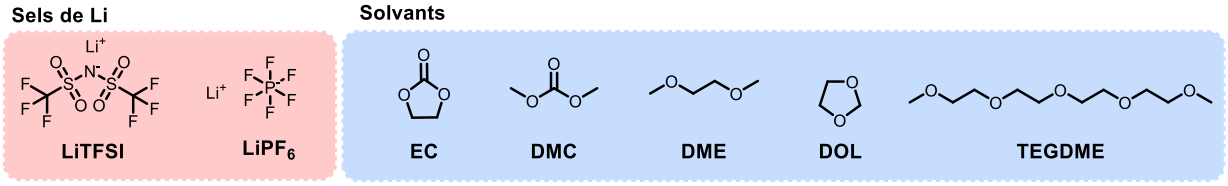

Schéma 1.6 Sels et solvants récurrents des électrolytes de cellules Li-ion commerciales.[45-47,53]

1.3.5. Les quinones

Les quinones forment une famille de composés cycliques insaturés substitués par des fonctions carbonyles (Schéma 1.7).[53,54] Divers analogues avec des fonctions imines ou oximes peuvent également être classés dans cette famille. Ces motifs sont abondants dans la nature, notamment comme pigments utilisés depuis des siècles telles que la lawsone (**7**, Schéma 1.7) et l'alizarine (**2**, Figure 1.2). Aujourd'hui, ces mêmes composés sont intensivement testés comme MEO.[55–60] En effet, les quinones participent à des processus rédox réversibles en solution et sont étudiés depuis longtemps.[53] Leur $C_{th,}$ supérieure à 200 mA·h·g^{-1} pour les *p*-benzo- (**8**), naphto- (**9**) et anthraquinones (**10**) peu substituées, surpasse celle des matériaux cathodiques d'usage (140 et 165 mA·h·g^{-1} pour $LiCoO_2$ et $LiFePO_4$ respectivement).[16,47,48] Les quinones peuvent aussi être réduites en présence de différents cations mono ou divalents (Li^+, Na^+, K^+, Mg^{2+} et d'autres) et sont compatibles aux électrolytes aqueux. Généralement, les quinones participent à des processus rédox à 2 électrons en milieu acide aqueux et à 1 électron dans les solvants organiques. Leur structure peut être dérivée pour incorporer plusieurs fonctions réductibles et ainsi augmenter leur C_{th}, ou incorporer des groupements électrodonneurs afin d'augmenter leur potentiel de réduction. Le potentiel de réduction des *o*-quinones (**11**) est souvent plus élevé que celui de leurs analogues *p*-substitués à cause de l'allégement des contraintes stériques entre les hétéroatomes des liens doubles vicinaux.[58]

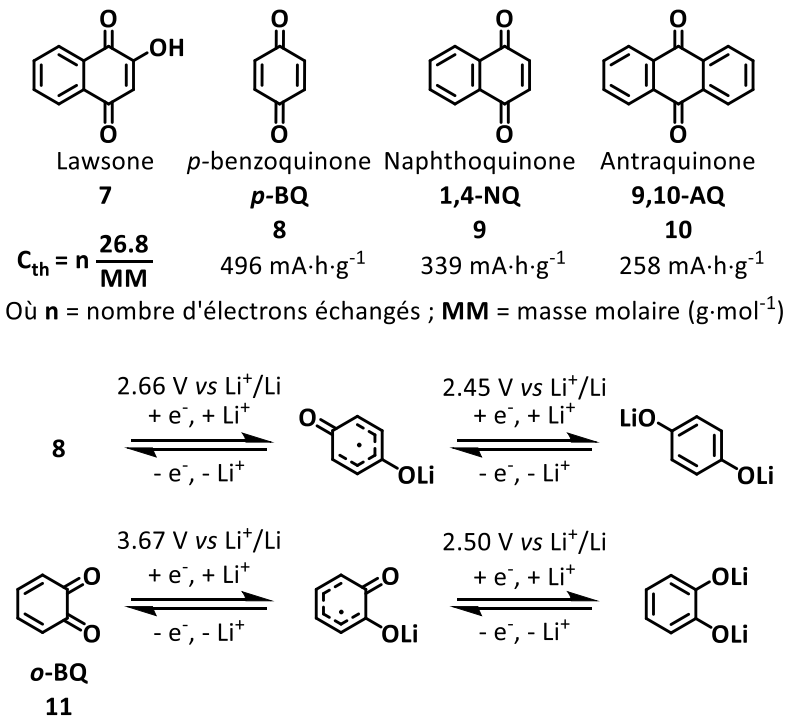

Schéma 1.7 Quinones étudiées comme matière active cathodiques et processus rédox impliqués.[58]

Malgré leurs propriétés attractives, plusieurs facteurs limitent l'utilisation des quinones et hydroquinones sous leur forme native en tant que MEO. D'abord, elles ont tendance à se dissoudre dans les solvants organiques typiquement utilisés dans les électrolytes de cellules Li-ion commerciales (Schéma 1.4). Cela entraîne une chute progressive de la capacité spécifique (C_{spe}) de la cellule au cours des cycles de charge/décharge. Une importante quantité d'additifs est également nécessaire à pallier leur faible conductivité électrique. Finalement, leurs potentiels de réduction sont généralement plus faibles que ceux des matériaux cathodiques inorganiques, ce qui diminue la quantité d'énergie stockable dans la cellule.[56,57,60] Plusieurs stratégies permettent de surmonter ces limitations. D'une part, les quinones peuvent être utilisées sous forme de matériaux composites dans lesquels elles sont liées de manière covalente à un support carboné comme du graphène ou des nanotubes de carbone.[57,60] Leurs supports carbonés leur confèrent une meilleure conductivité et contribuent parfois à la capacité spécifique de l'électrode. Néanmoins, ils ajoutent de la masse rédox-inactive à la cellule électrochimique au détriment de la quantité d'énergie stockable. D'autres approches reposent sur l'ingénierie cristalline (Chapitre 1.2.3) pour

générer des assemblages quinoïdes rédox-actifs, conducteurs et perméables aux ions ainsi qu'à l'électrolyte.

1.3.5.1. Supramolécules, matériaux covalents et de coordination

Concevoir des matériaux quinoïdes cristallins de masse molaire élevée semble *a priori* une stratégie raisonnable et simple pour réduire la solubilité des quinones dans les solvants organiques. Il faut veiller toutefois à ce que le nombre de leurs unités rédox soit suffisamment élevé pour compenser la baisse de la capacité théorique induit par l'augmentation de la masse molaire. Dans cette optique, des composés quinonoïdes dérivés de la diphénoquinone (**12** et **13)** et du motif triptycène (**14** et **15**) ont été synthétisés (Figure 1.9).[61–63] Ces molécules cristallisent en réseaux poreux ou en feuillets, en principe perméables à la percolation de l'électrolyte et des charges et participent également à des processus rédox réversibles en solution et à l'état solide.

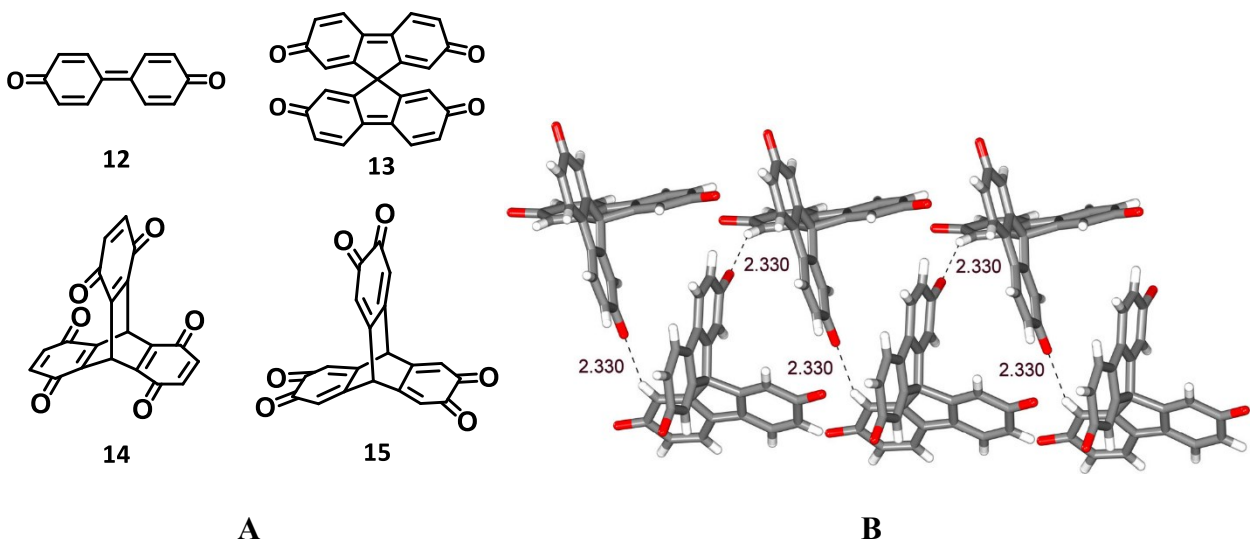

Figure 1.9 (**A**) Schémas structuraux de la diphénoquinone (**12**), bis(diphénoquinone) (**13**) et des isomères *p*- (**14**) et *o*- (**15**) du triptycène(trisquinone). (**B**) Structure cristalline du composé **13** montrant les molécules liées par des interactions C-H···O (pointillés). Code couleur : O, rouge; C, gris; H, blanc. La figure **B** est reproduite avec la permission de la référence 63, © 2022 *American Chemical Society*.[62–64]

Polymériser les quinones en matériaux insolubles (**16** et **17**), conducteurs ioniques et électriques et à capacité théorique élevée est également une stratégie intéressante.[44,56,60,64,65] La quantité d'additif conducteur de telles cellules seraient amoindrie par rapport à celles utilisant de petites molécules dans lesquelles le ratio massique matière active:additif avoisine souvent 1:1 relativement. Les COFs sont également étudiés pour leurs surfaces π étendues dans l'espoir de conduire l'électricité en deux dimensions et générer des feuillets perméables aux ions.[32,34,66,67] En l'occurrence, la condensation de l'isomère 1,2,4,5 de la benzènetétramine et du triquinoyl étudiés par Nietzki (Chapitre 1.1.) a été utilisée pour produire un COF (**18**) fait d'unités diquinoxalinophénazine pouvant en théorie accepter 6 électrons réversiblement (Schéma 1.8).[68]

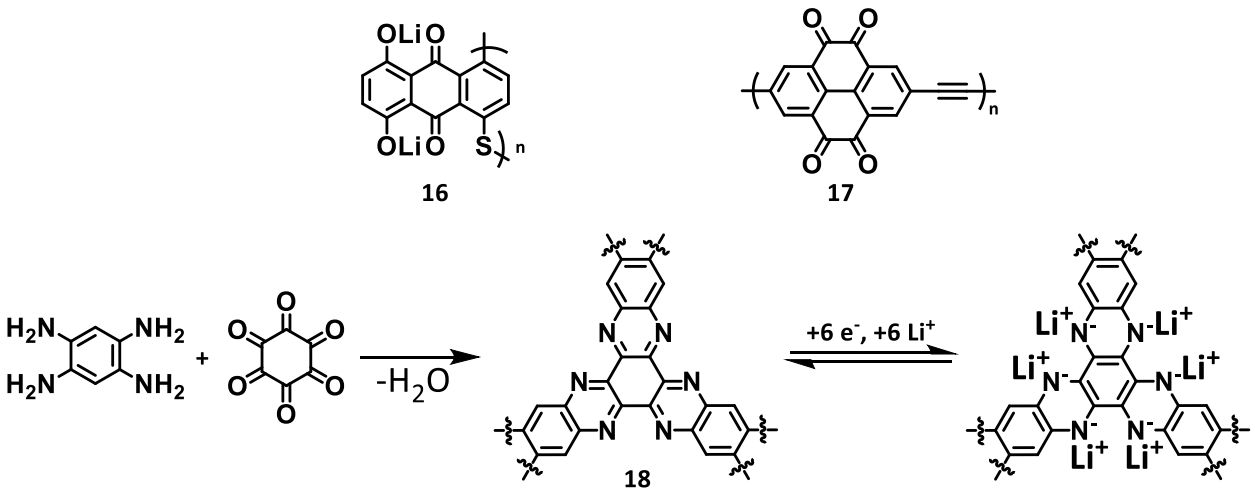

Schéma 1.8 Structures de polymères (**16** et **17**) et d'un COF (**18**) étudiés comme MEO.[68]

Les anions quinoïdes sont peu solubles dans les électrolytes de type polyéthers ou carbonates (Schéma 1.6). Des sels générés à partir d'anions organiques et de cations alcalins (entre autres Li^+, Na^+, K^+ et Mg^{2+}), alcalino-terreux ou des métaux de transition peuvent donc être utilisés comme matière active cathodique de cellule métal-ions.[45,52,60,69–71] De tels composés ont été étudié dans les laboratoires de l'Université de Montréal, du temps où le Prof. Michel Armand y effectuait des recherches pour le CNRS.[72] Son équipe étudia notamment des sels de squarate (**19**), crotonate (**20**) et de rhodizonate (**21**) de Li^+, Cu^{2+}, Pb^{2+} et Ba^{2+} (Schéma 1.9) dont certains d'entre eux ont été isolés et étudiés par Nietzki (Chapitre 1.1.).

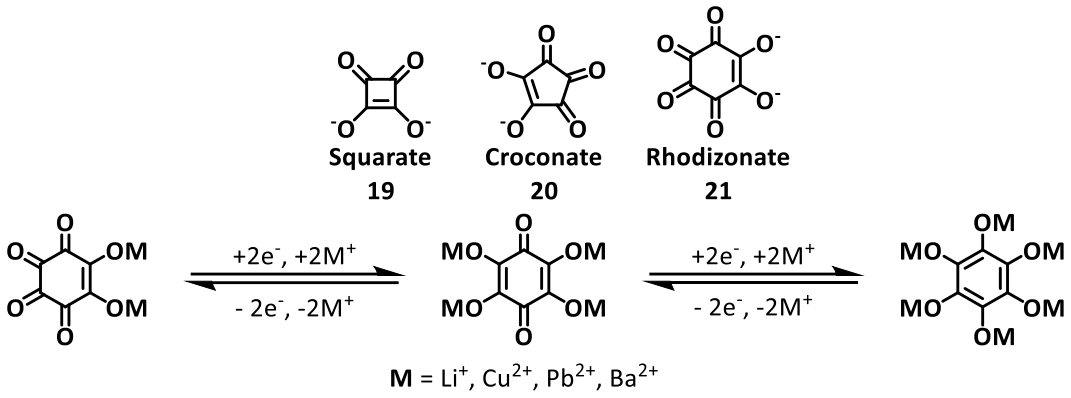

Schéma 1.9 Base conjuguées d'hydroxyquinones pouvant générer des sels de haute capacité théorique et processus rédox pertinents aux MEO.

Est-il possible de combiner les propriétés électromagnétiques et la densité des métaux à la légèreté et la flexibilité des matières organiques ? Si oui, alors les composés de coordination (complexes, polymères et MOFs) apparaissent comme de prometteurs substituts aux matériaux cathodiques d'usage,[67,73] d'abord parce que les cations métalliques et leurs ligands peuvent contribuer à la capacité du matériau (**Schéma 1.10**). Ces composés pourraient également s'avérer conducteurs dans les 3 dimensions de l'espace si le recouvrement adéquat de leurs orbitales le permet. Les polymères de coordination et les MOFs peuvent aussi être conçus pour s'organiser en feuillets ou générer des pores perméables à l'électrolyte et aux ions. Dans les faits les matériaux cathodiques dérivés de MOFs démontrent souvent de faibles valeurs de C_{spe} et de conductivité et subissent parfois des réarrangements structuraux. Ils n'en demeurent pas moins des matériaux novateurs dont les méthodes de synthèse et caractérisation structurale et mécanistique se perfectionnent progressivement. En outre, ils font aussi office de patrons sacrificiels carbonisés pour générer des carbones graphitiques performants en tant qu'électrodes.[67,74]

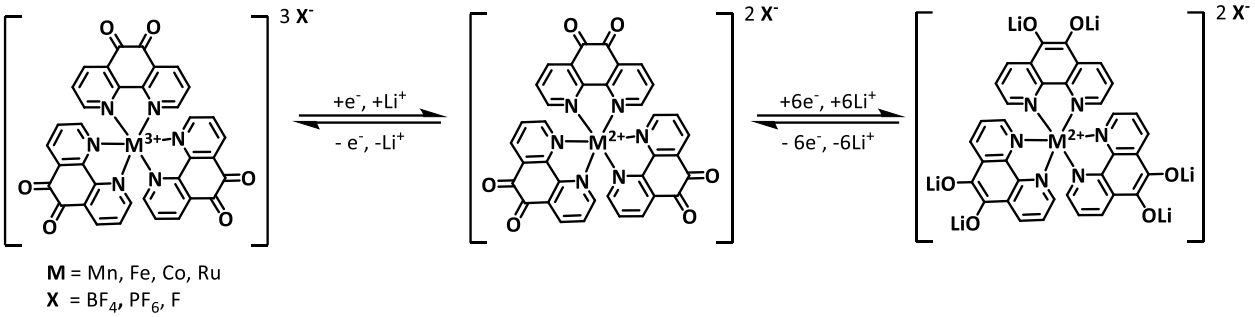

Schéma 1.10 Processus rédox de complexes tris(9,10-phénanthroline-*o*-quinone) de Mn, Fe, Co et Ru utilisés comme matière active de cathode de cellules Li-ion. [73]

1.4. Objectifs de la thèse

L'ingénierie cristalline offre plusieurs solutions aux problématiques énergétiques contemporaines par la conception de matériaux poreux, conducteurs et rédox-actifs. Nous nous sommes initialement intéressés à la possibilité de préparer de tels matériaux à partir de l'isomère 1,2,4,5 de la benzènetétramine (1,2,4,5-BTA). En effet, ce dernier arbore 4 fonctions amines primaires autour d'un noyau benzénique rigide lui permettant de former de liens covalents ou de coordination directionnels, ainsi qu'être rédox-actif. Ces caractéristiques ont d'ailleurs motivé de multiples études utilisant ce motif comme unité de construction modulaire (Chapitre 2.1.2.50). Entre nos mains cependant, plusieurs d'entre elles ne se sont pas avérées reproductibles. Le composé 1,2,4,5-BTA s'est également révélé particulièrement réactif en solution même dépourvue d'oxygène (Figure 1.10). Bien que ce phénomène complique la préparation solvothermale de matériaux cristallins, il est rarement évoqué dans les articles récents et les dernières études de la réactivité du motif ont été conduites par le groupe de Nieztki il y a presque 150 ans. De plus, aucune structure cristalline résolue de 1,2,4,5-BTA et de plusieurs de ses dérivés n'avaient été publiées. Considérant tous ces aspects, nous avons étudié la réactivité intrinsèque et d'autres propriétés de 1,2,4,5-BTA en solution et, ainsi que les caractéristiques de plusieurs de ses dérivés en solution et à l'état solide. De cette manière, nous avons collecté des données cristallographiques et spectroscopiques pertinentes à la préparation solvothermales de matériaux cristallins dérivés de ces molécules.

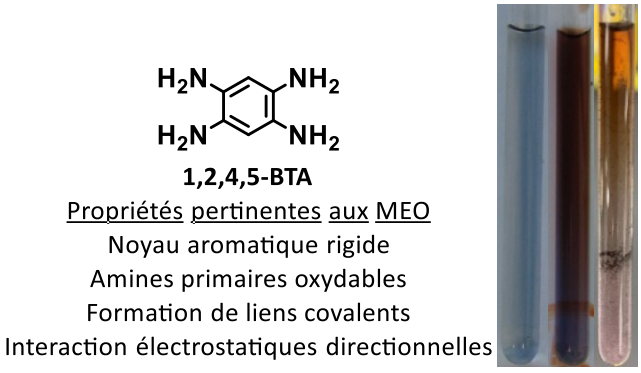

Figure 1.10 (**A**) Propriétés de 1,2,4,5-BTA pertinentes aux MEO et (**B**) évolution de l'aspect d'une solution aqueuse de BTA (de gauche à droite) après 40 min, 20 h et 48 h.

Le Chapitre 2 de la thèse relate nos observations concernant l'organisation de 1,2,4,5-BTA et de sa forme oxydée caractérisés à l'état de monocristaux. Des voies de synthèse revisitées et à plus hauts rendements de ces composés y sont également détaillées. Le second chapitre décrit les produits d'hydrolyse de 1,2,4,5-BTA en milieu acide. Comme ce dernier, ces composés n'avaient pas beaucoup été caractérisés à l'état solide bien qu'également étudiés pour la synthèse de matériaux plus complexes. Le troisième chapitre regroupe les résultats d'une étude cristallographique de sels de sulfate et de bisulfate des isomères 1,2,4,5 et 1,2,3,4 de BTA. Finalement, un chapitre de conclusions et perspectives clôturera la thèse en résumant l'ensemble des résultats collectés et décrira nos stratégies d'utilisation des composés dérivés de 1,2,4,5-BTA pour la préparation de nouveaux matériaux cristallins. Il décrira également la découverte fortuite d'une nouvelle famille de molécules organiques pertinentes à l'électronique organique.

Références

1. Amalore, C.; Bouquillon, A.; Descamps-Lequime, S. *La Chimie et l'art*; EDP Sciences Les Ulis: Les Ulis, 2015.
2. Wei-Haas, M. Bornéo : Découverte Des plus Anciennes Peintures Figuratives de l'Histoire. *National Geographic* **2018**. https://www.nationalgeographic.fr/histoire/cette-peinture-rupestre-figurative-est-la-plus-ancienne-jamais-mise-au-jour.
3. Nietzki, R.; Vaucher, Charles.; Favre, C. Guyot, A. *Chimie des matières colorantes organiques*, traduit de la 3^{e} ed originale; G. Carré et C. Naud: Paris, 1901.
4. Holme, I. Sir William Henry Perkin: A Review of His Life, Work and Legacy. *Color. Technol.* **2006**, *122* (5), 235–251.
5. Graebe, C.; Liebermann, C. Ueber Künstliches Alizarin. *Ber. Dtsch. Chem. Ges.* **1869**, *2* (1), 332–334.
6. Dahlia Milon. *Dahlia Milon : Teinture végétale et Plantes colorantes.* https://dahliamilon.com/
7. Baeyer, A.; Drewsen, V. Darstellung von Indigblau Aus Orthonitrobenzaldehyd. *Ber. Dtsch. Chem. Ges.* **1882**, *15* (2), 2856–2864.
8. Ost, H. Rudolf Nietzki †. *Angew. Chem.* **1917**, *30* (95), 285–287.
9. Noelting, E. Rudolf Nietzki. 1847–1917. *Helv. Chim. Acta* **1918**, *1* (1), 343–430.
10. Rupe, H. Rudolf Nietzki. *Ber. Dtsch. Chem. Ges.* **1919**, *52* (1), A1–A28.
11. Marieb, E. Nicpon.; Lachaîne, René.; Hoehn, Katja.; Moussakova, Linda. *Anatomie et physiologie humaines*; Pearson : ERPI: Paris; Saint-Laurent, 2015.
12. Steed, J. W.; Atwood, J. L. *Supramolecular Chemistry*. John Wiley & Sons: New York, 2013.
13. Hao, Z.; Iqbal, A. Some Aspects of Organic Pigments. *Chem. Soc. Rev.* **1997**, *26* (3), 203–213.
14. Datta, S.; Grant, D. J. W. Crystal Structures of Drugs: Advances in Determination, Prediction and Engineering. *Nat. Rev. Drug Discov.* **2004**, *3* (1), 42–57.
15. Zhu, L.; Liu, X.-Q.; Jiang, H.-L.; Sun, L.-B. Metal–Organic Frameworks for Heterogeneous Basic Catalysis. *Chem. Rev.* **2017**, *117* (12), 8129–8176.
16. Kim, T.; Song, W.; Son, D.-Y.; Ono, L. K.; Qi, Y. Lithium-Ion Batteries: Outlook on Present, Future, and Hybridized Technologies. *J. Mater. Chem. A* **2019**, *7* (7), 2942–2964.
17. Wuest, J. D. Atoms and the Void: Modular Construction of Ordered Porous Solids. *Nat. Commun.* **2020**, *11* (1), 4652.

18. Davey, R. J.; Allen, K.; Blagden, N.; Cross, W. I.; Lieberman, H. F.; Quayle, M. J.; Righini, S.; Seton, L.; Tiddy, G. J. T. Crystal Engineering – Nucleation, the Key Step. *CrystEngComm* **2002**, *4* (47), 257–264.
19. Desiraju, G. R. Crystal Engineering: A Brief Overview. *J. Chem. Sci.* **2010**, *122* (5), 667–675.
20. Corpinot, M. K.; Bučar, D.-K. A Practical Guide to the Design of Molecular Crystals. *Cryst. Growth Des.* **2019**, *19* (2), 1426–1453.
21. Lin, R.-B.; He, Y.; Li, P.; Wang, H.; Zhou, W.; Chen, B. Multifunctional Porous Hydrogen-Bonded Organic Framework Materials. *Chem. Soc. Rev.* **2019**, *48* (5), 1362–1389.
22. History - The Cambridge Crystallographic Data Centre (CCDC) https://www.ccdc.cam.ac.uk/theccdcprofile/history/
23. Desiraju, G. R. Supramolecular Synthons in Crystal Engineering—A New Organic Synthesis. *Angew. Chem. Int. Ed.* **1995**, *34* (21), 2311–2327.
24. Simard, M.; Su, D.; Wuest, J. D. Use of Hydrogen Bonds to Control Molecular Aggregation. Self-Assembly of Three-Dimensional Networks with Large Chambers. *J. Am. Chem. Soc.* **1991**, *113* (12), 4696–4698..
25. Etter, M. C. Encoding and Decoding Hydrogen-Bond Patterns of Organic Compounds. *Acc. Chem. Res.* **1990**, *23* (4), 120–126.
26. Luo, J.; Wang, J.-W.; Zhang, J.-H.; Lai, S.; Zhong, D.-C. Hydrogen-Bonded Organic Frameworks: Design, Structures and Potential Applications. *CrystEngComm* **2018**, *20* (39), 5884–5898.
27. Brunet, P.; Simard, M.; Wuest, J. D. Molecular Tectonics. Porous Hydrogen-Bonded Networks with Unprecedented Structural Integrity. *J. Am. Chem. Soc.* **1997**, *119* (11), 2737–2738.
28. Mastalerz, M.; Oppel, I. M. Rational Construction of an Extrinsic Porous Molecular Crystal with an Extraordinary High Specific Surface Area. *Angew. Chem. Int. Ed.* **2012**, *51* (21), 5252–5255.
29. Geng, K.; He, T.; Liu, R.; Dalapati, S.; Tan, K. T.; Li, Z.; Tao, S.; Gong, Y.; Jiang, Q.; Jiang, D. Covalent Organic Frameworks: Design, Synthesis, and Functions. *Chem. Rev.* **2020**, *120* (16), 8814–8933.
30. Beaudoin, D.; Maris, T.; Wuest, J. D. Constructing Monocrystalline Covalent Organic Networks by Polymerization. *Nat. Chem.* **2013**, *5* (10), 830–834.

31. Ma, T.; Kapustin, E. A.; Yin, S. X.; Liang, L.; Zhou, Z.; Niu, J.; Li, L.-H.; Wang, Y.; Su, J.; Li, J.; Wang, X.; Wang, W. D.; Wang, W.; Sun, J.; Yaghi, O. M. Single-Crystal X-Ray Diffraction Structures of Covalent Organic Frameworks. *Science* **2018**, *361* (6397), 48–52.
32. Kandambeth, S.; Mallick, A.; Lukose, B.; Mane, M. V.; Heine, T.; Banerjee, R. Construction of Crystalline 2D Covalent Organic Frameworks with Remarkable Chemical (Acid/Base) Stability via a Combined Reversible and Irreversible Route. *J. Am. Chem. Soc.* **2012**, *134* (48), 19524–19527.
33. Ostroverkhova, O. Organic Optoelectronic Materials: Mechanisms and Applications. *Chem. Rev.* **2016**, *116* (22), 13279–13412.
34. Kandambeth, S.; Dey, K.; Banerjee, R. Covalent Organic Frameworks: Chemistry beyond the Structure. *J. Am. Chem. Soc.* **2019**, *141* (5), 1807–1822.
35. Horcajada, P.; Gref, R.; Baati, T.; Allan, P. K.; Maurin, G.; Couvreur, P.; Férey, G.; Morris, R. E.; Serre, C. Metal–Organic Frameworks in Biomedicine. *Chem. Rev.* **2012**, *112* (2), 1232–1268.
36. Valvekens, P.; Jonckheere, D.; Baerdemaeker, T. D.; Kubarev, A. V.; Vandichel, M.; Hemelsoet, K.; Waroquier, M.; Speybroeck, V. V.; Smolders, E.; Depla, D.; Roeffaers, M. B. J.; Vos, D. D. Base Catalytic Activity of Alkaline Earth MOFs: A (Micro)Spectroscopic Study of Active Site Formation by the Controlled Transformation of Structural Anions. *Chem. Sci.* **2014**, *5* (11), 4517–4524.
37. Xie, L. S.; Skorupskii, G.; Dincă, M. Electrically Conductive Metal–Organic Frameworks. *Chem. Rev.* **2020**, *120* (16), 8536–8580.
38. Yaghi, O. M.; Kalmutzki, M. J.; Diercks, C. S. Emergence of Metal-Organic Frameworks. In *Introduction to Reticular Chemistry*; Wiley-VCH Verlag GmbH: Weinheim, 2019; pp 1–27.
39. Yaghi, O. M.; Kalmutzki, M. J.; Diercks, C. S. Building Units of MOFs. In *Introduction to Reticular Chemistry*; Wiley-VCH Verlag GmbH: Weinheim, 2019; 57–81.
40. Terminology of Metal–Organic Frameworks and Coordination Polymers (IUPAC Recommendations 2013). *Pure Appl. Chem.* **2013**, *85* (8), 1715–1724.
41. Voort, P. van der; Leus, K.; Canck, E. de. *Introduction to Porous Materials*, First edition.; Wiley: Hoboken, NJ, 2019.
42. Li, H.; Eddaoudi, M.; O'Keeffe, M.; Yaghi, O. M. Design and Synthesis of an Exceptionally Stable and Highly Porous Metal-Organic Framework. *Nature* **1999**, *402* (6759), 276–279.

43. Reddy, T. *Linden's Handbook of Batteries, 4th Edition*; McGraw-Hill Education: New York 2010.
44. Muench, S.; Wild, A.; Friebe, C.; Häupler, B.; Janoschka, T.; Schubert, U. S. Polymer-Based Organic Batteries. *Chem. Rev.* **2016**, *116* (16), 9438–9484.
45. Friebe, C.; Lex-Balducci, A.; Schubert, U. S. Sustainable Energy Storage: Recent Trends and Developments toward Fully Organic Batteries. *ChemSusChem* **2019**, *12* (18), 4093–4115.
46. Poizot, P.; Dolhem, F.; Gaubicher, J. Progress in All-Organic Rechargeable Batteries Using Cationic and Anionic Configurations: Toward Low-Cost and Greener Storage Solutions? *Curr. Opin. Electrochem.* **2018**, *9*, 70–80.
47. Nitta, N.; Wu, F.; Lee, J. T.; Yushin, G. Li-Ion Battery Materials: Present and Future. *Mater. Today* **2015**, *18* (5), 252–264.
48. Tarascon, J.-M.; Armand, M. Issues and Challenges Facing Rechargeable Lithium Batteries. *Nature* **2001**, *414* (6861), 359–367.
49. Mizushima, K.; Jones, P. C.; Wiseman, P. J.; Goodenough, J. B. LixCoO2 (0. *Mater. Res. Bull.* **1980**, *15* (6), 783–789.
50. Goodenough, J. B. How We Made the Li-Ion Rechargeable Battery. *Nat. Electron.* **2018**, *1* (3), 204–204.
51. *« Voilà pourquoi on meurt »*. Amnistie internationale Canada francophone. https://amnistie.ca/sinformer/publications/rapport/voila-pourquoi-on-meurt
52. Shea, J. J.; Luo, C. Organic Electrode Materials for Metal Ion Batteries. *ACS Appl. Mater. Interfaces* **2020**, *12* (5), 5361–5380.
53. Patai, S., Ed. *The Chemistry of Quinonoid Compounds;* Patai's Chemistry of Functional Groups, John Wiley & Sons: New York, 1974.
54. Patai, S.; Rappoport, Z., Eds. *The Chemistry of the Quinonoid Compounds*; Patai's Chemistry of Functional Groups, John Wiley & Sons: New York, 1988.
55. Alt, H.; Binder, H.; Klempert, G.; Köhling, A.; Sandstede, G. Evaluation of Organic Battery Electrodes: Voltammetric Study of the Redox Behaviour of Solid Quinones. *J. Appl. Electrochem.* **1972**, *2* (3), 193–200.
56. Häupler, B.; Wild, A.; Schubert, U. S. Carbonyls: Powerful Organic Materials for Secondary Batteries. *Adv. Energy Mater.* **2015**, *5* (11), 1402034.

57. Miroshnikov, M.; Divya, K. P.; Babu, G.; Meiyazhagan, A.; Reddy Arava, L. M.; Ajayan, P. M.; John, G. Power from Nature: Designing Green Battery Materials from Electroactive Quinone Derivatives and Organic Polymers. *J. Mater. Chem. A* **2016**, *4* (32), 12370–12386.
58. Miao, L.; Liu, L.; Shang, Z.; Li, Y.; Lu, Y.; Cheng, F.; Chen, J. The Structure–Electrochemical Property Relationship of Quinone Electrodes for Lithium-Ion Batteries. *Phys. Chem. Chem. Phys.* **2018**, *20* (19), 13478–13484.
59. Miroshnikov, M.; Kato, K.; Babu, G.; Kumar, N.; Mahankali, K.; Hohenstein, E.; Wang, H.; Satapathy, S.; Divya, K. P.; Asare, H.; Arava, L. M. R.; Ajayan, P. M.; John, G. Nature-Derived Sodium-Ion Battery: Mechanistic Insights into Na-Ion Coordination within Sustainable Molecular Cathode Materials. *ACS Appl. Energy Mater.* **2019**, *2* (12), 8596–8604.
60. Han, C.; Li, H.; Shi, R.; Zhang, T.; Tong, J.; Li, J.; Li, B. Organic Quinones towards Advanced Electrochemical Energy Storage: Recent Advances and Challenges. *J. Mater. Chem. A* **2019**, *7* (41), 23378–23415.
61. Kwon, J. E.; Hyun, C.-S.; Ryu, Y. J.; Lee, J.; Min, D. J.; Park, M. J.; An, B.-K.; Park, S. Y. Triptycene-Based Quinone Molecules Showing Multi-Electron Redox Reactions for Large Capacity and High Energy Organic Cathode Materials in Li-Ion Batteries. *J. Mater. Chem. A* **2018**, *6* (7), 3134–3140.
62. Langis-Barsetti, S.; Maris, T.; Wuest, J. D. Triptycene 1,2-Quinones and Quinols: Permeable Crystalline Redox-Active Molecular Solids. *J. Org. Chem.* **2018**, *83* (24), 15426–15437.
63. Néron, S.; Morency, M.; Chen, L.; Maris, T.; Rochefort, D.; Iftimie, R.; Wuest, J. D. Diphenoquinones Redux. *J. Org. Chem.* **2022**, *87* (12), 7673–7695.
64. Petronico, A.; Bassett, K. L.; Nicolau, B. G.; Gewirth, A. A.; Nuzzo, R. G. Toward a Four-Electron Redox Quinone Polymer for High Capacity Lithium Ion Storage. *Adv. Energy Mater.* **2018**, *8* (5), 1700960.
65. Xie, J.; Chen, W.; Long, G.; Gao, W.; J. Xu, Z.; Liu, M.; Zhang, Q. Boosting the Performance of Organic Cathodes through Structure Tuning. *J. Mater. Chem. A* **2018**, *6* (27), 12985–12991.
66. Wang, S.; Wang, Q.; Shao, P.; Han, Y.; Gao, X.; Ma, L.; Yuan, S.; Ma, X.; Zhou, J.; Feng, X.; Wang, B. Exfoliation of Covalent Organic Frameworks into Few-Layer Redox-Active

Nanosheets as Cathode Materials for Lithium-Ion Batteries. *J. Am. Chem. Soc.* **2017**, *139* (12), 4258–4261.

67. Cui, X.; Dong, H.; Chen, S.; Wu, M.; Wang, Y. Progress and Perspective of Metal- and Covalent-Organic Frameworks and Their Derivatives for Lithium-Ion Batteries. *Batter. Supercaps* **2021**, *4* (1), 72–97.
68. Li, X.; Wang, H.; Chen, H.; Zheng, Q.; Zhang, Q.; Mao, H.; Liu, Y.; Cai, S.; Sun, B.; Dun, C.; Gordon, M. P.; Zheng, H.; Reimer, J. A.; Urban, J. J.; Ciston, J.; Tan, T.; Chan, E. M.; Zhang, J.; Liu, Y. Dynamic Covalent Synthesis of Crystalline Porous Graphitic Frameworks. *Chem* **2020**, *6* (4), 933–944.
69. Chen, H.; Armand, M.; Demailly, G.; Dolhem, F.; Poizot, P.; Tarascon, J.-M. From Biomass to a Renewable LiXC6O6 Organic Electrode for Sustainable Li-Ion Batteries. *ChemSusChem* **2008**, *1* (4), 348–355.
70. Chen, H.; Armand, M.; Courty, M.; Jiang, M.; Grey, C. P.; Dolhem, F.; Tarascon, J.-M.; Poizot, P. Lithium Salt of Tetrahydroxybenzoquinone: Toward the Development of a Sustainable Li-Ion Battery. *J. Am. Chem. Soc.* **2009**, *131* (25), 8984–8988.
71. Lee, M.; Hong, J.; Lopez, J.; Sun, Y.; Feng, D.; Lim, K.; Chueh, W. C.; Toney, M. F.; Cui, Y.; Bao, Z. High-Performance Sodium–Organic Battery by Realizing Four-Sodium Storage in Disodium Rhodizonate. *Nat. Energy* **2017**, *2* (11), 861–868.
72. Ravet, N.; Michot, C.; Armand, M. Novel Cathode Materials Based on Organic Couples for Lithium Batteries. *MRS Online Proc. Libr. Arch.* **1997**, *496*.
73. Lakraychi, A. E.; De Kreijger, S.; Gupta, D.; Elias, B.; Vlad, A. Phendione–Transition-Metal Complexes with Bipolar Redox Activity for Lithium Batteries. *ChemSusChem* **2020**, *13* (9), 2225–2231.
74. Liao, Y.; Li, C.; Lou, X.; Hu, X.; Ning, Y.; Yuan, F.; Chen, B.; Shen, M.; Hu, B. Carbon-Coated Li3V2(PO4)3 Derived from Metal-Organic Framework as Cathode for Lithium-Ion Batteries with High Stability. *Electrochimica Acta* **2018**, *271*, 608–616.

Chapitre 2. Redorer l'héritage de Rudolf Nietzki : benzène-1,2,4,5-tétraamine et composés dérivés

2.1. Introduction

En 1887, Nietzki et son étudiant Eduard Hagenbach préparèrent des sels de la benzène-1,2,4,5-tétramine (1,2,4,5-BTA, **1**) considérée comme le premier dérivé synthétique du benzène arborant plus de 4 fonctions amines. Ils obtinrent d'abord le composé **1** à partir du *N*,*N*′-(1,3-phénylène)diacétamide par nitration, hydrolyse et réduction subséquentes et, 10 ans plus tard, à partir du 1,3-dichlorobenzène par un autre procédé (Schéma 2.1), les chercheurs allemands parvinrent aussi à isoler des sels du produit d'oxydation du composé **1**, la 2,5-diamino-*p*-quinonediimine (**2**). Bien que les composés **1** et **2** soient aujourd'hui étudiés pour des applications optoélectroniques, peu de données de caractérisation de leur état solide, notamment cristallographiques, ont été publiées. Le composé **2** pourrait en l'occurrence exister sous différentes formes qui semblent n'avoir été étudiées que de façon théorique. C'est ainsi que nous nous sommes intéressés aux structures solides des composés **1** et **2**. Nous nous sommes également penchés sur les différentes formes du composé **2** de façon expérimentale et théorique.

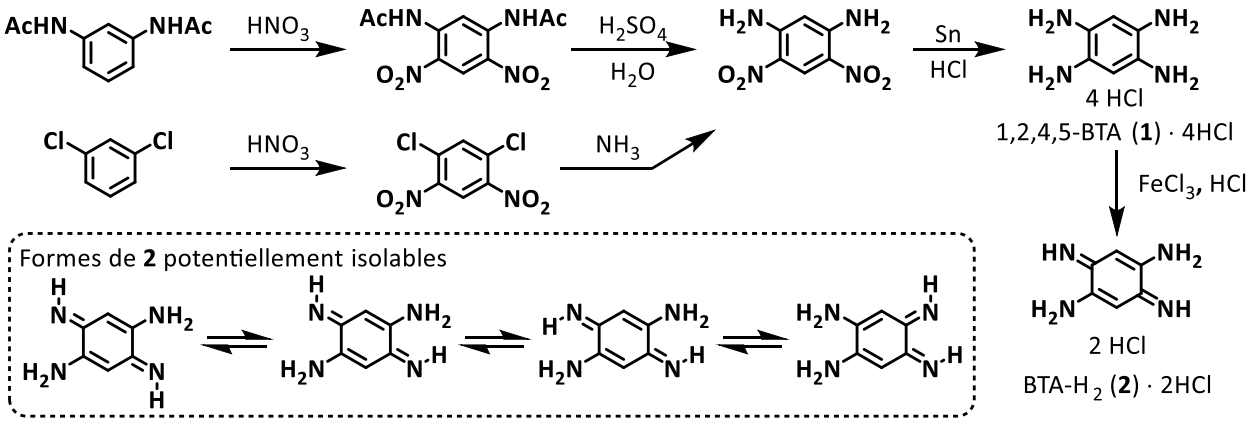

Schéma 2.1 Résumé d'une partie des travaux de Nietzki, Hagenbach et Schedler.[16,18,71]

Refreshing the Legacy of Rudolf Nietzki: Benzene-1,2,4,5-tetramine and Related Compounds

Johann O. E. Sosoe, Cédric Malveau, Thierry Maris, Radu Iftimie, and James D. Wuest

Published in *The Journal of Organic Chemistry*

J. Org. Chem. **2023**, *88* (23), 16302–16314.

JOES conceived the project, executed the experiments, and wrote the initial draft of the manuscript.

CM carried out all NMR experiments.

TM carried out all crystallographic studies.

RI carried out all computational calculations.

JDW helped identify experiments to perform and contributed to writing the final version of the manuscript.

Abstract

Like hydroquinones and quinones, aromatic compounds with multiple NH_2 groups and the corresponding quinonediimines have the potential to serve as the components of useful redox-active organic materials. Benzene-1,2,4,5-tetramine (BTA) and its oxidized form BTA-H_2 offer a promising redox pair of this type, and the compounds have proven to be useful in many areas of chemistry. However, key aspects of their behavior have remained poorly studied, such as the nature of their protonated forms, their preferred molecular structures, their reactivity, and their organization in condensed phases. In the present work, we have used a combination of improved methods of synthesis, computation, spectroscopic studies, and structural analyses to develop a deeper understanding of BTA, BTA-H_2, their salts, and related compounds. The new knowledge is expected to accelerate exploitation of the compounds in areas of materials science where desirable properties can only be attained by properly controlling the organization of molecular components.

Introduction

New redox-active organic materials are being developed for many uses, such as making batteries that are efficient, cheap, lightweight, and composed only of abundant elements.[1–11] Substances of special prominence in this field include hydroquinones and quinones, which are interconverted by redox reactions that are typically rapid and reversible. However, many less familiar redox pairs are attractive candidates for study. Among the potential alternatives are aromatic compounds with multiple NH_2 groups and the corresponding quinonediimines, such as benzene-1,2,4,5-tetramine (**1**; BTA) and its oxidized form (BTA-H_2), which can be represented by structure **2**. Interest in compounds of this type is increasing as new green methods of amination emerge, allowing complex arylamines to be synthesized from phenolic precursors derived from renewable resources.[12–14] In addition, related aminoquinones are widespread in nature and play diverse roles, as exemplified by the antitumor antibiotic mitomycin C.[15]

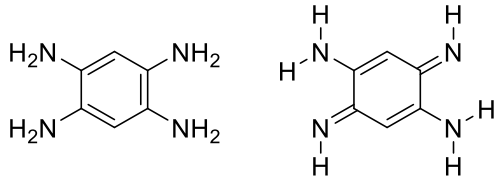

1 (BTA) **2** (BTA-H_2)

The active development of arenes with multiple amino groups was triggered by William Perkin's discovery in the 1850s that anilines can be converted into useful synthetic dyes. This finding quickly expanded the scope of industrial chemistry, drew attention to the reactivity of simple arylamines, and motivated attempts to make more complex derivatives. Despite substantial efforts, the synthesis of benzenetetramines was not reported until the end of the 19th century, when Rudolf Nietzki and coworkers described making BTA (**1**) and its isomers in the form of salts.[16–18]

Nietzki (1847–1917) is an unfamiliar figure to many modern organic chemists, but he made farsighted contributions in areas of enduring importance.[19–21] Nietzki's impact can be measured by the frequency with which compounds first made in his research group are used

today. In particular, BTA (**1**) and its derivatives are at the center of an imposing array of projects, including studies in which the compounds are used as precursors of redox-active materials,[22–28] ligands in coordination chemistry,[29–39] components for making metal-organic frameworks (MOFs) and covalent organic frameworks (COFs) by modular construction,[40–47] monomers for producing polymers,[48–53] components of switches and sensors,[54,55] precursors for synthesizing diverse heterocyclic compounds,[56–59] and enzyme inhibitors for use in treating cancer.[60]

Paradoxically, even though BTA (**1**), its oxidized form BTA-H_2 (**2**), and related compounds have been available for over a century and are widely used, many fundamental properties have not been studied adequately. For example, surprisingly little has been done to reveal how molecules of this type are arranged in the crystalline state, despite the likelihood of discovering novel patterns of hydrogen bonding, charge transfer, and other interactions, as found in structures composed of analogous hydroquinones and quinones.[61] To learn more about BTA (**1**) and its derivatives, we have improved their methods of synthesis, studied their reactions, crystallized selected compounds, and solved their structures by X-ray diffraction. Our results create a foundation for using the compounds in new ways in the future, particularly as components of redox-active materials for storing energy.

Results and Discussion

Syntheses of BTA (1), Its Oxidized Form BTA-H2 (2), Their Salts, and Related Compounds. Tetrahydrochloride salt BTA (**1**)•4HCl was made by modifying a route initially devised by Nietzki and Schedler (Scheme 1).[16,59,62–66] Nitration of 1,3-dichlorobenzene gave 1,5-dichloro-2,4-dinitrobenzene (**3**) as the major product, along with smaller amounts of 1,3-dichloro-2,4-dinitrobenzene (**4**).[67] Isomer **3** can be isolated in pure form by fractional crystallization, but we found it expedient to synthesize tetrahydrochloride salt BTA (**1**)•4HCl without purifying any intermediates. The mixture of isomers **3** and **4** was converted into 4,6-dinitrobenzene-1,3-diamine (**5**) and its isomer **6** by heating with NH_3. The mixture of products was reduced with $SnCl_2$/HCl to give hydrochloride salts of BTA (**1**) and isomeric benzene-1,2,3,4-tetramine (**7**).[17,68-70] Purification of these salts is simple because BTA (**1**)•4HCl is less soluble in H_2O and can be

separated by filtration in 41% overall yield. Benzene-1,2,3,4-tetramine (**7**) can then be recovered from the filtrate as its sulfate salt **7** • H_2SO_4 in 37% overall yield.

Scheme 1. Syntheses of BTA (1) and Related Compounds

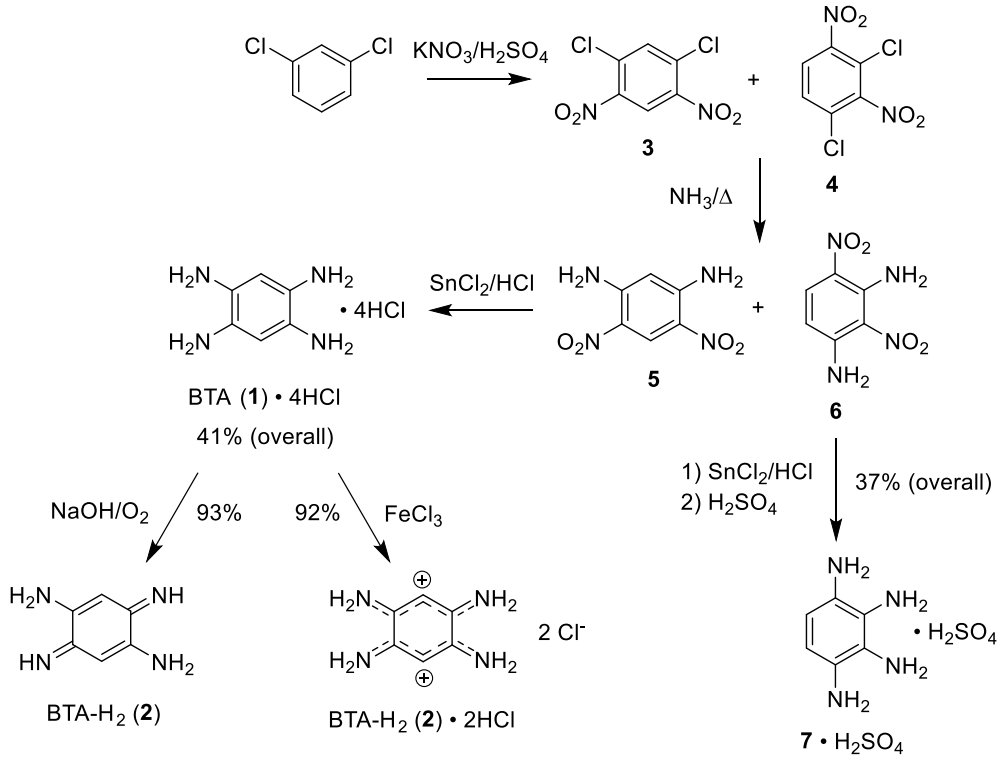

Oxidized form BTA-H_2 (**2**) was obtained as the free base by exposing aqueous solutions of salt BTA (**1**)•4HCl to air in the presence of Cs_2CO_3 or NaOH (Scheme 1).[35] In related experiments, free base BTA (**1**) and dihydrochloride salt BTA (**1**)•2HCl could be obtained in the form of crystals suitable for structural analysis. The dihydrochloride salt of oxidized product BTA-H_2 (**2**) was conveniently prepared by treating salt BTA (**1**)•4HCl with aqueous $FeCl_3$.[71] With care, all derivatives of BTA (**1**) in Scheme 1 can be synthesized, crystallized, and extensively characterized. Nevertheless, the compounds are reactive and undergo various transformations such as hydrolyses and oxidations, often with striking changes of color.[72] Together, the methods summarized in Scheme 1 provide access to BTA (**1**) and various derivatives, as well as to similarly useful isomer **7** and related compounds.

Structures of BTA (1), Dihydrochloride Salt BTA (1)•2HCl, and Tetrahydrochloride Salt BTA (1)•4HCl.

Unprotonated benzenetetramines are oxidized rapidly in air and are rarely handled in pure form. However, we were able to grow crystals of BTA (**1**) from 1 M aqueous NaOH in the form of colorless plates and to solve their structure by X-ray diffraction. Selected crystallographic data are summarized in Tableau II - 1, and representations of the structure are provided in Figure 2.1. As often observed in arylamines,[73–79] the NH_2 groups in BTA (**1**) are pyramidal, and the average sum of bond angles at nitrogen is 334.7°. The four atoms of nitrogen lie close to the average plane of the aromatic ring, and the two pairs of adjacent NH_2 groups are oriented in such a way that the two planes bisecting the angles H–N–H cut the average plane of the aromatic ring at angles of about 70°. This orientation allows the lone pairs of nitrogen to be partially aligned with the π-system and permits neighboring NH_2 groups to form two close intramolecular N–H···N contacts, with an average H···N distance ($d_{H\cdots N}$) of 2.597 Å. Within each molecule of BTA (**1**), the average values of $d_{C–N}$ and $d_{C–C}$ (1.424 and 1.394 Å, respectively) resemble those found in other arylamines.

Tableau II - 1 Crystallographic Data for BTA (**1**), Dihydrochloride Salt BTA (**1**)•2HCl, and Tetrahydrochloride Salt BTA (**1**)•4HCl

compound	**BTA (1)**	**BTA (1)•2HCl**	**BTA (1)•4HCl**
CCDC[a] number	2283757	2283758	2283761
description	colorless plates	light brown plates	colorless blocks
crystal syst	monoclinic	monoclinic	orthorhombic
space group	$P2_1/c$	$P2_1/c$	*Pnnm*
a (Å)	7.7694(5)	9.4236(6)	8.0533(3)
b (Å)	5.5029(3)	14.5883(10)	9.6682(3)
c (Å)	7.4694(5)	9.7872(7)	7.3499(3)
α (deg)	90	90	90
β (deg)	101.064(4)	94.083(3)	90
γ (deg)	90	90	90
V (Å^3)	313.41(3)	1342.07(16)	572.27(4)

Z	2	6	2
Z'	0.5	1.5	0.25
ρ_{calc} (g cm^{-3})	1.464	1.567	1.648
T (K)	150	150	150
R_1, $I > 2\sigma(I)$	0.0475	0.0458	0.0224
wR_2, $I > 2\sigma(I)$	0.1215	0.1313	0.0562
GoF	1.071	1.110	1.121

[a]Cambridge Crystallographic Data Centre

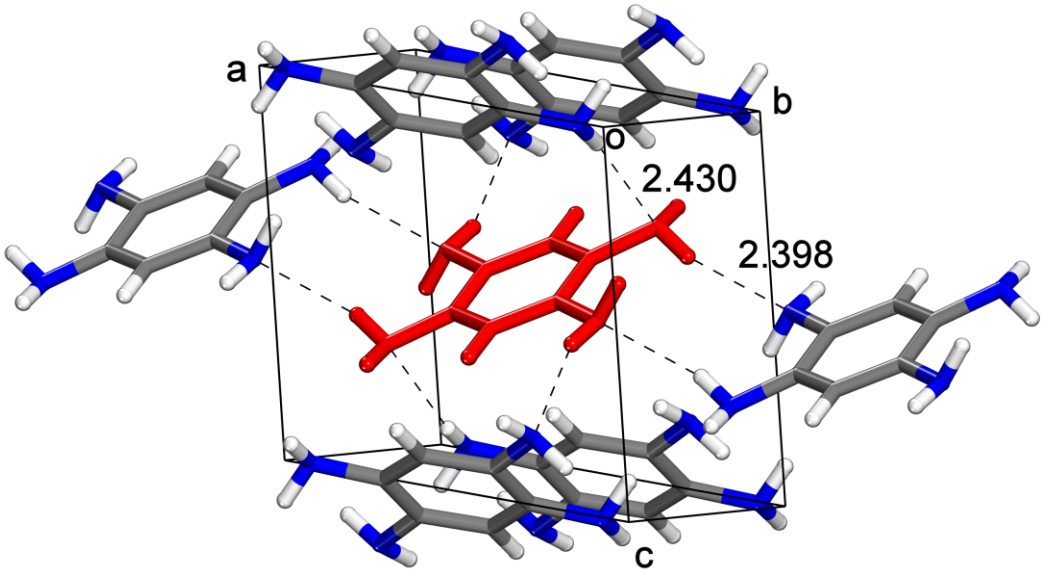

a

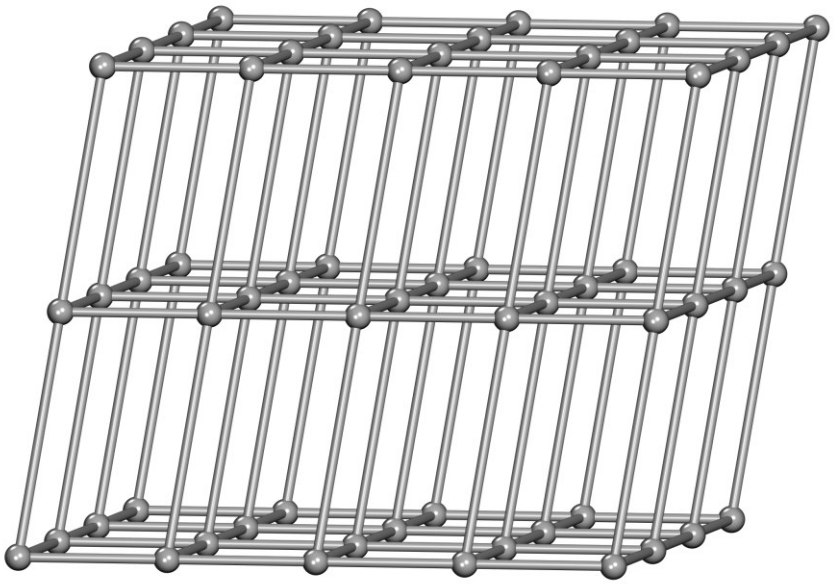

b

Figure 2.1 Representations of the structure of $P2_1/c$ crystals of BTA (**1**) grown from H_2O. (a) View showing a central molecule (red), its six neighbors, and the primary intermolecular N−H···N hydrogen bonds (broken lines), with $d_{H\cdots N}$ given in Å. Unless stated otherwise, atoms of carbon appear in gray, hydrogen in white, and nitrogen in blue. (b) The resulting hydrogen-bonded *pcu* network, with spheres representing the centroid of each molecule of BTA (**1**) and with lines connecting each sphere to its six hydrogen-bonded neighbors, as shown in Figure 2.1.a.

Each NH_2 group in molecules of BTA (**1**) engages in two primary intermolecular N–H···N hydrogen bonds (Figure 2.1.a), once as donor and once as acceptor, with values of $d_{H\cdots N}$ equal to 2.398 and 2.430 Å (corresponding to values of $d_{N\cdots N}$ equal to 3.251 and 3.276 Å). The closest intramolecular N–H···N contacts are significantly longer (values of $d_{H\cdots N}$ equal to 2.575 and 2.619 Å). Each molecule of BTA (**1**) is linked to six neighbors by the primary intermolecular hydrogen bonds, giving rise to the six-connected *pcu* network shown in Figure 2.1.b. The network is reinforced by secondary interactions between each molecule and its neighbors, including two longer N–H···N hydrogen bonds ($d_{N\cdots N}$ = 3.419 Å), two N–H··· π interactions ($d_{H\cdots C}$ = 2.775 Å), and two C–H··· π interactions ($d_{H\cdots C}$ = 2.612 Å).

Light brown crystals of dihydrochloride salt BTA (**1**)•2HCl were grown from H_2O by partial deprotonation of the corresponding tetrahydrochloride salt, and their structure was resolved by X-ray diffraction. Table II - 1 includes selected crystallographic data, and Figure 2.2 provides a representation of the structure. *N*-Protonation of arenes with multiple NH_2 substituents is normally favored, but *C*-protonated tautomers have been characterized in certain cases.[80,81] BTA (**1**) undergoes double *N*-protonation, which can in principle give rise to three different dications **8**–**10**. Gas-phase stability is expected to decrease in the order **8** > **9** > **10**, based on decreased charge separation and the reduced opportunity to form intramolecular N–H^+···N interactions in dication **10**.

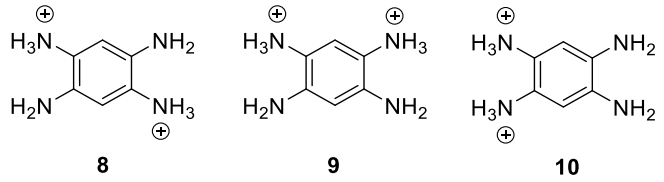

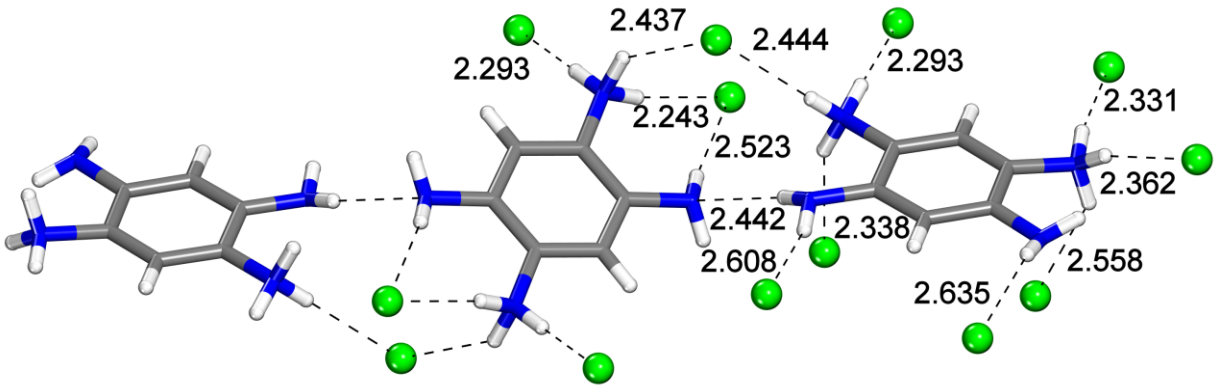

Figure 2.2 Representation of key interactions in the structure of $P2_1/c$ crystals of dihydrochloride salt BTA (**1**)•2HCl grown from H_2O, showing a *p*-dication **8** flanked by two *m*-dications **9**. Primary N–H^+···Cl^- and N–H···N hydrogen bonds are indicated by broken lines, with $d_{H\cdots N}$ and $d_{H\cdots Cl}$ given in Å. Atoms of carbon appear in gray, hydrogen in white, chlorine in green, and nitrogen in blue.

Unexpectedly, the observed crystals of salt BTA (**1**)•2HCl incorporate a 1:1 ratio of *p*-dication **8** and *m*-dication **9**. In both forms, the NH_2 groups are pyramidal, and the average sums of bond angles at nitrogen are 332.5° (*p*-dication) and 344.4° (*m*-dication). In both dications, the four atoms of nitrogen lie near the average plane of the aromatic ring, and the two NH_2 groups are oriented in such a way that angles of about 80° are formed by the average plane of the aromatic ring and the two planes bisecting the angles H–N–H. This orientation allows partial alignment of the lone pairs of the NH_2 groups with the π-system but does not lead to intramolecular N–H···N interactions that are much shorter than the sum of the van der Waals radii of nitrogen and hydrogen. In both *p*-dication **8** and *m*-dication **9**, the average values of $d_{C–C}$ (1.393 and 1.392 Å, respectively), $d_{C–N}$ for the NH_2 groups (1.401 and 1.390 Å, respectively), and $d_{C–N}$ for the NH_3^+ groups (1.443 and 1.462 Å, respectively) are all similar to those observed in related arylamines and their hydrochloride salts.[73–79,82–88]

Figure 2.2 shows that N–H···N hydrogen bonds are present in the structure of salt BTA (**1**)•2HCl, but ionic $N–H^+\cdots Cl^-$ hydrogen bonds appear to be dominant. Each atom of hydrogen in each NH_3^+ group engages in a short interaction of this type, and the NH_2 groups take part in additional $N–H\cdots Cl^-$ hydrogen bonds. The combined presence of two different cations and various types of interactions gives rise to a complex structure and underscores the difficulty of using arenes with multiple NH_3^+ and NH_2 groups as modules for building predictably ordered solids.

Colorless crystals of tetrahydrochloride salt BTA (**1**)•4HCl suitable for analysis by X-ray diffraction were grown by layering a saturated aqueous solution over concentrated aqueous HCl and allowing the mixture to stand. Selected crystallographic data are presented in Table II - 1, and representations of the structure appear in Figure 2.3. Exclusive *N*-protonation is observed, the non-hydrogen atoms in each tetracation are essentially coplanar, the average values of $d_{C–C}$ and $d_{C–N}$ are normal (1.387 and 1.458 Å, respectively), and the only short contacts arise from ionic $N–H^+\cdots Cl^-$ hydrogen bonds.

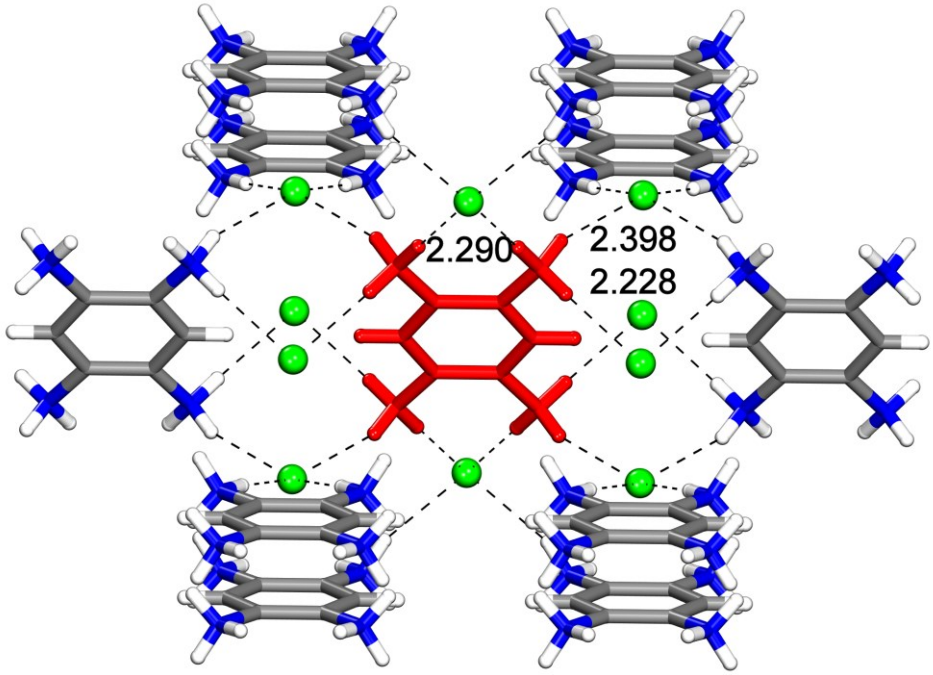

a

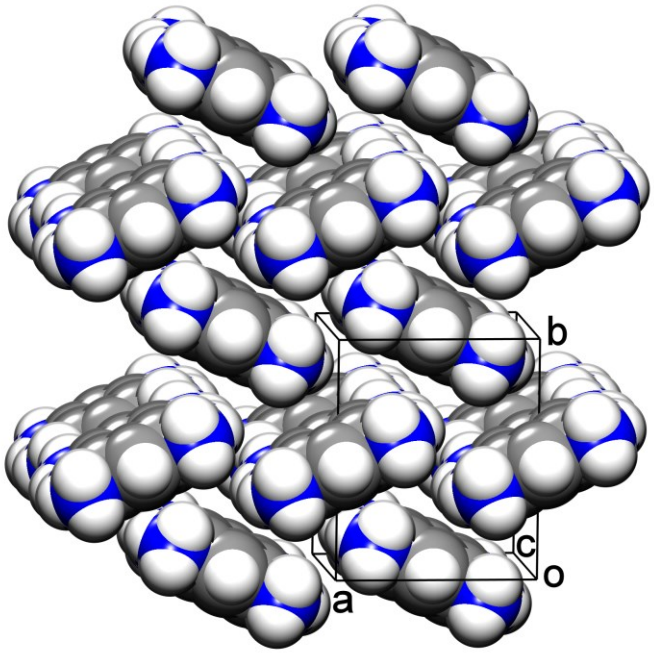

Figure 2.3 Representations of the structure of *Pnnm* crystals of tetrahydrochloride salt BTA (**1**)•4HCl grown from H_2O. (a) View showing a central tetracation (red), the primary associated chloride ions, and neighboring cations linked directly by chloride. The principal ionic N−$H^+\cdots Cl^-$ hydrogen bonds are shown as broken lines, with $d_{H\cdots Cl}$ given in Å. Unless stated otherwise, atoms appear in standard colors. (b) View of the structure along the *c*-axis, with chloride ions omitted and the tetracations shown in a space-filling representation.

Figure 2.3.a shows the immediate environment of each tetracation. Ten surrounding chloride ions form short ionic N–$H^+\cdots Cl^-$ hydrogen bonds. In turn, these chlorides link each tetracation to ten neighboring cations. Two chloride ions are chelated by each tetracation ($d_{H\cdots Cl}$ = 2.290 and $d_{N\cdots Cl}$ = 3.177 Å) and are held close to the plane defined by its non-hydrogen atoms, whereas the other eight chloride ions lie above and below the plane (average $d_{H\cdots Cl}$ = 2.233 and average $d_{N\cdots Cl}$ = 3.125 Å). As shown in Figure 2.3.a, four of the ten associated chloride ions accept two primary N–$H^+\cdots Cl^-$ hydrogen bonds, and the other six chloride ions accept four of these interactions, approximately in the same plane.

The tetracations are aligned to form tapes, which are packed in a herringbone arrangement (Figure 2.3.b). A noteworthy feature of the structure is that each tetracation BTA (**1**) • $4H^+$ can in principle serve as a donor in forming a total of 12 N–$H^+\cdots Cl^-$ hydrogen bonds, but the four associated chloride ions have the potential to act as acceptors in a total of 16 of these interactions. As a result, the numbers of donors and acceptors are mismatched, and some of the chloride ions are not fully coordinated. Complementary information about the structure of crystalline tetrahydrochloride salt BTA (**1**)•4HCl was provided by solid-state CP/MAS $^{13}C\{^1H\}$ and $^{15}N\{^1H\}$ NMR spectroscopy. The observation of only two signals in the ^{13}C NMR spectrum and one in the ^{15}N spectrum is consistent with the high molecular symmetry of the *Pnnm* structure and confirms the absence of significant amounts of other solid forms.[89]

Structures of BTA-H_2 (2).

Red crystals of quinonediimine BTA-H_2 (**2**) were grown by adding salt BTA (**1**)•4HCl to a 1 M aqueous solution of NaOH and allowing the mixture to stand at 20 °C for 18 h in contact with air. Table II - 2 compiles selected crystallographic data, and Figure 2.4 represents the structure. Molecules of BTA-H_2 (**2**) are related to methine dyes and incorporate two coupled cyanine subunits.[90] The C–N, C=N, C–C, and C=C bond lengths reflect the characteristic conjugation and bond alternation within the subunits. In particular, the average values of $d_{C–N}$ and $d_{C=N}$ (1.347 and 1.294 Å, respectively) resemble those observed in related compounds.[57,91–93] The average value of $d_{C2–C3}$ and $d_{C5–C6}$ is short (1.356 Å), the average of $d_{C1–C2}$ and $d_{C4–C5}$ is longer (1.433 Å), and the average of $d_{C3–C4}$ and $d_{C1–C6}$ is longest (1.502 Å). Within each cyanine subunit, the atoms are virtually coplanar, but the planes of the two subunits are slightly skewed.

Tableau II - 2 Structural Data for BTA-H_2 (**2**) and Dihydrochloride Salt BTA-H_2 (**2**)•2HCl

compound	**BTA-H_2 (2)**	**BTA-H_2 (2)•2HCl**
CCDC number	2283760	2283759
description	red fragments	dark blocks
crystal syst	orthorhombic	monoclinic
space group	$Pna2_1$	$P2_1/n$
a (Å)	10.7151(10)	5.3141(2)
b (Å)	7.7840(8)	7.3724(3)
c (Å)	7.2910(8)	11.3921(5)
α (deg)	90	90
β (deg)	90	99.436(1)
γ (deg)	90	90
V (Å^3)	608.12(11)	440.28(3)
Z	4	2
Z'	1	0.5
ρ_{calc} (g · cm^{-3})	1.487	1.577
T (K)	100	150
R_1, $I > 2\sigma(I)$	0.0537	0.0287
wR_2, $I > 2\sigma(I)$	0.1456	0.0756
GoF	1.228	1.108

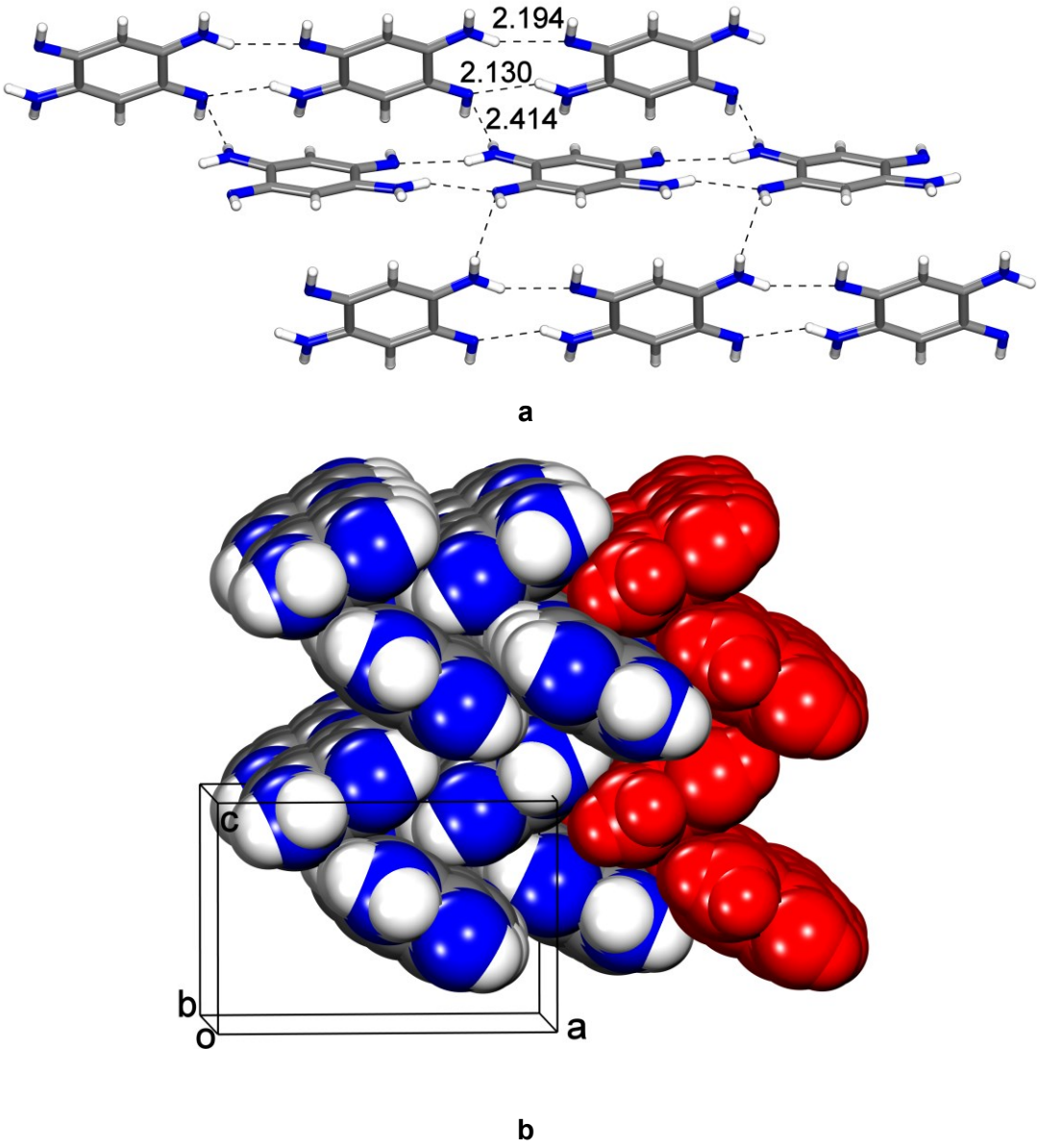

Figure 2.4 Representations of the structure of *Pna*2$_1$ crystals of BTA-H_2 (**2**) grown from H_2O. (a) View showing how multiple intermolecular N–H···N hydrogen bonds (broken lines, with $d_{H\cdots N}$ given in Å) link molecules of BTA-H_2 (**2**) end-to-end to form tapes, and how neighboring tapes are joined by additional N–H···N hydrogen bonds to produce corrugated sheets. (b) View along the *b*-axis showing the herringbone packing of corrugated sheets in a space-filling representation, with one sheet highlighted in red. In both views, atoms appear in standard colors unless stated otherwise.

Molecules of BTA-H_2 (**2**) engage in intramolecular N–H···N hydrogen bonds (average values of $d_{N\cdots N}$ and $d_{H\cdots N}$ are 2.686 and 2.376 Å, respectively) and are linked end-to-end by intermolecular N–H···N hydrogen bonds (average values of $d_{N\cdots N}$ and $d_{H\cdots N}$ are 2.999 and 2.162 Å, respectively) to form tapes aligned with the *b*-axis (Figure 2.4.a). Neighboring tapes are joined by additional N–H···N hydrogen bonds ($d_{N\cdots N}$ = 3.286 Å and $d_{H\cdots N}$ = 2.414 Å) to produce corrugated sheets, which are packed in a herringbone arrangement (Figure 2.4.b). Molecules in the *Pna*2_1 structure of BTA-H_2 (**2**) do not have an axis of C_2 symmetry, so certain peaks in the CP/MAS $^{13}C\{^1H\}$ and $^{15}N\{^1H\}$ NMR spectra are split; nevertheless, the data confirm that samples crystallized under the reported conditions are essentially phase-pure.[89]

It is noteworthy that the observed *Pna*2_1 crystals of BTA-H_2 are composed uniquely of molecules that adopt *E*,*E*-1,4-quinonediimine structure **2** rather than various plausible alternatives, such as *E*,*Z*-1,4-quinonediimine structure **11**, *E*,*Z*-1,2-isomer **12**, or the zwitterionic product **13** of intramolecular proton transfer. The closely related compound represented by structure **14**, which is the formal product of oxidizing 4,6-diaminoresorcinol, has been shown to exist as zwitterion **15** in the crystalline state.[94] In contrast, the analogous dihydroxybenzoquinone prefers 1,4-quinonoid structure **16** in the crystalline state instead of 1,2-isomer **17** or zwitterion **18**.[95] In general, 1,2-benzoquinones are destabilized by unfavorable alignment of polarized C=O bonds; however, analogous interactions are expected to be less important in benzoquinonediimines, and differences arising from inter- and intramolecular hydrogen bonding may also affect the relative stability of possible forms.

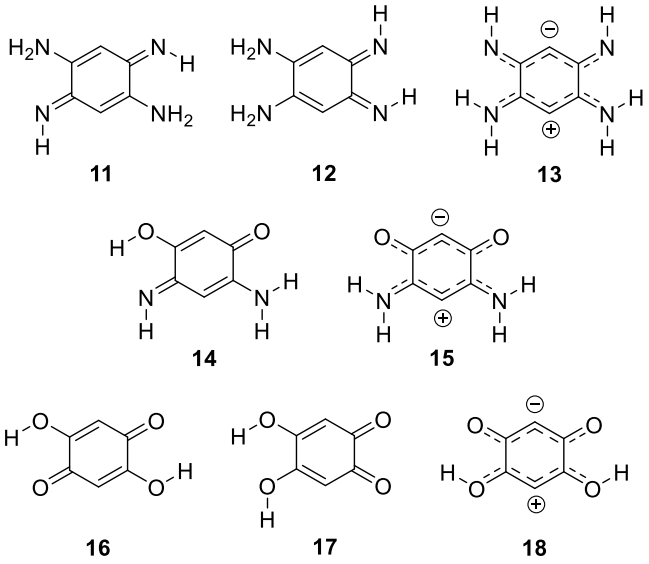

To help understand why BTA-H_2 (**2**), zwitterion **15**, and the analogous hydroxyquinone **16** adopt their observed structures, we used DFT calculations at the RωB97M(2)[96]/def2-QZVPPD[97-99]//RωB97X-D3[100–103]/6-311+G(2df,2p) level to estimate the relative energies of potential forms, both in the gas phase and in a medium with the dielectric constant of H_2O, using the conductor-like PCM approach (C-PCM).[104] Additional details related to the computational approach, including checks confirming that the restricted DFT approach is appropriate, are provided in the section on Computational and Experimental Methods. The results of the calculations are summarized in Tables II - 3–5. The data suggest that the observed forms of BTA-H_2 (**2**) and the analogous hydroxyquinone **16** are significantly more stable than their potential isomers under all conditions examined. In contrast, zwitterion **15** is predicted to be only slightly less stable than isomeric quinoneimine **14** in the gas phase and to become favored when the dielectric constant of the medium is sufficiently high. The data in Tables II - 3–5 reveal a general preference for 1,4-quinonoid forms, both for quinones and quinonediimines, and for structures with intramolecular hydrogen bonds.

Tableau II - 3 Relative Electronic Potential Energies (ΔE) and Dipole Moments (μ) of BTA-H_2 (**2**) and Potential Isomers in the Gas Phase and in a Medium with the Dielectric Constant of H_2O, as Estimated by DFT Calculations at the RωB97M(2)/def2-QZVPPD//RωB97X-D3/6-311+G(2df,2p) Level, with a C-PCM Approach for Assessing Solvent Effects

structure		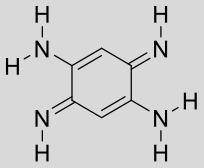 **2** (BTA-H_2)	 **11**	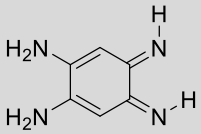 **12**	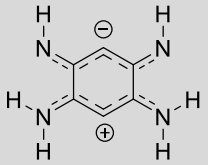 **13**
gas phase	ΔE (kcal mol^{-1})	0.0	5.6	10.0	14.5
	μ (D)	0.0	2.8	6.3	5.1
H_2O	ΔE (kcal mol^{-1})	0.0	2.8	5.6	9.8
	μ (D)	0.0	3.9	10.8	7.6

Tableau II - 4 Relative Electronic Potential Energies (ΔE) and Dipole Moments (μ) of Quinoneimine **14** and Zwitterion **15** in the Gas Phase and in a Medium with the Dielectric Constant of H_2O, as Estimated by DFT Calculations at the RωB97M(2)/def2-QZVPPD//RωB97X-D3/6-311+G(2df,2p) Level, with a C-PCM Approach for Assessing Solvent Effects

structure	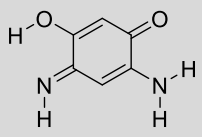 **14**	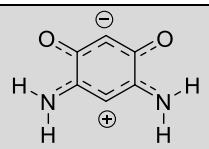 **15**	
gas phase	ΔE (kcal mol^{-1})	0.0	1.4
	μ (D)	4.1	8.3
H_2O	ΔE (kcal mol^{-1})	8.7	0.0
	μ (D)	5.7	11.9

Tableau II - 5 Relative Electronic Potential Energies (ΔE) and Dipole Moments (μ) of Hydroxyquinone **16** and Potential Isomers in the Gas Phase and in a Medium with the Dielectric Constant of H_2O, as Estimated by DFT Calculations at the RωB97M(2)/def2-QZVPPD//RωB97X-D3/6-311+G(2df,2p) Level, with a C-PCM Approach for Assessing Solvent Effects

structure		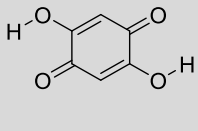 **16**	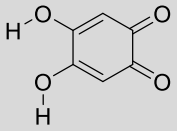 **17**	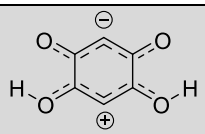 **18**
gas phase	ΔE (kcal mol^{-1})	0.0	17.5	12.6
	μ (D)	0.0	7.3	3.2
H_2O	ΔE (kcal mol^{-1})	0.0	8.3	10.8
	μ (D)	0.0	11.0	5.0

The molecular structure of quinonediimine BTA-H_2 (**2**) observed in the solid state appears suitable for automerization by intramolecular migrations of hydrogen (eq. 1). Such reactions have attracted attention because they can be used to create molecular switches.[105] Unimolecular automerizations of this type have been studied experimentally and computationally,[106–115] particularly in the cases of dihydroxybenzoquinone **16** and azophenine (**19**), which can be produced by oxidizing aniline. However, the reactivity of parent compound BTA-H_2 (**2**) has been largely overlooked. Conceivable mechanisms for the unimolecular automerization of compound **2** include (1) a concerted shift of two hydrogens via a single transition state, represented by structure **20**; or (2) a sequential process involving an intermediate (such as zwitterion **13** or a singlet diradical, as represented by structure **21**) and two transition states. In addition, inspection of Figure 2.4.a suggests that automerization might occur in the solid state by coordinated intermolecular transfers of hydrogen within the characteristic hydrogen-bonded tapes observed in crystalline BTA-H_2 (**2**). Such transfers would not necessarily change the tapes themselves but would disrupt inter-tape hydrogen bonding. As a result, solid-state automerization of BTA-H_2 (**2**) is not expected to be efficient.

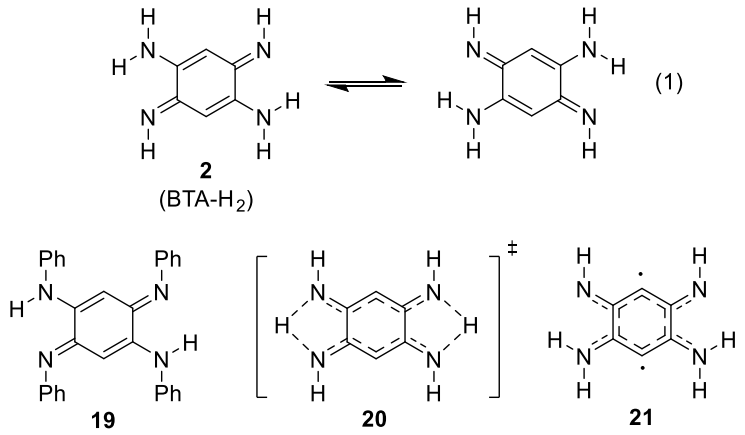

At 25 °C, the CP/MAS $^{13}C\{^{1}H\}$ NMR spectrum of crystalline BTA-H_2 (**2**) showed five primary peaks, along with the corresponding spinning sidebands (Figure 2.5.a). The spectrum reflects the low molecular symmetry of the *Pna*2$_1$ form of the compound and is consistent with slow solid-state automerization, as expected on the basis of the observed hydrogen-bonded structure. In addition, the corresponding $^{13}C\{^{1}H\}$ NMR spectrum in solution (DMSO-d_6 containing small amounts of NaOH) showed three sharp signals at 25 °C (Figure 2.5.b), which suggests that the compound exists primarily as *E*,*E*-1,4-quinonediimine **2**, both in the crystalline state and in solution, and that automerization is again slow. ^{1}H and $^{13}C\{^{1}H\}$ NMR spectra recorded in DMSO-d_6 at higher temperatures showed broadening and coalescence, but decomposition occurred simultaneously, and we were unable to measure E_a reliably.[89]

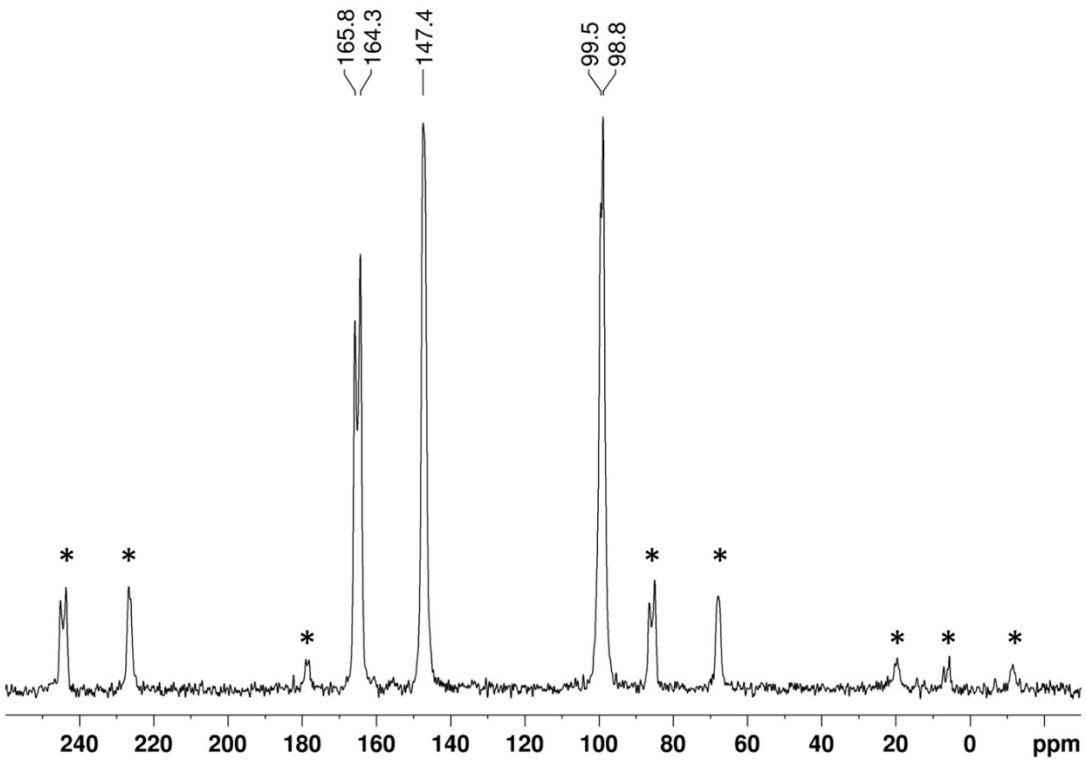
165.8
164.3
147.4
99.5
98.8
*
*
*
*
*
*
*
240
220
200
180
160
140
120
100
80
60
40
20
0
ppm

a

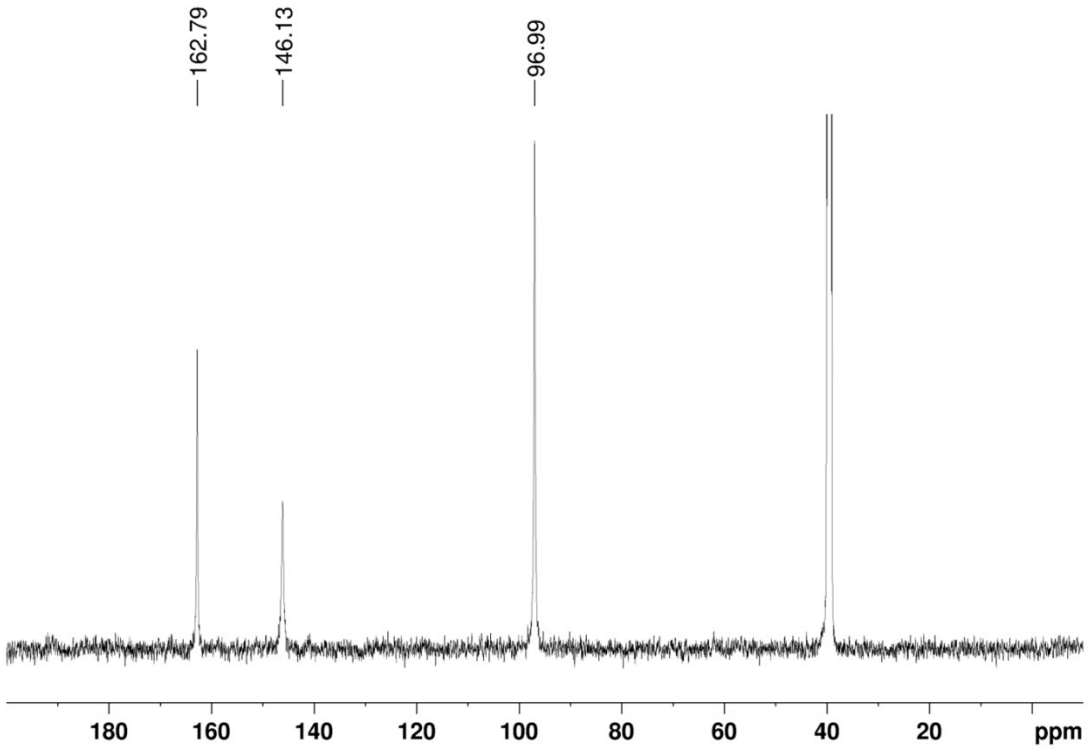

Figure 2.5 (a) CP/MAS $^{13}C\{^{1}H\}$ NMR spectrum (151 MHz, 12 kHz) of BTA-H_2 (**2**) in the crystalline *Pna*2_1 form, with spinning sidebands identified by asterisks. (b) $^{13}C\{^{1}H\}$ NMR spectrum (101 MHz) of BTA-H_2 (**2**) at 25 °C in solution (DMSO-d_6 containing small amounts of NaOH).

In contrast, phenyl-substituted analogue azophenine (**19**) has been shown to automerize readily in the solid state and in solution, as demonstrated by analyses using variable-temperature IR and NMR spectroscopy.[106,107] Little information was provided about the solid form of compound **19** used in this earlier work. However, two polymorphs are known to exist,[91,92] and molecules adopt *E*,*E*-1,4-quinonediimine structure **19** in both cases, with short intramolecular N–H···N distances (average value of $d_{H\cdots N}$ = 2.091 Å). Azophenine (**19**) thus adopts a molecular structure expected to be suitable for unimolecular automerization, as in the case of BTA-H_2 (**2**).

However, compound **19** forms no intermolecular hydrogen bonds in either known polymorph, so solid-state automerization can occur without disrupting a network of strong directional interactions. In solution, the rate of automerization of azophenine (**19**) and its entropy of activation were found to be essentially independent of the polarity of the solvent, and E_a was determined to be 11.4 kcal mol^{-1} in 1,2-dichloroethane-d_4.[106] The observed rates and kinetic isotope effects ruled out automerization by a concerted shift of two atoms of hydrogen but were considered to be consistent with sequential alternatives involving formation of an intermediate, either a weakly solvated zwitterion or a singlet diradical. In addition, the conclusion that automerization of azophenine (**19**) is stepwise rather than concerted is consistent with the results of computational studies.[108,109]

The unique hydrogen-bonded crystalline structure of BTA-H_2 (**2**) helps explain why its solid-state automerization is slower than that of analogue **19**, but the observation that BTA-H_2 (**2**) also reacts more slowly in solution shows that other factors must also be involved. In particular, the rates may differ because N–H bonds broken in the automerization of BTA-H_2 (**2**) are expected to be stronger than those in phenyl-substituted analogue **19**, and the effects of tunnelling may be different in the two systems. For further insight, we used DFT calculations at the RωB97M(2)/def2-QZVPPD//RωB97X-D3/6-311+G(2df,2p) level, along with a C-PCM approach for assessing solvent effects, to estimate the relative energies of the following species: (1) BTA-H_2 (**2**); (2) transition state **20** for the concerted shift of two atoms of hydrogen; (3) potential intermediate **13** resulting from the sequential transfer of a proton; and (4) the transition state leading to formation of this intermediate. The results of the calculations are summarized in Table II - 6 for singlet ground-state processes occurring in the gas phase and in a medium with the dielectric constant of H_2O. In all cases, the calculated electronic wavefunctions were found to be stable, suggesting that structures with diradical character are probably restricted to the excited-state singlet manifold.

Tableau II - 6 Computational Analysis of Automerization, Showing Relative Electronic Potential Energies (*E*), Enthalpies (*H*), and Free Energies (*G*) for BTA-H_2 (**2**), Potential Transition State **20**, Potential Intermediate **13**, and Related Transition States, as Assessed by Ground-State DFT Calculations at the RωB97M(2)/def2-QZVPPD//RωB97X-D3/6-311+G(2df,2p) Level, Using the C-PCM Approach to Assess Solvent Effects, for Processes Occurring at 298 K in the Gas Phase or in a Medium with the Dielectric Constant of H_2O

structure	relative values in the gas phase (kcal mol^{-1})			relative values in H_2O (kcal mol^{-1})		
	E	*H*°	*G*°	*E*	*H*°	*G*°
BTA-H_2 (**2**)	0.0	0.0	0.0	0.0	0.0	0.0
Transition state **20**	34.0	27.8	30.0	37.8	31.4	33.4
Zwitterion **13**	14.5	14.2	15.3	9.7	10.0	10.9
Transition state leading to zwitterion **13**	21.3	18.2	19.8	21.8	18.5	19.8

The data in Table II - 6 show that thermally induced unimolecular automerization of BTA-H_2 (**2**) is expected to occur by a sequential mechanism, as observed in the related cases of dihydroxybenzoquinone **16** and azophenine (**19**). The value of the Arrhenius energy of activation E_a predicted by using conventional transition-state theory (CTST)[116,117] is $E_a = \Delta H^{\circ\ddagger} + RT = 18.8$ kcal mol^{-1} for automerization of BTA-H_2 (**2**) in the gas phase. This value is consistent with our experimental studies using variable-temperature NMR spectroscopy and is significantly higher than values measured under similar conditions for analogues **16** (4.7 kcal mol^{-1})[115] and **19** (11.4 kcal mol^{-1}).[106] Note that the enthalpy of activation $\Delta H^{\circ\ddagger}$ calculated in the present work includes zero-point vibration, but no hydrogen tunnelling effects or corrections for multiple crossing of the dividing surface at the col.[117] Nevertheless, the logarithm of the pre-exponential Arrhenius factor *A*, as determined by CTST according to eq. 2, is equal to 12.1 and 12.3 in the gas phase and in H_2O, respectively, according to the data shown in Table II - 6. These values can be compared with those of log (A /s^{-1}) = 11.62 ± 0.14, 11.94 ± 0.17, and 12.05 ± 0.25 measured by Rumpel and

Limbach for k^{HH}, k^{HD}, and k^{DD}, respectively, in the automerization of azophenine (**19**) in $C_2D_2Cl_4$.[106] The similarity of the values is consistent with the hypothesis that BTA-H_2 (**2**) and azophenine (**19**) have a common mechanism for thermally-induced automerization, consisting of a sequential proton transfer leading to a zwitterionic intermediate via a transition state with a polarity similar to that of the reactant.

$$A = e\frac{k_B T}{h}e^{\frac{\Delta S^{\circ\ddagger}}{R}} \quad (2)$$

Structures of Dihydrochloride Salt BTA-H_2 (2)·2HCl.

Dihydrochloride salt BTA-H_2 (**2**)•2HCl could be obtained in the form of dark crystals by adding saturated aqueous solutions of $FeCl_3$ to solutions of tetrahydrochloride salt BTA (**1**)•4HCl in 1 M aqueous HCl. Selected crystallographic data are provided in Table II - 2, and a view of the structure appears in Figure 2.6. The salt contains dications composed of two protonated cyanine subunits. In each, the two C–N bonds are short and nearly equal in length ($d_{N–C}$ = 1.313 and 1.324 Å), and the two C–C bonds are also closely similar ($d_{C–C}$ = 1.386 and 1.394 Å), which is consistent with expectations for a delocalized dication in a crystal structure lacking full molecular symmetry. The C–C bonds connecting the two individual cationic cyanine subunits are long ($d_{C–C}$ = 1.495 Å), thereby reducing charge repulsion and allowing all four NH_2 groups to lie close to the average molecular plane of each dication. Similar values of $d_{C–C}$ and $d_{C–N}$ have been observed in salts of substituted analogues.[118–120] Solid-state CP/MAS $^{13}C\{^1H\}$ and $^{15}N\{^1H\}$ NMR spectra confirmed that the crystalline solid is essentially phase-pure, and splitting of peaks in the spectra is consistent with the low molecular symmetry of the $P2_1/n$ structure.[89]

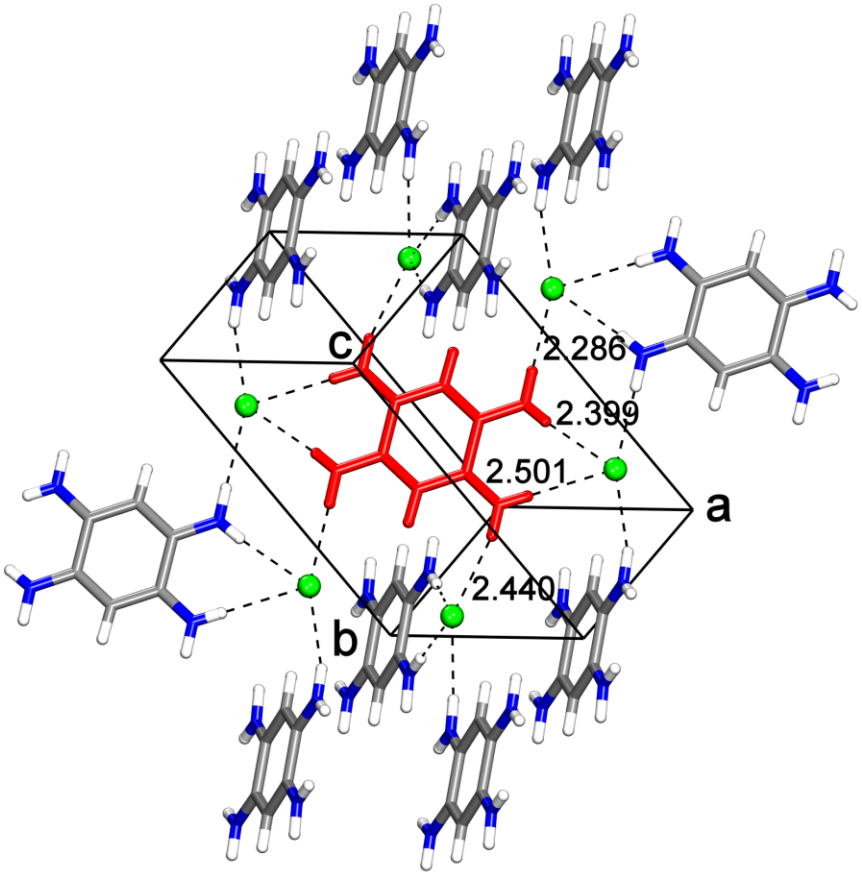

Figure 2.6 Representation of the primary interactions in the structure of $P2_1/n$ crystals of dihydrochloride salt BTA-H_2 (**2**)•2HCl grown from H_2O, showing a central dication (red) and the 10 neighbors linked by six bridging chloride ions. Ionic N–$H^+\cdots Cl^-$ hydrogen bonds are indicated by broken lines (with $d_{H\cdots Cl}$ given in Å), and atoms appear in standard colors unless stated otherwise.

Each dication interacts directly with six virtually coplanar chloride ions by forming a total of eight ionic N–$H^+\cdots Cl^-$ hydrogen bonds (Figure 2.6), with values of $d_{H\cdots Cl}$ lying in the range 2.286–2.501 Å (corresponding to values of $d_{N\cdots Cl}$ in the range 3.170–3.316 Å). All chloride ions in the structure accept four N–$H^+\cdots Cl^-$ hydrogen bonds lying roughly in the same plane. Each dication BTA-H_2 (**2**)•$2H^+$ can in principle act as a donor in forming a total of eight N–$H^+\cdots Cl^-$ hydrogen bonds, and the two associated chloride ions have the potential to serve as acceptors in a total of eight of these interactions, as demonstrated by the structure of salt BTA (**1**)•4HCl. As a result, the numbers of donors and acceptors are matched, and the full potential of

the components to form hydrogen bonds is attained. These observations suggest that hydrochloride salts formed by arenes with multiple NH_2 groups and the corresponding quinonediimines will tend to crystallize to form structures with the largest possible number of ionic $N–H^+\cdots Cl^-$ hydrogen bonds, up to a limit of four of these interactions per chloride ion.

Conclusions

Like hydroquinones and quinones, aromatic compounds with multiple NH_2 groups and the corresponding quinonediimines have the potential to serve as the components of useful redox-active materials. BTA (**1**) and BTA-H_2 (**2**) form a promising redox pair of this type, and the compounds have proven to be useful in many areas of chemistry. However, many aspects of their behavior have remained poorly studied, such as the nature of their protonated forms, their preferred molecular structures, their reactivity, and their organization in condensed phases. In the present work, we have used a combination of improved methods of synthesis, computation, spectroscopic studies, and structural analyses to develop a deeper understanding of BTA (**1**), BTA-H_2 (**2**), their salts, and related compounds. The new knowledge is expected to accelerate exploitation of the compounds in areas of materials science where desirable properties can only be attained by properly controlling the organization of molecular components. Further study of the physical properties of these compounds, including their electrochemical behavior, is expected to clarify their suitability as components of redox-active materials.

Computational and Experimental Methods

Methodology Used in Calculations Related to the Behavior of BTA-H_2 (2) and Analogues. DFT calculations related to the behavior of BTA-H_2 (**2**) and analogues were performed using Spartan '20 Version 1.1.4 software (Wavefunction, Inc.), with Q-Chem 5.1 as the computational engine.[121] To guide selection of the methods employed, we used the conceptual flowchart of decision-making in chemical calculations recently proposed by Bursch and coauthors.[122] Initial structures were generated using the graphical interface of Spartan'20, and molecular flexibility was considered by performing all relevant rotations around C–N and C–O single bonds. Conformations were initially retained if their energy was within 15 kcal mol^{-1} of the lowest-energy conformer, as calculated using the empirical MMFF force field implemented in Spartan'20.[123]

Geometry optimization was carried out in two steps to achieve a satisfactory balance of computational cost and accuracy. Geometries were first optimized using the ωB97X-D3 functional[100–103] with a relatively small 6-31+G(d) basis set, and only configurations within 10 kcal mol^{-1} of the lowest-energy conformer were retained. Configurations were then optimized using the same functional, but with the larger 6-311+G(2df,2p) basis set, and all configurations within 5 kcal mol^{-1} of the global minimum were retained. Finally, single-point energy calculations were carried out using the ωB97M(2) double-hybrid functional[96] and the def2-QZVPPD basis set.[97-99] This combination has been demonstrated to provide some of the most accurate results for conformers, reaction energies, and barriers.[121,122]

Structures on the potential energy surface were characterized by diagonalizing the Hessian matrix and counting the number of negative eigenvalues (number of imaginary frequencies). All structures were characterized as geometric minima (zero imaginary frequencies), except for the transition state leading to zwitterion **13,** which proved to be a first-order saddle point (topologically equivalent to the top of a mountain pass), and structure **20**, which was found to be a second-order saddle point (topologically equivalent to a summit). By animating the vibrational modes corresponding to the imaginary frequencies, we verified that first-order saddle points connected structures of BTA-H_2 (**2**) and zwitterionic intermediate **13**. In contrast, the mode

corresponding to the largest imaginary frequency of the second-order saddle point **20** connected the two reactant structures, whereas the mode corresponding to the lowest imaginary frequency connected the two possible zwitterionic structures.

Thermodynamic contributions to the room-temperature values of enthalpy, entropy, and free energy in Table II - 6 were computed using the usual rigid-rotor-harmonic-oscillator (RRHO) approach. A well-known problem of RRHO-based calculations of entropy is that the vibrational entropy is overestimated when vibrational frequencies become smaller than approximately 50 cm^{-1}.[124] No corrections to the RRHO approach were made in the present work because all frequencies were found to be larger than 60 cm^{-1}. This is in contrast to the default setting in Spartan'20, which sets the ideal gas constant R as the maximal contribution of any vibrational mode to the total entropy.

Calculations were carried out in the gas phase and in a medium with the dielectric constant of H_2O, using the conductor-like PCM approach (C-PCM),[104] as implemented in Q-Chem 5.1. C-PCM is a purely electrostatic model and does not consider contributions from cavity creation and van der Waals interactions between solute and solvent; however, these contributions should play a minor role, because solvent-accessible areas are likely to be similar for all participants in the intramolecular proton-transfer reactions that are being analyzed.

All calculations were carried out for species in the electronic ground state using the restricted DFT formalism, which is appropriate if the wavefunction has a single-reference character. No indication of multi-reference character was detected: HOMO-LUMO gaps were always larger than 5 eV, and all restricted DFT wavefunctions were found to be stable with respect to the RKS-UKS (restricted to unrestricted) and RKS-CRKS (real to complex) transformations.[125]

Experimental Methodology. All starting materials were purchased from commercial suppliers and used without further purification. Thin-layer chromatography was performed on glass-supported silica gel plates, and products were detected using a UV lamp.

CP/MAS $^{13}C\{^{1}H\}$ and $^{15}N\{^{1}H\}$ NMR experiments were performed at 303 K on a Bruker Avance 600 MHz spectrometer, operating at 14.1 T (^{13}C frequency 151 MHz, ^{15}N frequency 61 MHz) and equipped with a 4 mm MAS probe. A standard cross-polarization pulse sequence was used with a contact time of 2 ms and a repetition time of 2.5 s. The spinning rate was in the range 10 – 12 kHz, and temperatures were calibrated with external $PbNO_3$. Chemical shifts were calibrated on the CH ^{13}C signal of adamantane (set to 38.48 ppm) as indirect reference.

VT NMR experiments in solution were performed on a Bruker Avance III 400 MHz spectrometer, operating at 9.4 T (^{1}H frequency 400 MHz, ^{13}C frequency 101 MHz) and equipped with a Prodigy probe. Temperatures were calibrated with external ethylene glycol. ^{1}H NMR experiments were performed with eight scans, a repetition time of 5 s, an acquisition time of 1.3 s, and a 30° pulse of 4 µs. $^{13}C\{^{1}H\}$ experiments were performed with a spin-echo experiment, using 96 or 400 scans, a repetition time of 2 s, an acquisition time of 1.6 s, and an echo time of 200 µs.

Tetrahydrochloride Salt of Benzene-1,2,4,5-tetramine (BTA (1)•4HCl). KNO_3 (14 g, 140 mmol) was added to cold (4 °C) H_2SO_4 containing about 30% H_2O (50 mL, ρ = 1.6 g cm^{-3}), and the mixture was stirred to produce a solution. 1,3-Dichlorobenzene (8.0 mL, 10 g, 68 mmol) was added in a single portion, the mixture was heated at 140 °C for 21 h. After thin-layer chromatography confirmed that the reaction was complete, the mixture was cooled to 90 °C and poured onto crushed ice (150 g) to produce a yellow solid, which was separated by filtration, washed with H_2O, and dried under vacuum. The product (15 g, 63 mmol) contained 1,5-dichloro-2,4-dinitrobenzene (**3**) and 1,3-dichloro-2,4-dinitrobenzene (**4**) as major and minor components, respectively. **Caution!** 1,5-Dichloro-2,4-dinitrobenzene (**3**) has been reported to be a potent skin irritant that may cause severe blisters.[63,64] The mixture of isomers **3** and **4** was used in the next step without further purification. If pure isomer **3** is needed, the compound can easily be crystallized by dissolving the crude mixture in a minimal amount of boiling EtOH and allowing the solution to cool slowly to 20 °C.

A sample of the mixture of isomers **3** and **4** (4.0 g, 17 mmol) was suspended in ethylene glycol (17 mL), concentrated aqueous NH_3 was added (8.5 mL, ρ = 0.90 g cm^{-3}), and the vigorously

stirred mixture was heated in an oil bath behind a weighted safety shield at 140 °C for 20 h in a screw-capped pressure reactor fitted with a perfluoroelastomer O-ring. The mixture was then cooled, and the resulting solid was separated by filtration, washed with cold H_2O, and dried under vacuum. This yielded a mixture of 4,6-dinitrobenzene-1,3-diamine (**5**) and 2,4-dinitrobenzene-1,3-diamine (**6**) as an orange solid (3.3 g, 17 mmol), which was used in the following step without further purification.

A solution was prepared by adding anhydrous $SnCl_2$ (10 g, 53 mmol) to stirred concentrated aqueous HCl (15 mL, $\rho \approx 1.2$ g cm^{-3}) at 4 °C, and a mixture of dinitrodiamines **5** and **6** (1.5 g, 7.6 mmol) was added in portions at a rate that kept the temperature below 60 °C. After the addition was complete, the mixture was stirred at 20 °C for 40 min. The resulting precipitate was separated by filtration, washed sparingly with concentrated aqueous HCl, and dried under vacuum to give the tetrahydrochloride salt of benzene-1,2,4,5-tetramine (BTA (**1**) • 4HCl) as a colorless solid (0.96 g, 3.4 mmol), which corresponds to an overall yield of 41% starting from 1,3-dichlorobenzene. From the filtrate, a sulfate salt of benzene-1,2,3,4-tetramine (**7**) could be recovered as described below. Salt BTA (**1**)•4HCl could be recrystallized by placing a cold solution in H_2O (4 °C) on top of a cold underlayer of concentrated aqueous HCl (4 °C): ^{1}H NMR (400 MHz, D_2O) δ 6.88 (s, 2H); ^{13}C{ 1H} NMR (101 MHz, D_2O) δ 124.8, 116.1; CP/MAS ^{13}C{^{1}H} NMR (151 MHz) δ 128.4, 123.5; CP/MAS ^{15}N{^{1}H} NMR (61 MHz) δ 59.7; HRMS (ESI-TOF) *m/z* calcd for $C_6H_{11}N_4$ $[M]^+$ 139.0978, found 139.0969.

Sulfate Salt of Benzene-1,2,3,4-tetramine (7•H_2SO_4). A sulfate salt of benzene-1,2,3,4-tetramine (**7**) could be recovered from the filtrate obtained in the final step of the synthesis of the tetrahydrochloride salt of benzene-1,2,4,5-tetramine (BTA (**1**)•4HCl). This was achieved by pouring the filtrate onto ice (50 g), adding cold EtOH (4 °C, 50 mL), and inducing crystallization by adding droplets of concentrated H_2SO_4 ($\rho \approx 1.8$ g cm^{-3}). The resulting precipitate was separated by filtration, washed with cold EtOH, and dried in vacuum to give the sulfate salt of benzene1,2,3,4-tetramine (**7** • H_2SO_4) as a crystalline solid (0.72 g, 3.0 mmol, 37% overall yield): ^{1}H NMR (400 MHz, D_2O containing added DCl to increase solubility) δ 6.78 (s, 2H); ^{13}C{1H}

NMR (101 MHz, D_2O) δ 126.5, 121.3, 117.7. The structure of the product was confirmed by single-crystal Xray diffraction.[126]

3,6-Diiminocyclohexa-1,4-diene-1,4-diamine (BTA-H_2 (2)). Tetrahydrochloride salt BTA (**1**)•4HCl (0.39 g, 1.4 mmol) was stirred with aqueous NaOH (1.0 M, 10 mL) for 72 h at 20 °C in contact with air. The resulting precipitate was separated by filtration, washed with cold H_2O, and dried under vacuum to give 3,6-diiminocyclohexa-1,4-diene-1,4-diamine (BTA-H_2 (**2**)) as a brown solid (0.18 g, 1.3 mmol, 93%): ^{1}H NMR (400 MHz, DMSO-d_6) δ 9.35 (bs, 2H), 5.80 (bs, 4H), 5.43 (s, 2H); ^{13}C{^{1}H} NMR (101 MHz, DMSO-d_6) δ 162.8, 146.1, 97.0; CPMAS ^{13}C{^{1}H} NMR (151 MHz) δ 165.7, 164.3, 147.4, 99.5, 98.8; CP/MAS ^{15}N{^{1}H} NMR (61 MHz) δ 271.5, 263.8, 70.3; HRMS (ESI-TOF) *m/z* calcd for $C_6H_9N_4$ $[M + H]^+$ 137.08217, found 137.08153.

2,5-Diaminocyclohexa-2,5-diene-1,4-diiminium Dichloride (BTA-H_2 (2)•2HCl). Tetrahydrochloride salt BTA (**1**)•4 HCl (1.0 g, 3.6 mmol) was dissolved in aqueous HCl (1.0 M, 40 mL), and a saturated aqueous solution of $FeCl_3$ (20 mL) was added. The mixture was left unstirred at 20 °C for 48 h in contact with air. The resulting precipitate was separated by filtration, washed with aqueous HCl (6.0 M, 50 mL), and dried under vacuum to give 2,5-diaminocyclohexa-2,5-diene-1,4-diiminium dichloride (BTA-H_2 (**2**)•2HCl) as a brown solid (0.68 g, 3.3 mmol, 92%): ^{1}H NMR (700 MHz, DMSO-d_6) δ 10.4 (bs, 8H), 5.91 (bs, 2H); ^{13}C{^{1}H} NMR (176 MHz, DMSO-d_6) δ 155.7, 92.2; CP/MAS ^{13}C{^{1}H} NMR (151 MHz) δ 155.0, 154.1, 92.5; CP/MAS ^{15}N{^{1}H} NMR (61 MHz) δ 142.9, 125.2. HRMS (ESI-TOF) *m/z* calcd for $C_6H_9N_4$ $[M - H]^+$ 137.0825, found 137.0822.

Crystallizations. Crystals for structural analysis by X-ray diffraction were grown in the following ways. Crystals of BTA (**1**) and BTA (**1**)•2HCl formed from mixtures obtained by adding BTA (**1**)•4HCl to aqueous solutions of NaOH. Salt BTA (**1**)•4HCl was crystallized from aqueous HCl. Crystals of BTA-H_2 (**2**) were obtained by adding salt BTA (**1**)•4HCl to a 1 M aqueous solution of NaOH and leaving the mixture in contact with air. Compound BTA-H_2 (**2**)•2HCl was obtained as dark crystals by adding saturated aqueous solutions of $FeCl_3$ to solutions of salt BTA (**1**)•4HCl in 1 M aqueous HCl.

Associated Content

Data Availability Statement: The data underlying this study are available in the published article and its Supporting Information.

Supporting Information: The Supporting Information is available free of charge at https://pubs.acs.org/doi/10.1021/acs.joc.3c01793. Additional crystallographic data (including thermal atomic displacement parameter plots), supplemental computational information, and spectroscopic data.

Accession Codes: CCDC 2283757–2283761 contain the supplementary crystallographic data for this paper. These data can be obtained free of charge via www.ccdc.cam.ac.uk/data_request/cif, or by emailing data_request@ccdc.cam.ac.uk, or by contacting The Cambridge Crystallographic Data Centre, 12 Union Road, Cambridge CB2 1EZ, UK; fax: +44 1223 336033.

Notes. The authors have no competing financial interests to declare.

Acknowledgments. Financial support from the Natural Sciences and Engineering Research Council (NSERC) of Canada (RGPIN-2019-05469 and RGPIN-2017-06194) is gratefully acknowledged by J. D. W. and R. I. In addition, J. D. W. thanks the Canada Foundation for Innovation (Project 30910) and the Canada Research Chairs Program for their generous support. J. O. E. S. is grateful to the Université de Montréal for a graduate fellowship. The authors also thank Dr. Pedro Aguiar for advice related to NMR spectroscopy and the Centre régional de spectrométrie de masse for providing mass spectra. In addition, the authors are grateful for support provided by the Centre en chimie verte et catalyse and the Centre québécois sur les matériaux fonctionnels, two strategic clusters funded by the Fonds de recherche du Québec – Nature et technologies (FRQNT).

References

1. Kim, J.; Kim, Y.; Yoo, J.; Kwon, G.; Ko, Y.; Kang, K. Organic Batteries for a Greener Rechargeable World. *Nat. Rev. Mater.* **2023**, *8*, 55–70.
2. Chen, Y.; Dai, H.; Fan, K.; Zhang, G.; Tang, M.; Gao, Y.; Zhang, C.; Guan, L.; Mao, M.; Liu, H.; Zhai, T.; Wang, C. A Recyclable and Scalable High-Capacity Organic Battery. *Angew. Chem. Int. Ed.* **2023**, e202302539.
3. Chen, X.; Yin, X.; Aslam, J.; Sun, W.; Wang, Y. Recent Progress and Design Principles for Rechargeable Lithium Organic Batteries. *Electrochem. Energy Rev.* **2022**, *5*, 12.
4. Kato, K.; Puthirath, A. B.; Mojibpour, A.; Miroshnikov, M.; Satapathy, S.; Thangavel, N. K.; Mahankali, K.; Dong, L.; Arava, L. M. R.; John, G.; Bharadwaj, P.; Babu, G.; Ajayan, P. M. Light-Assisted Rechargeable Lithium Batteries: Organic Molecules for Simultaneous Energy Harvesting and Storage. *Nano Lett.* **2021**, *21*, 907–913.
5. Esser, B.; Dolhem, F.; Becuwe, M.; Poizot, P.; Vlad, A.; Brandell, D. A Perspective on Organic Electrode Materials and Technologies for Next Generation Batteries. *J. Power Sources* **2021**, *482*, 228814.
6. Goujon, N.; Casado, N.; Patil, N.; Marcilla, R.; Mecerreyes, D. Organic Batteries Based on Just Redox Polymers. *Prog. Polym. Sci.* **2021**, *122*, 101449.
7. Lakraychi, A. E.; Dolhem, F.; Vlad, A.; Becuwe, M. Organic Negative Electrode Materials for Metal-Ion and Molecular-Ion Batteries: Progress and Challenges from a Molecular Engineering Perspective. *Adv. Energy Mater.* **2021**, *11*, 2101562.
8. Shea, J. J.; Luo, C. Organic Electrode Materials for Metal Ion Batteries. *ACS Appl. Mater. Interfaces* **2020**, 12, 5361–5380.
9. Poizot, P.; Gaubicher, J.; Renault, S.; Dubois, L.; Liang, Y.; Yao, Y. Opportunities and Challenges for Organic Electrodes in Electrochemical Energy Storage. *Chem. Rev.* **2020**, *120*, 6490–6557.
10. Lu, Y.; Chen, J. Prospects of Organic Electrode Materials for Practical Lithium Batteries. *Nat. Rev. Chem.* **2020**, *4*, 127–142.
11. Muench, S.; Wild, A.; Friebe, C.; Häupler, B.; Janoschka, T.; Schubert, U. S. Polymer-Based Organic Batteries. *Chem. Rev.* **2016,** *116*, 9438–9484.

12. Qiu, Z.; Li, C.-J. Transformations of Less-Activated Phenols and Phenol Derivatives via C−O Cleavage. *Chem. Rev.* **2020**, *120*, 10454–10515.
13. Asha, A.; Ravindran, J.; Suma, S.; Suresh, C. H.; Lankalapalli, R. S. Synthesis of 2,5-Diamino-*p*-benzoquinones via Aerobic Oxidative $C(sp^2)$-$C(sp^2)$ Bond Cleavage and Mechanistic Studies. *ChemistrySelect* **2020**, *5*, 2545–2550.
14. Lardy, S. W.; Luong, K. C.; Schmidt, V. A. Formal Aniline Synthesis from Phenols through Deoxygenative N-Centered Radical Substitution. *Chem. Eur. J.* **2019**, *25*, 15267–15271.
15. Crooke, S. T.; Bradner, W. T. Mitomycin C: A Review. *Can. Treat. Rev.* **1976**, *3*, 121–139.
16. Nietzki, R.; Schedler, A. Synthese von symmetrischem Tetramidobenzol mittels Dinitrodichlorbenzol. *Ber. dtsch. chem. Ges.* **1897**, *30*, 1666–1669.
17. Nietzki, R.; Schmidt, L. Ueber das benachbarte Tetramidobenzol. *Ber. dtsch. chem. Ges.* **1889**, *22*, 1648–1653.
18. Nietzki, R.; Hagenbach, E. Ueber Tetramidobenzol und seine Derivate. *Ber. dtsch. chem. Ges.* **1887**, *20*, 328–338.
19. Rupe, H. Rudolf Nietzki. *Ber. dtsch. chem. Ges.* **1919**, *52*, A1–A28.
20. Noelting, E. Rudolf Nietzki. 1847–1917. *Helv. Chim. Acta* **1918**, *1*, 343–430.
21. Ost, H. Rudolf Nietzki. *Angew. Chem.* **1917**, *30*, 285–287.
22. Sang, Z.; Liu, J.; Zhang, X.; Yin, L.; Hou, F.; Liang, J. One-Dimensional π−d Conjugated Conductive Metal−Organic Framework with Dual Redox-Active Sites for High-Capacity and Durable Cathodes for Aqueous Zinc Batteries. *ACS Nano* **2023**, *17*, 3077–3087.
23. Wang, J.; Liu, X.; Jia, H.; Apostol, P.; Guo, X.; Lucaccioni, F.; Zhang, X.; Zhu, Q.; Morari, C.; Gohy, J.-F.; Vlad, A. A High-Voltage Organic Framework for High-Performance Na- and K-Ion Batteries. *ACS Energy Lett.* **2022**, *7*, 668–674.
24. Yang, D.; Liang, Z.; Tang, P.; Zhang, C.; Tang, M.; Li, Q.; Biendicho, J. J.; Li, J.; Heggen, M.; Dunin-Borkowski, R. E.; Xu, M.; Llorca, J.; Arbiol, J.; Morante, J. R.; Chou, S.-L.; Cabot, A. A High Conductivity 1D π–d Conjugated Metal–Organic Framework with Efficient Polysulfide Trapping-Diffusion-Catalysis in Lithium–Sulfur Batteries. *Adv. Mater.* **2022**, *34*, 2108835.
25. Kapaev, R. R.; Shestakov, A. F.; Vasil'ev, S. G.; Stevenson, K. J. Conjugated Ladder-Type Polymer with Hexaazatriphenylene Units as a Cathode Material for Lithium, Sodium, and Potassium Batteries. *ACS Appl. Energy Mater.* **2021**, *4*, 10423–10427.

26. Baymuratova, G. R.; Khatmullina, K. G.; Yakuschenko, I. K.; Tulibaeva, G. Z.; Savinykh, T. A.; Troshin, P. A.; Shestakov, A. F.; Yarmolenko, O. V. Synthesis and Investigation of a New Organic Electrode Material Based on Condensation Product of Triquinoyl with 1,2,4,5-Tetraaminobenzene. *J. Electroanal. Chem.* **2021**, *889*, 115234.
27. Sutton, A. L.; Abrahams, B. F.; D'Alessandro, D. M.; Goerigk, L.; Hudson, T. A.; Robson, R.; Usov, P. M. Semi-Conducting Mixed-Valent $X_4TCNQ^{I-/II-}$ (X = H, F) Charge-Transfer Complexes with $C_6H_2(NH_2)_4$. *J. Mater. Chem. C* **2020**, *8*, 9422−9426.
28. Kapaev, R. R.; Olthof, S.; Zhidkov, I. S.; Kurmaev, E. Z.; Stevenson, K. J.; Meerholz, K.; Troshin, P. A. Nickel(II) and Copper(II) Coordination Polymers Derived from 1,2,4,5-Tetraaminobenzene for Lithium-Ion Batteries. *Chem. Mater.* **2019**, *31*, 5197–5205.
29. Wäckerlin, C.; Cahlík, A.; Goikoetxea, J.; Stetsovych, O.; Medvedeva, D.; Redondo, J.; Švec, M.; Delley, B.; Ondráček, M.; Pinar, A.; Blanco-Rey, M.; Kolorenč, J.; Arnau, A.; Jelínek, P. Role of the Magnetic Anisotropy in Atomic-Spin Sensing of 1D Molecular Chains. *ACS Nano* **2022**, *16*, 16402–16413.
30. Zhang, F.; Wang, P.; Zhao, R.; Wang, Y.; Wang, J.; Han, B.; Liu, Z. Tuning d-Band Structure of Cu^{II} in Coordinated Polymer via d–π Conjugation for Improving CO_2 Electroreduction Selectivity toward C_2 Products. *ChemSusChem* **2022**, *15*, e202201267.
31. Wu, H.-Y.; Yang, C.-Y.; Li, Q.; Kolhe, N. B.; Strakosas, X.; Stoeckel, M.-A.; Wu, Z.; Jin, W.; Savvakis, M.; Kroon, R.; Tu, D.; Woo, H. Y.; Berggren, M.; Jenekhe, S. A.; Fabiano, S. Influence of Molecular Weight on the Organic Electrochemical Transistor Performance of Ladder-Type Conjugated Polymers. *Adv. Mater.* **2022**, *34*, 2106235.
32. Santhini, V. M.; Wäckerlin, C.; Cahlík, A.; Ondráček, M.; Pascal, S.; Matěj, A.; Stetsovych, O.; Mutombo, P.; Lazar, P.; Siri, O.; Jelínek, P. 1D Coordination π–d Conjugated Polymers with Distinct Structures Defined by the Choice of the Transition Metal: Towards a New Class of Antiaromatic Macrocycles. *Angew. Chem. Int. Ed.* **2021**, *60*, 439–445.
33. Wan, Y.; Sun, Y.; Wu, X.; Yang, J. Ambipolar Half-Metallicity in One-Dimensional Metal−(1,2,4,5-Benzenetetramine) Coordination Polymers via Carrier Doping. *J. Phys. Chem. C* **2018**, *122*, 989–994.
34. Chen, Z.; Canard, G.; Jacquemin, D.; Bucher, C.; Giorgi, M.; Siri, O. Hetero-Bimetallic Effect as a Route to Access Multinuclear Complexes. *Inorg. Chem.* **2018**, *57*, 12536–12542.

35. Pascal, S.; Siri, O. Benzoquinonediimine Ligands: Synthesis, Coordination Chemistry and Properties. *Coord. Chem. Rev.* **2017**, *350*, 178–195.
36. Audi, H.; Chen, Z.; Charaf-Eddin, A.; D'Aléo, A.; Canard, G.; Jacquemin, D.; Siri, O. Extendable Nickel Complex Tapes that Reach NIR Absorptions. *Chem. Commun.* **2014**, *50*, 15140–15143.
37. Jeon, I.-R.; Park, J. G.; Xiao, D. J.; Harris, T. D. An Azophenine Radical-Bridged Fe_2 Single-Molecule Magnet with Record Magnetic Exchange Coupling. *J. Am. Chem. Soc.* **2013**, *135*, 16845–16848.
38. Frantz, S.; Rall, J.; Hartenbach, I.; Schleid, T.; Záliš, S.; Kaim, W. Metal-Induced Tautomerization of *p*- to *o*-Quinone Compounds: Experimental Evidence from Cu^I and Re^I Complexes of Azophenine and DFT Studies. *Chem. Eur. J.* **2004**, *10*, 149–154.
39. Masui, H.; Lever, A. B. P.; Dodsworth, E. S. Substituent Effects and Bonding Characteristics in (*o*-Benzoquinone diimine)bis(bipyridine)ruthenium (II) Complexes. *Inorg. Chem.* **1993**, *32*, 258–267.
40. Parvatkar, P. T.; Kandambeth, S.; Shaikh, A. C.; Nadinov, I.; Yin, J.; Kale, V. S.; Healing, G.; Emwas, A.-H.; Shekhah, O.; Alshareef, H. N.; Mohammed, O. F.; Eddaoudi, M. A Tailored COF for Visible-Light Photosynthesis of 2,3-Dihydrobenzofurans. *J. Am. Chem. Soc.* **2023**, *145*, 5074–5082.
41. Lin, Y.; Cui, H.; Liu, C.; Li, R.; Wang, S.; Qu, G.; Wei, Z.; Yang, Y.; Wang, Y.; Tang, Z.; Li, H.; Zhang, H.; Zhi, C.; Lv, H. A Covalent Organic Framework as a Long-Life and High-Rate Anode Suitable for Both Aqueous Acidic and Alkaline Batteries. *Angew. Chem. Int. Ed.* **2023**, *62*, e202218745.
42. Zhi, Q.; Liu, W.; Jiang, R.; Zhan, X.; Jin, Y.; Chen, X.; Yang, X.; Wang, K.; Cao, W.; Qi, D.; Jiang, J. Piperazine-Linked Metalphthalocyanine Frameworks for Highly Efficient Visible-Light-Driven H_2O_2 Photosynthesis. *J. Am. Chem. Soc.* **2022**, *144*, 21328–21336.
43. Zhang, J.; Kong, Y.-R.; Liu, Y.; Luo, H.-B.; Zou, Y.; Zang, S.-Q.; Ren, X.-M. Superprotonic Conduction of Acidified Benzimidazole-Linked Covalent Organic Framework. *ACS Materials Lett.* **2022**, *4*, 2597–2603.
44. Zheng, Q.; Li, X.; Zhang, Q.; Lee, D.; Mao, H.; Yang, C.; Bustillo, K. C.; Reimer, J. A.; Liu, Y.; Jiang, J.; Zheng, H. A Covalent Organic Framework Onion Structure. *Mater. Today* **2022**, *60*, 98−105.

45. Li, X.; Wang, H.; Chen, H.; Zheng, Q.; Zhang, Q.; Mao, H.; Liu, Y.; Cai, S.; Sun, B.; Dun, C.; Gordon, M. P.; Zheng, H.; Reimer, J. A.; Urban, J. J.; Ciston, J.; Tan, T.; Chan, E. M.; Zhang, J.; Liu, Y. Dynamic Covalent Synthesis of Crystalline Porous Graphitic Frameworks. *Chem* **2020**, *6*, 933−944.
46. Kim, S.; Choi, H. C. Light-Promoted Synthesis of Highly-Conjugated Crystalline Covalent Organic Framework. *Commun. Chem.* **2019**, *2*, 60.
47. Hisaki, I.; Affendy, N. Q. E.; Tohnai, N. Precise Elucidations of Stacking Manners of Hydrogen-Bonded Two-Dimensional Organic Frameworks Composed of X-Shaped π-Conjugated Systems. *CrystEngComm* **2017**, *19*, 4892−4898.
48. Yang, Q.; Liu, Y.; Xiang, L.; Zhang, J.; Yin, Y.; Xu, F.; Mai, Y. A General Synthetic Method towards Conjugated Microporous Polymers with Ordered Bicontinuous Mesostructures. *Chem. Commun.* **2023**, *59*, 4742−4745.
49. Xu, J.; Li, W.; Liu, W.; Jing, J.; Zhang, K.; Liu, L.; Yang, J.; Zhu, E.; Li, J.; Zhu, Y. Efficient Photocatalytic Hydrogen and Oxygen Evolution by Side-Group Engineered Benzodiimidazole Oligomers with Strong Built-in Electric Fields and Short-Range Crystallinity. *Angew. Chem. Int. Ed.* **2022**, *61*, e202212243.
50. Shin, S.-H.; Noh, H.-J.; Kim, Y.-H.; Im, Y.-K.; Mahmood, J.; Baek, J.-B. Forming Layered Conjugated Porous BBL Structures. *Polym. Chem.* **2019**, *10*, 4185−4193.
51. Seo, W.; Carpenter, K. L.; Gaugler, J. A.; Shao, W.; Werling, K. A.; Fournier, P. M.; Lambrecht, D. S.; Star, A. Polybenzobisimidazole-Derived Two-Dimensional Supramolecular Polymer. *J. Polym. Sci. A Polym. Chem.* **2017**, *55*, 1095−1101.
52. Gajiwala, H. M.; Zand, R. Synthesis and Characterization of Thermally Stable Polymers Containing Phenazine. *Polymer* **2000**, *41*, 2009−2015.
53. Szita, J.; Marvel, C. S. Partial Ladder Polymers with Anthraquinone Units. Reaction of 1,2,5,6-Tetraaminoanthraquinone with *p*-Benzoquinone Derivatives. *J. Polym. Sci. A1* **1972**, *9*, 415−421.
54. Audi, H.; Viero, Y.; Alwhaibi, N.; Chen, Z.; Iazykov, M.; Heynderickx, A.; Xiao, F.; Guérin, D.; Krzeminski, C.; Grace, I. M.; Lambert, C. J.; Siri, O.; Vuillaume, D.; Lenfant, S.; Klein, H. Electrical Molecular Switch Addressed by Chemical Stimuli. *Nanoscale* **2020**, *12*, 10127−10139.

55. Guo, Z.; Song, N. R.; Moon, J. H.; Kim, M.; Jun, E. J.; Choi, J.; Lee, J. Y.; Bielawski, C. W.; Sessler, J. L.; Yoon, J. A Benzobisimidazolium-Based Fluorescent and Colorimetric Chemosensor for CO_2. *J. Am. Chem. Soc.* **2012**, *134*, 17846−17849.
56. Chen, Z.; Bert, M.; Pascal, S.; Canard, G.; Siri, O. Versatile Transamination in Quinonediimine Chemistry: Towards a Novel Class of Water Soluble UV/Violet Chromophores. *Tetrahedron Lett.* **2019**, *60*, 151024.
57. Edzang, J. A.; Chen, Z.; Audi, H.; Canard, G.; Siri, O. Transamination at the Crossroad of the One-Pot Synthesis of N-Substituted Quinonediimines and C-Substituted Benzobisimidazoles. *Org. Lett.* **2016**, *18*, 5340−5343.
58. Bindewald, E.; Lorenz, R.; Hübner, O.; Brox, D.; Herten, D.-P.; Kaifer, E.; Himmel, H.-J. Tetraguanidino-Functionalized Phenazine and Fluorene Dyes: Synthesis, Optical Properties and Metal Coordination. *Dalton Trans.* **2015**, *44*, 3467−3485.
59. Le, H. T. M.; El-Hamdi, N. S.; Miljanić, O. Š. Benzobisimidazole Cruciform Fluorophores. *J. Org. Chem.* **2015**, *80*, 5210−5217.
60. Golubovskaya, V.; Curtin, L.; Groman, A.; Sexton, S.; Cance, W. G. In Vivo Toxicity, Metabolism and Pharmacokinetic Properties of FAK Inhibitor 14 or Y15 (1,2,4,5-Benzenetetramine Tetrahydrochloride). *Arch. Toxicol.* **2015**, *89*, 1095−1101.
61. Néron, S.; Morency, M.; Malveau, C.; Maris, T.; Iftimie, R.; Wuest, J. D. Diphenoquinhydrones and Related Hydrogen-Bonded Charge-Transfer Complexes. *J. Org. Chem.* **2022**, *87*, 15796−15805.
62. Ritter, J. C.; Hargis, A. Process for the Synthesis of 1,3-Diamino-4,6-dinitrobenzene. US 8 7071 812 B1, 2011.
63. Boyer, J. H.; Buriks, R. S.; Toggweiler, U. The Preparation of 6,7-Disubstituted Quinoxalines. *J. Am. Chem. Soc.* **1960**, *82*, 2213−2215.
64. Boyer, J. H.; Buriks, R. S. 2,4,5-Triaminonitrobenzene. *Org. Synth.* **1960**, *40*, 96–97.
65. Ruggli, P.; Fischer, R. Über die reduktive Spaltung von m-Phenylendiamin-Disazofarbstoffen zu Derivaten des Tetra-aminobenzols. *Helv. Chim. Acta* **1945**, *28*, 1270−1280.
66. Holleman, A. F. Sur le remplacement de substituants dans le noyau benzénique. *Rec. Trav. Chim. Pays-Bas* **1920**, *39*, 435−480.
67. Dann, A. T. CCCXXV. The Dinitration of *m*-Dichlorobenzene. *J. Chem. Soc.* **1929**, 2460–2462.

68. Mataka, S.; Shimojyo, Y.; Hashimoto, I.; Tashiro, M. Benzodiimidazoles by Reaction of Benzenetetramines and Benzenehexamines with Dimethylformamide and Its Dimethyl Acetal. *Liebigs Ann.* **1995**, 1823–1825.
69. Mataka, S.; Ikezaki, Y.; Takahashi, K.; Tori-i, A.; Tashiro, M. Nucleophilic Substitution Reaction of 4-Bromobenzo[1,2-*c*;3,4-*c′*]bis[1,2,5]thiadiazole and Reduction of Hydroxy and Methoxy Derivative to the Corresponding 1,2,3,4-Benzenetetramine. *Heterocycles* **1992**, *33*, 791–800.
70. Mataka, S.; Eguchi, H.; Takahashi, K.; Hatta, T.; Tashiro, M. Sulfur Nitrides in Organic Chemistry. 18. Preparation and Reduction of Benzo[1,2-*c*:3,4-*c′*:5,6-*c″*]tris- and Benzo[1,2-*c*:3,4-*c′*]bis[1,2,5]thiadiazole. A Convenient Route to Benzenehexamine and 1,2,3,4-Benzenetetramine. *Bull. Chem. Soc. Jpn.* **1989**, *62*, 3127–3131
71. Nietzki, R. Ueber einige Hexaderivate des Benzols. *Ber. dtsch. chem. Ges.* **1887**, *20*, 2114–2118.
72. Sosoe, J. O. E.; Maris, T.; Iftimie, R.; Wuest, J. D. Making 4,6-Diaminoresorcinol and Derivatives by the Hydrolysis of Benzene-1,2,4,5-tetramine. Manuscript in preparation.
73. Czapik, A.; Gdaniec, M. A New Polymorph of Benzene-1,2-diamine: Isomorphism with 2-Aminophenol and Two-Dimensional Isostructurality of Polymorphs. *Acta Crystallogr.* **2010**, *C66*, o198–o201.
74. Czapik, A.; Konowalska, H.; Gdaniec, M. *p*-Phenylenediamine and Its Dihydrate: Two-Dimensional Isomorphism and Mechanism of the Dehydration Process, and N–H···N and N–H···π Interactions. *Acta Crystallogr.* **2010**, *C66*, o128–o132.
75. Betz, R.; Klüfers, P.; Mayer, P. *m*-Phenylenediamine. *Acta Crystallogr.* **2008**, *E64*, o2501.
76. Laliberté, D.; Maris, T.; Demers, E.; Helzy, F.; Arseneault, M.; Wuest, J. D. Molecular Tectonics. Hydrogen-Bonded Networks Built from Tetra- and Hexaanilines. *Cryst. Growth Des.* **2005**, *5*, 1451−1456.
77. Nakai, H.; Saito, T.; Yamakawa, M. Structure of *N*,*N*-Dimethyl-1,4-phenylenediamine. *Acta Crystallogr.* **1988**, *C44*, 1057–1059.
78. Stålhandske, C. 1,2-Diaminobenzene, $C_6H_4(NH_2)_2$. *Cryst. Struct. Commun.* **1981**, *10*, 1081–1086.
79. Povet'eva, Z. P.; Zvonkova, Z. V. Crystal Structure of *p*-Phenylenediamine. *Kristallografiya* **1975**, *20*, 69–73.

80. Glatzhofer, D. T.; Khan, M. A. *N*,*N*',*N*''-Triphenyl-l,3,5-triaminobenzene and Its σ Complex on Protonation: A Stable *N*,*N*',*N*''-Triphenyl-2,4,6-triaminocyclohexadienylium Cation. *Acta Crystallogr.* **1993**, *C49*, 2128−2133.
81. Knoche, W.; Schoeller, W. W.; Schomäcker, R.; Vogel, S. Protonation of 1,3,5-Triaminobenzenes in Aqueous Solutions. Thermodynamics and Kinetics of the Formation of Stable σ-Complexes. *J. Am. Chem. Soc.* **1988**, *110*, 7484−7489.
82. Kapoor, I. P. S.; Srivastava, P.; Singh, G. Preparation, Crystal Structure and Thermal Decomposition of Phenylenediammonium Dichloride Salts. *Indian J. Chem.* **2007**, *46A*, 1277−1282.
83. Anderson, K. M.; Goeta, A. E.; Hancock, K. S. B.; Steed, J. W. Unusual Variations in the Incidence of $Z' > 1$ in Oxo-Anion Structures. *Chem. Commun.* **2006**, 2138–2140.
84. Domenicano, A.; Foresti Serantoni, E.; Riva di Sanseverino, L. Structural Studies of Benzene Derivatives. I. Refinement of the Crystal Structure of *p*-Phenylenediamine Dihydrochloride. *Acta Crystallogr.* **1977**, *B33*, 1664–1668.
85. Stålhandske, C. A Neutron Diffraction Study of 1,2-Diaminobenzene Monohydrochloride. *Acta Crystallogr.* **1976**, *B32*, 2806–2809.
86. Stålhandske, C. The Crystal Structure of *o*-Phenylenediamine Dihydrochloride. *Acta Crystallogr.* **1974**, *B30*, 1586–1589.
87. Stålhandske, C. The Crystal Structure of *o*-Phenylenediamine Hydrochloride. *Acta Chem. Scand.* **1972**, *26*, 2962–2963.
88. Chandrasekaran, R. Crystal Structure of *p*-Phenylenediamine Dihydrochloride. *Acta Crystallogr.* **1969**, *B25*, 369–374.
89. For additional details, see the Supporting Information.
90. Dähne, S.; Leupold, D. Coupling Principles in Organic Dyes. *Angew. Chem. Int. Ed.* **1966**, *5*, 984–993.
91. Ohno, K.; Fujihara, T.; Nagasawa, A. An Orthorhombic Polymorph of N^1,N^4-Diphenyl-3,6-bis(phenylimino)cyclohexa-1,4-diene-1,4-diamine. *Acta Crystallogr.* **2014**, *E70*, o495–o496.
92. Ohno, K.; Maruyama, H.; Fujihara, T.; Nagasawa, A. N^1,N^4-Diphenyl-3,6-bis(phenylimino)cyclohexa-1,4-diene-1,4-diamine. *Acta Crystallogr.* **2014**, *E70*, o303–o304.

93. Blake, A. J.; Hubberstey, P.; Quinlan, D. J. Bandrowski's Base. *Acta Crystallogr.* **1996**, *C52*, 1774–1776.
94. Yang, Q.-Z.; Siri, O.; Braunstein, P. Tunable N-Substitution in Zwitterionic Benzoquinonemonoimine Derivatives: Metal Coordination, Tandemlike Synthesis of Zwitterionic Metal Complexes, and Supramolecular Structures. *Chem. Eur. J.* **2005**, *11*, 7237–7246.
95. Semmingsen, D. The Crystal and Molecular Structure of 2,5-Dihydroxy-1,4-benzoquinone at -162 °C. *Acta. Chem. Scand.* **1977**, *B31*, 11–14.
96. Mardirossian, N.; Head-Gordon, M. Survival of the Most Transferable at the Top of Jacob's Ladder: Defining and Testing the ωB97M(2) Double Hybrid Density Functional. *J. Chem. Phys*. **2018**, 148, 241736.
97. Hellweg, A.; Rappoport, D. Development of New Auxiliary Basis Functions of the Karlsruhe Segmented Contracted Basis Sets Including Diffuse Basis Functions (def2-SVPD, def2-TZVPPD, and def2-QVPPD) for RI-MP2 and RI-CC Calculations. *Phys. Chem. Chem. Phys*. **2015**, 17, 1010–1017.
98. Rappoport, D.; Furche, F. Property-Optimized Gaussian Basis Sets for Molecular Response Calculations. *J. Chem. Phys*. **2010**, 133, 134105.
99. Weigend, F.; Ahlrichs, R. Balanced Basis Sets of Split Valence, Triple Zeta Valence and Quadruple Zeta Valence Quality for H to Rn: Design and Assessment of Accuracy. *Phys. Chem. Chem. Phys*. **2005**, 7, 3297–3305.
100. Lin, Y.-S.: Li, G.-D.; Mao, S.-P.; Chai, J.-D. Long-Range Corrected Hybrid Density Functionals with Improved Dispersion Correction. *J. Chem. Theory Comput*. **2013**, 9, 263–272.
101. Grimme, S.; Antony, J.; Ehrlich, S.; Krieg, H. A Consistent and Accurate *ab initio* Parametrization of Density Functional Dispersion Correction (DFT-D) for the 94 Elements H-Pu. *J. Chem. Phys*. **2010**, 132, 154104.
102. Chai, J.-D.; Head-Gordon, M. Systematic Optimization of Long-Range Corrected Hybrid Density Functionals. *J. Chem. Phys*. **2008**, 128, 084106.
103. Chai, J.-D.; Head-Gordon, M. Long-Range Corrected Hybrid Density Functionals with Damped Atom-Atom Dispersion Corrections. *Phys. Chem. Chem. Phys*. **2008**, 10, 6615–6620.

104. Cossi, M.; Rega, N.; Scalmani, G.; Barone, V. Energies, Structures, and Electronic Properties of Molecules in Solution with the C-PCM Solvation Model. *J. Comput. Chem*. **2003**, 24, 669–681.
105. Simpson, G. J.; Hogan, S. W. L.; Caffio, M.; Adams, C. J.; Früchtl, H.; van Mourik, T.; Schaub, R. New Class of Metal Bound Molecular Switches Involving H-Tautomerism. *Nano Lett.* **2014**, *14*, 634–639.
106. Rumpel, H.; Limbach, H.-H. NMR Study of Kinetic HH/HD/DD Isotope, Solvent, and Solid-State Effects on the Double Proton Transfer in Azophenine. *J. Am. Chem. Soc.* **1989**, *111*, 5429–5441.
107. Rumpel, H.; Limbach, H.-H.; Zachmann, G. Liquid- and Solid-State Infrared and Near-Infrared Study of the Proton Dynamics in Azophenine. *J. Phys. Chem.* **1989**, *93*, 1812–1818.
108. Holloway, M. K.; Reynolds, C. H.; Merz, K. M., Jr. An ab Initio Investigation of the Double Proton Shift in Azophenine. *J. Am. Chem. Soc.* **1989**, *111*, 3466–3468.
109. Dewar, M. J. S.; Merz, K. M., Jr. On the Double Proton Shift in Azophenine. *J. Mol. Struct.* **1985**, *124*, 183–185.
110. Limbach, H.-H.; Hennig, J.; Gerritzen, D.; Rumpel, H. Primary Kinetic HH/HD/DH/DD Isotope Effects and Proton Tunnelling in Double Proton-Transfer Reactions. *Faraday Discuss. Chem. Soc.* **1982**, *74*, 229–243.
111. Tahermansouri, H.; Moradi, S.; Sayyadi, R. Heteroatom Effect on Intramolecular Double Proton Transfer of 3,6-Diiminocyclohexa-1,4-diene-1,4-diamine: A Theoretical Study. *Indian J. Chem.* **2011**, *50A*, 180–184.
112. Ujike, K.; Kudoh, S.; Nakata, M. UV-Induced Single and Double Hydrogen-Atom Migrations in 3,6-Diimino-1,4-cyclohexadiene-1,4-diamine in a Low-Temperature Argon Matrix. *Chem. Phys. Lett.* **2005**, *409*, 52–56.
113. Topaler, M. S.; Mamaev, V. M.; Gluz, Y. B.; Minkin, V. I.; Simkin, B. Y. Tunnelling Effects in the Double Proton Transfer Reaction of 2,5-Dihydroxy-1,4-benzoquinone. *J. Mol. Struct.* **1991**, *236*, 393–401.
114. Bren, V. A.; Chernoivanov, V. A.; Konstantinovskii, L. E.; Nivorozhkin, L. E.; Zhdanov, Y. A.; Minkin, V. I. Diotropic Proton Migrations in a Series of 2,5-Dihydroxy-1,4-benzoquinones. *Dokl. Akad. Nauk SSSR* **1980**, *251*, 1129−1132.

115. Graf, F. Dynamics of Proton Tautomerism in 2,5-Dihydroxy-*p*-benzoquinone: A ^{13}C NMR and CNDO Study. *Chem. Phys. Lett.* **1979**, *62*, 291−294.
116. Wynne-Jones, W. F. K.; Eyring, H. The Absolute Rate of Reactions in Condensed Phases. *J. Chem. Phys.* **1935**, *3*, 492–502.
117. Laidler, K. J. *Chemical Kinetics*, 3rd ed.; Pearson, New York, 1987; Chapter 4.7.
118. Ohno, K.; Fujihara, T.; Nagasawa, A. Formation of Boron, Nickel(II) and Iridium(III) Complexes with an Azophenine Derivative: Isomerization, Delocalization and Extension of the π-Conjugated System on Coordination. *Polyhedron* **2014**, *81*, 715–722.
119. Siri, O.; Braunstein, P.; Rohmer, M.-M.; Bénard, M.; Welter, R. Novel "Potentially Antiaromatic", Acidichromic Quinonediimines with Tunable Delocalization of Their 6 π-Electron Subunits. *J. Am. Chem. Soc.* **2003**, *125*, 13793–13803.
120. Elbl, K.; Krieger, C.; Staab, H. A. 1,2,4,5-Tetrakis(dimethylamino)benzene, a New Electron Donor with Unusual Properties. *Angew. Chem. Int. Ed.* **1986**, *25*, 1023–1024.
121. Epifanovsky, E. et al. Software for the Frontiers of Quantum Chemistry: An Overview of Developments in the Q-Chem 5 Package. *J. Chem. Phys*. **2021**, 155, 084801.
122. Bursch, M.; Mewes, J.-M.; Hansen, A.; Grimme S. Best-Practice DFT Protocols for Basic Molecular Computational Chemistry. *Angew. Chem. Int. Ed*. **2022**, 61, e202205735.
123. Halgren, T. A. Merck Molecular Force Field. I. Basis, Form, Scope, Parameterization, and Performance of MMFF94. *J. Comp. Chem*. **1996**, 17, 490–519.
124. Pracht, P.; Grimme, S. Calculation of Absolute Molecular Entropies and Heat Capacities Made Simple. *Chem. Sci*. **2021**, 12, 6551–6568.
125. Seeger, R.; Pople, J. A. Self-Consistent Molecular Orbital Methods. XVIII. Constraints and Stability in Hartree-Fock Theory. *J. Chem. Phys.* **1977**, 66, 3045–3050.
126. Sosoe, J. O. E.; Maris, T.; Wuest, J. D. Strongly Hydrogen-Bonded Networks Formed by Sulfate and Bisulfate Salts of Benzenetetramines. *Cryst. Growth Des.* **2023**, *23*, 8865−8874.

2.2. Conclusions

Nous sommes parvenus à caractériser BTA (**1**), BTA (**1**) · 2HCl, BTA (**1**) · 4HCl, BTA-H_2 (**2**) et BTA-H_2 (**2**) · 2HCl par SCXRD et, lorsque possible, CPMAS ^{13}C et ^{15}N. Malgré sa grande sensibilité à l'air, la base libre **1** a pu être isolée sous forme de monocristaux d'une solution du sel BTA (**1**) · 4HCl dissous dans le NaOH 1 M. Malgré toute nos précautions (*freeze-pump-thaw* et filtration sous argon), nous n'avons malheureusement pas été en mesure de la préparer en plus grande quantité d'un solvant dégazé par, ni par la réduction catalytique de son précurseur **5**, ou encore par la réduction au $NaBH_4$ de sa forme oxydée **2**. À chaque fois des mélanges de solides sensibles à l'air ont été collectés. Il est possible que la pauvre solubilité et/ou la faible acidité des sels mono, di et tri-protonés du motif **1** dans les solutions alcalines concentrés utilisés soit limitante. Nous n'avons pas encore essayé de préparer la base libre **1** de $NaOH_{(aq)}$ concentré, chaud ou bouillant et dépourvu d'oxygène pour vérifier cette hypothèse.

Nous avons également étudié la tautomérie du produit d'oxydation **2** (Schéma 2.2**)**. Seul l'isomère *E*,*E*-1,4-quinonediimine est isolé sous forme solide ou en solution. Contrairement à d'autres quinones analogues, les électrons π du composé **2** sont faiblement délocalisés à travers ses unités cyanines. De plus, le composé décompose avant d'isomériser lors d'expériences RMN à température variable. Appuyés par nos calculs théoriques, ces résultats nous laissent penser que le moment dipolaire minimisé et les ponts hydrogène intramoléculaires de l'isomère *E*,*E* contribuent à sa stabilité. Sa barrière énergétique d'isomérisation se retrouvait conséquemment plus haute que celles d'autres processus délétères à l'intégrité de la structure. La délocalisation des électrons π à l'intérieur des unités cyanines du composé diprotoné BTA-H_2 (**2**) · 2HCl est cependant plus importante que dans sa base libre en solution et l'état solide.

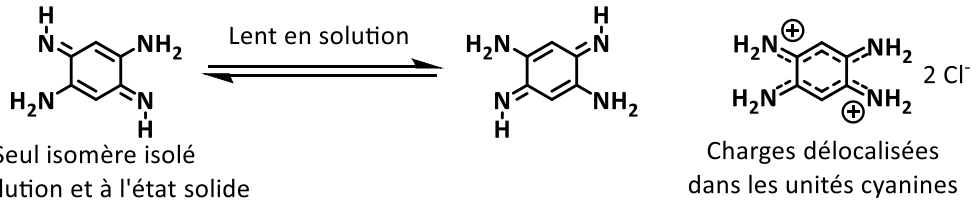

Schéma 2.2 Résumé des observations concernant le composé BTA-H_2 (**2**)

Notre étude aura également permis de rendre la synthèse de BTA (**1**) · 4HCl plus expéditive que les méthodes rapportées à ce jour. La réduction du précurseur **5** est notamment effectuée en 1 h à 20 °C et à l'air ambiant avec seulement 7 équivalents de $SnCl_2$, plutôt qu'en un jour à reflux sous atmosphère inerte avec 9 équivalents de $SnCl_2$. Notre protocole revisité permet également d'isoler l'isomère 1,2,3,4 de BTA (**7**). Bien qu'il fût décrit pour la première fois par Nietzki en 1889, seuls des résultats d'analyse élémentaire avaient depuis été publiés pour cet isomère (Schéma 2.3).[20,68-70] Ce composé est particulièrement utile pour préparer des pyrazinoquinoxalines substituées étudiées comme ligands de coordination et composés rédox. Par ailleurs, nous n'avons pas encore été en mesure d'isoler la base libre ou des sels de la forme oxydée de l'isomère 1,2,3,4-BTA, bien plus soluble dans l'eau et les acides que l'isomère 1,2,4,5. Il est toutefois possible d'oxyder l'isomère **7** dissous en solution et de le caractériser par RMN ^{1}H, résultats qui seront rapportés dans le cadre d'une étude plus complète de ce composé élusif et versatile. Finalement, une étude similaire à celle de la publication de ce chapitre pourrait être menée sur les autres composés quinoïdes isolés par Nietzki à partir du sel de nitrate de BTA-H_2 (**2**). En effet, l'ensemble de ces motifs peuvent être préparés par des procédés simples et présentent des caractéristiques toutes aussi pertinentes aux applications optoélectroniques.

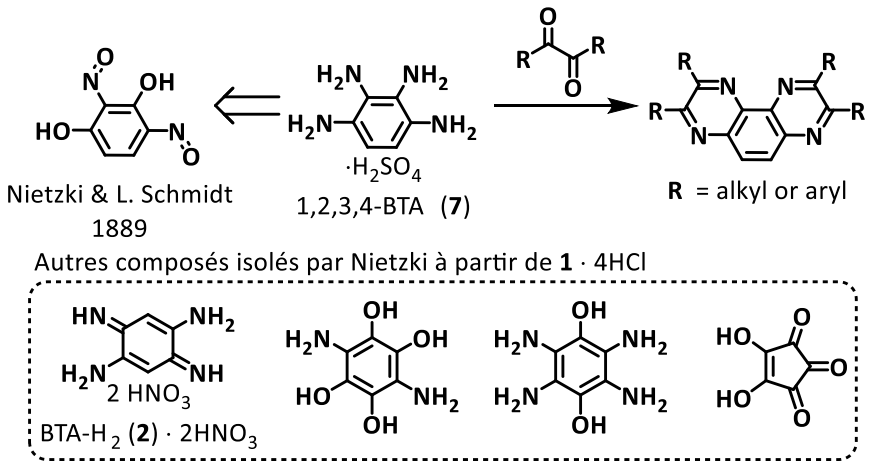

Schéma 2.3 Synthèse de pyrazinoquinoxalines substituées dérivées de 1,2,3,4-BTA (**7**) et autres composés quinoïdes isolés par Nietzki et pertinents à l'électronique organique.

Chapitre 3. Robustes réseaux de ponts hydrogène formés par des sels de sulfate et bisulfate de benzènetétramines

3.1. Introduction

Les sels dérivés de motifs quinoïdes sont étudiés comme substituts aux matériaux cathodiques de batteries. Contrairement à leurs substituants hydroxyles, les amines forment plus facilement des sels avec les acides qu'avec les alcalis. Ce type de sels ne semble pas avoir été autant étudié que ceux dérivés d'hydroxyde de métaux alcalins ou alcalino-terreux. Dans le domaine de l'ingénierie cristalline cependant, plusieurs HOFs construits par des ponts hydrogène liants des fonctions ammonium à des sulfates ou à des acides sulfoniques ont été construits, mais peu sont dérivés du motif BTA. En fait, peu de structures cristallines de sulfates ou de bisulfates de phénylammoniums ont été publiées jusqu'à maintenant. Nous avons donc entrepris une étude cristallographique de plusieurs sels de sulfate et de bisulfate de l'isomère 1,2,4,5-BTA (**1**), sa forme oxydée (**2**) et son homologue 1,2,3,4-BTA (**3**) pour étudier les structures de ces solides (**Schéma 3.1**). En l'occurrence, Nietzki et son groupe isolèrent les sels 1,2,4,5-BTA (**1**) · $3H_2SO_4$, 1,2,4,5-BTA (**1**) · H_2SO_4 et 1,2,3,4-BTA (**3**) · H_2SO_4 pertinents aux applications rédox et à l'ingénierie cristalline, mais dont les structures cristallines n'avaient pas été résolues.

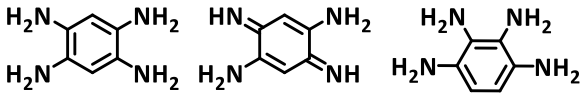

Schéma 3.1 Motifs dont les sels de sulfates et de bisulfates sont à l'étude.

Strongly Hydrogen-Bonded Networks Formed by Sulfate and Bisulfate Salts of Benzenetetramines

Johann O. E. Sosoe, Thierry Maris, and James D. Wuest

Published in *Cryst. Growth Des.*

Cryst. Growth Des. **2023**, *23* (12), 8865–8874.

JOES executed the experiments.

TM carried out all crystallographic studies.

JDW conceived the project and identified experiments to perform.

Abstract

Benzenetetramines, like other aromatic compounds with multiple NH_2 groups, are easily oxidized and are attractive candidates for use as components of redox-active organic materials. However, many aspects of the chemistry of benzenetetramines and related compounds remain poorly understood, such as the nature of their salts and their preferred patterns of association, which determine how they can be used to construct predictably ordered redox-active solids. To provide relevant new information, we have studied a series of sulfate and bisulfate salts of the 1,2,4,5- and 1,2,3,4-isomers, which have been found to crystallize as strongly hydrogen-bonded networks. The results of this work promise to facilitate the use of benzenetetramines and other complex arylamines as components of redox-active organic solids.

Introduction

New redox-active organic materials are sought for many uses, such as storing energy in batteries that are cheap, effective, and made primarily from abundant elements.[1–11] Potentially suitable materials can be derived from familiar redox pairs such as hydroquinones and quinones, which typically react rapidly and reversibly. However, attractive alternatives include aromatic compounds with multiple NH_2 groups and the quinoneimines produced by their oxidation. In recent work,[12,13] we have begun to explore the potential of these redox pairs by studying the particular cases of benzene-1,2,4,5-tetramine (**1**; 1,2,4,5-BTA), its product of oxidation **2**, their salts, and related series of compounds based on benzene-1,2,3,4-tetramine (**3**; 1,2,3,4-BTA). At present, redox-active materials derived from hydroquinones and quinones are considered to be particularly advantageous because they can often be made from renewably produced phenolic precursors. However, emerging green methods of amination promise to make analogous arylamines and their oxidized forms equally available.[14–16] Moreover, quinonoid analogues with various combinations of C–OH, C=O, C–NH_2, and C=NH bonds are commonly encountered as natural products,[17] as exemplified by mitomycin C, a diaminoquinone with antitumor and antibiotic properties.[18]

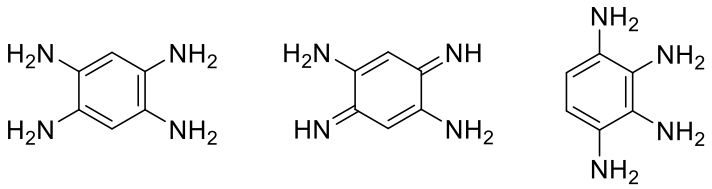

1 (1,2,4,5-BTA) **2** **3** (1,2,3,4-BTA)

Selecting 1,2,4,5-BTA (**1**) for detailed study is warranted because the compound is at the center of an impressive range of projects in which it is used as a precursor of redox-active materials,[19–25] a ligand in coordination chemistry,[26–36] a component of metal-organic frameworks (MOFs) and covalent organic frameworks (COFs),[37–44] a monomer for producing polymers,[45–50] a component of switches and sensors,[51,52] a precursor for synthesizing diverse heterocyclic compounds,[53–56] and an enzyme inhibitor for use in treating cancer.[57] However, fuller exploitation

of 1,2,4,5-BTA (**1**) and analogues such as 1,2,3,4-BTA (**3**) will require a better understanding of their fundamental properties, such as the nature of their salts and their preferred patterns of association in the solid state, which will determine how they are best used as the components of redox-active materials. To provide useful new information, we have studied a series of sulfate and bisulfate salts of 1,2,4,5-BTA (**1**) and 1,2,3,4-BTA (**3**), and we have found that they crystallize as strongly hydrogen-bonded networks. Few structures of arylammonium sulfates/bisulfates and related salts have been reported previously,[58–62] so our work provides a fuller guide to the potential of these compounds to serve as modules for constructing predictably ordered solids.

Results and Discussion

Synthesis of Sulfate and Bisulfate Salts of 1,2,4,5-BTA (1) and 1,2,3,4-BTA (3).

Tetrahydrochloride salt 1,2,4,5-BTA (**1**) • 4HCl was prepared by modifying a method initially devised by Nietzki and Schedler.[12,63] As first observed by Nietzki and Hagenbach,[64] solutions made by adding the tetrahydrochloride salt to H_2SO_4 or its aqueous solutions deposited crystals of sulfate and bisulfate salts of 1,2,4,5-BTA (**1**) on standing. Sulfate salt 1,2,3,4-BTA (**3**) • H_2SO_4 was prepared by a similar method.[12] Formation under these conditions reveals that the new salts are poorly soluble and presumably give rise to robust structures held together by extensive networks of ionic hydrogen bonds.[65]

Structures of Sulfate and Bisulfate Salts of 1,2,4,5-BTA (1).

Crystals were formed at 20 °C from solutions made by adding the tetrahydrochloride salt of 1,2,4,5-BTA (**1**) to concentrated H_2SO_4, and they proved to correspond to a mixed sulfate/bisulfate salt with the composition H_4(1,2,4,5-BTA)$^{4+}$ (**1** • $4H^+$) SO_4^{2-} $2HSO_4^-$. Selected crystallographic data are summarized in Table III - 1, and representations of the structure are provided in Figure 3.1. The locations of atoms of hydrogen in all structures in Table III - 1 were determined by methods described in detail in the Supporting Information, and the stated lengths of H−O and H−N bonds are not normalized with respect to distances determined by neutron

diffraction. *N*-Tetraprotonation of 1,2,4,5-BTA (**1**) is observed, as in the case of the tetrachloride salt.[12] *N*-Protonation of arenes with multiple NH_2 substituents appears to be generally favored, although *C*-protonated isomers have been characterized in certain cases.[66,67] In each tetracation $H_4(1,2,4,5\text{-BTA})^{4+}$ (**1** • $4H^+$), the non-hydrogen atoms are essentially coplanar, and the average lengths of the C–C and C–N bonds ($d_{C\text{-}C}$ = 1.390 Å and $d_{C–N}$ = 1.452 Å) are closely similar to those found in the analogous tetrachloride salt (1.387 and 1.458 Å, respectively).

Tableau III - 1 Crystallographic Data for Sulfate and Bisulfate Salts of 1,2,4,5-BTA (**1**) and 1,2,3,4-BTA (**3**)

compound	**$H_4(1,2,4,5\text{-BTA})^{4+}$ SO_4^{2-} $2HSO_4^-$**	**$H_3(1,2,4,5\text{-BTA})^{3+}$ SO_4^{2-} HSO_4^-**	**$H_3(1,2,4,5\text{-BTA})^{3+}$ SO_4^{2-} HSO_4^-**	**$H_4(1,2,4,5\text{-BTA})^{4+}$ $4HSO_4^-$**	**$H_3(1,2,4,5\text{-BTA})^{3+}$ $1.5SO_4^{2-}$ • $2H_2O$**	**$H_2(1,2,3,4\text{-BTA})^{2+}$ SO_4^{2-}**
CCDC[a] number	2285045	2285043	2285044	2285046	2285047	2285042
description	colorless blocks	colorless plates	colorless needles	colorless plates	colorless plates	colorless plates
crystal syst	monoclinic	triclinic	monoclinic	monoclinic	monoclinic	monoclinic
space group	*P*2/*c*	$P\bar{1}$	*Cc*	*C*2/*m*	$P2_1/n$	$P2_1/c$
a (Å)	9.3639(3)	7.4480(5)	9.2289(6)	7.4291(3)	7.6040(4)	6.4293(4)
b (Å)	8.0701(2)	9.8087(7)	17.9408(12)	16.7187(6)	33.9391(19)	7.6672(5)
c (Å)	10.3114(3)	17.1698(11)	7.3308(5)	7.1695(3)	9.6678(5)	18.4558(12)
α (deg)	90	83.536(4)	90	90	90	90
β (deg)	90.497(1)	81.860(4)	104.825(3)	100.443(2)	90.578(3)	93.007(3)
γ (deg)	90	81.853(4)	90	90	90	90
V (Å^3)	779.18(4)	1233.68(14)	1173.38(14)	875.74(6)	2494.9(2)	908.52(10)
Z	2	4	4	2	4	4
Z′	0.5	2	1	0.25	1	1
ρ_{calc} (g · cm^{-3})	1.843	1.815	1.893	2.012	1.711	1.727
T (K)	150	150	150	100	150	150
R_1, $I > 2\sigma(I)$	0.0386	0.0599	0.0291	0.0506	0.0971	0.0451
wR_2, $I > 2\sigma(I)$	0.0971	0.1580	0.0742	0.1242	0.2158	0.1135
GoF	1.126	1.073	0.999	1.055	1.080	1.067

[a]Cambridge Crystallographic Data Centre

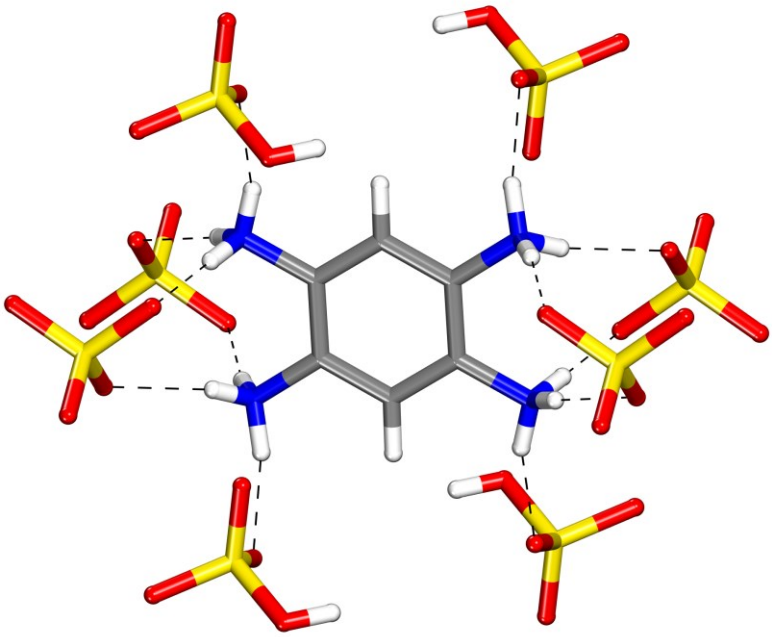

a

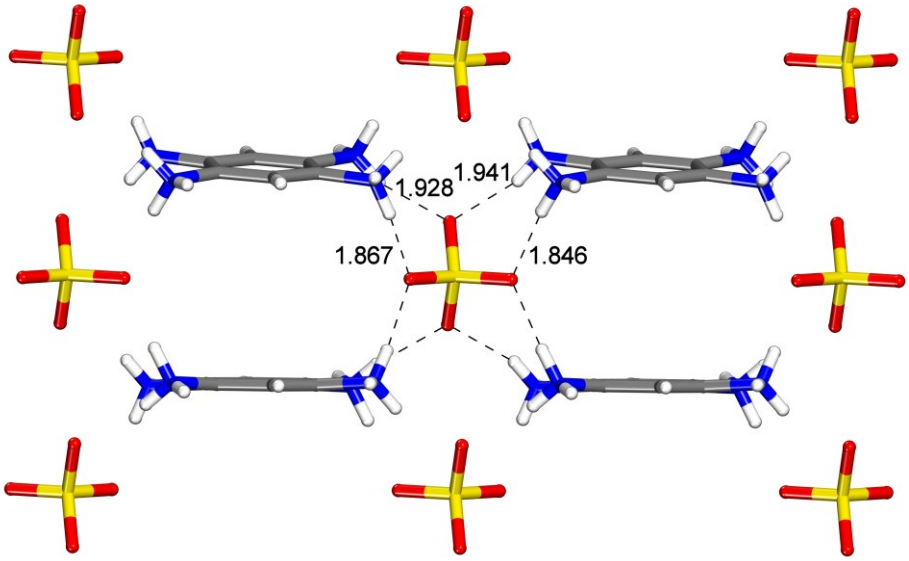

b

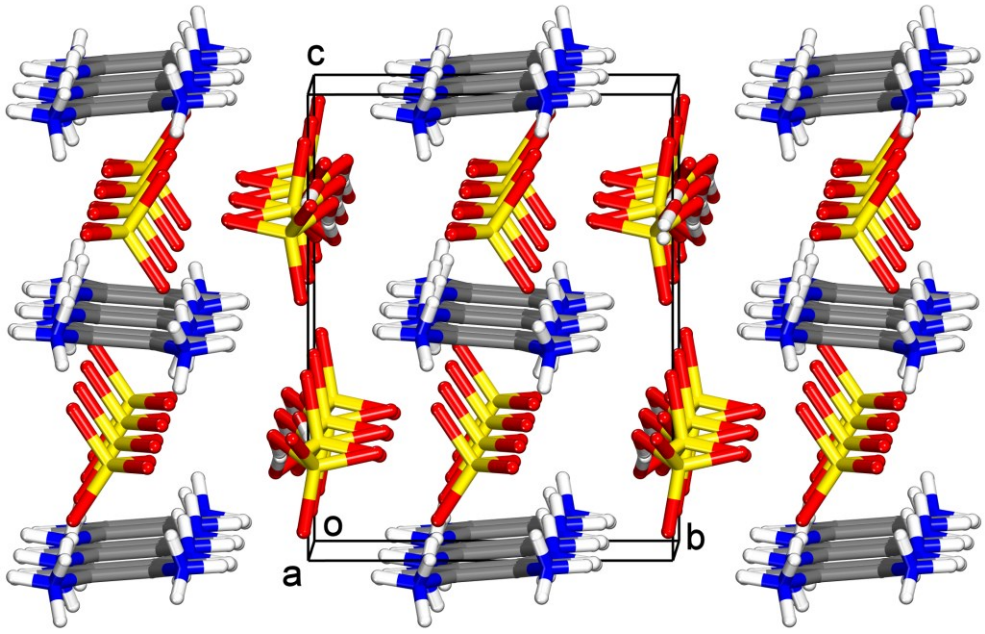

Figure 3.1 Representations of the structure of *P*2*/c* crystals of salt H_4(1,2,4,5-BTA)$^{4+}$ (**1** • $4H^+$) SO_4^{2-} $2HSO_4^-$ grown from H_2SO_4. (a) View along the *c*-axis showing how each tetracation forms a total of 12 primary ionic N–$H^+\cdots O^-$ hydrogen bonds with four surrounding sulfate ions and four bisulfate ions. (b) View along the *b*-axis showing how each sulfate ion forms a total of eight ionic N–$H^+\cdots O^-$ hydrogen bonds with four surrounding tetracations, thereby linking them into layers parallel to the *ac*-plane. (c) View along the *a*-axis showing how vertical layers of sulfate-linked tetracations are joined by N–$H^+\cdots O^-$ hydrogen bonds with intervening layers in which rows of bisulfate ions with disordered atoms of hydrogen are connected by O–$H\cdots O^-$ hydrogen bonds. In the views, broken lines denote hydrogen bonds, and atoms of carbon appear in gray, hydrogen in white, nitrogen in blue, oxygen in red, and sulfur in yellow. Bisulfate ions with disordered hydrogen atoms are shown in one of two statistically equivalent positions.

As suggested by the low solubility of the salt, tetracations H_4(1,2,4,5-BTA)$^{4+}$ (**1** • $4H^+$) are linked to sulfate and bisulfate ions by an extensive network of ionic N–$H^+\cdots O^-$ hydrogen bonds (Figure 3.1.a). Each NH_3^+ group engages in three N–$H^+\cdots O^-$ hydrogen bonds; therefore, the capacity of the tetracations to serve as donors of hydrogen bonds is extensively exploited. The

length of $N–H^+\cdots O^-$ hydrogen bonds involving sulfate (average value of $d_{H\cdots O}$ = 1.896 Å, corresponding to an average value of $d_{N\cdots O}$ = 2.737 Å) is shorter than the length of bonds to bisulfate (average value of $d_{H\cdots O}$ = 1.950 Å, corresponding to an average value of $d_{N\cdots O}$ = 2.784 Å). Similar distances are observed in other anilinium sulfates and bisulfates.[58–61] The structure of the corresponding tetrahydrochloride salt 1,2,4,5-BTA (**1**) • 4HCl is also highly hydrogen-bonded;[12] however, $N–H^+\cdots Cl^-$ interactions are generally longer and weaker than analogous $N–H^+\cdots O^-$ interactions, so the network formed by the chloride salt is expected to be less robust.

In determining the architecture formed by crystallizing salt H_4(1,2,4,5-BTA)$^{4+}$ (**1** • $4H^+$) SO_4^{2-} $2HSO_4^-$, sulfate ions play a key role. Each interacts with four surrounding tetracations to form a total of eight ionic $N–H^+\cdots O^-$ hydrogen bonds (Figure 3.1.b), thereby generating layers parallel to the *ac*-plane. These layers are joined to form a three-dimensional structure by additional hydrogen bonds involving intervening layers in which bisulfate ions with disordered atoms of hydrogen are connected by $O–H\cdots O^-$ hydrogen bonds to produce chains aligned with the *a*-axis (Figure 3.1.c).

In solutions prepared by dissolving tetrahydrochloride salt 1,2,4,5-BTA (**1**) • 4HCl in aqueous H_2SO_4 (40% H_2SO_4 by volume), the amine presumably exists largely in the form of tetracation H_4(1,2,4,5-BTA)$^{4+}$ (**1** • $4H^+$). Surprisingly, however, crystals grown under these conditions proved to correspond to a mixed 1:1 sulfate:bisulfate salt of trication H_3(1,2,4,5-BTA)$^{3+}$ (**1** • $3H^+$). Table III - 1 compiles selected crystallographic data, and Figure 3.2 provides representations of the structure. *N*-Triprotonation of 1,2,4,5-BTA (**1**) is observed in both molecules in the asymmetric unit, and the non-hydrogen atoms in each trication are essentially coplanar. The average value of $d_{C–C}$ is normal (1.389 Å), and the average length of the $C–NH_3^+$ bonds (1.456 Å) is significantly longer than the average length of the $C–NH_2$ bonds (1.378 Å), as observed in related compounds.[12] The unprotonated NH_2 groups in the two inequivalent trications are markedly pyramidal, as noted in other arylamines,[12] and the average sum of the bond angles is 337.4°. The NH_2 groups are oriented in such a way that planes bisecting the angles H–N–H cut the average planes of the aromatic rings at an average angle of about 85°, which allows the lone pairs of nitrogen to be well aligned with the π-systems.

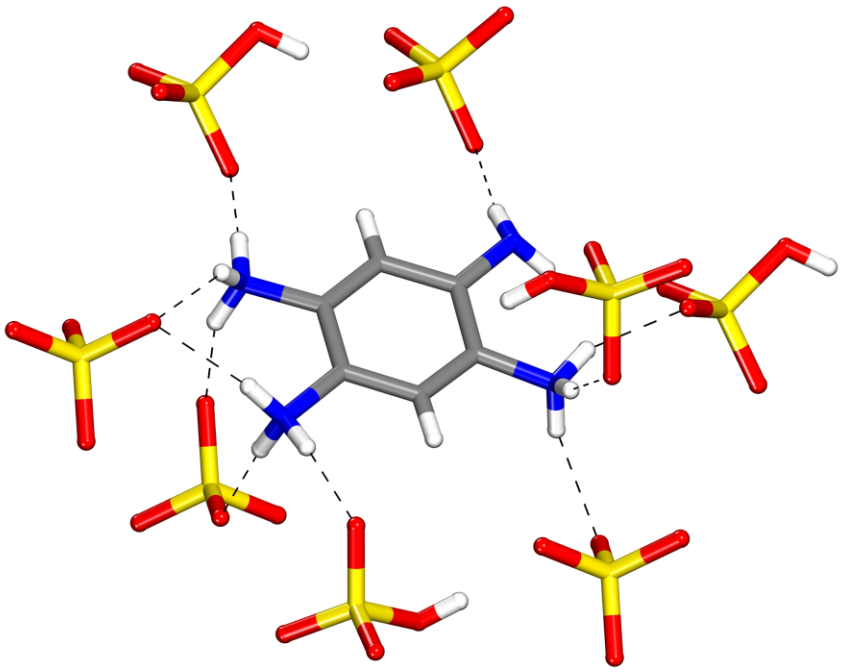

a

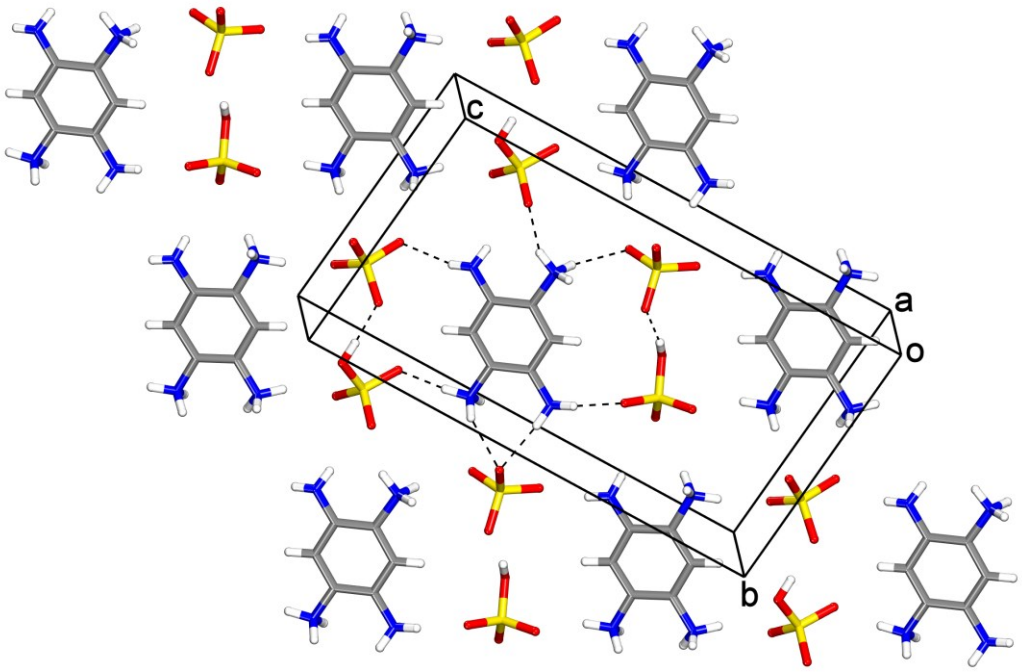

b

Figure 3.2 Representations of the structure of $P\bar{1}$ crystals of salt H_3(1,2,4,5-BTA)$^{3+}$ (**1** • $3H^+$) SO_4^{2-} HSO_4^- grown from aqueous H_2SO_4. (a) View of one of the two symmetry-inequivalent trications, showing how its three NH_3^+ groups form a total of nine primary N–H···O hydrogen bonds with surrounding sulfate and bisulfate ions. The single NH_2 group takes part in an additional N–H···O hydrogen bond with sulfate, with one short N–H···O bond and another interaction that is substantially longer. Of the eight surrounding ions, six lie close to the average plane of the trication. (b) View along the *a*-axis, showing how characteristic sheets are formed by N–H···O hydrogen bonding of the symmetry-inequivalent trications with coplanar pairs of sulfate and bisulfate ions linked by O–H···O hydrogen bonds. In both views, broken lines denote hydrogen bonds, and atoms appear in standard colors.

The three NH_3^+ groups of each trication form a total of nine primary ionic N–H^+···O^- hydrogen bonds with surrounding sulfate and bisulfate ions, as illustrated in Figure 3.2.a for one of the two symmetry-inequivalent trications. In this way, the capacity of the NH_3^+ groups to serve as hydrogen-bond donors is extensively used. The single NH_2 group takes part in additional hydrogen bonding with sulfate, with one short N–H···O bond and another interaction that is substantially longer. The average value of $d_{H\cdots O}$ for the ionic N–H^+···O^- hydrogen bonds is similar to the value observed in the structure of *P2/c* crystals of H_4(1,2,4,5-BTA)$^{4+}$ (**1** • $4H^+$) SO_4^{2-} $2HSO_4^-$, as well as in the structures of other anilinium sulfates and bisulfates.[58–61] The overall structure is composed of characteristic sheets (Figure 3.2.b), which result from in-plane hydrogen bonding of both symmetry-inequivalent trications with coplanar pairs of sulfate and bisulfate ions linked by O–H···O hydrogen bonds. Stacking of the sheets allows the formation of additional out-of-plane N–H^+···O^- hydrogen bonds and gives rise to a structure in which the trications are linked in three dimensions by bridging sulfate and bisulfate ions.

Recrystallization of $P\bar{1}$ crystals of salt H_3(1,2,4,5-BTA)$^{3+}$ (**1** • $3H^+$) SO_4^{2-} HSO_4^- from H_2O led to formation of a *Cc* polymorph. Crystallographic data are summarized in Table III - 1, and representations of the structure appear in Figure 3.3. In the new form, *N*-triprotonation is again favored, and the non-hydrogen atoms in each trication are nearly coplanar. Normal average

values are observed for the lengths of C–C bonds (1.388 Å), C–NH_3^+ bonds (1.462 Å), and C–NH_2 bonds (1.391 Å). In addition, the unprotonated NH_2 group is notably pyramidal, and the sum of the bond angles is 329.4°. The NH_2 group is oriented so that the plane bisecting the angle H–N–H cuts the average plane of the aromatic ring at an average angle of about 82°, allowing the lone pair of nitrogen to be well aligned with the π-system.

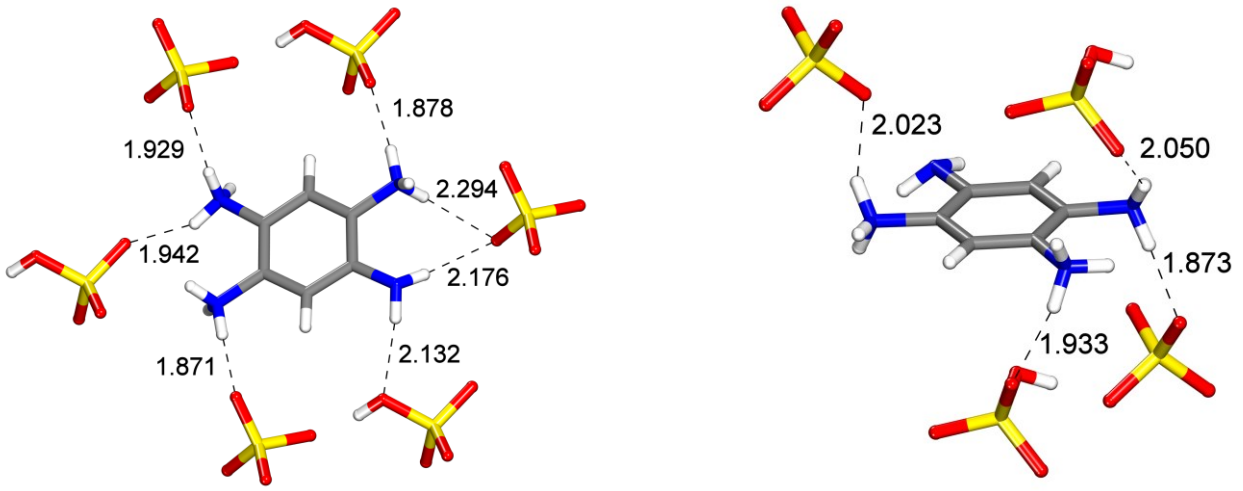

a **b**

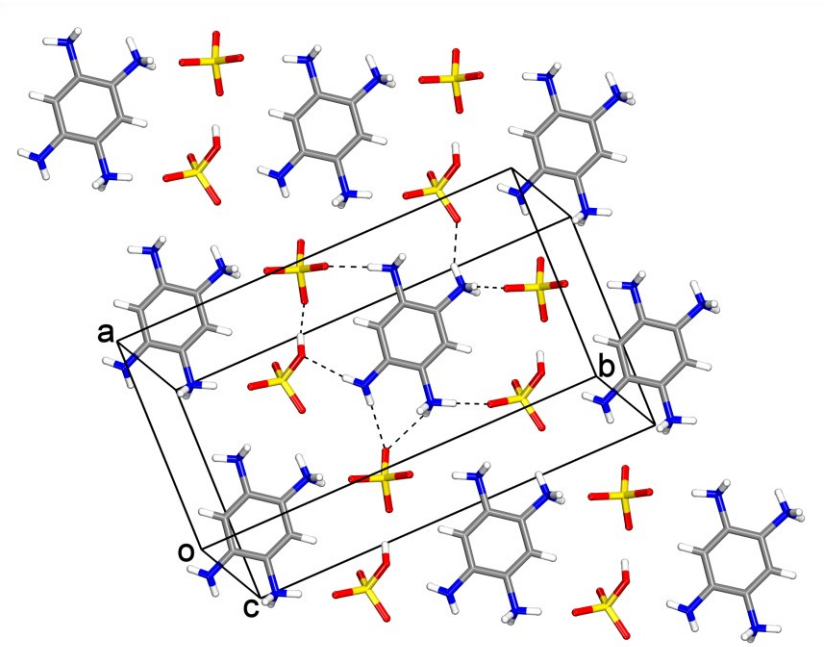

c

Figure 3.3 Representations of the structure of *Cc* crystals of salt H_3(1,2,4,5-BTA)$^{3+}$ (**1** • $3H^+$) SO_4^{2-} HSO_4^- grown from H_2O. (a) View showing how the NH_3^+ and NH_2 groups of each cation form a total of seven primary N–H···O hydrogen bonds with six nearly coplanar sulfate and bisulfate ions. (b) View showing how each trication engages in four additional primary N–H···O hydrogen bonds with four other sulfate and bisulfate ions. (c) View of a corrugated sheet formed by N–H···O hydrogen bonding of the trications with coplanar pairs of sulfate and bisulfate ions linked by O–H···O hydrogen bonds. Broken lines denote hydrogen bonds, values of $d_{H\cdots O}$ are given in Å, and atoms appear in standard colors.

As in the $P\bar{1}$ polymorph of salt H_3(1,2,4,5-BTA)$^{3+}$ (**1** • $3H^+$) SO_4^{2-} HSO_4^-, the three NH_3^+ groups of each trication in form *Cc* engage in a total of nine primary ionic N–H^+···O^- hydrogen bonds with surrounding sulfate and bisulfate ions (Figure 3.3). In addition, the single NH_2 group takes part as a donor in the formation of two more N–H···O hydrogen bonds. In this way, the capacity of the NH_3^+ and NH_2 groups to serve as donors is extensively exploited, and each trication participates in a total of 11 hydrogen bonds involving five sulfate ions and five bisulfate

ions. The *Cc* polymorph is presumably more stable than the $P\bar{1}$ form, which has a lower density and incorporates fewer hydrogen bonds per trication. Of the 10 surrounding ions in the *Cc* structure, six lie close to the average molecular plane of the trication (Figure 3.3a), and four others are placed above and below the plane (Figure 3.3.b). Figure 3.3.c shows that the resulting structure closely resembles the one formed by the $P\bar{1}$ polymorph (Figure 3.2.b). Characteristic sheets are again produced by in-plane hydrogen bonding of trications with coplanar pairs of sulfate and bisulfate ions linked by O–H···O hydrogen bonds. Stacking of the sheets leads to the formation of additional out-of-plane $N–H^+\cdots O^-$ hydrogen bonds and yields a network in which the trications are bridged in three dimensions by sulfate and bisulfate ions.

Solutions prepared by dissolving tetrahydrochloride salt 1,2,4,5-BTA (**1**) • 4HCl in concentrated H_2SO_4 also yielded crystals of a bisulfate salt of composition $H_4(1,2,4,5\text{-BTA})^{4+}$ (**1** • $4H^+$) $4HSO_4^-$. Selected crystallographic data appear in Table III - 1, and representations of the structure are provided in Figure 3.4. *N*-Tetraprotonation of 1,2,4,5-BTA (**1**) is observed, the non-hydrogen atoms in each tetracation are essentially coplanar, and the average values of $d_{C–C}$ (1.383 Å) and $d_{C–N}$ (1.458 Å) are normal. Figure 3.4a shows how the NH_3^+ groups of each tetracation interact with 12 surrounding disordered bisulfate ions to form a total of 16 primary $N–H^+\cdots O$ hydrogen bonds, some of which are bifurcated. Eight of the hydrogen-bonded bisulfate ions lie close to the average plane of the central tetracation (Figure 3.4b), and four others are positioned above and below the plane (Figure 3.4.c). As expected, $N–H^+\cdots O$ hydrogen bonds involving the OH groups of bisulfate are longer ($d_{H\cdots O}$ = 2.280 Å and $d_{N\cdots O}$ = 2.743 Å) than those involving O^- (average values of $d_{H\cdots O}$ = 2.015 Å, $d_{N\cdots O}$ = 2.839 Å). The observed structure can be considered to be constructed from hydrogen-bonded sheets in which tetracations are bridged by the eight coplanar bisulfate ions (Figure 3.4.d). Stacking of the sheets then allows the tetracations to form additional out-of-plane $N–H^+\cdots O$ hydrogen bonds with bisulfate ions in neighboring sheets, thereby creating a three-dimensional hydrogen-bonded network.

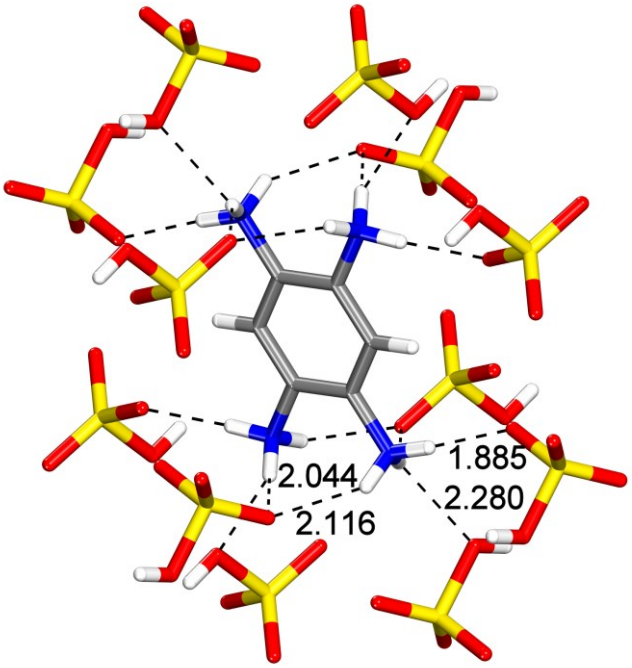

a

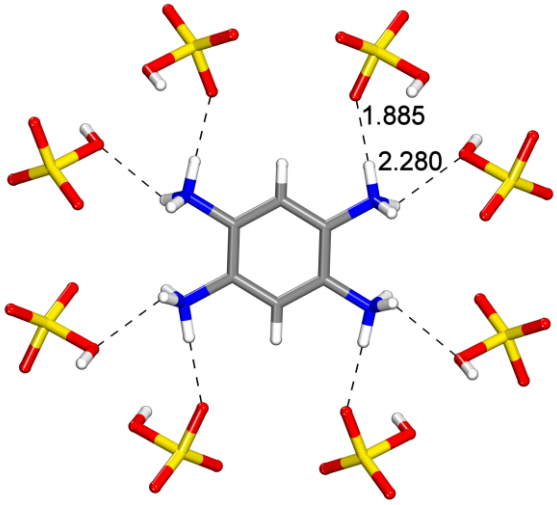

b

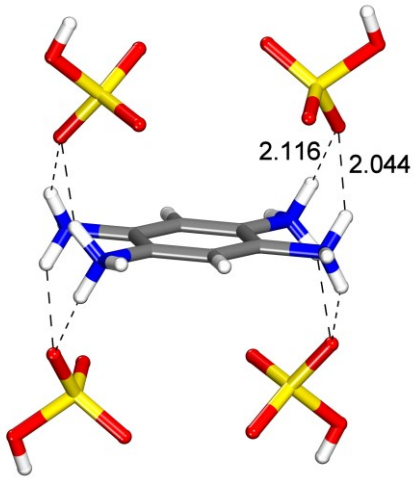

c

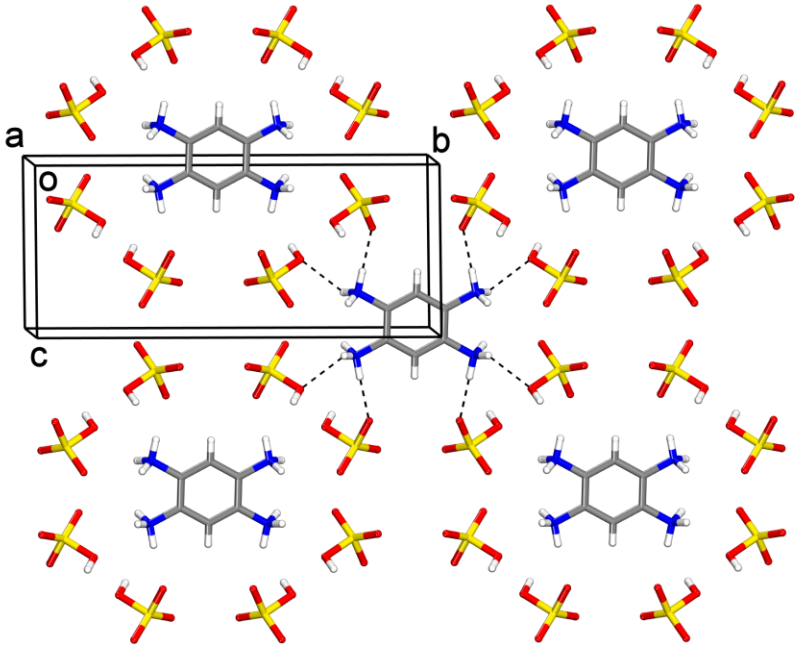

Figure. 4 Representations of the structure of *C*2/*m* crystals of salt H_4(1,2,4,5-BTA)$^{4+}$ (**1** • $4H^+$) $4HSO_4^-$ grown from concentrated H_2SO_4. (a) View showing how each tetracation takes part in a total of 16 primary N–H^+···O hydrogen bonds with 12 surrounding bisulfate ions. (b) View showing that eight of the hydrogen-bonded bisulfate ions lie close to the average molecular plane of the tetracation. (c) View showing that the other four bisulfate ions lie above and below the plane of the tetracation. (d) View showing how the observed structure is constructed from sheets in which tetracations are bridged by the coplanar bisulfate ions. In all views, broken lines signify key hydrogen bonds, with values of $d_{H\cdots O}$ given in Å. Atoms appear in standard colors, and bisulfate ions are shown in one of two statistically equivalent disordered positions.

Under certain conditions, sulfate salts of 1,2,4,5-BTA (**1**) can be obtained in the form of hydrates. Mixtures prepared by adding tetrahydrochloride salt 1,2,4,5-BTA (**1**) • 4HCl to dilute aqueous H_2SO_4 (0.2 M) yielded crystals of composition H_3(1,2,4,5-BTA)$^{3+}$ (**1** • $3H^+$) $1.5SO_4^-$ • $2H_2O$. Table III - 1 presents selected crystallographic data 1, and Figure 3.5 provides a representation of the structure. *N*-Triprotonation of BTA (**1**) is observed, the non-hydrogen atoms

in each trication are nearly coplanar, and the average lengths of C–C bonds (1.388 Å), C–NH_3^+ bonds (1.462 Å), and C–NH_2 bonds (1.370 Å) have normal values. In addition, the unprotonated NH_2 groups are pyramidal, and the average sum of the bond angles is 343.4°. All N–H bonds in the NH_3^+ and NH_2 groups of each trication are used to form N–H···O hydrogen bonds with sulfate ions and included molecules of H_2O (Figure 3.5.a). The observed structure can be considered to be constructed from stacks of trications that are bridged by sulfate ions and molecules of H_2O, thereby creating a three-dimensional hydrogen-bonded network (Figure 3.5.b).

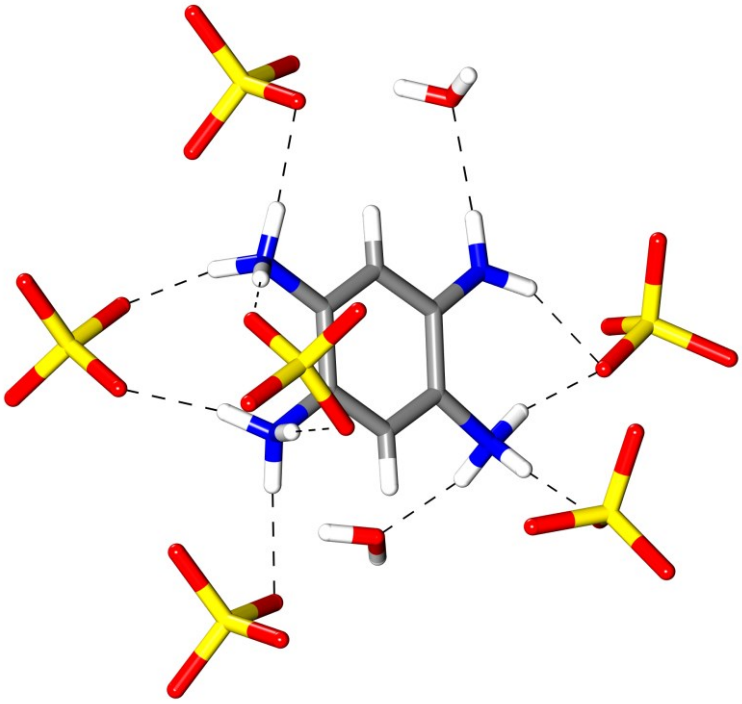

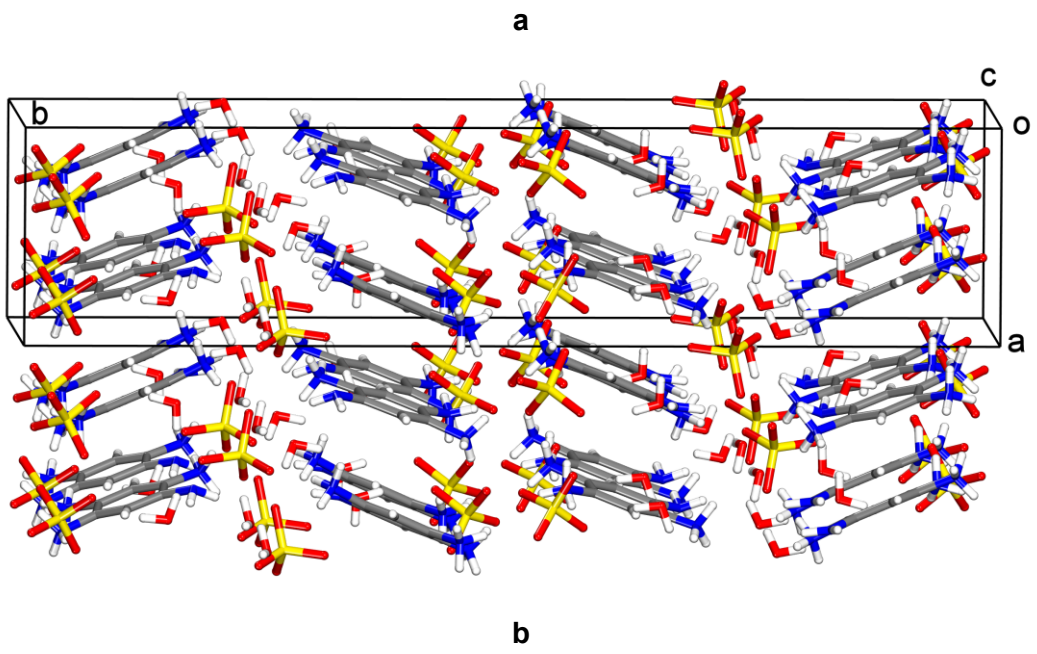

Figure 3.5 Representation of the structure of $P2_1/n$ crystals of salt H_3(1,2,4,5-BTA)$^{3+}$ (**1** • $3H^+$) $1.5SO_4^-$ • $2H_2O$ grown from 0.2 M aqueous H_2SO_4. (a) View of one of the two symmetry-inequivalent trications, showing how all N–H bonds in the NH_3^+ and NH_2 groups are used to form N–H···O hydrogen bonds with sulfate ions and included molecules of H_2O. (b) View showing stacks of trications that are bridged by sulfate ions and molecules of H_2O, thereby creating a three-dimensional hydrogen-bonded network. Atoms appear in standard colors, and a disordered sulfate ion is shown in one of two statistically equivalent positions.

Structure of the Sulfate Salt of 1,2,3,4-BTA (3).

1,2,3,4-BTA (**3**) was isolated and characterized as a crystalline sulfate salt of composition H_2(1,2,3,4-BTA)$^{2+}$ (**3** • $2H^+$) SO_4^{2-}.[12] Selected crystallographic data are summarized in Table III - 1, and representations of the structure appear in Figure 3.6. *N*-Protonation is observed, as in the case of salts of 1,2,4,5-BTA (**1**). In principle, *N*-diprotonation can give rise to three different dications **4**−**7**. Gas-phase stability is expected to decrease in the order **4** > **5** > **6** > **7**, based on decreased charge separation and the reduced opportunity to form intramolecular N–H^+···N hydrogen bonds.

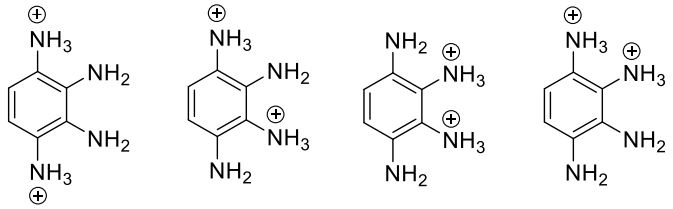

4 **5** **6** **7**

In fact, the observed crystals of sulfate salt H_2(1,2,3,4-BTA)$^{2+}$ (**3** • $2H^+$) SO_4^{2-} incorporate only dication **4**. The NH_2 groups are pyramidal, and the average sum of bond angles at nitrogen is 328.8°. All four atoms of nitrogen lie near the average plane of the aromatic ring, and the two NH_2 groups are oriented in such a way that angles of 48 and 69° are formed by the average plane of the aromatic ring and the two planes bisecting the angles H–N–H. This orientation allows partial alignment of the lone pairs of the NH_2 groups with the π-system but does not lead to intramolecular N–H^+···N interactions that are shorter than the sum of the van der Waals radii of nitrogen and hydrogen. The average values of $d_{C–C}$ (1.393 Å), $d_{C–N}$ for the NH_2 groups (1.390 Å), and $d_{C–N}$ for the NH_3^+ groups (1.471 Å) resemble those observed in related salts.

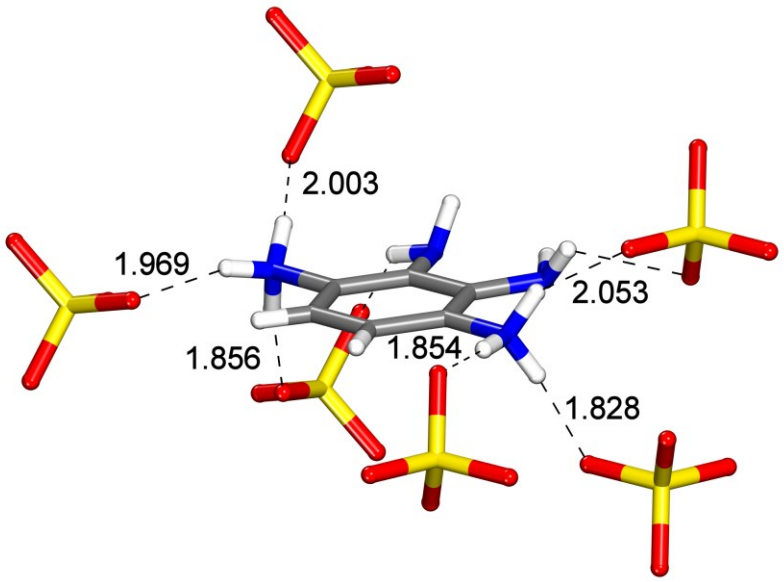

a

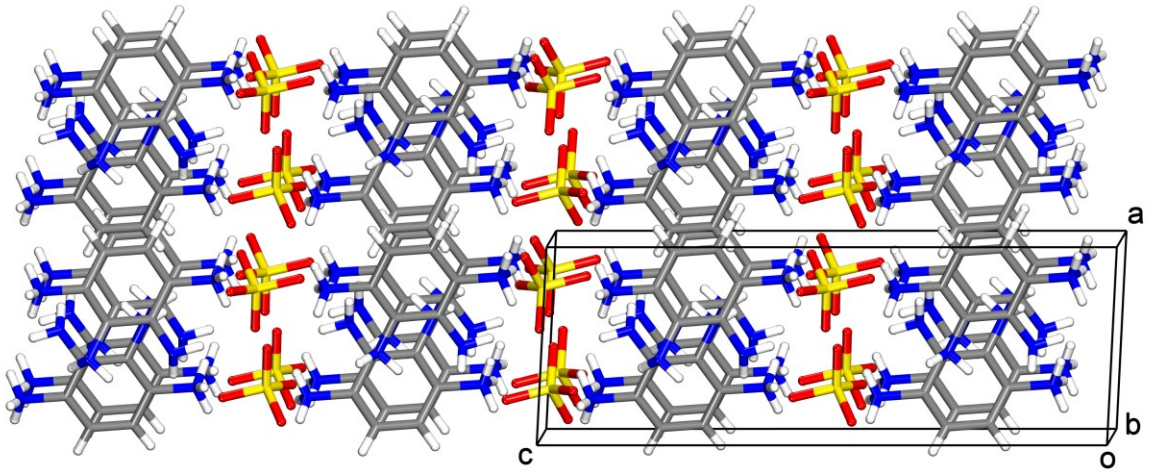

b

Figure 3.6 Representations of the structure of $P2_1/c$ crystals of salt $H_2(1,2,3,4\text{-BTA})^{2+}$ (**3** • $2H^+$) SO_4^{2-} grown from $EtOH/H_2O/H_2SO_4$. (a) View showing how the two NH_3^+ groups of each dication form a total of six primary $N–H^+\cdots O^-$ hydrogen bonds with six surrounding sulfate ions and how each of the two NH_2 groups takes part in an additional $N–H\cdots O^-$ hydrogen bond with sulfate. (b) View along the *b*-axis, showing how alternating layers of dications and sulfate ions are linked by N–H···O hydrogen bonds to form a three-dimensional network. Broken lines denote hydrogen bonds, values of $d_{H\cdots O}$ for primary hydrogen bonds are given in Å, and atoms appear in standard colors.

The two NH_3^+ groups of each dication take part in a total of six primary $N–H^+\cdots O^-$ hydrogen bonds with six surrounding sulfate ions (Figure 3.6.a), so the capacity of the dications to serve as donors of hydrogen bonds is extensively exploited. The average value of $d_{H\cdots O}$ for these primary hydrogen bonds is 1.927 Å (corresponding to an average value of $d_{N\cdots O}$ = 2.797 Å), and the reinforcing $N–H\cdots O^-$ hydrogen bonds formed by the NH_2 groups are longer (average value of $d_{H\cdots O}$ = 2.344 Å, corresponding to an average value of $d_{N\cdots O}$ = 3.004 Å). Similar distances are observed in other anilinium sulfates and bisulfates.[58–61] In the resulting structure, alternating layers of dications and sulfate ions are linked by N–H···O hydrogen bonds to form a three-dimensional network (Figure 3.6.b).

Conclusions

Like hydroquinones and quinones, aromatic compounds with multiple NH_2 groups and the corresponding quinonediimines are candidates for use as the components of redox-active organic materials. 1,2,4,5-BTA (**1**) and diimine **2** form a redox pair of this type and are attractive targets for further study, as are 1,2,3,4-BTA (**3**) and its oxidized forms. However, many aspects of the chemistry of these compounds are poorly understood, such as the nature of their salts and their preferred patterns of association, which determine how they can be used to construct predictably ordered redox-active solids. In the course of recent work with 1,2,4,5-BTA (**1**), 1,2,3,4-BTA (**3**), and related compounds,[12,13] we prepared a series of crystalline sulfate/bisulfate salts and solved their structures. Our analyses confirmed a preference for *N*-protonation and showed that each NH_3^+ group tends to take part in three primary $N–H^+\cdots O$ hydrogen bonds with surrounding sulfate and bisulfate ions. The observed structures typically consist of sheets or layers in which cations derived from benzenetetramines are bridged by sulfate and bisulfate ions, leading to the formation of robust networks in which all components are positioned in three dimensions by strong directional interactions. These structural preferences are desirable in materials designed for use in electrodes, where strongly bonded solids help ensure low solubility in electrolytes and where layered structures can be expected to facilitate ionic diffusion during charging and discharging. In future work, we plan to examine the structures of sulfate/bisulfate salts of compound **2** and related products of oxidation, as well as their interconversion with salts of 1,2,4,5-BTA (**1**) and analogues via solid-state redox reactions. Together, these studies promise to facilitate the use of complex arylamines as components of redox-active organic solids.

Experimental Methods

Tetrahydrochloride salt 1,2,4,5-BTA (**1**) • 4HCl and sulfate salt 1,2,3,4-BTA (**3**) • H_2SO_4 were prepared by reported methods.[12] All other reagents were purchased from commercial suppliers and used without further purification.

Crystallization of H_4(1,2,4,5-BTA)$^{4+}$ SO_4^{2-} 2 HSO_4^-. Tetrahydrochloride salt 1,2,4,5-BTA (**1**) • 4HCl (404 mg, 1.42 mmol) was added to concentrated H_2SO_4 (25 mL), and the mixture was left unstirred at 20 °C. Clusters of colorless platelets were deposited within a few days.

Crystallization of H_3(1,2,4,5-BTA)$^{3+}$ SO_4^{2-} HSO_4^- (*P*$\bar{1}$ Form). Concentrated H_2SO_4 (4 mL) and H_2O (6 mL) were precooled to 4 °C, and the acid was added slowly to the H_2O. Tetrahydrochloride salt 1,2,4,5-BTA (**1**) • 4HCl (82 mg, 0.29 mmol) was then added, and the mixture was left unstirred at 20 °C. Colorless blocks started to appear within two days.

Crystallization of H_3(1,2,4,5-BTA)$^{3+}$ SO_4^{2-} HSO_4^- (*Cc* Form). A sample of the *P*$\bar{1}$ form of H_3(1,2,4,5-BTA)$^{3+}$ SO_4^{2-} HSO_4^- (28 mg, 0.084 mmol) was suspended in H_2O (1 mL). The mixture was heated to produce a solution, and slow cooling to 20 °C led to the precipitation of colorless needles of the *Cc* form.

Crystallization of H_4(1,2,4,5-BTA)$^{4+}$ 4HSO_4^-. Tetrahydrochloride salt 1,2,4,5-BTA (**1**) • 4HCl (178 mg, 0.627 mmol) was added to concentrated H_2SO_4 (20 mL), and the mixture was left unstirred at 20 °C. Colorless plates appeared after two days.

Crystallization of H_3(1,2,4,5-BTA)$^{3+}$ 1.5SO_4^{2-} • 2H_2O. Tetrahydrochloride salt 1,2,4,5-BTA (**1**) • 4HCl (1.0 g, 3.5 mmol) was added to 0.2 M aqueous H_2SO_4 (40 mL), and the mixture was left unstirred at 20 °C. Under these conditions, colorless plates appeared within minutes.

Crystallization of H_2(1,2,3,4-BTA)$^{2+}$ SO_4^{2-}. As reported,[12] concentrated H_2SO_4 was added to the corresponding hydrochloride salt in cold aqueous EtOH, and crystallization was allowed to proceed.

Supporting Information Available: Additional crystallographic details (including thermal atomic displacement parameter plots). This material is available free of charge via the Internet at http://pubs.acs.org.

Accession Codes: CCDC 2285042–2285047 contain the supplementary crystallographic data for this paper. These data can be obtained free of charge via www.ccdc.cam.ac.uk/data_request/cif, or by emailing data_request@ccdc.cam.ac.uk, or by contacting The Cambridge Crystallographic Data Centre, 12 Union Road, Cambridge CB2 1EZ, UK; fax: +44 1223 336033.

Notes. The authors have no competing financial interests to declare.

Acknowledgments. The authors thank the Natural Sciences and Engineering Research Council (NSERC) of Canada for financial support (RGPIN-2019-05469). In addition, J. D. W. is grateful to the Canada Foundation for Innovation (Project 30910) and the Canada Research Chairs Program for their generous support. J. O. E. S. thanks the Université de Montréal for a graduate fellowship. The authors are also grateful to the *Centre en chimie verte et catalyse* and the *Centre québécois sur les matériaux fonctionnels*, two strategic clusters funded by the Fonds de recherche du Québec – Nature et technologies (FRQNT).

References

1. Kim, J.; Kim, Y.; Yoo, J.; Kwon, G.; Ko, Y.; Kang, K. Organic Batteries for a Greener Rechargeable World. *Nat. Rev. Mater.* **2023**, *8*, 55–70.
2. Chen, Y.; Dai, H.; Fan, K.; Zhang, G.; Tang, M.; Gao, Y.; Zhang, C.; Guan, L.; Mao, M.; Liu, H.; Zhai, T.; Wang, C. A Recyclable and Scalable High-Capacity Organic Battery. *Angew. Chem. Int. Ed.* **2023**, e202302539.
3. Chen, X.; Yin, X.; Aslam, J.; Sun, W.; Wang, Y. Recent Progress and Design Principles for Rechargeable Lithium Organic Batteries. *Electrochem. Energy Rev.* **2022**, *5*, 12.
4. Kato, K.; Puthirath, A. B.; Mojibpour, A.; Miroshnikov, M.; Satapathy, S.; Thangavel, N. K.; Mahankali, K.; Dong, L.; Arava, L. M. R.; John, G.; Bharadwaj, P.; Babu, G.; Ajayan, P. M. Light-Assisted Rechargeable Lithium Batteries: Organic Molecules for Simultaneous Energy Harvesting and Storage. *Nano Lett.* **2021**, *21*, 907–913.
5. Esser, B.; Dolhem, F.; Becuwe, M.; Poizot, P.; Vlad, A.; Brandell, D. A Perspective on Organic Electrode Materials and Technologies for Next Generation Batteries. *J. Power Sources* **2021**, *482*, 228814.
6. Goujon, N.; Casado, N.; Patil, N.; Marcilla, R.; Mecerreyes, D. Organic Batteries Based on Just Redox Polymers. *Prog. Polym. Sci.* **2021**, *122*, 101449.
7. Lakraychi, A. E.; Dolhem, F.; Vlad, A.; Becuwe, M. Organic Negative Electrode Materials for Metal-Ion and Molecular-Ion Batteries: Progress and Challenges from a Molecular Engineering Perspective. *Adv. Energy Mater.* **2021**, *11*, 2101562.
8. Shea, J. J.; Luo, C. Organic Electrode Materials for Metal Ion Batteries. *ACS Appl. Mater. Interfaces* **2020**, 12, 5361–5380.
9. Poizot, P.; Gaubicher, J.; Renault, S.; Dubois, L.; Liang, Y.; Yao, Y. Opportunities and Challenges for Organic Electrodes in Electrochemical Energy Storage. *Chem. Rev.* **2020**, *120*, 6490–6557.
10. Lu, Y.; Chen, J. Prospects of Organic Electrode Materials for Practical Lithium Batteries. *Nat. Rev. Chem.* **2020**, *4*, 127–142.
11. Muench, S.; Wild, A.; Friebe, C.; Häupler, B.; Janoschka, T.; Schubert, U. S. Polymer-Based Organic Batteries. *Chem. Rev.* **2016,** *116*, 9438–9484.

12. Sosoe, J. O. E.; Malveau, C.; Maris, T.; Iftimie, R.; Wuest, J. D. Refreshing the Legacy of Rudolf Nietzki: Benzene-1,2,4,5-tetramine and Related Compounds. *J. Org. Chem.* **2023**, *88*, 16302-16314.
13. Sosoe, J. O. E.; Maris, T.; Iftimie, R.; Wuest, J. D. Making 4,6-Diaminoresorcinol and Derivatives by the Hydrolysis of Benzene-1,2,4,5-tetramine. Manuscript in preparation.
14. Qiu, Z.; Li, C.-J. Transformations of Less-Activated Phenols and Phenol Derivatives via C−O Cleavage. *Chem. Rev.* **2020**, *120*, 10454–10515.
15. Asha, A.; Ravindran, J.; Suma, S.; Suresh, C. H.; Lankalapalli, R. S. Synthesis of 2,5-Diamino-*p*-benzoquinones via Aerobic Oxidative $C(sp^2)$-$C(sp^2)$ Bond Cleavage and Mechanistic Studies. *ChemistrySelect* **2020**, *5*, 2545–2550.
16. Lardy, S. W.; Luong, K. C.; Schmidt, V. A. Formal Aniline Synthesis from Phenols through Deoxygenative N-Centered Radical Substitution. *Chem. Eur. J.* **2019**, *25*, 15267–15271.
17. Klopčič, I.; Sollner Dolenc, M. Chemicals and Drugs Forming Reactive Quinone and Quinone Imine Metabolites. *Chem. Res. Toxicol.* **2019**, *32*, 1–34.
18. Crooke, S. T.; Bradner, W. T. Mitomycin C: A Review. *Can. Treat. Rev.* **1976**, *3*, 121–139.
19. Sang, Z.; Liu, J.; Zhang, X.; Yin, L.; Hou, F.; Liang, J. One-Dimensional π−d Conjugated Conductive Metal−Organic Framework with Dual Redox-Active Sites for High-Capacity and Durable Cathodes for Aqueous Zinc Batteries. *ACS Nano* **2023**, *17*, 3077–3087.
20. Wang, J.; Liu, X.; Jia, H.; Apostol, P.; Guo, X.; Lucaccioni, F.; Zhang, X.; Zhu, Q.; Morari, C.; Gohy, J.-F.; Vlad, A. A High-Voltage Organic Framework for High-Performance Na- and K-Ion Batteries. *ACS Energy Lett.* **2022**, *7*, 668–674.
21. Yang, D.; Liang, Z.; Tang, P.; Zhang, C.; Tang, M.; Li, Q.; Biendicho, J. J.; Li, J.; Heggen, M.; Dunin-Borkowski, R. E.; Xu, M.; Llorca, J.; Arbiol, J.; Morante, J. R.; Chou, S.-L.; Cabot, A. A High Conductivity 1D π–d Conjugated Metal–Organic Framework with Efficient Polysulfide Trapping-Diffusion-Catalysis in Lithium–Sulfur Batteries. *Adv. Mater.* **2022**, *34*, 2108835.
22. Kapaev, R. R.; Shestakov, A. F.; Vasil'ev, S. G.; Stevenson, K. J. Conjugated Ladder-Type Polymer with Hexaazatriphenylene Units as a Cathode Material for Lithium, Sodium, and Potassium Batteries. *ACS Appl. Energy Mater.* **2021**, *4*, 10423–10427.
23. Baymuratova, G. R.; Khatmullina, K. G.; Yakuschenko, I. K.; Tulibaeva, G. Z.; Savinykh, T. A.; Troshin, P. A.; Shestakov, A. F.; Yarmolenko, O. V. Synthesis and Investigation of a

New Organic Electrode Material Based on Condensation Product of Triquinoyl with 1,2,4,5-Tetraaminobenzene. *J. Electroanal. Chem.* **2021**, *889*, 115234.

24. Sutton, A. L.; Abrahams, B. F.; D'Alessandro, D. M.; Goerigk, L.; Hudson, T. A.; Robson, R.; Usov, P. M. Semi-Conducting Mixed-Valent $X_4TCNQ^{I-/II-}$ (X = H, F) Charge-Transfer Complexes with $C_6H_2(NH_2)_4$. *J. Mater. Chem. C* **2020**, *8*, 9422−9426.
25. Kapaev, R. R.; Olthof, S.; Zhidkov, I. S.; Kurmaev, E. Z.; Stevenson, K. J.; Meerholz, K.; Troshin, P. A. Nickel(II) and Copper(II) Coordination Polymers Derived from 1,2,4,5-Tetraaminobenzene for Lithium-Ion Batteries. *Chem. Mater.* **2019**, *31*, 5197–5205.
26. Wäckerlin, C.; Cahlík, A.; Goikoetxea, J.; Stetsovych, O.; Medvedeva, D.; Redondo, J.; Švec, M.; Delley, B.; Ondráček, M.; Pinar, A.; Blanco-Rey, M.; Kolorenč, J.; Arnau, A.; Jelínek, P. Role of the Magnetic Anisotropy in Atomic-Spin Sensing of 1D Molecular Chains. *ACS Nano* **2022**, *16*, 16402–16413.
27. Zhang, F.; Wang, P.; Zhao, R.; Wang, Y.; Wang, J.; Han, B.; Liu, Z. Tuning d-Band Structure of Cu^{II} in Coordinated Polymer via d–π Conjugation for Improving CO_2 Electroreduction Selectivity toward C_2 Products. *ChemSusChem* **2022**, *15*, e202201267.
28. Wu, H.-Y.; Yang, C.-Y.; Li, Q.; Kolhe, N. B.; Strakosas, X.; Stoeckel, M.-A.; Wu, Z.; Jin, W.; Savvakis, M.; Kroon, R.; Tu, D.; Woo, H. Y.; Berggren, M.; Jenekhe, S. A.; Fabiano, S. Influence of Molecular Weight on the Organic Electrochemical Transistor Performance of Ladder-Type Conjugated Polymers. *Adv. Mater.* **2022**, *34*, 2106235.
29. Santhini, V. M.; Wäckerlin, C.; Cahlík, A.; Ondráček, M.; Pascal, S.; Matěj, A.; Stetsovych, O.; Mutombo, P.; Lazar, P.; Siri, O.; Jelínek, P. 1D Coordination π–d Conjugated Polymers with Distinct Structures Defined by the Choice of the Transition Metal: Towards a New Class of Antiaromatic Macrocycles. *Angew. Chem. Int. Ed.* **2021**, *60*, 439–445.
30. Wan, Y.; Sun, Y.; Wu, X.; Yang, J. Ambipolar Half-Metallicity in One-Dimensional Metal−(1,2,4,5-Benzenetetramine) Coordination Polymers via Carrier Doping. *J. Phys. Chem. C* **2018**, *122*, 989–994.
31. Chen, Z.; Canard, G.; Jacquemin, D.; Bucher, C.; Giorgi, M.; Siri, O. Hetero-Bimetallic Effect as a Route to Access Multinuclear Complexes. *Inorg. Chem.* **2018**, *57*, 12536–12542.
32. Pascal, S.; Siri, O. Benzoquinonediimine Ligands: Synthesis, Coordination Chemistry and Properties. *Coord. Chem. Rev.* **2017**, *350*, 178–195.

33. Audi, H.; Chen, Z.; Charaf-Eddin, A.; D'Aléo, A.; Canard, G.; Jacquemin, D.; Siri, O. Extendable Nickel Complex Tapes that Reach NIR Absorptions. *Chem. Commun.* **2014**, *50*, 15140–15143.
34. Jeon, I.-R.; Park, J. G.; Xiao, D. J.; Harris, T. D. An Azophenine Radical-Bridged Fe_2 Single-Molecule Magnet with Record Magnetic Exchange Coupling. *J. Am. Chem. Soc.* **2013**, *135*, 16845–16848.
35. Frantz, S.; Rall, J.; Hartenbach, I.; Schleid, T.; Záliš, S.; Kaim, W. Metal-Induced Tautomerization of *p*- to *o*-Quinone Compounds: Experimental Evidence from Cu^I and Re^I Complexes of Azophenine and DFT Studies. *Chem. Eur. J.* **2004**, *10*, 149–154.
36. Masui, H.; Lever, A. B. P.; Dodsworth, E. S. Substituent Effects and Bonding Characteristics in (*o*-Benzoquinone diimine)bis(bipyridine)ruthenium (II) Complexes. *Inorg. Chem.* **1993**, *32*, 258–267.
37. Parvatkar, P. T.; Kandambeth, S.; Shaikh, A. C.; Nadinov, I.; Yin, J.; Kale, V. S.; Healing, G.; Emwas, A.-H.; Shekhah, O.; Alshareef, H. N.; Mohammed, O. F.; Eddaoudi, M. A Tailored COF for Visible-Light Photosynthesis of 2,3-Dihydrobenzofurans. *J. Am. Chem. Soc.* **2023**, *145*, 5074–5082.
38. Lin, Y.; Cui, H.; Liu, C.; Li, R.; Wang, S.; Qu, G.; Wei, Z.; Yang, Y.; Wang, Y.; Tang, Z.; Li, H.; Zhang, H.; Zhi, C.; Lv, H. A Covalent Organic Framework as a Long-Life and High-Rate Anode Suitable for Both Aqueous Acidic and Alkaline Batteries. *Angew. Chem. Int. Ed.* **2023**, *62*, e202218745.
39. Zhi, Q.; Liu, W.; Jiang, R.; Zhan, X.; Jin, Y.; Chen, X.; Yang, X.; Wang, K.; Cao, W.; Qi, D.; Jiang, J. Piperazine-Linked Metalphthalocyanine Frameworks for Highly Efficient Visible-Light-Driven H_2O_2 Photosynthesis. *J. Am. Chem. Soc.* **2022**, *144*, 21328–21336.
40. Zhang, J.; Kong, Y.-R.; Liu, Y.; Luo, H.-B.; Zou, Y.; Zang, S.-Q.; Ren, X.-M. Superprotonic Conduction of Acidified Benzimidazole-Linked Covalent Organic Framework. *ACS Materials Lett.* **2022**, *4*, 2597–2603.
41. Zheng, Q.; Li, X.; Zhang, Q.; Lee, D.; Mao, H.; Yang, C.; Bustillo, K. C.; Reimer, J. A.; Liu, Y.; Jiang, J.; Zheng, H. A Covalent Organic Framework Onion Structure. *Mater. Today* **2022**, *60*, 98−105.
42. Li, X.; Wang, H.; Chen, H.; Zheng, Q.; Zhang, Q.; Mao, H.; Liu, Y.; Cai, S.; Sun, B.; Dun, C.; Gordon, M. P.; Zheng, H.; Reimer, J. A.; Urban, J. J.; Ciston, J.; Tan, T.; Chan, E. M.;

Zhang, J.; Liu, Y. Dynamic Covalent Synthesis of Crystalline Porous Graphitic Frameworks. *Chem* **2020**, *6*, 933−944.

43. Kim, S.; Choi, H. C. Light-Promoted Synthesis of Highly-Conjugated Crystalline Covalent Organic Framework. *Commun. Chem.* **2019**, *2*, 60.
44. Hisaki, I.; Affendy, N. Q. E.; Tohnai, N. Precise Elucidations of Stacking Manners of Hydrogen-Bonded Two-Dimensional Organic Frameworks Composed of X-Shaped π-Conjugated Systems. *CrystEngComm* **2017**, *19*, 4892−4898.
45. Yang, Q.; Liu, Y.; Xiang, L.; Zhang, J.; Yin, Y.; Xu, F.; Mai, Y. A General Synthetic Method towards Conjugated Microporous Polymers with Ordered Bicontinuous Mesostructures. *Chem. Commun.* **2023**, *59*, 4742−4745.
46. Xu, J.; Li, W.; Liu, W.; Jing, J.; Zhang, K.; Liu, L.; Yang, J.; Zhu, E.; Li, J; Zhu, Y. Efficient Photocatalytic Hydrogen and Oxygen Evolution by Side-Group Engineered Benzodiimidazole Oligomers with Strong Built-in Electric Fields and Short-Range Crystallinity. *Angew. Chem. Int. Ed.* **2022**, *61*, e202212243.
47. Shin, S.-H.; Noh, H.-J.; Kim, Y.-H.; Im, Y.-K.; Mahmood, J.; Baek, J.-B. Forming Layered Conjugated Porous BBL Structures. *Polym. Chem.* **2019**, *10*, 4185−4193.
48. Seo, W.; Carpenter, K. L.; Gaugler, J. A.; Shao, W.; Werling, K. A.; Fournier, P. M.; Lambrecht, D. S.; Star, A. Polybenzobisimidazole-Derived Two-Dimensional Supramolecular Polymer. *J. Polym. Sci. A Polym. Chem.* **2017**, *55*, 1095−1101.
49. Gajiwala, H. M.; Zand, R. Synthesis and Characterization of Thermally Stable Polymers Containing Phenazine. *Polymer* **2000**, *41*, 2009−2015.
50. Szita, J.; Marvel, C. S. Partial Ladder Polymers with Anthraquinone Units. Reaction of 1,2,5,6-Tetraaminoanthraquinone with *p*-Benzoquinone Derivatives. *J. Polym. Sci. A1* **1972**, *9* (2), 415−421.
51. Audi, H.; Viero, Y.; Alwhaibi, N.; Chen, Z.; Iazykov, M.; Heynderickx, A.; Xiao, F.; Guérin, D.; Krzeminski, C.; Grace, I. M.; Lambert, C. J.; Siri, O.; Vuillaume, D.; Lenfant, S.; Klein, H. Electrical Molecular Switch Addressed by Chemical Stimuli. *Nanoscale* **2020**, *12*, 10127−10139.
52. Guo, Z.; Song, N. R.; Moon, J. H.; Kim, M.; Jun, E. J.; Choi, J.; Lee, J. Y.; Bielawski, C. W.; Sessler, J. L.; Yoon, J. A Benzobisimidazolium-Based Fluorescent and Colorimetric Chemosensor for CO_2. *J. Am. Chem. Soc.* **2012**, *134*, 17846−17849.

53. Chen, Z.; Bert, M.; Pascal, S.; Canard, G.; Siri, O. Versatile Transamination in Quinonediimine Chemistry: Towards a Novel Class of Water Soluble UV/Violet Chromophores. *Tetrahedron Lett.* **2019**, *60*, 151024.
54. Edzang, J. A.; Chen, Z.; Audi, H.; Canard, G.; Siri, O. Transamination at the Crossroad of the One-Pot Synthesis of N-Substituted Quinonediimines and C-Substituted Benzobisimidazoles. *Org. Lett.* **2016**, *18*, 5340−5343.
55. Bindewald, E.; Lorenz, R.; Hübner, O.; Brox, D.; Herten, D.-P.; Kaifer, E.; Himmel, H.-J. Tetraguanidino-Functionalized Phenazine and Fluorene Dyes: Synthesis, Optical Properties and Metal Coordination. *Dalton Trans.* **2015**, *44*, 3467−3485.
56. Le, H. T. M.; El-Hamdi, N. S.; Miljanić, O. Š. Benzobisimidazole Cruciform Fluorophores. *J. Org. Chem.* **2015**, *80*, 5210−5217.
57. Golubovskaya, V.; Curtin, L.; Groman, A.; Sexton, S.; Cance, W. G. In Vivo Toxicity, Metabolism and Pharmacokinetic Properties of FAK Inhibitor 14 or Y15 (1,2,4,5-Benzenetetramine Tetrahydrochloride). *Arch. Toxicol.* **2015**, *89*, 1095−1101.
58. Fun, H.-K.; Arshad, S.; Dinesha; Laxmeshwar, S.; Nagaraja, G. K. Bis(4-fluoroanilinium) Sulfate. *Acta. Crystallogr.* **2011**, *E67*, o2408.
59. Boutobba, Z.; Direm, A.; Benali-Cherif, N. Anilinium Hydrogen Sulfate. *Acta. Crystallogr.* **2010**, *E66*, o595−o596.
60. Kapoor, I. P. S.; Srivastava, P.; Singh, G.; Fröhlich, R. Preparation, Crystal Structure and Microwave Studies on Ring-Substituted Arylammonium Hydrogen Sulfate Salts. *Indian. J. Chem.* **2007**, *46A*, 1283−1288.
61. Kapoor, I. P. S.; Srivastava, P.; Singh, G.; Fröhlich, R. Preparation, Characterization and Crystal Structure of Phenylene-1,3-diammonium Sulfate. *Indian. J. Chem.* **2006**, *45A*, 1820−1824.
62. Jayaraman, K.; Choudhury, A.; Rao, C. N. R. Sulfates of Organic Diamines: Hydrogen-Bonded Structures and Properties. *Solid State Sci.* **2002**, *4*, 413−422.
63. Nietzki, R.; Schedler, A. Synthese von symmetrischem Tetramidobenzol mittels Dinitrodichlorbenzol. *Ber. dtsch. chem. Ges.* **1897**, *30*, 1666–1669.
64. Nietzki, R.; Hagenbach, E. Ueber Tetramidobenzol und seine Derivate. *Ber. dtsch. chem. Ges.* **1887**, *20*, 328–338.

65. Ward, M. D. Charge-Assisted Hydrogen-Bonded Networks. *Struct. Bonding (Berlin)* **2009**, *132*, 1−23.
66. Glatzhofer, D. T.; Khan, M. A. *N*,*N*',*N*''-Triphenyl-l,3,5-triaminobenzene and Its σ Complex on Protonation: A Stable *N*,*N*',*N*''-Triphenyl-2,4,6-triaminocyclohexadienylium Cation. *Acta Crystallogr.* **1993**, *C49*, 2128−2133.
67. Knoche, W.; Schoeller, W. W.; Schomäcker, R.; Vogel, S. Protonation of 1,3,5-Triaminobenzenes in Aqueous Solutions. Thermodynamics and Kinetics of the Formation of Stable σ-Complexes. *J. Am. Chem. Soc.* **1988**, *110*, 7484−7489.

For Table of Contents Use Only

Strongly Hydrogen-Bonded Networks Formed by
Sulfate and Bisulfate Salts of Benzenetetramines

Johann O. E. Sosoe, Thierry Maris, and James D. Wuest

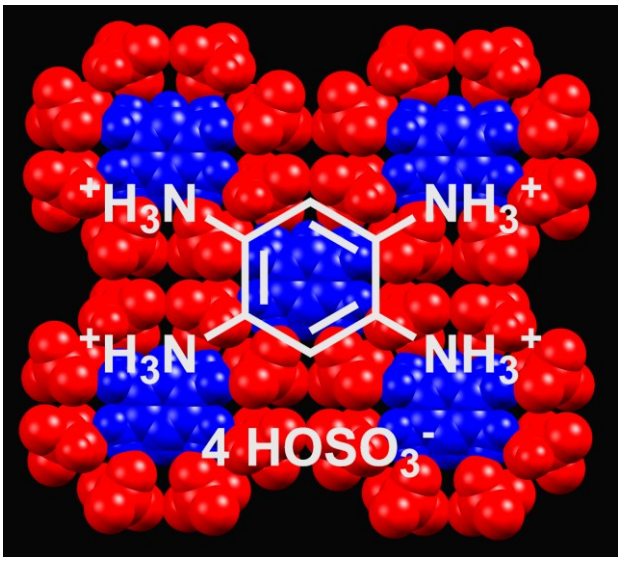

Synopsis. Benzene-1,2,4,5-tetramine and benzene-1,2,3,4-tetramine form crystalline salts in which *N*-protonated cations are bridged by multiple sulfate or bisulfate ions to give robust three-dimensional hydrogen-bonded structures.

3.2. Conclusions

Six nouvelles structures cristallines ont pu être résolues : deux sulfates (H_3(1,2,4,5-BTA)$^{3+}$ · 1.5SO_4^{2-} ·2 H_2O et H_2(1,2,3,4-BTA)$^{2+}$ ·SO_4^{2-}), trois sulfates/bisulfates mixtes (H_4(1,2,4,5-BTA)$^{4+}$ ·SO_4^{2-} ·2HSO_4^-, H_3(1,2,4,5-BTA)$^{3+}$ ·SO_4^{2-} ·HSO_4^- et H_3(1,2,4,5-BTA)$^{3+}$ ·SO_4^{2-} ·HSO_4^-) et un bisulfate (H_4(1,2,4,5-BTA)$^{4+}$ ·4HSO_4^-). Les sels de sulfate et/ou bisulfate de l'isomère 1,2,4,5-BTA **1** sont beaucoup moins solubles dans l'eau pure à 20 °C que le chlorhydrate H_4(1,2,4,5-BTA)$^{4+}$ ·4Cl^- décrit au chapitre précédant. L'origine de cette différence semble résider dans la capacité des anions bisulfates à former davantage de ponts hydrogène avec les cations ammoniums (ainsi qu'avec les sulfates des sels mixtes) que l'ion chlorure. Surprenamment, des sels du cation trivalent H_3(1,2,4,5-BTA)$^{3+}$ ont aussi été isolés. Leur formation semble favorisée dans le H_2SO_4 dilué alors que les de H_4(1,2,4,5-BTA)$^{4+}$ ont été collectés dans l'acide concentré. L'isomère 1,2,3,4 de BTA semble plus propice à inclure des anions bisulfites que son homologue 1,2,3,4 dont seul un sulfate a été isolé. Celui-ci semble également cristalliser préférentiellement sous sa forme protonée aux positions 1 et 4, dont le dipôle et les interactions stéréoélectroniques sont minimisées par rapport aux positions alternatives. Les sels de l'isomère 1,2,3,4 de BTA sont par ailleurs bien plus solubles dans l'eau et les acides que ceux de l'isomère 1,2,4,5. Finalement, aucun sulfate dérivé de la quinonediimine **2** n'a pu être isolé jusqu'à maintenant. Celle-ci n'est pas totalement soluble dans H_2SO_4 concentré, mais est partiellement soluble dans l'acide dilué. Seuls des mélanges complexes de solides extirpés de solutions acides devenues mauve ont pu être isolés. Cette couleur est caractéristique de produits d'hydrolyse qui seront décrits au chapitre suivant.

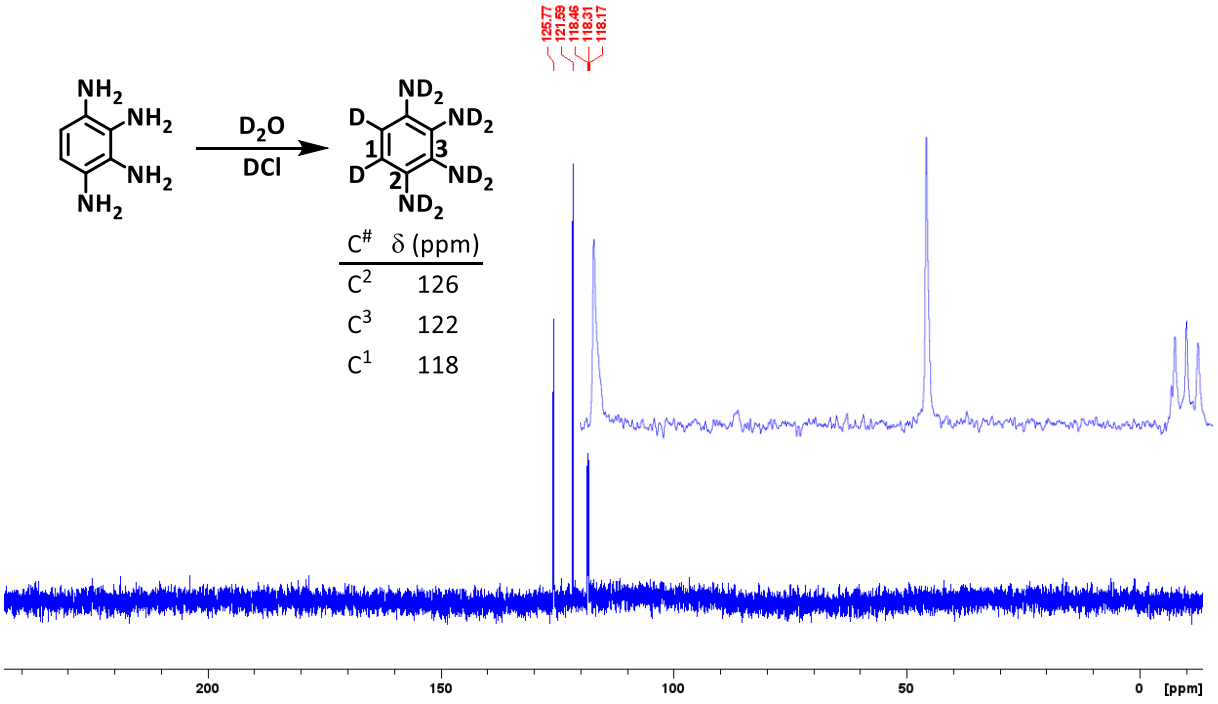
NH2
NH2
NH2
NH2
D2O
DCl
ND2
ND2
ND2
ND2
D
D
1
2
3
C# δ (ppm)
C2 126
C3 122
C1 118
125.77
121.59
118.46
118.31
118.17
200
150
100
50
0
[ppm]

A

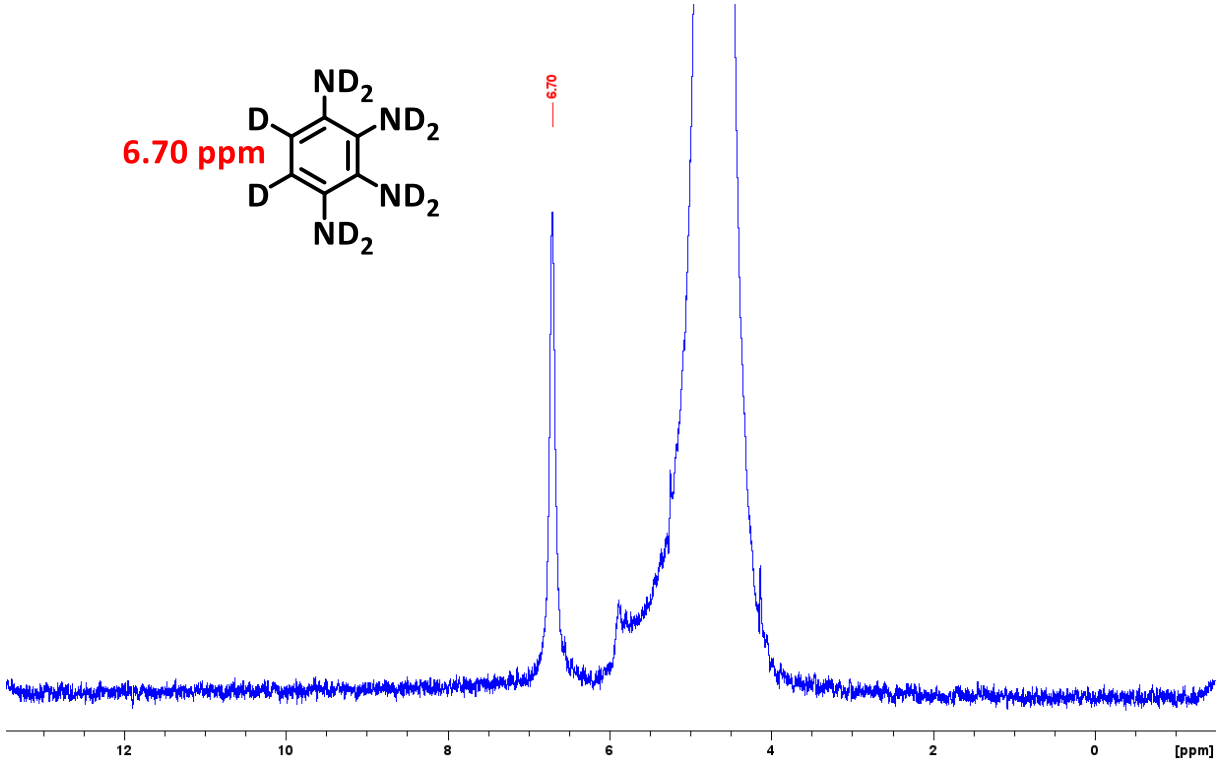

B

Figure 3.7 Spectres RMN (**A**) $^{13}C\{^{1}H\}$ et (**B**) ^{2}H de 1,2,3,4-BTA (**3**) dissous dans du D_2O contenant du DCl témoignant de l'échange des noyaux ^{1}H du cycle aromatique pour des ^{2}H.

L'ensemble des sels étudiés sont *N*-protonés à l'état solide. Pourtant, la *C*-protonation des isomères de BTA en solution est non-négligeable. En effet, l'ensemble des protons de l'isomère 1,2,3,4 sont échangés pour des deutériums en quelques heures dans le mélange D_2O/DCl utilisé pour sa caractérisation par RMN (Figure 3.7). Le chapitre suivant décrira d'ailleurs les produits d'hydrolyse émanant de la *C*-protonation de 1,2,4,5-BTA.

Chapitre 4. Étude expérimentale et théorique de l'hydrolyse de la benzène-1,2,4,5-tétramine et de composés analogues

4.1. Introduction

Les solutions aqueuses de l'isomère 1,2,4,5 de BTA sont sujettes à de frappants changements de couleurs dépendants de leur concentration, pH et exposition à l'air. À pH neutre, elles peuvent devenir mauves sur plusieurs jours ou en quelques minutes dans le HCl concentré chaud. Dans ces conditions, la recristallisation de 1,2,4,5-BTA · 4HCl génèrent des cristaux clairs de ce dernier accompagnés de cristaux sombre du chlorhydrate du 2,4-diaminorésorcinol (DAR ·2HCl, Figure 4.1). L'hydrolyse de 1,2,4,5-BTA en DAR n'avait étonnamment pas été décrite par Nietzki qui connaissait pourtant les deux composés (Chapitre 5). Seuls Siri et Braunstein ont observé un processus similaire lors de l'acétylation de 1,2,4,5-BTA · 4HCl dans des conditions différentes. Comme cette réaction d'hydrolyse peut nuire à la préparation solvothermale de matériaux rédox, nous l'avons étudiée pour mieux la comprendre. Cette étude nous permettait également de nous familiariser avec le motif DAR et sa forme oxydée, tous deux également étudiés pour l'optoélectronique et dont les structures cristallines n'avaient pas été résolues.

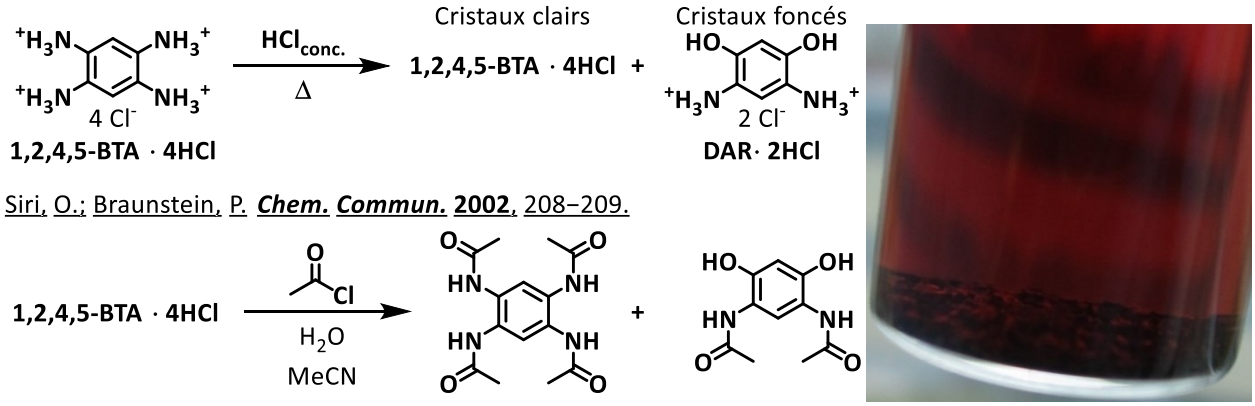

Figure 4.1 Produits de la recristallisation de 1,2,4,5-BTA · 4HCl dans le HCl concentré isolés de de la solution mère photographiée à droite et processus similaire rapporté dans la littérature.

Experimental and Computational Study of the Hydrolysis of Benzene-1,2,4,5-tetramine and Related Compounds

Johann O. E. Sosoe, Thierry Maris, Radu Iftimie, and James D. Wuest

Manuscript about to be submitted to *The Journal of Organic Chemistry*

JOES conceived the project, executed the experiments, and wrote the initial draft of the manuscript.

TM carried out all crystallographic studies.

RI carried out all computational calculations.

JDW helped identify experiments to perform and contributed to writing the final version of the manuscript.

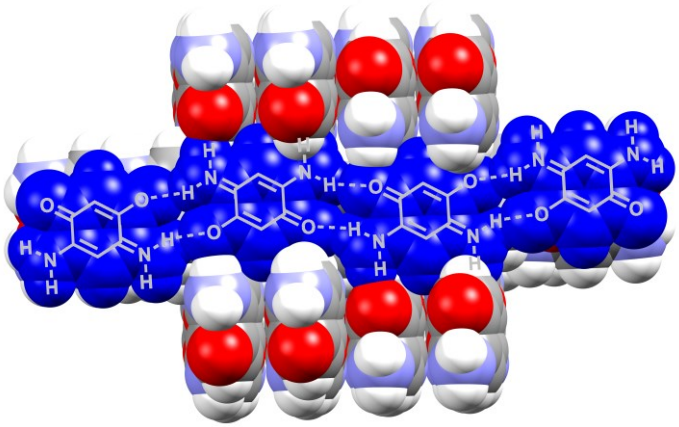

Abstract

In principle, aromatic compounds with multiple NH_2 groups and their oxidized forms can serve as components of redox-active organic materials. Benzene-1,2,4,5-tetramine (BTA) and analogues are promising compounds of this type. However, key aspects of their chemistry remain little studied, such as their susceptibility to hydrolysis (which will determine their suitability for use in aqueous media) and their preferred patterns of association (which will help control their behavior in the solid state). To provide new information, we have used experimental and computational methods to study the hydrolysis of BTA in aqueous acid. As part of this work, we have determined the structures of 4,6-diaminoresorcinol (as its dihydrochloride salt) and its unusual zwitterionic product of oxidation. Our results provide a better understanding of how arenes with multiple OH and NH_2 groups are arranged in the solid state and how complex arylamines can be used as components of redox-active organic materials.

Introduction

The development of new redox-active organic compounds promises to lead to innovations in many areas, such as the creation of batteries that are efficient, cheap, and composed primarily of abundant elements.[1–11] Redox pairs of special interest in this field include hydroquinones and quinones, which typically react rapidly and reversibly. However, a vast number of attractive alternatives can be created by replacing the C–OH and C=O bonds of complex hydroquinones and quinones with the C–NH_2 and C=NH bonds of arylamines and quinoneimines. In recent work,[12,13] we have begun to explore the potential of these compounds by studying the synthesis, structure, and reactions of benzene-1,2,4,5-tetramine (**1**; BTA), its oxidized form **2** (BTA-H_2), their salts, and related compounds.

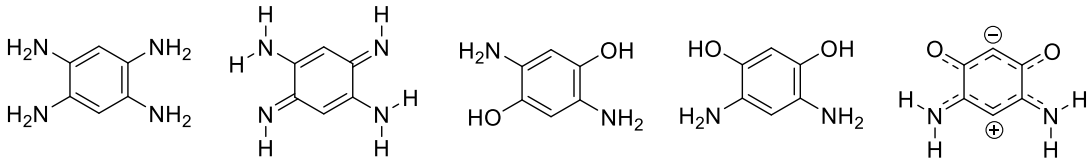

Making redox-active materials from hydroquinones and quinones is ecologically advantageous because many suitable precursors can be obtained from renewable sources. These benefits are shared by analogous amines and imines, which can often be synthesized from phenolic precursors by green methods of amination.[14–16] Moreover, aminoquinones and related hybrid structures with various combinations of C–OH, C=O, C–NH_2, and C=NH bonds are widely encountered in nature and play diverse roles,[17] as exemplified by the antitumor antibiotic mitomycin C, which is a diaminoquinone.[18]

Early motivation for studying arylamines came from William Perkin's discovery in the 1850s that useful synthetic dyes can be made from anilines. The discovery triggered a rapid expansion of the scope of industrial chemistry, drew attention to the special reactivity of anilines,

and identified arenes with multiple NH_2 groups as compounds of interest. Benzenetetramines proved to be elusive, however, and methods for making them were not reported until decades later, when Rudolf Nietzki and coworkers described the synthesis of BTA (**1**) and its isomers in the form of salts.[19-21] Although Nietzki is unfamiliar to many modern organic chemists, he has had an enduring impact on the field,[22–24] and compounds first made in his research group are widely used today. In particular, BTA (**1**) and its derivatives are at the center of an impressive range of projects in which the compounds are employed as precursors of redox-active materials,[25–31] ligands in coordination chemistry,[32–42] components of metal-organic frameworks (MOFs) and covalent organic frameworks (COFs),[43–50] monomers for producing polymers,[51–56] components of switches and sensors,[57,58] precursors for synthesizing diverse heterocyclic compounds,[59–62] and enzyme inhibitors for use in treating cancer.[63]

Despite the importance of BTA (**1**) and analogues, few studies have examined basic properties that will help define the best ways to use the compounds as components of advanced redox-active materials. For example, little is known about the susceptibility of the compounds to hydrolysis, which will determine their suitability for use in aqueous media. Similarly, their preferred patterns of association in the solid state have not been clearly identified, so attempts to design materials with properties that depend on proper organization of the molecular components are unlikely to be successful. Poor understanding of the fundamental behavior of BTA (**1**) and related compounds will delay their exploitation in areas where they promise to be useful. To provide new information, we have used experimental and computational methods to study the hydrolysis of BTA (**1**) in aqueous acid. The primary products of hydrolysis are salts of 2,5-diaminohydroquinone (**3**; DAHQ) and 4,6-diaminoresorcinol (**4**; DAR), which can be converted by oxidation into the unusual zwitterion **5** (DAR-H_2). Crystallographic studies of compound **4** (as its dihydrochloride salt), zwitterion **5**, and its hydrochloride salt have helped identify the preferred solid-state arrangements of arenes with multiple OH and NH_2 groups.

Results and Discussion

Hydrolysis of Tetrahydrochloride Salt BTA (1) • 4HCl in Aqueous Acid.

Tetrahydrochloride salt BTA (**1**) • 4HCl was made by a modified method based on a route initially devised by Nietzki and Schedler.[12,19] Hydrolysis by heating the compound in 1.0 M aqueous HCl at 100 °C for 3 h yielded an approximately 9:1 mixture of dihydrochloride salts DAHQ (**3**) • 2HCl and DAR (**4**) • 2HCl (Scheme 1). The trihydrochloride salt of 2,4,5-triaminophenol (**6**; TAP) is presumably an intermediate in this process. Compounds **3** and **4** are susceptible to oxidation by O_2 and were therefore not separated and isolated directly. Instead, the mixture of products was converted into the corresponding hexaacetylated derivatives **7** and **8** (Scheme 1), which were separated by chromatography.

Scheme 1

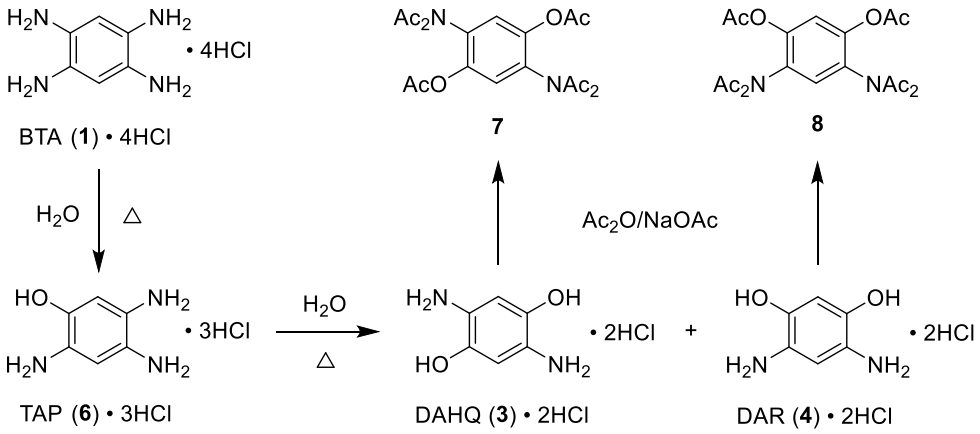

Aqueous solutions of DAR (**4**) • 2HCl are colorless but turn purple in contact with air as zwitterion DAR-H_2 (**5**) or its salts are formed by oxidation. The identity of DAR-H_2 (**5**) was debated at length in the early literature,[64–66] and the matter was not resolved until the compound and *N*,*N*'-disubstituted derivatives were characterized unambiguously by Braunstein, Siri, and coworkers.[67-70] Such oxidations and the hydrolyses in Scheme 1 illustrate the rich chemistry of aromatic compounds with multiple amino groups, as well as the close connection between arylamines and phenolic analogues.

The hydrolysis of simple anilinium salts in acidic media to give phenols (eq 1) is thermodynamically favorable, primarily because it converts the salt of a weak base (aniline) into the salt of a stronger base (NH_3). However, the reaction is not normally efficient, and we were surprised to observe that salt BTA (**1**) • 4HCl undergoes hydrolysis under relatively mild conditions. The related conversion of benzene-1,3-diamine into resorcinol requires heating in strong aqueous acid at high temperatures,[71] and the hydrolysis of benzene-1,3,5-triamine to give phloroglucinol is also slow.[72]

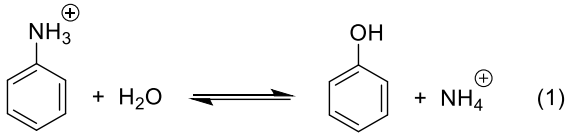

Putative intermediate TAP (**6**) • 3HCl can plausibly arise from salt BTA (**1**) • 4HCl in at least two ways: (1) conversion of *N*-tetraprotonated form **9** of BTA (**1**) into *C*-protonated tautomer **10** and subsequent hydrolysis or (2) conversion of *N*-triprotonated form **11** of BTA (**1**) into *C*-protonated tautomer **12** and subsequent hydrolysis (Scheme 2). *N*-Tetraprotonated form **9** is observed in crystals of salt BTA (**1**) • 4HCl[12] and is presumably also an important species in aqueous solution, along with *N*-triprotonated form **11**. *N*-Protonation of arenes with multiple NH_2 substituents is normally favored, although *C*-protonated isomers have been characterized in certain cases.[73,74] Standard iminium hydrolysis is expected to convert *C*-protonated tautomers **10** or **12** into trication TAP (**6**) • $3H^+$, which can then undergo a second transformation of the same type to give DAHQ (**3**) • 2HCl and DAR (**4**) • 2HCl. Further hydrolysis is expected to be slow, as illustrated by the behavior of benzene-1,3-diamine. The relatively high susceptibility of tetracation **9** or trication **11** to hydrolysis can be attributed to special stabilization of *C*-protonated tautomers **10** or **12** by resonance involving unprotonated NH_2 groups.

Scheme 2

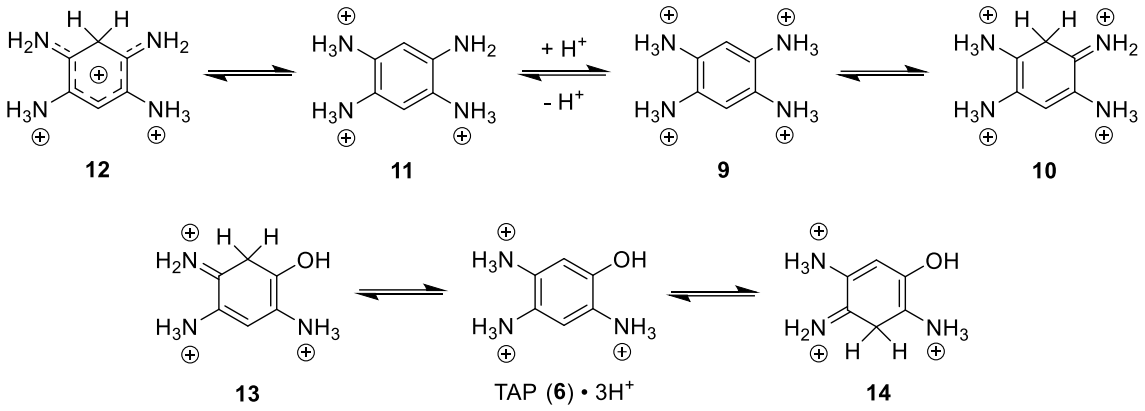

For further insight, we assessed the relative energies of species in Scheme 2 and related structures by using DFT calculations at the RωB97M(2)[75]/def2-QZVPPD[76-78]//RωB97X-D3[79–82]/6-311+G(2df,2p) level in a medium with the dielectric constant of H_2O, as evaluated by the conductor-like PCM approach (C-PCM).[83] Additional details are provided in the section on Computational and Experimental Methods, and the results of the calculations are summarized in Table IV - 1. In various entries in Table IV - 1, the species in equilibrium can in principle exist as alternative tautomers; however, only the forms determined to have the lowest free energy are illustrated, although the energies of all other tautomers were calculated.

Tableau IV - 1 Relative Electronic Potential Energies (ΔE) and Values of $\Delta G°$ for Reactions Related to Scheme 2 at 298 K in a Medium with the Dielectric Constant of H_2O, as Estimated by DFT Calculations at the RωB97M(2)/def2-QZVPPD//RωB97X-D3/6-311+G(2df,2p) Level, with a C-PCM Approach for Assessing Solvent Effects

reaction		ΔE (kcal mol^{-1})	$\Delta G°$ (kcal mol^{-1})
1	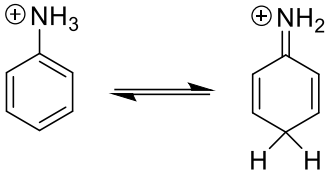	17.3	15.6
2	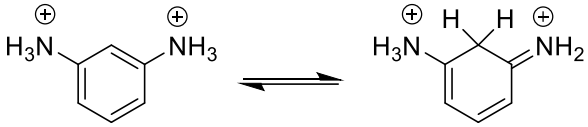	18.6	17.1
3	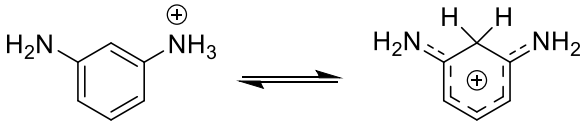	7.8	5.5
4	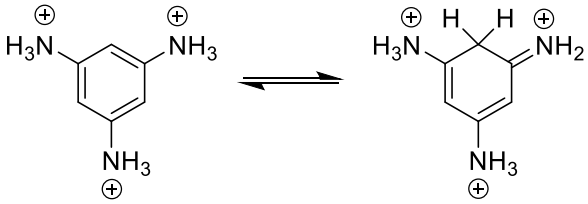	22.1	20.7
5	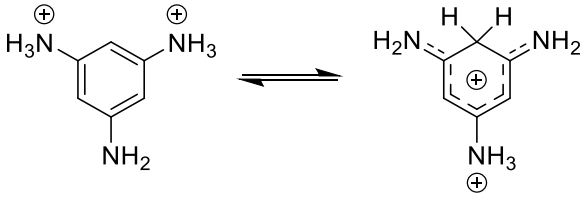	9.1	6.9
6	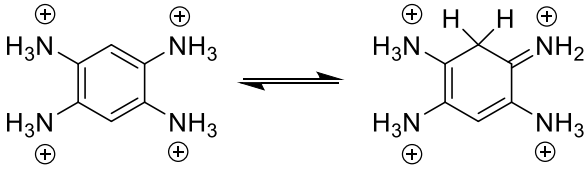 **9** **10**	23.8	21.6

7	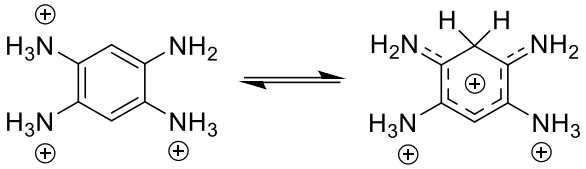 **11** **12**	8.8	6.4
8	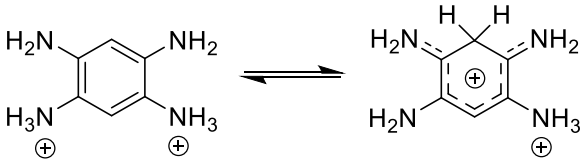	14.5	12.1
9		14.6	11.4
10	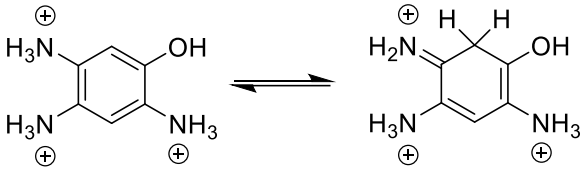 TAP (**6**) • $3H^+$ **13**	16.0	13.3
11	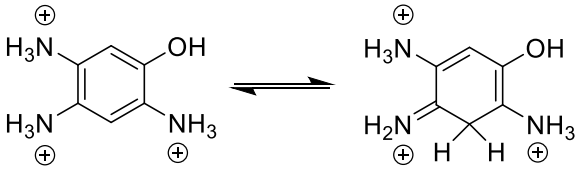 TAP (**6**) • $3H^+$ **14**	23.3	20.5
12	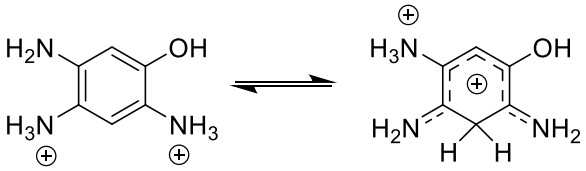 TAP (**6**) • $2H^+$	15.0	12.4
13	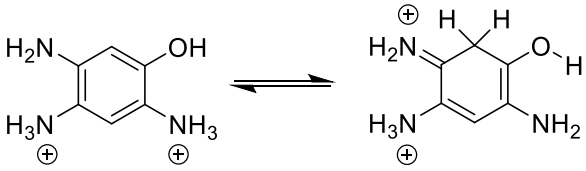 TAP (**6**) • $2H^+$	21.6	20.0

The data in Table IV - 1 are consistent with the observation that hydrolysis becomes faster as the degree of amination increases, as well as with the hypothesis that forming *C*-protonated tautomers is an essential step in the mechanism of hydrolysis. ΔG for converting the *N*-protonated form of anilinium into the most stable *C*-protomer is calculated to be highly unfavorable (15.6 kcal mol^{-1}; entry 1). The identity of the preferred sites of kinetic and thermodynamic protonation of aniline under various conditions has been debated extensively,[84–88] but our results and other studies indicate that the *N*-protomer is strongly favored in solution. Similarly, *N*-to-*C* prototropy in diprotonated benzene-1,3-diamine is also predicted to have a high value of ΔG (17.1 kcal mol^{-1}; entry 2). In contrast, transforming *N*-monoprotonated benzene-1,3-diamine into the most stable *C*-protomer is much less costly (5.5 kcal mol^{-1}; entry 3). However, the values of pK_{a1} and pK_{a2} for the corresponding dication are 2.3 and 5.0, respectively,[89] so the concentration of monoprotonated form in excess aqueous HCl is low.

As the degree of amination increases, the fully protonated form becomes more acidic, and a point is reached when the concentration of incompletely protonated forms becomes kinetically significant, and the corresponding *C*-protomers are stabilized by the presence of multiple NH_2 groups. As illustrated by entries 4 and 5, the hydrolysis of benzene-1,3,5-triamine in aqueous acid presumably occurs via the dication, and entries 6−9 are consistent with the hypothesis that the hydrolysis of BTA (**1**) requires the trication. Entries 10−13 suggest that the hydrolysis of protonated TAP (**6**) may involve either the corresponding dication or trication and can thereby give salts of both DAHQ (**3**) and DAR (**4**), as observed. These products are formed when O_2 is excluded, so hydrolysis does not appear to involve oxidized intermediates such as salts of BTA-H_2 (**2**).

Structures of Dihydrochloride Salt DAR (4)•2HCl, DAR-H_2 (5), and Hydrochloride Salt DAR-H_2 (5)•HCl•H_2O.

Crystallization of dihydrochloride salt DAR (**3**) • 2HCl from H_2O led to the concomitant formation of $P2_1/n$ and $P\bar{1}$ polymorphs. Selected crystallographic data are summarized in Table IV - 2, and representations of the structures are provided in Figures 4.2–.5. Previous studies of tetrahydrochloride salt BTA (**1**) • 4HCl, dihydrochloride salt BTA-H_2 (**2**) • 2HCl, and related compounds have suggested that chloride salts formed by arenes with multiple NH_2 groups and the corresponding quinonediimines will tend to crystallize to form structures with multiple ionic N–$H^+\cdots Cl^-$ hydrogen bonds, up to a limit of four of these interactions per chloride ion.[12] Each dication DAR (**4**) • $2H^+$ can in principle act as a donor in forming a total of six ionic N–$H^+\cdots Cl^-$ hydrogen bonds and two O–H$\cdots Cl^-$ hydrogen bonds, and the two associated chloride ions have the potential to serve as acceptors in forming a total of eight hydrogen bonds. As a result, the numbers of donors and acceptors are matched, and the full potential of the components to form hydrogen bonds can be attained.

Tableau IV - 2 Crystallographic Data for Salt DAR (**4**) • 2HCl, DAR-H_2 (**5**), and DAR-H_2 (**5**) • HCl • H_2O

compound	**DAR (4) • 2 HCl**	**DAR (4) • 2 HCl**	**DAR-H_2 (5)**	**DAR-H_2 (5) • HCl • H_2O**
CCDC[a] number	2287338	2287337	2287339	2287340
description	colorless plates	colorless plates	red plates	red blocks
crystal syst	monoclinic	triclinic	orthorhombic	triclinic
space group	$P2_1/n$	$P\bar{1}$	*Pbcn*	$P\bar{1}$
a (Å)	8.1398(2)	6.5434(7)	5.3190(3)	7.0626(2)
b (Å)	8.8075(2)	7.8257(8)	10.9737(6)	7.8209(2)
c (Å)	12.8609(3)	8.8710(9)	10.1606(6)	8.7484(2)
α (deg)	90	77.323(5)	90	107.601(1)
β (deg)	104.620(1)	77.963(5)	90	105.293(1)
γ (deg)	90	75.866(6)	90	109.088(1)

V (Å^3)	892.16(4)	423.96(8)	593.07(6)	394.445(18)
Z	4	2	4	2
Z'	1	1	0.5	1
ρ_{calc} (g cm^{-3})	1.586	1.669	1.547	1.605
T (K)	150	150	150	150
R_1, $I > 2\sigma(I)$	0.0260	0.0541	0.0358	0.0273
wR_2, $I > 2\sigma(I)$	0.0691	0.1630	0.0855	0.0824
GoF	1.104	1.123	1.030	1.031

[a]Cambridge Crystallographic Data Centre

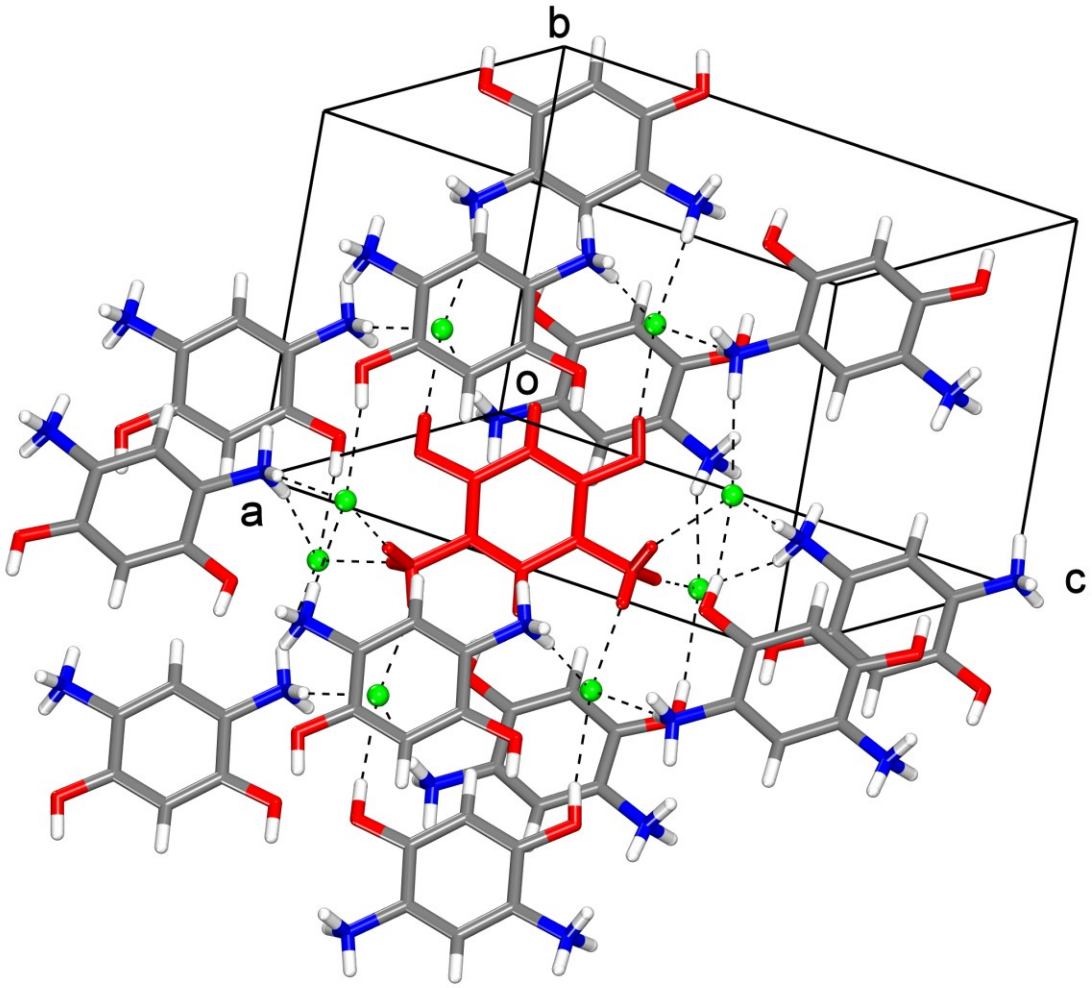

Figure 4.2 Representation of the structure of $P2_1/n$ crystals of dihydrochloride salt DAR (**4**) • 2HCl grown from H_2O, showing a central dication (red) and the twelve neighbors linked by eight bridging chloride ions. $N–H^+\cdots Cl^-$ and $O–H\cdots Cl^-$ hydrogen bonds are indicated by broken lines. Unless stated otherwise, atoms of carbon appear in gray, hydrogen in white, nitrogen in blue, and chlorine in green.

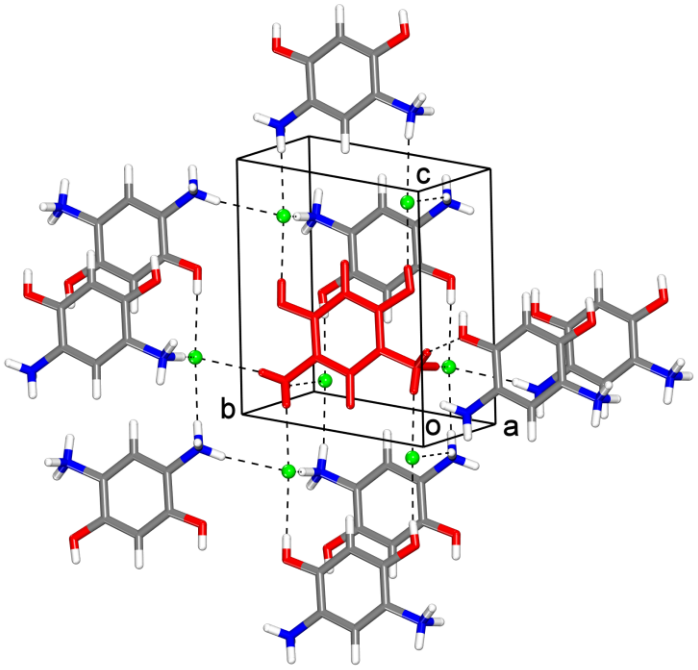

Figure 4.3 Representation of the structure of $P\bar{1}$ crystals of dihydrochloride salt DAR (**4**) • 2HCl grown from H_2O, showing a central dication (red), eight neighbors linked by seven bridging chloride ions, and a single neighbor connected directly by an N–H^+···O hydrogen bond. Hydrogen bonds are indicated by broken lines, and atoms appear in standard colors unless stated otherwise.

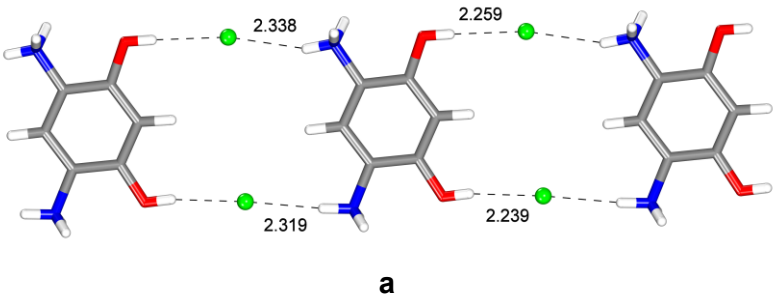

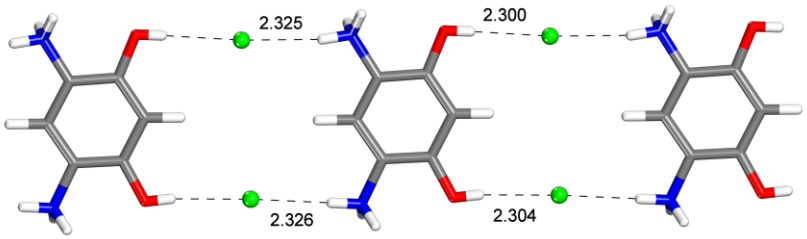

b

Figure 4.4 Representations of chloride-bridged tapes observed in the structures of both polymorphs of dihydrochloride salt DAR (**4**) • 2HCl grown from H_2O. (a) $P2_1/n$ polymorph. (b) $P\bar{1}$ polymorph. In both views, $N–H^+\cdots Cl^-$ and $O–H\cdots Cl^-$ hydrogen bonds are indicated by broken lines, values of $d_{H\cdots Cl}$ are given in Å, and atoms appear in standard colors.

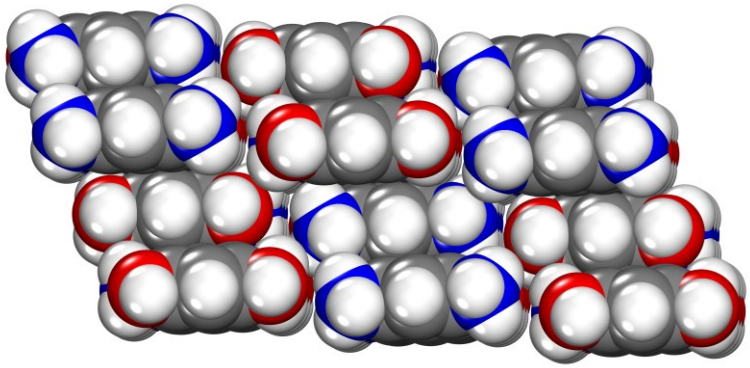

a

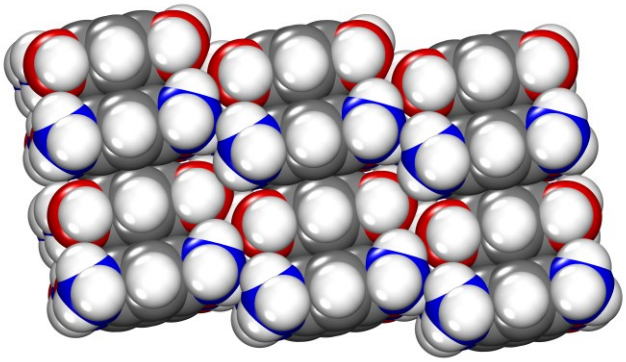

b

Figure 4.5 Space-filling representations of the structures of the two polymorphs of dihydrochloride salt DAR (**4**) • 2HCl grown from H_2O, as viewed along the characteristic chloride-bridged tapes. (a) $P2_1/n$ polymorph. (b) $P\bar{1}$ polymorph. In both views, chloride ions are omitted, and other atoms appear in standard colors.

The observed $P2_1/n$ structure is consistent with these expectations (Figure 4.2). Each dication DAR (**4**) • $2H^+$ interacts with eight surrounding chloride ions to form a total of eight hydrogen bonds. Two are O–H···Cl^- hydrogen bonds, with average values of $d_{H\cdots Cl}$ and $d_{O\cdots Cl}$ equal to 2.249 and 3.054 Å, respectively, and six are ionic N–H^+···Cl^- hydrogen bonds, with values of $d_{H\cdots Cl}$ in the range 2.196–2.422 Å (corresponding to values of $d_{N\cdots Cl}$ in the range 3.119–3.243 Å). Each dication is thereby linked to a total of twelve neighbors by bridging chloride ions. Intramolecular distances involving the adjacent NH_3^+ and OH groups have values of $d_{H\cdots O}$ lying in the range 2.497–2.710 Å and are therefore longer than distances in the primary external hydrogen bonds to chloride. Other geometric parameters related to the NH_3^+ groups, including the average length of C–N bonds (1.456 Å), are similar to those found in the hydrochloride salts of other arylamines.[90–96]

The $P\bar{1}$ polymorph has a related structure (Figure 4.3), and each dication DAR (**4**) • $2H^+$ again engages in a total of eight hydrogen bonds. Two are O–H···Cl^- hydrogen bonds (with average values of $d_{H\cdots Cl}$ and $d_{O\cdots Cl}$ equal to 2.302 and 3.046 Å, respectively), and five are ionic N–H^+···Cl^- hydrogen bonds (with values of $d_{H\cdots Cl}$ in the range 2.325–2.456 Å, corresponding to

values of $d_{N\cdots Cl}$ in the range 3.163–3.210 Å). In this way, each dication is linked to a total of eight neighbors by bridging chloride ions, and a ninth neighbor is joined directly by an $N–H^+\cdots O$ hydrogen bond. Both polymorphs incorporate geometrically similar tapes in which dications are linked end-to-end by $N–H^+\cdots Cl^-$ and $O–H\cdots Cl^-$ hydrogen bonds (Figure 4.4). The ultimate structures consist of stacks of these tapes (Figure 4.5), and the observed differences in hydrogen bonding arise from how neighboring tapes are positioned.

Assignment of a zwitterionic structure to oxidized product DAR-H_2 (**5**) in the solid state is based on a previous structural analysis of the crystalline monohydrate.[68] We have found that an anhydrous *Pbcn* form can be obtained as red plates by crystallizing compound **5** from saturated $NaHCO_3$. Table IV-2 includes selected crystallographic data, and Figure 4.6 provides representations of the structure, which is again zwitterionic. The compound belongs to the family of methine dyes and incorporates a cationic cyanine subunit coupled with the anionic enolate of a β-diketone. The C–N and C–C bond lengths within the cyanine subunit (1.314 and 1.384 Å, respectively) show symmetric delocalization and closely resemble those found in the hydrate (average values of 1.314 and 1.388 Å, respectively). Similarly, the C–O and C–C bond lengths within the enolate subunit in the anhydrous form (1.257 and 1.391 Å, respectively) are close to those observed in the hydrate (average values of 1.255 and 1.396 Å, respectively). The two C–C bonds connecting the cyanine and enolate subunits in the anhydrous form are long (1.526 Å), as they are in the hydrate (average value of 1.517 Å). In both structures, all atoms lie close to the average molecular plane.

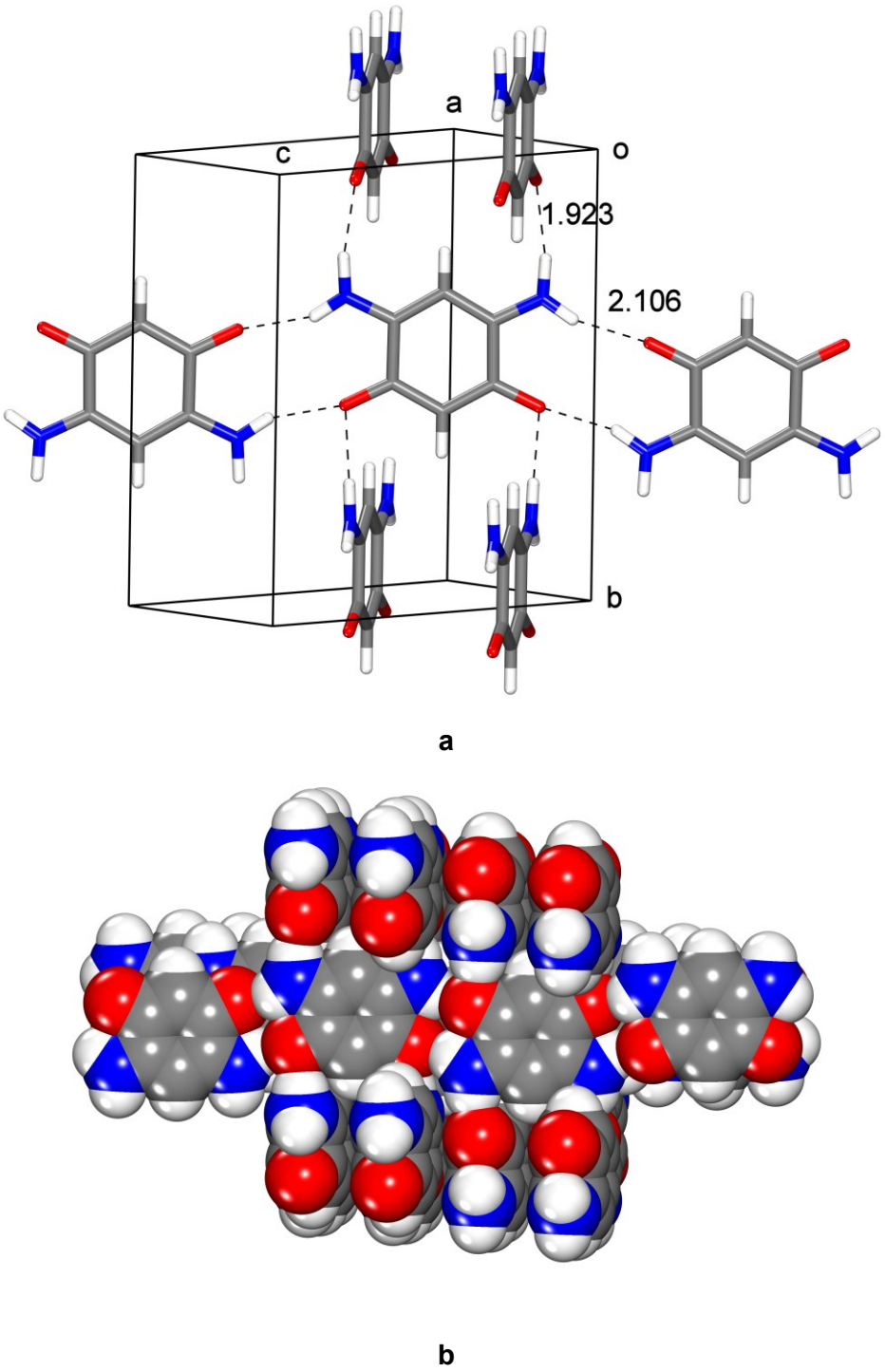

Figure 4.6 Representations of the structure of *Pbcn* crystals of anhydrous zwitterion DAR-H_2 (**5**) grown from H_2O. (a) View showing how ionic N–$H^+\cdots O^-$ hydrogen bonds join the zwitterions to form tapes, which are connected by similar interactions to other tapes lying at an angle of

approximately 77°. (b) Related space-filling representation of the interconnected tapes. Hydrogen bonds are indicated by broken lines in Figure 4.6.a, with values of $d_{H\cdots O}$ given in Å. Atoms appear in standard colors in both images.

In principle, the two anionic oxygen atoms of zwitterion DAR-H_2 (**5**) can accept a total of four hydrogen bonds, and the two cationic NH_2 groups can serve as donors of four hydrogen bonds. This matched capacity gives rise to an elegant structure that is fully hydrogen-bonded (Figure 4.6). Molecules of the zwitterion are linked end-to-end to form tapes held together by ionic N–$H^+\cdots O^-$ hydrogen bonds with $d_{H\cdots O}$ = 2.106 Å ($d_{N\cdots O}$ = 2.908 Å). The corresponding intramolecular N–$H^+\cdots O^-$ distances are significantly longer ($d_{H\cdots O}$ = 2.278 Å). Each tape is connected on both sides by additional ionic N–$H^+\cdots O^-$ hydrogen bonds to other tapes, which lie at an angle of approximately 77°. Comparison of the structures of the anhydrous and hydrated forms of zwitterion DAR-H_2 (**5**) reveals a close underlying relationship. In the hydrate, molecules are linked by similar pairs of ionic N–$H^+\cdots O^-$ hydrogen bonds to form dimers; however, extension of the dimers to produce oligomeric tapes, as observed in the anhydrous form, is disrupted by hydrogen bonding to molecules of water.

Red crystals of hydrated monohydrochloride salt DAR-H_2 (**5**) • HCl • H_2O precipitated after DAR (**4**) • 2HCl was added to $FeCl_3$ diluted in 1 M HCl. Selected crystallographic data are provided in Table IV-2, and a view of the structure appears in Figure 4.7. Cation DAR-H_2 (**5**) • H^+ can be represented by structure **15**, and the cationic cyanine subunit is weakly linked to the enol form of a β-diketone by long C–C bonds (average value of d_{C-C} = 1.509 Å). Within the cyanine subunit, d_{C-N} (1.318 and 1.324 Å) and d_{C-C} (1.382 and 1.396 Å) show nearly symmetric delocalization and closely resemble the values observed in the structure of zwitterion DAR-H_2 (**5**) itself. Clear alternation of single and double C–C bonds is observed in the enol subunit, and the values of d_{C-C} are 1.352 and 1.439 Å.

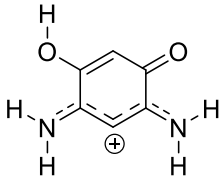

15

(DAR-H_2 • H^+)

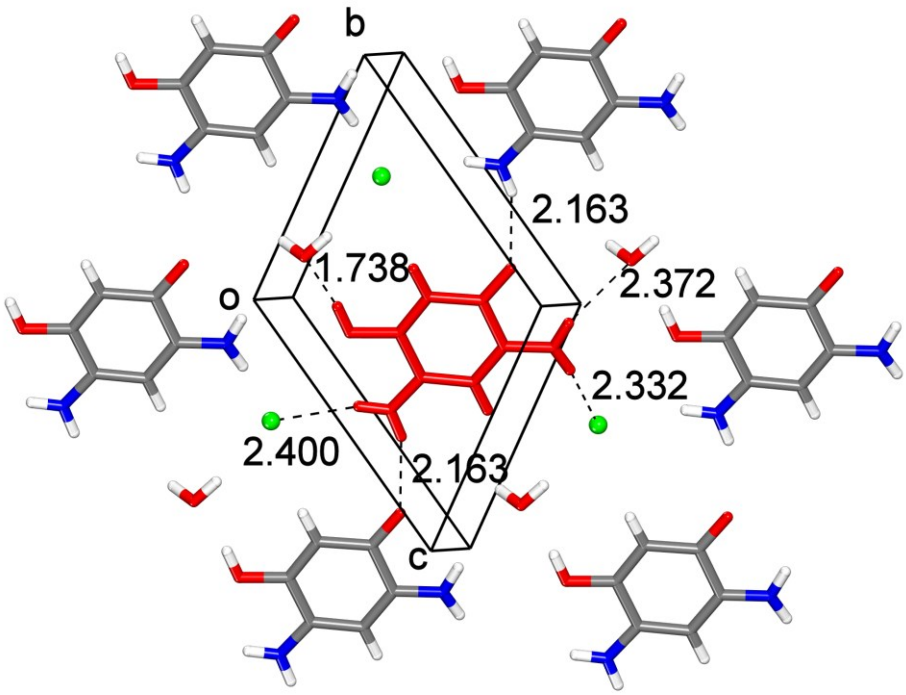

Figure 4.7 Representation of the structure of $P\bar{1}$ crystals of hydrated monochloride salt DAR-H_2 (**5**) • HCl • H_2O grown from 1 M HCl, showing part of a sheet in which a central cation (red) is surrounded by six neighbors. Two are linked directly by N–H^+···O hydrogen bonds, and the others are bridged by chloride ions and molecules of H_2O. Hydrogen bonds involving the central cation are indicated by broken lines, with values of $d_{H\cdots O}$ and $d_{H\cdots Cl}$ given in Å. Atoms appear in standard colors unless stated otherwise.

All atoms in cation DAR-H_2 (**5**) • H^+ are nearly coplanar, and two intramolecular N–H^+···O hydrogen bonds are present ($d_{H\cdots O}$ = 2.246 and 2.252 Å). The resulting structure is

composed of hydrogen-bonded sheets in which each cation is surrounded by six neighbors (Figure 4.7). Two are linked directly by N–H^+···O hydrogen bonds, and the others are bridged by chloride ions and molecules of H_2O. Each chloride ion accepts a total of four primary hydrogen bonds, two contributed by molecules of H_2O ($d_{O\cdots Cl}$ = 3.054 and 3.145 Å) and two by the NH_2 groups of cation DAR-H_2 (**5**) • H^+($d_{N\cdots Cl}$ = 3.179 and 3.208 Å). A three-dimensional network is generated by inter-sheet hydrogen bonds involving molecules of H_2O.

Conclusions

Aromatic compounds with multiple NH_2 groups and the corresponding quinonediimines are potential alternatives to hydroquinones and quinones as the components of useful redox-active organic materials. BTA (**1**) and BTA-H_2 (**2**) illustrate a promising redox pair of this type, and the compounds have been shown to be useful in many areas of chemistry. Unfortunately, many aspects of their chemistry remain poorly understood, such as their susceptibility to hydrolysis (which will determine their suitability for use in aqueous media) and their preferred patterns of association (which will help control their behavior in the solid state). To provide new information, we have used experimental and computational methods to study the hydrolysis of tetrahydrochloride salt BTA (**1**) • 4HCl and related compounds. In addition, crystallographic studies of dihydrochloride salt DAR (**4**) • 2HCl, its unusual zwitterionic product of oxidation DAR-H_2 (**5**), and a hydrochloride salt of the zwitterion have helped identify the preferred solid-state arrangements of arenes with multiple OH and NH_2 groups. Our work is expected to accelerate exploitation of these compounds in areas of materials science where desirable properties can only be attained by properly controlling the organization of their molecular components.

Computational and Experimental Methods

Methodology Used in Calculations Related to the Hydrolysis of Tetrahydrochloride Salt BTA (1) • 4HCl. DFT calculations were performed using Spartan '20 Version 1.1.4 software (Wavefunction, Inc.), with Q-Chem 5.1 as the computational engine.[97] To guide selection of the methods employed, we used the conceptual flowchart of decision-making in chemical calculations recently proposed by Bursch and coauthors.[98] Initial structures were generated using the graphical interface of Spartan'20, and molecular flexibility was considered by performing all relevant rotations around C–N and C–O single bonds. Conformations were initially retained if their energy was within 15 kcal mol^{-1} of the lowest-energy conformer, as calculated using the empirical MMFF force field implemented in Spartan'20.[99]

Geometry optimization was carried out in two steps to achieve a satisfactory balance of computational cost and accuracy. Geometries were first optimized using the ωB97X-D3 functional[79–82] with a relatively small 6-31+G(d) basis set, and only configurations within 10 kcal mol^{-1} of the lowest-energy conformer were retained. Configurations were then optimized using the same functional, but with the larger 6-311+G(2df,2p) basis set, and all configurations within 5 kcal mol^{-1} of the global minimum were retained. Vibrational frequencies were subsequently computed by using the relatively large DFT integration grid (100,434) corresponding to the keyword VERYBIGGRID in Spartan'20. Finally, single-point energy calculations were carried out using the ωB97M(2) double-hybrid functional[75] and the def2-QZVPPD basis set.[76-78] This combination has been demonstrated to provide some of the most accurate results for conformers, reaction energies, and barriers.[97,98]

Calculations were carried out in a medium with the dielectric constant of H_2O, using the conductor-like PCM approach (C-PCM),[83] as implemented in Q-Chem 5.1. C-PCM is a purely electrostatic model and does not consider contributions from cavity creation and van der Waals interactions between solute and solvent; however, these contributions should play a minor role, because solvent-accessible areas are likely to be similar for all participants in the reactions that are being analyzed.

Several *C*-protonated structures in Table IV - 1 displayed vibrational frequencies lower than 50 cm^{-1}. Such low frequencies are sometimes sensitive to the DFT integration grid and can lead to significant overestimation of entropies calculated by the commonly used rigid-rotor harmonic-oscillator approach.[100,101] We found that the numerical values of these low vibrational frequencies changed very little when we used the large DFT integration grid (250,947) in Spartan'20 (keyword HUGEGRID). Nevertheless, to correct for overestimating the amount of phase-space available to very low frequencies and wide-amplitude motions, we modified the calculation of entropy as suggested by Truhlar and collaborators.[102,103] This involved repeating entropy calculations with all vibrational frequencies lower than 50 cm^{-1} raised to 50 cm^{-1} (keyword CLAMPTHERMO=1.2 in Spartan'20).

Experimental Methodology. All starting materials were purchased from commercial suppliers and used without further purification.

Hydrolysis of Tetrahydrochloride Salt BTA (1) • 4HCl. In a 25 mL tricol equipped with a condenser, argon was generously sparged into 1 M HCl (1.01 g/mL, 15 mL) for 30 min using a glass gas entry. After BTA · 4HCl (195 mg, 0.687 mmol) was added in one portion, the solution was purged under inert air for additional 5 min at 20 °C before being heated 3 h at 150 °C. The initially yellowish solution would turn greenish overtime. Once cooled to room temperature, the reaction mixture was poured on saturated HCl cooled in an ice bath. The so formed precipitate was collected by filtration to yield a colorless powder (131 mg). This crude mixture of products was then treated with acetic anhydride and sodium acetate to allow product separation by flash chromatography under the form of both O- and N-acetylated species.

Synthesis and Crystallization of Dihydrochloride Salt DAR (4) • 2HCl. Single crystals of **4** • 2HCl suitable for SCXRD were obtained by allow hot solutions of **1** • 4HCl dissolved in concentrated HCl to slowly cool to 20 °C.

Synthesis and Crystallization of Zwitterion DAR-H_2 (5).[66] Single crystals of **5** suitable for SCXRD were obtained by letting a solution of **4** • 2HCl in saturated $NaHCO_3$ unstirred for 24 h. As Typke also noted, zwitterion **5** was best obtained by dissolving **4** • 2HCl (500 mg, 2.35 mmol) into a solution of 2 mL of aqueous NH_3 (0.81 g/mL) diluted in H_2O (10 mL). Ambient air was allowed on diffuse into the thoroughly stirred solution for 3 h. Desired product **5** was then collected by filtration and dried to yield a deep purple powder (291 mg, 99%). Spectroscopic data were in accordance with reported results.[67]

Crystallization of Hydrochloride Salt DAR-H_2 (5) • HCl • H_2O. Single crystals of **5**• HCl • H_2O were obtained by letting a solution of **4** • 2HCl (500 mg) in 1 M HCl (40 mL) and saturated aqueous FeCl (20 mL) unstirred for 24 h at 20 °C in contact with air.

Supporting Information Available: Additional crystallographic details (including thermal atomic displacement parameter plots), supplementary computational information, and spectroscopic data. This material is available free of charge via the Internet at http://pubs.acs.org.

Accession Codes: CCDC 2287337–2287340 contain the supplementary crystallographic data for this paper. These data can be obtained free of charge via www.ccdc.cam.ac.uk/data_request/cif, or by emailing data_request@ccdc.cam.ac.uk, or by contacting The Cambridge Crystallographic Data Centre, 12 Union Road, Cambridge CB2 1EZ, UK; fax: +44 1223 336033.

Notes. The authors have no competing financial interests to declare.

Acknowledgments. Financial support from the Natural Sciences and Engineering Research Council (NSERC) of Canada (RGPIN-2019-05469) is gratefully acknowledged. In addition, J. D. W. thanks the Canada Foundation for Innovation (Project 30910) and the Canada Research Chairs Program for their generous support. J. O. E. S. is grateful to the Université de Montréal for a graduate fellowship. The authors also thank the *Centre régional de spectrométrie de masse* for providing mass spectra, and they are grateful for additional support from the *Centre en chimie verte et catalyse* and the *Centre québécois sur les matériaux fonctionnels*, two strategic clusters funded by the Fonds de recherche du Québec – Nature et technologies (FRQNT).

References

1. Kim, J.; Kim, Y.; Yoo, J.; Kwon, G.; Ko, Y.; Kang, K. Organic Batteries for a Greener Rechargeable World. *Nat. Rev. Mater.* **2023**, *8*, 55–70.
2. Chen, Y.; Dai, H.; Fan, K.; Zhang, G.; Tang, M.; Gao, Y.; Zhang, C.; Guan, L.; Mao, M.; Liu, H.; Zhai, T.; Wang, C. A Recyclable and Scalable High-Capacity Organic Battery. *Angew. Chem. Int. Ed.* **2023**, e202302539.
3. Chen, X.; Yin, X.; Aslam, J.; Sun, W.; Wang, Y. Recent Progress and Design Principles for Rechargeable Lithium Organic Batteries. *Electrochem. Energy Rev.* **2022**, *5*, 12.
4. Kato, K.; Puthirath, A. B.; Mojibpour, A.; Miroshnikov, M.; Satapathy, S.; Thangavel, N. K.; Mahankali, K.; Dong, L.; Arava, L. M. R.; John, G.; Bharadwaj, P.; Babu, G.; Ajayan, P. M. Light-Assisted Rechargeable Lithium Batteries: Organic Molecules for Simultaneous Energy Harvesting and Storage. *Nano Lett.* **2021**, *21*, 907–913.
5. Esser, B.; Dolhem, F.; Becuwe, M.; Poizot, P.; Vlad, A.; Brandell, D. A Perspective on Organic Electrode Materials and Technologies for Next Generation Batteries. *J. Power Sources* **2021**, *482*, 228814.
6. Goujon, N.; Casado, N.; Patil, N.; Marcilla, R.; Mecerreyes, D. Organic Batteries Based on Just Redox Polymers. *Prog. Polym. Sci.* **2021**, *122*, 101449.
7. Lakraychi, A. E.; Dolhem, F.; Vlad, A.; Becuwe, M. Organic Negative Electrode Materials for Metal-Ion and Molecular-Ion Batteries: Progress and Challenges from a Molecular Engineering Perspective. *Adv. Energy Mater.* **2021**, *11*, 2101562.
8. Shea, J. J.; Luo, C. Organic Electrode Materials for Metal Ion Batteries. *ACS Appl. Mater. Interfaces* **2020**, 12, 5361–5380.
9. Poizot, P.; Gaubicher, J.; Renault, S.; Dubois, L.; Liang, Y.; Yao, Y. Opportunities and Challenges for Organic Electrodes in Electrochemical Energy Storage. *Chem. Rev.* **2020**, *120*, 6490–6557.
10. Lu, Y.; Chen, J. Prospects of Organic Electrode Materials for Practical Lithium Batteries. *Nat. Rev. Chem.* **2020**, *4*, 127–142.
11. Muench, S.; Wild, A.; Friebe, C.; Häupler, B.; Janoschka, T.; Schubert, U. S. Polymer-Based Organic Batteries. *Chem. Rev.* **2016,** *116*, 9438–9484.

12. Sosoe, J. O. E.; Malveau, C.; Maris, T.; Iftimie, R.; Wuest, J. D. Refreshing the Legacy of Rudolf Nietzki: Benzene-1,2,4,5-tetramine and Related Compounds. Submitted for publication (copy attached).
13. Sosoe, J. O. E.; Maris, T.; Wuest, J. D. Strongly Hydrogen-Bonded Networks Formed by Sulfate and Bisulfate Salts of Benzenetetramines. Submitted for publication (copy attached).
14. Qiu, Z.; Li, C.-J. Transformations of Less-Activated Phenols and Phenol Derivatives via C−O Cleavage. *Chem. Rev.* **2020**, *120*, 10454–10515.
15. Asha, A.; Ravindran, J.; Suma, S.; Suresh, C. H.; Lankalapalli, R. S. Synthesis of 2,5-Diamino-*p*-benzoquinones via Aerobic Oxidative $C(sp^2)$-$C(sp^2)$ Bond Cleavage and Mechanistic Studies. *ChemistrySelect* **2020**, *5*, 2545–2550.
16. Lardy, S. W.; Luong, K. C.; Schmidt, V. A. Formal Aniline Synthesis from Phenols through Deoxygenative N-Centered Radical Substitution. *Chem. Eur. J.* **2019**, *25*, 15267–15271.
17. Klopčič, I.; Sollner Dolenc, M. Chemicals and Drugs Forming Reactive Quinone and Quinone Imine Metabolites. *Chem. Res. Toxicol.* **2019**, *32*, 1–34.
18. Crooke, S. T.; Bradner, W. T. Mitomycin C: A Review. *Can. Treat. Rev.* **1976**, *3*, 121–139.
19. Nietzki, R.; Schedler, A. Synthese von symmetrischem Tetramidobenzol mittels Dinitrodichlorbenzol. *Ber. dtsch. chem. Ges.* **1897**, *30*, 1666–1669.
20. Nietzki, R.; Schmidt, L. Ueber das benachbarte Tetramidobenzol. *Ber. dtsch. chem. Ges.* **1889**, *22*, 1648–1653.
21. Nietzki, R.; Hagenbach, E. Ueber Tetramidobenzol und seine Derivate. *Ber. dtsch. chem. Ges.* **1887**, *20*, 328–338.
22. Rupe, H. Rudolf Nietzki. *Ber. dtsch. chem. Ges.* **1919**, *52*, A1–A28.
23. Noelting, E. Rudolf Nietzki. 1847–1917. *Helv. Chim. Acta* **1918**, *1*, 343–430.
24. Ost, H. Rudolf Nietzki. *Angew. Chem.* **1917**, *30*, 285–287.
25. Sang, Z.; Liu, J.; Zhang, X.; Yin, L.; Hou, F.; Liang, J. One-Dimensional π−d Conjugated Conductive Metal−Organic Framework with Dual Redox-Active Sites for High-Capacity and Durable Cathodes for Aqueous Zinc Batteries. *ACS Nano* **2023**, *17*, 3077–3087.
26. Wang, J.; Liu, X.; Jia, H.; Apostol, P.; Guo, X.; Lucaccioni, F.; Zhang, X.; Zhu, Q.; Morari, C.; Gohy, J.-F.; Vlad, A. A High-Voltage Organic Framework for High-Performance Na- and K-Ion Batteries. *ACS Energy Lett.* **2022**, *7*, 668–674.

27. Yang, D.; Liang, Z.; Tang, P.; Zhang, C.; Tang, M.; Li, Q.; Biendicho, J. J.; Li, J.; Heggen, M.; Dunin-Borkowski, R. E.; Xu, M.; Llorca, J.; Arbiol, J.; Morante, J. R.; Chou, S.-L.; Cabot, A. A High Conductivity 1D π–d Conjugated Metal–Organic Framework with Efficient Polysulfide Trapping-Diffusion-Catalysis in Lithium–Sulfur Batteries. *Adv. Mater.* **2022**, *34*, 2108835.
28. Kapaev, R. R.; Shestakov, A. F.; Vasil'ev, S. G.; Stevenson, K. J. Conjugated Ladder-Type Polymer with Hexaazatriphenylene Units as a Cathode Material for Lithium, Sodium, and Potassium Batteries. *ACS Appl. Energy Mater.* **2021**, *4*, 10423–10427.
29. Baymuratova, G. R.; Khatmullina, K. G.; Yakuschenko, I. K.; Tulibaeva, G. Z.; Savinykh, T. A.; Troshin, P. A.; Shestakov, A. F.; Yarmolenko, O. V. Synthesis and Investigation of a New Organic Electrode Material Based on Condensation Product of Triquinoyl with 1,2,4,5-Tetraaminobenzene. *J. Electroanal. Chem.* **2021**, *889*, 115234.
30. Sutton, A. L.; Abrahams, B. F.; D'Alessandro, D. M.; Goerigk, L.; Hudson, T. A.; Robson, R.; Usov, P. M. Semi-Conducting Mixed-Valent $X_4TCNQ^{I-/II-}$ (X = H, F) Charge-Transfer Complexes with $C_6H_2(NH_2)_4$. *J. Mater. Chem. C* **2020**, *8*, 9422−9426.
31. Kapaev, R. R.; Olthof, S.; Zhidkov, I. S.; Kurmaev, E. Z.; Stevenson, K. J.; Meerholz, K.; Troshin, P. A. Nickel(II) and Copper(II) Coordination Polymers Derived from 1,2,4,5-Tetraaminobenzene for Lithium-Ion Batteries. *Chem. Mater.* **2019**, *31*, 5197–5205.
32. Wäckerlin, C.; Cahlík, A.; Goikoetxea, J.; Stetsovych, O.; Medvedeva, D.; Redondo, J.; Švec, M.; Delley, B.; Ondráček, M.; Pinar, A.; Blanco-Rey, M.; Kolorenč, J.; Arnau, A.; Jelínek, P. Role of the Magnetic Anisotropy in Atomic-Spin Sensing of 1D Molecular Chains. *ACS Nano* **2022**, *16*, 16402–16413.
33. Zhang, F.; Wang, P.; Zhao, R.; Wang, Y.; Wang, J.; Han, B.; Liu, Z. Tuning d-Band Structure of Cu^{II} in Coordinated Polymer via d–π Conjugation for Improving CO_2 Electroreduction Selectivity toward C_2 Products. *ChemSusChem* **2022**, *15*, e202201267.
34. Wu, H.-Y.; Yang, C.-Y.; Li, Q.; Kolhe, N. B.; Strakosas, X.; Stoeckel, M.-A.; Wu, Z.; Jin, W.; Savvakis, M.; Kroon, R.; Tu, D.; Woo, H. Y.; Berggren, M.; Jenekhe, S. A.; Fabiano, S. Influence of Molecular Weight on the Organic Electrochemical Transistor Performance of Ladder-Type Conjugated Polymers. *Adv. Mater.* **2022**, *34*, 2106235.
35. Santhini, V. M.; Wäckerlin, C.; Cahlík, A.; Ondráček, M.; Pascal, S.; Matěj, A.; Stetsovych, O.; Mutombo, P.; Lazar, P.; Siri, O.; Jelínek, P. 1D Coordination π–d Conjugated Polymers

with Distinct Structures Defined by the Choice of the Transition Metal: Towards a New Class of Antiaromatic Macrocycles. *Angew. Chem. Int. Ed.* **2021**, *60*, 439–445.

36. Wan, Y.; Sun, Y.; Wu, X.; Yang, J. Ambipolar Half-Metallicity in One-Dimensional Metal−(1,2,4,5-Benzenetetramine) Coordination Polymers via Carrier Doping. *J. Phys. Chem. C* **2018**, *122*, 989–994.
37. Chen, Z.; Canard, G.; Jacquemin, D.; Bucher, C.; Giorgi, M.; Siri, O. Hetero-Bimetallic Effect as a Route to Access Multinuclear Complexes. *Inorg. Chem.* **2018**, *57*, 12536–12542.
38. Pascal, S.; Siri, O. Benzoquinonediimine Ligands: Synthesis, Coordination Chemistry and Properties. *Coord. Chem. Rev.* **2017**, *350*, 178–195.
39. Audi, H.; Chen, Z.; Charaf-Eddin, A.; D'Aléo, A.; Canard, G.; Jacquemin, D.; Siri, O. Extendable Nickel Complex Tapes that Reach NIR Absorptions. *Chem. Commun.* **2014**, *50*, 15140–15143.
40. Jeon, I.-R.; Park, J. G.; Xiao, D. J.; Harris, T. D. An Azophenine Radical-Bridged Fe_2 Single-Molecule Magnet with Record Magnetic Exchange Coupling. *J. Am. Chem. Soc.* **2013**, *135*, 16845–16848.
41. Frantz, S.; Rall, J.; Hartenbach, I.; Schleid, T.; Záliš, S.; Kaim, W. Metal-Induced Tautomerization of *p*- to *o*-Quinone Compounds: Experimental Evidence from Cu^I and Re^I Complexes of Azophenine and DFT Studies. *Chem. Eur. J.* **2004**, *10*, 149–154.
42. Masui, H.; Lever, A. B. P.; Dodsworth, E. S. Substituent Effects and Bonding Characteristics in (*o*-Benzoquinone diimine)bis(bipyridine)ruthenium (II) Complexes. *Inorg. Chem.* **1993**, *32*, 258–267.
43. Parvatkar, P. T.; Kandambeth, S.; Shaikh, A. C.; Nadinov, I.; Yin, J.; Kale, V. S.; Healing, G.; Emwas, A.-H.; Shekhah, O.; Alshareef, H. N.; Mohammed, O. F.; Eddaoudi, M. A Tailored COF for Visible-Light Photosynthesis of 2,3-Dihydrobenzofurans. *J. Am. Chem. Soc.* **2023**, *145*, 5074–5082.
44. Lin, Y.; Cui, H.; Liu, C.; Li, R.; Wang, S.; Qu, G.; Wei, Z.; Yang, Y.; Wang, Y.; Tang, Z.; Li, H.; Zhang, H.; Zhi, C.; Lv, H. A Covalent Organic Framework as a Long-Life and High-Rate Anode Suitable for Both Aqueous Acidic and Alkaline Batteries. *Angew. Chem. Int. Ed.* **2023**, *62*, e202218745.

45. Zhi, Q.; Liu, W.; Jiang, R.; Zhan, X.; Jin, Y.; Chen, X.; Yang, X.; Wang, K.; Cao, W.; Qi, D.; Jiang, J. Piperazine-Linked Metalphthalocyanine Frameworks for Highly Efficient Visible-Light-Driven H_2O_2 Photosynthesis. *J. Am. Chem. Soc.* **2022**, *144*, 21328–21336.
46. Zhang, J.; Kong, Y.-R.; Liu, Y.; Luo, H.-B.; Zou, Y.; Zang, S.-Q.; Ren, X.-M. Superprotonic Conduction of Acidified Benzimidazole-Linked Covalent Organic Framework. *ACS Materials Lett.* **2022**, *4*, 2597–2603.
47. Zheng, Q.; Li, X.; Zhang, Q.; Lee, D.; Mao, H.; Yang, C.; Bustillo, K. C.; Reimer, J. A.; Liu, Y.; Jiang, J.; Zheng, H. A Covalent Organic Framework Onion Structure. *Mater. Today* **2022**, *60*, 98−105.
48. Li, X.; Wang, H.; Chen, H.; Zheng, Q.; Zhang, Q.; Mao, H.; Liu, Y.; Cai, S.; Sun, B.; Dun, C.; Gordon, M. P.; Zheng, H.; Reimer, J. A.; Urban, J. J.; Ciston, J.; Tan, T.; Chan, E. M.; Zhang, J.; Liu, Y. Dynamic Covalent Synthesis of Crystalline Porous Graphitic Frameworks. *Chem* **2020**, *6*, 933−944.
49. Kim, S.; Choi, H. C. Light-Promoted Synthesis of Highly-Conjugated Crystalline Covalent Organic Framework. *Commun. Chem.* **2019**, *2*, 60.
50. Hisaki, I.; Affendy, N. Q. E.; Tohnai, N. Precise Elucidations of Stacking Manners of Hydrogen-Bonded Two-Dimensional Organic Frameworks Composed of X-Shaped π-Conjugated Systems. *CrystEngComm* **2017**, *19*, 4892−4898.
51. Yang, Q.; Liu, Y.; Xiang, L.; Zhang, J.; Yin, Y.; Xu, F.; Mai, Y. A General Synthetic Method towards Conjugated Microporous Polymers with Ordered Bicontinuous Mesostructures. *Chem. Commun.* **2023**, *59*, 4742−4745.
52. Xu, J.; Li, W.; Liu, W.; Jing, J.; Zhang, K.; Liu, L.; Yang, J.; Zhu, E.; Li, J; Zhu, Y. Efficient Photocatalytic Hydrogen and Oxygen Evolution by Side-Group Engineered Benzodiimidazole Oligomers with Strong Built-in Electric Fields and Short-Range Crystallinity. *Angew. Chem. Int. Ed.* **2022**, *61*, e202212243.
53. Shin, S.-H.; Noh, H.-J.; Kim, Y.-H.; Im, Y.-K.; Mahmood, J.; Baek, J.-B. Forming Layered Conjugated Porous BBL Structures. *Polym. Chem.* **2019**, *10*, 4185−4193.
54. Seo, W.; Carpenter, K. L.; Gaugler, J. A.; Shao, W.; Werling, K. A.; Fournier, P. M.; Lambrecht, D. S.; Star, A. Polybenzobisimidazole-Derived Two-Dimensional Supramolecular Polymer. *J. Polym. Sci. A Polym. Chem.* **2017**, *55*, 1095−1101.

55. Gajiwala, H. M.; Zand, R. Synthesis and Characterization of Thermally Stable Polymers Containing Phenazine. *Polymer* **2000**, *41*, 2009−2015.
56. Szita, J.; Marvel, C. S. Partial Ladder Polymers with Anthraquinone Units. Reaction of 1,2,5,6-Tetraaminoanthraquinone with *p*-Benzoquinone Derivatives. *J. Polym. Sci. A1* **1972**, *9*, 415−421.
57. Audi, H.; Viero, Y.; Alwhaibi, N.; Chen, Z.; Iazykov, M.; Heynderickx, A.; Xiao, F.; Guérin, D.; Krzeminski, C.; Grace, I. M.; Lambert, C. J.; Siri, O.; Vuillaume, D.; Lenfant, S.; Klein, H. Electrical Molecular Switch Addressed by Chemical Stimuli. *Nanoscale* **2020**, *12*, 10127−10139.
58. Guo, Z.; Song, N. R.; Moon, J. H.; Kim, M.; Jun, E. J.; Choi, J.; Lee, J. Y.; Bielawski, C. W.; Sessler, J. L.; Yoon, J. A Benzobisimidazolium-Based Fluorescent and Colorimetric Chemosensor for CO_2. *J. Am. Chem. Soc.* **2012**, *134*, 17846−17849.
59. Chen, Z.; Bert, M.; Pascal, S.; Canard, G.; Siri, O. Versatile Transamination in Quinonediimine Chemistry: Towards a Novel Class of Water Soluble UV/Violet Chromophores. *Tetrahedron Lett.* **2019**, *60*, 151024.
60. Edzang, J. A.; Chen, Z.; Audi, H.; Canard, G.; Siri, O. Transamination at the Crossroad of the One-Pot Synthesis of N-Substituted Quinonediimines and C-Substituted Benzobisimidazoles. *Org. Lett.* **2016**, *18*, 5340−5343.
61. Bindewald, E.; Lorenz, R.; Hübner, O.; Brox, D.; Herten, D.-P.; Kaifer, E.; Himmel, H.-J. Tetraguanidino-Functionalized Phenazine and Fluorene Dyes: Synthesis, Optical Properties and Metal Coordination. *Dalton Trans.* **2015**, *44*, 3467−3485.
62. Le, H. T. M.; El-Hamdi, N. S.; Miljanić, O. Š. Benzobisimidazole Cruciform Fluorophores. *J. Org. Chem.* **2015**, *80*, 5210−5217.
63. Golubovskaya, V.; Curtin, L.; Groman, A.; Sexton, S.; Cance, W. G. In Vivo Toxicity, Metabolism and Pharmacokinetic Properties of FAK Inhibitor 14 or Y15 (1,2,4,5-Benzenetetramine Tetrahydrochloride). *Arch. Toxicol.* **2015**, *89*, 1095−1101.
64. Hurion Beaugeard, N.; Matti, J. Contributions à la connaissance des relations existent entre la constitution chimique et les propriétés thérapeutiques. *Bull. Soc. Chim. Fr.* **1956**, 1612–1615.
65. Kehrmann, F.; Betsch, G. Ueber 1.4-Diaminochinon. *Ber. dtsch. chem. Ges.* **1897**, *30*, 2096–2103.

66. Typke, P. G. W. Ueber Nitroderivate des Resorcins. *Ber. dtsch. chem. Ges.* **1883**, *16*, 551–557.
67. Yang, Q.-Z.; Siri, O.; Braunstein, P. First Transamination Reactions for the One-Pot Synthesis of Substituted Zwitterionic Quinones. *Chem. Commun.* **2005**, 2660−2662.
68. Yang, Q.-Z.; Siri, O.; Braunstein, P. Tunable N-Substitution in Zwitterionic Benzoquinonemonoimine Derivatives: Metal Coordination, Tandemlike Synthesis of Zwitterionic Metal Complexes, and Supramolecular Structures. *Chem. Eur. J.* **2005**, *11*, 7237−7246.
69. Braunstein, P.; Siri, P.; Taquet, J.-p.; Rohmer, M.-M.; Bénard, M.; Welter, R. A 6π + 6π Potentially Antiaromatic Zwitterion Preferred to a Quinoidal Structure: Its Reactivity Toward Organic and Inorganic Reagents. *J. Am. Chem. Soc.* **2003**, *125*, 12246−12256.
70. Siri, O.; Braunstein, P. Unprecedented Zwitterion in Quinonoid Chemistry. *Chem. Commun.* **2002**, 208−209.
71. Greco, N. P. Hydrolysis of Meta-Phenylenediamine. US 3862246, January 21, 1975.
72. Shchurova, I. A.; Alekseyeva, N. A.; Sysolyatin, S. V.; Malykhin, V. V. A Comparative Study of the Synthesis and Hydrolysis of *sym*-Triaminobenzene Homologues. *Molecules* **2022**, *27*, 8595.
73. Glatzhofer, D. T.; Khan, M. A. *N*,*N*',*N*''-Triphenyl-l,3,5-triaminobenzene and Its *σ* Complex on Protonation: A Stable *N*,*N*',*N*''-Triphenyl-2,4,6-triaminocyclohexadienylium Cation. *Acta Crystallogr.* **1993**, *C49*, 2128−2133.
74. Knoche, W.; Schoeller, W. W.; Schomäcker, R.; Vogel, S. Protonation of 1,3,5-Triaminobenzenes in Aqueous Solutions. Thermodynamics and Kinetics of the Formation of Stable *σ*-Complexes. *J. Am. Chem. Soc.* **1988**, *110*, 7484−7489.
75. Mardirossian, N.; Head-Gordon, M. Survival of the Most Transferable at the Top of Jacob's Ladder: Defining and Testing the ωB97M(2) Double Hybrid Density Functional. *J. Chem. Phys*. **2018**, *148*, 241736.
76. Hellweg A.; Rappoport, D. Development of New Auxiliary Basis Functions of the Karlsruhe Segmented Contracted Basis Sets Including Diffuse Basis Functions (def2-SVPD, def2-TZVPPD, and def2-QVPPD) for RI-MP2 and RI-CC Calculations. *Phys. Chem. Chem. Phys*. **2015**, *17*, 1010–1017.

77. Rappoport, D.; Furche, F. Property-Optimized Gaussian Basis Sets for Molecular Response Calculations. *J. Chem. Phys*. **2010**, *133*, 134105.
78. Weigend, F.; Ahlrichs, R. Balanced Basis Sets of Split Valence, Triple Zeta Valence and Quadruple Zeta Valence Quality for H to Rn: Design and Assessment of Accuracy. *Phys. Chem. Chem. Phys*. **2005**, *7*, 3297–3305.
79. Lin, Y.-S.: Li, G.-D.; Mao, S.-P.; Chai, J.-D. Long-Range Corrected Hybrid Density Functionals with Improved Dispersion Correction. *J. Chem. Theory Comput*. **2013**, *9*, 263–272.
80. Grimme, S.; Antony, J.; Ehrlich, S.; Krieg, H. A Consistent and Accurate *ab initio* Parametrization of Density Functional Dispersion Correction (DFT-D) for the 94 Elements H-Pu. *J. Chem. Phys*. **2010**, *132*, 154104.
81. Chai, J.-D.; Head-Gordon, M. Systematic Optimization of Long-Range Corrected Hybrid Density Functionals. *J. Chem. Phys*. **2008**, *128*, 084106.
82. Chai, J.-D.; Head-Gordon, M. Long-Range Corrected Hybrid Density Functionals with Damped Atom-Atom Dispersion Corrections. *Phys. Chem. Chem. Phys*. **2008**, *10*, 6615–6620.
83. Cossi, M.; Rega, N.; Scalmani, G.; Barone, V. Energies, Structures, and Electronic Properties of Molecules in Solution with the C-PCM Solvation Model. *J. Comput. Chem*. **2003**, *24*, 669–681.
84. Kune, C.; Delvaux, C.; Haler, J. R. N.; Quinton, L.; Eppe, G.; De Pauw, E.; Far, J. A Mechanistic Study of Protonated Aniline to Protonated Phenol Substitution Considering Tautomerization by Ion Mobility Mass Spectrometry and Tandem Mass Spectrometry. *J. Am. Soc. Mass Spectrom.* **2019**, *30*, 2238–2249.
85. Bagno, A.; Terrier, F. Carbon and Nitrogen Basicity of Aminothiophenes and Anilines. *J. Phys. Chem. A* **2001**, *105*, 6537–6542.
86. Russo, N.; Toscano, M.; Grand, A.; Mineva, T. Proton Affinity and Protonation Sites of Aniline. Energetic Behavior and Density Functional Reactivity Indices. *J. Phys. Chem. A* **2000**, *104*, 4017–4021.
87. Roy, R. K.; de Proft, F.; Geerlings, P. Site of Protonation in Aniline and Substituted Anilines in the Gas Phase: A Study via the Local Hard and Soft Acids and Bases Concept. *J. Phys. Chem. A* **1998**, *102*, 7035–7040.

88. Smith, R. L.; Chyall, L. J.; Beasley, B. J.; Kenttämaa, H. I. The Site of Protonation of Aniline. *J. Am. Chem. Soc.* **1995**, *117*, 7971–7973.
89. Vandenbelt, J. M.; Henrich, C.; Vanden Berg, S. G. Comparison of pK_a' Values Determined by Electrometric Titration and Ultraviolet Absorption Methods. *Anal. Chem.* **1954**, *25*, 726–727.
90. Kapoor, I. P. S.; Srivastava, P.; Singh, G. Preparation, Crystal Structure and Thermal Decomposition of Phenylenediammonium Dichloride Salts. *Indian J. Chem.* **2007**, *46A*, 1277−1282.
91. Anderson, K. M.; Goeta, A. E.; Hancock, K. S. B.; Steed, J. W. Unusual Variations in the Incidence of $Z' > 1$ in Oxo-Anion Structures. *Chem. Commun.* **2006**, 2138–2140.
92. Domenicano, A.; Foresti Serantoni, E.; Riva di Sanseverino, L. Structural Studies of Benzene Derivatives. I. Refinement of the Crystal Structure of *p*-Phenylenediamine Dihydrochloride. *Acta Crystallogr.* **1977**, *B33*, 1664–1668.
93. Stålhandske, C. A Neutron Diffraction Study of 1,2-Diaminobenzene Monohydrochloride. *Acta Crystallogr.* **1976**, *B32*, 2806–2809.
94. Stålhandske, C. The Crystal Structure of *o*-Phenylenediamine Dihydrochloride. *Acta Crystallogr.* **1974**, *B30*, 1586–1589.
95. Stålhandske, C. The Crystal Structure of *o*-Phenylenediamine Hydrochloride. *Acta Chem. Scand.* **1972**, *26*, 2962–2963.
96. Chandrasekaran, R. Crystal Structure of *p*-Phenylenediamine Dihydrochloride. *Acta Crystallogr.* **1969**, *B25*, 369–374.
97. Epifanovsky, E. et al. Software for the Frontiers of Quantum Chemistry: An Overview of Developments in the Q-Chem 5 Package. *J. Chem. Phys*. **2021**, *155*, 084801.
98. Bursch, M.; Mewes, J.-M.; Hansen, A.; Grimme S. Best-Practice DFT Protocols for Basic Molecular Computational Chemistry. *Angew. Chem. Int. Ed*. **2022**, *61*, e202205735.
99. Halgren, T. A. Merck Molecular Force Field. I. Basis, Form, Scope, Parameterization, and Performance of MMFF94. *J. Comp. Chem*. **1996**, *17*, 490–519.
100. Bootsma, A. N.; Wheeler, S. Popular Integration Grids Can Result in Large Errors in DFT-Computed Free Energies. *ChemRxiv*. Cambridge: Cambridge Open Engage; 2019; DOI: 10.26434/chemrxiv.8864204.v5.

101. Grimme, S. Supramolecular Binding Thermodynamics by Dispersion-Corrected Density Functional Theory. *Chem. Eur. J*. **2012**, *18*, 9955–9964.
102. Zhao, Y.; Truhlar, D. G. Computational Characterization and Modeling of Buckyball Tweezers: Density Functional Study of Concave-Convex π···π interactions. *Phys. Chem. Chem. Phys*. **2008**, *10*, 2813–2818.
103. Ribeiro, R. F.; Marenich, A. V.; Cramer, C. J.; Truhlar, D. G. Use of Solution-Phase Vibrational Frequencies in Continuum Models for the Free Energy of Solvation. *J. Phys. Chem. B* **2011**, *115*, 14556–14562.

4.2. Conclusions

L'ensemble de nos tentatives d'hydrolyse ont jusqu'à maintenant généré un produit brut constitué de DAHQ (**3**) • 2HCl, DAR (**4**) • 2HCl et BTA (**1**) • 4HCl dans un ratio de 10 : 1.1 : 0.2. La sensibilité de l'ensemble de ces composés au pH et à l'oxygène limite leur séparation directe en solution. Nous avons donc décidé d'acétyler le brut de la réaction d'hydrolyse afin de collecter des produits stables pouvant être séparés par chromatographie. En effet, l'acétylation est un procédé de dérivation simple, rapide, à haut rendement et réalisable en milieu suffisamment acide pour inhiber la dégradation des sels de départ. Pour valider cette approche, les composés **3** • 2HCl et **4** • 2HCl (respectivement acheté d'une source commerciale et synthétisé) ont été indépendamment acétylés dans des conditions similaires générant ainsi des produits hexaacétylés **7** et **8** (Figure 4.8). Aucune donnée de caractérisation par RMN, HMRS ou SCXRD n'a d'ailleurs été publiée pour ces produits, ce qui nous offre l'opportunité de publier une étude connexe sur l'arrangement solide de ces espèces. Une fois des conditions d'élution adaptées à la séparation des produits hexaacétylés déterminées, les produits bruts d'hydrolyse décrits plus hauts pourront être acétylés et séparés par chromatographie flash.

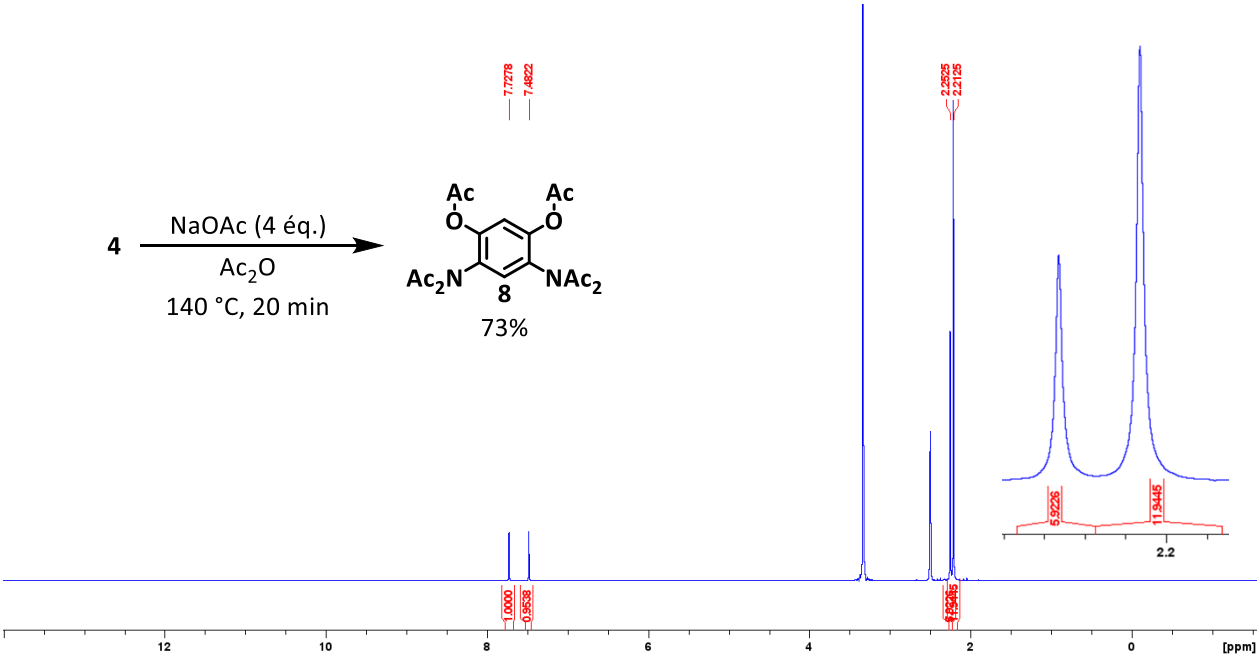

A

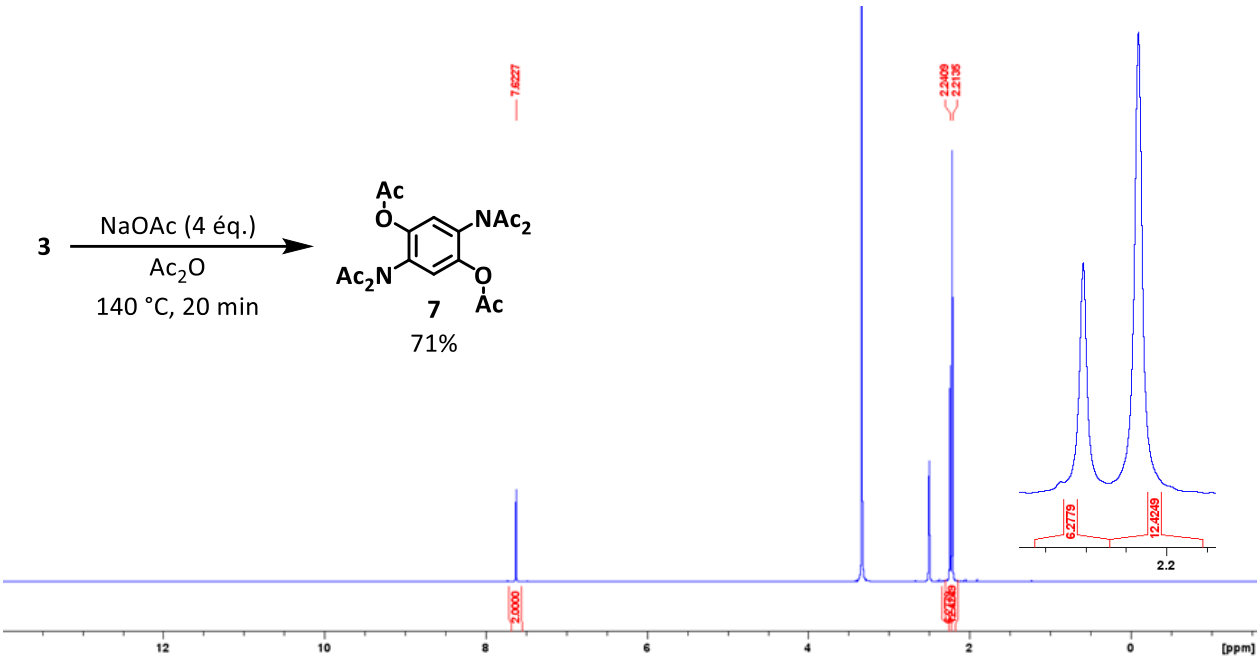

B

Figure 4.8 Spectres RMN ^{1}H (400 MHz, DMSO-D_6) des dérivés hexaacétylés de (**A**) de DAHQ (**3**) • 2HCl et (**B**) de DAHQ (**4**) • 2HCl.

Les résultats d'hydrolyse du sel **1** • 4HCl conduite sous argon suggèrent que le processus ne nécessite pas l'intervention d'intermédiaire oxydés. À titre de réaction contrôle, nous avons soumis la quinoneimine **2** à différentes conditions d'hydrolyse qui n'ont pour l'instant mené qu'à la récupération du produit de départ filtré à l'issue du processus. La couleur mauve des filtrats récupérés suggère pourtant la présence de quinones oxygénées. Mais comme les formes oxydées des hydroquinones **3** et **4** sont intensément colorées, elles pourraient y exister en faible quantité. De toute évidence, l'hydrolyse du composé **2** semble plus difficile à réaliser. La conversion de BTA en hydroquinone nous a amenés à nous questionner sur l'utilité d'un tel processus pour préparer DAR. Cette simple question nous conduit finalement à une nouvelle classe de composés inédits décrits dans le prochain chapitre.

Chapitre 5. Des composés inattendus

5.1. Notes

Ce projet a été réalisé avec l'aide de Loïc Carrier qui a réalisé l'ensemble des manipulations reliées à la synthèse et la caractérisation du composé **4** durant son stage de première année de baccalauréat. Les analyses cristallographiques ont été réalisées par Thierry Maris. Les atomes des structures cristallines présentées apparaissent en couleurs standards.

5.2. Introduction

En 1888, Nietzki et son étudiant F. Schmidt élucidèrent la structure de la 2,5-dihydroxy-*p*-benzoquinone (DHHQ-H_2, **1**) isolée par l'hydrolyse de la quinone du 4,6-diaminorésorcinol (DAR-H_2).[1,2] En faisant réagir le composé **1** avec de l'hydroxylamine dans du HCl dilué, ils obtinrent un produit de condensation alors considéré comme la 2,5-dihydroxybenzoquinonedioxime **2** (Schéma 5.1) Cette dernière, collectée sous la forme de feuillets cristallins au lustre argenté, colorait réversiblement les alcalis en brun et les acides en mauve. Plus tard, ils isoleront un sulfate de ce qui devait être la 2,5-diaminohydroquinone (DAHQ) issu de la réduction du composé **2**. En 1889, Friedrich Kehrmann, talentueux ancien étudiant de Nietzki qui travailla sur les quinoneoximes sous la supervision de ce dernier, invalidera la structure **2** proposée par son ancien professeur.[3] Selon lui, le produit de condensation de l'hydroxylamine est substitué en 1,3 (**3**) et non en 1,4. Il démontrera son hypothèse huit ans plus tard en publiant la synthèse totale de DAHQ et en comparant ses propriétés à celles de son isomère DAR.[4]

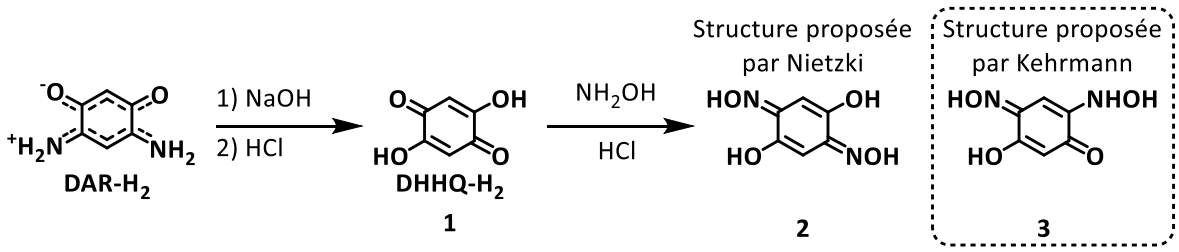

Schéma 5.1 Condensation de NH_2OH sur DHHQ-H_2 dont l'identité du produit est débattue.[1-4]

Nos travaux sur l'hydrolyse de l'isomère 1,2,4,5 de la benzènetétramine (1,2,4,5-BTA, Chapitre 4) nous ont conduits à nous intéresser aux procédés de synthèse de DAR, motif précurseur de plusieurs matériaux optoélectroniques.[5-8] Celui-ci est généralement synthétisé à partir de la résorcine par 1) nitration et réduction subséquentes, 2) double acétylation de Friedel-Craft suivie de réarrangements de Beckmann en condition réductrice ou 3) ou par d'autres procédés moins adaptés aux manipulations à l'échelle du gramme (Schéma 5.2). Ces procédés sont limités par leur sensibilité à la présence d'eau, leur bas rendements et/ou la génération d'intermédiaires explosifs. Plusieurs procédures d'acétylation/réarrangement de Beckmann se sont également avérées difficilement reproductibles entre nos mains. Pour toutes ces raisons, nous avons tenté de revisiter la synthèse de DAR à partir de DHHQ-H_2, produit de départ commercialement disponible, dérivé de la biomasse et converti en conditions douces. Aucune donnée de caractérisation récente de l'intermédiaire **2** ou **3**, quelle que fut sa structure, n'avait d'ailleurs été publiée depuis Nietzki et Kehrmann. Cela nous offrait donc l'opportunité d'étudier un composé aux caractéristiques structurales pertinentes à l'ingénierie cristalline et à l'électronique organique.

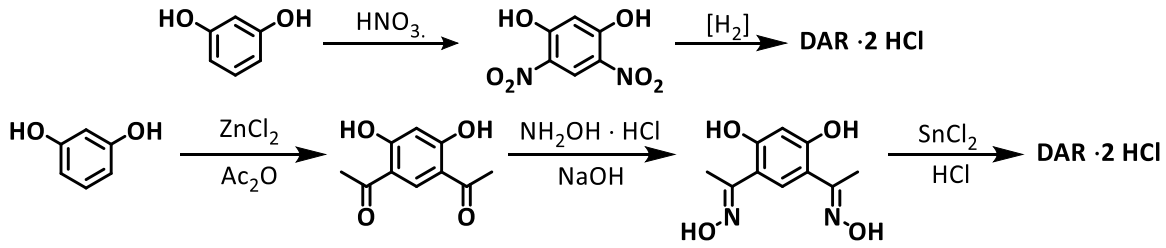

Schéma 5.2 Procédés de synthèse établis pour la synthèse de DAR ·2 HCl.[5-8]

5.3. Élucidation de la structure débattue

Faire réagir la dihydroxyquinone DHHQ-H_2 (**1**) avec une quantité stœchiométrique de chlorhydrate d'hydroxylamine dans l'eau à température pièce durant 24 h, conditions similaires à celles des chimistes allemands, nous permis d'isoler par filtration un solide aux reflets argentés. Celui-ci fut séparé du produit de départ résiduel par recristallisation dans l'eau chaude, dont il cristallise sous forme de plaquettes incolores analysables par diffraction de rayons-x sur monocristaux (SCXRD). Un hydrate d'un composé substitué en 1,3 fut ainsi obtenu (**4**, Figure 5.1). À notre grande surprise, le composé recristallisé est une 1,3-dioxime et non le composé quinoïde **3** proposée par Kehrmann. La structure déterminée par SCXRD corrobore aussi avec les résultats d'analyses RMN ^{1}H, ^{13}C et HSQC ^{1}H-^{13}C (Figure D1) de l'échantillon séché sous vide. En effet, quatre pics attribuables à chacun des hydrogènes du composé **4** sont visibles sur son spectre RMN ^{1}H (Figure 5.1.A). Le singulet caractéristique du pont méthylénique a d'ailleurs un déplacement chimique de 3.67 ppm. Seulement 3 pics sont cependant visibles sur le spectre RMN ^{13}C de la dioxime **4** (Figure 5.1.B). En effet, nous suspectons un équilibre céto-énol rapide au sein de son unité dicétone énolisée, causant un élargissement conséquent du pic des carbones associés. Ce phénomène est d'ailleurs également observé dans DHHQ-H_2, dont le déplacement chimique du pic de carbone concerné avoisine 173 ppm (Figure D3). Cet équilibre sera démontré dans le cadre d'une série d'expériences RMN à température variable conduites sur la dioxime **4**. Ces expériences nous permettront également de vérifier si la forme quinoïde **3** proposée par Kehrmann ou d'autres isomères sont accessibles. Le rendement isolé des conditions initiale de 49% a pu être augmenté à 93% en présence de 4 équivalents de $NH_2OH \cdot HCl$ sous atmosphère d'azote (Tableau D - 1). En effet, la présence d'air au cours de la condensation favorise la présence d'impuretés persistantes, même après recristallisation. Malgré l'excès d'hydroxylamine utilisé, aucun signe suggérant la formation d'une tétraoxime n'a été détecté dans ces conditions.

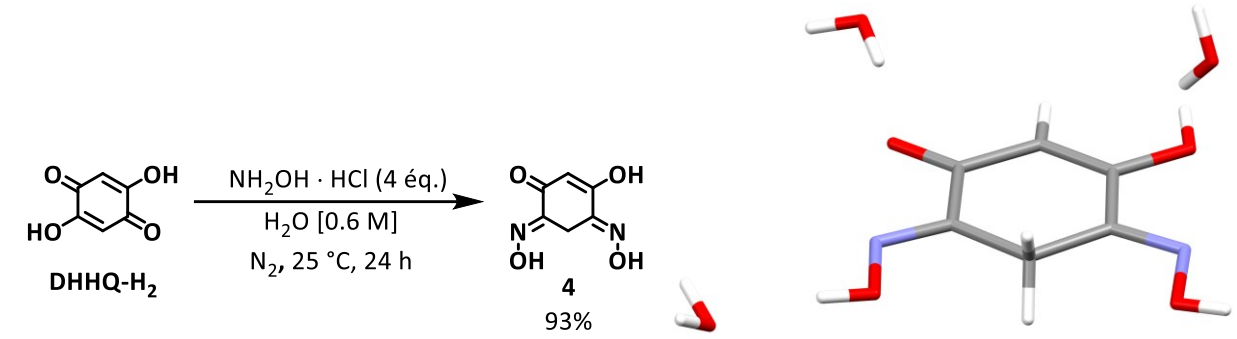
NH2OH · HCl (4 éq.)
H2O [0.6 M]
N2, 25 °C, 24 h
DHHQ-H2
4
93%

A

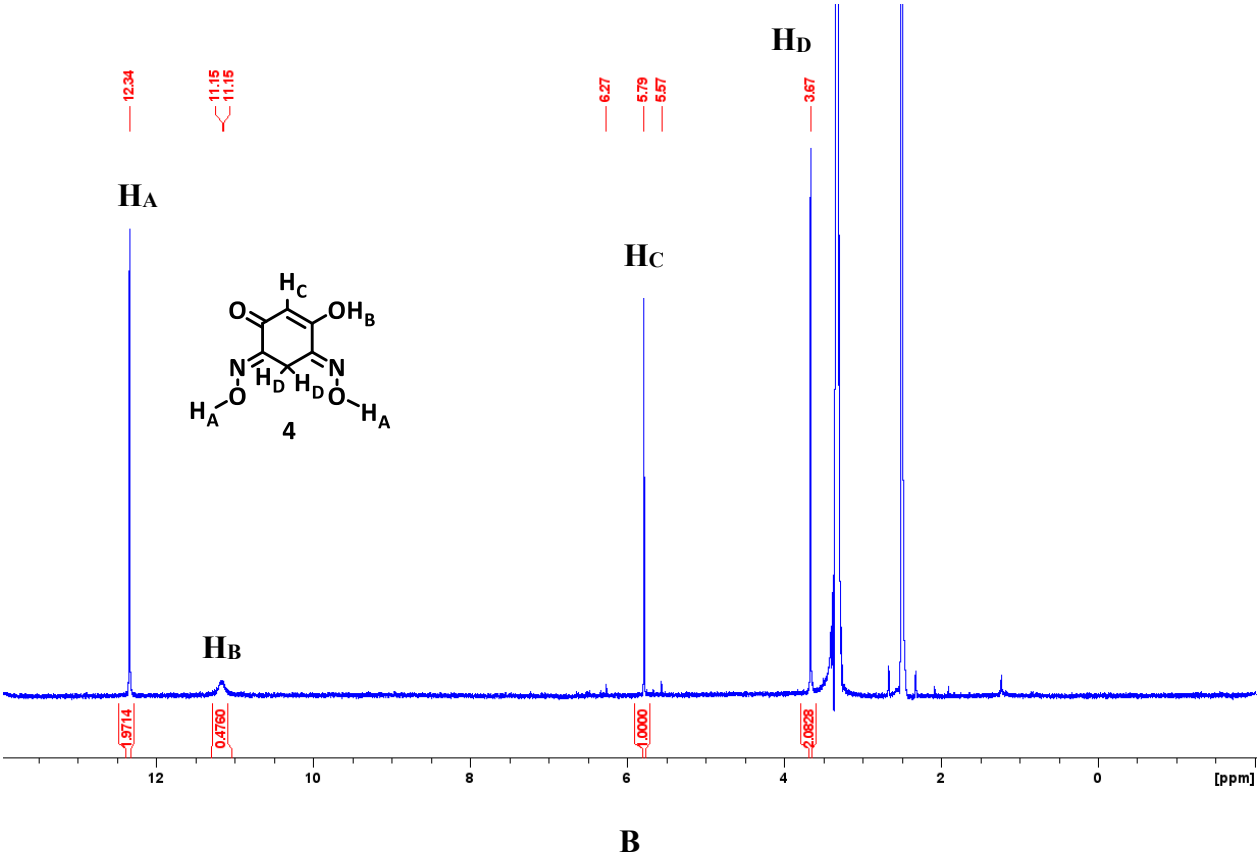
HA
HB
HC
HD
12.34
11.15
11.15
6.27
5.79
5.57
3.67
1.9714
0.4760
1.0000
2.0628
12
10
8
6
4
2
0
[ppm]
4

B

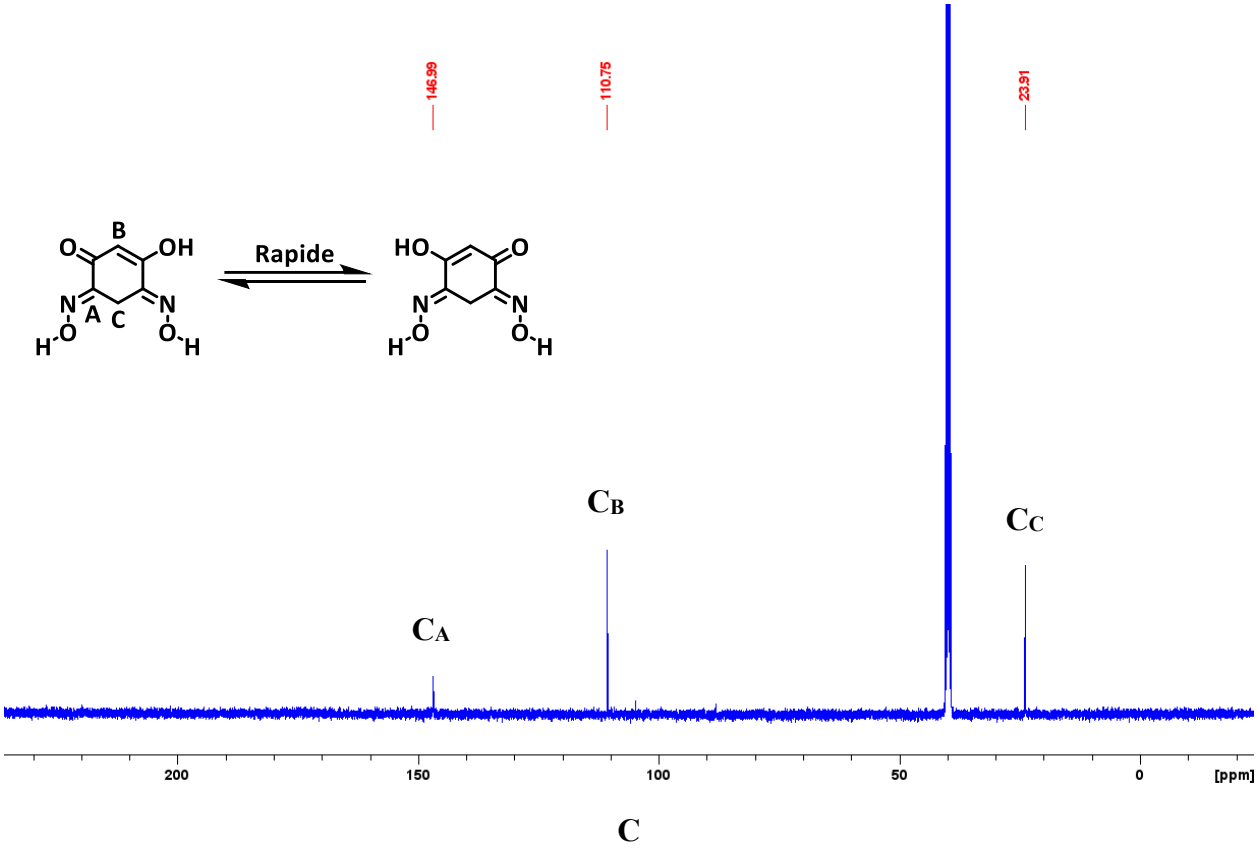

Figure 5.1 (**A**) Maille cristalline de la dioxime **4** recristallisée dans l'eau chaude. Spectres RMN (**A**) ^{1}H (400 MHz, DMSO-*d*$_6$) et (**C**) ^{13}C (DMSO-d$_6$, 100 MHz) du composé **4**.

La régiosélectivité de la condensation de $NH_2OH \cdot HCl$ sur DHHQ-H_2 pourrait potentiellement passer par l'intermédiaire monooxime **5** pouvant aussi exister sous les formes quinoïdes **6** et **7**. La délocalisation importante au sein de son unité dicétone-énolisée réduirait le caractère électrophile de cette dernière. La cétone en position méta relativement à l'oxime de **5**, serait alors plus susceptible à l'hydrolyse. Nous essayons présentement d'isoler l'intermédiaire afin de vérifier cette hypothèse et aussi de vérifier si le produit de substitution 1,4 est isolable dans d'autres conditions. En effet, le composé **2** ne semble pas non plus avoir été caractérisé, pas même par les chimistes allemands. En fait, très peu de composés 1,3-mono ou dioximes dérivés de dicétones cycliques avoir été étudiés.[9] Parmi eux figurent les composés **8** et **9** qui permirent à Nietzki de préparer l'isomère 1,2,3,4 de BTA et de déterminer la constitution de l'acide leuconique respectivement (Schéma 5.3).[10,11] La famille des 1,3-dioximes ne s'arrête pas là, car nous sommes parvenus à isoler un autre composé inattendu dérivé de la dioxime **4**.

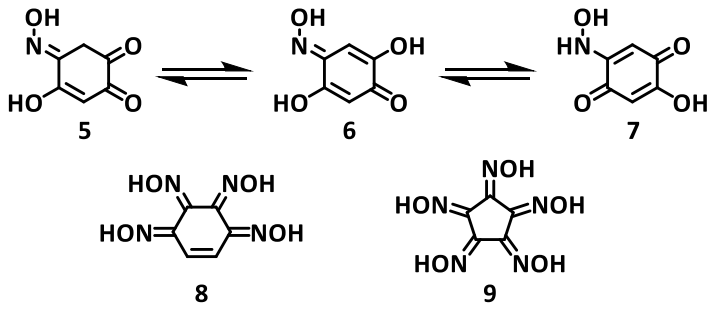

Schéma 5.3 Potentiels intermédiaires de la condensation de $NH_2OH \cdot HCl$ sur DHHQ-H_2 (**1**) et composés présentant au moins 1 unité 1,3-quinoneoxime décrits dans la littérature.[10,11]

En effet, chaque fois que la condensation de de $NH_2OH \cdot HCl$ sur DHHQ-H_2 a été réalisée à plus de 50 °C, le dimère **10** issu de la dioxime **4** a été isolé (Figure 5.2). Ce dernier a pu être cristallisé sous la forme d'un monohydrate dont la structure a pu être résolue. Il s'agit d'un composé méso dont la longueur de la liaison C-C reliant les monomères de 1.581 Å est plus grande que celles des liens C-C aliphatiques. Cette différence suggère que le lien C-C du dimère est plus faible qu'un lien C-C usuel et effectivement, le composé **10** est réduit en DAR · 2HCl par le chlorure d'étain. Encore une fois, les données de spectroscopie RMN et de spectrométrie de masse corroborent avec la structure proposée. En effet, le spectre RMN ^1H témoigne de la présence d'un hydrogène méthine à 5.51 ppm à la position reliant chaque moitié du composé méso et des intensités relatives attendues pour une telle structure. Le spectre RMN ^{13}C du dimère **10** est constitué de quatre pics dont celui de la fonction carbonyle à 174 ppm est élargi. Nous avons recensé peu de cas de dimérisation similaires à celle de notre dioxime **4**.[12,13] Dans chacun d'entre eux, la présence d'oxydants tels que l'oxygène de l'air semble être à l'origine de l'oxydation des monomères. En plus de vérifier l'implication de l'oxygène dans la dimérisation, nous nous intéressons également au bris du lien C-C central en conditions plus douces que l'usage de $SnCl_2$ dans le HCl concentré.

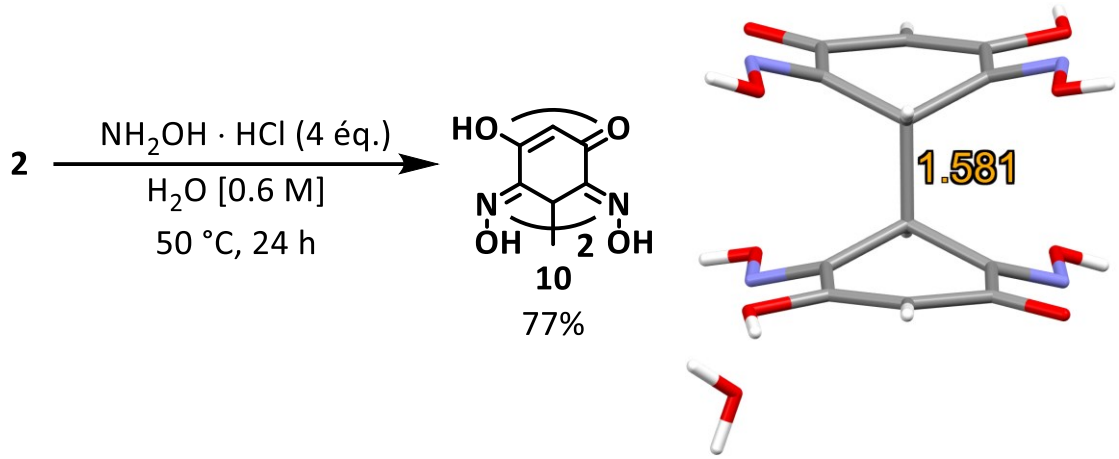
2
NH2OH · HCl (4 éq.)
H2O [0.6 M]
50 °C, 24 h
HO
O
N
N
OH
2
OH
10
77%
1.581

A

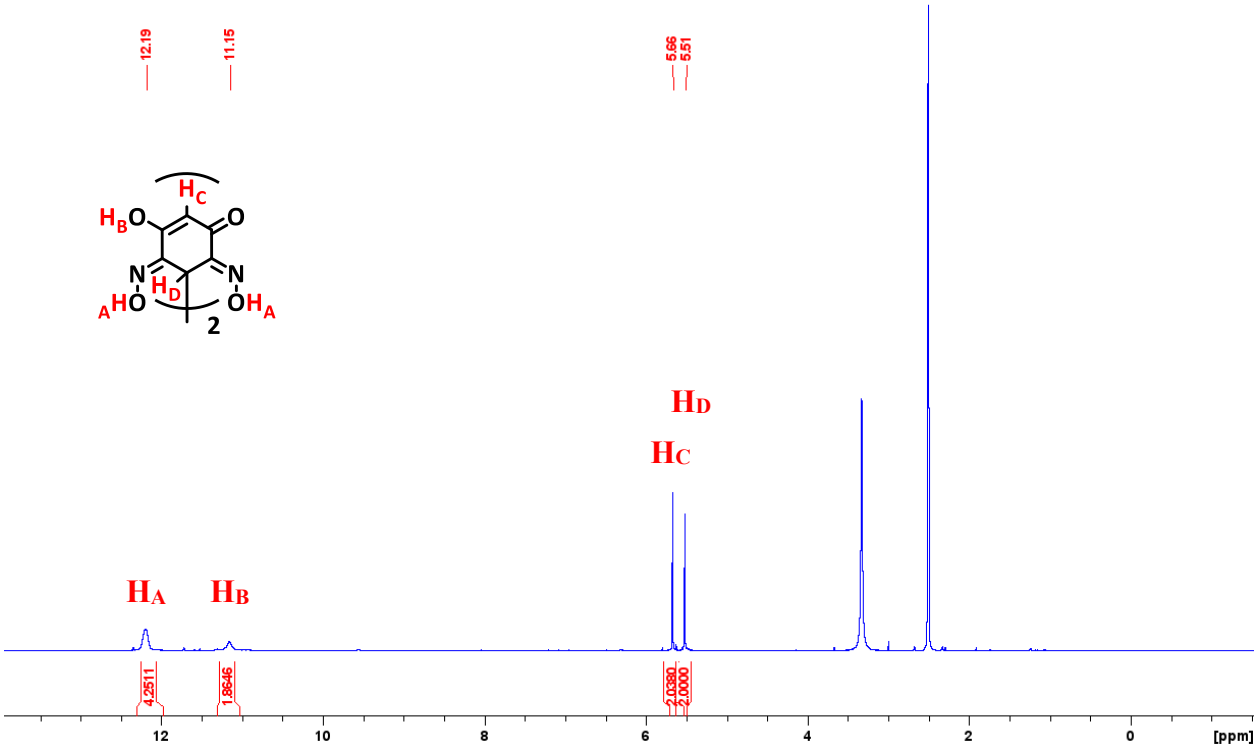
12.19
11.15
5.66
5.51
HC
HB
O
O
N
N
HD
AHO
OHA
2
HD
HC
HA
HB
4.2511
1.8646
2.0380
2.0000
12
10
8
6
4
2
0
[ppm]

B

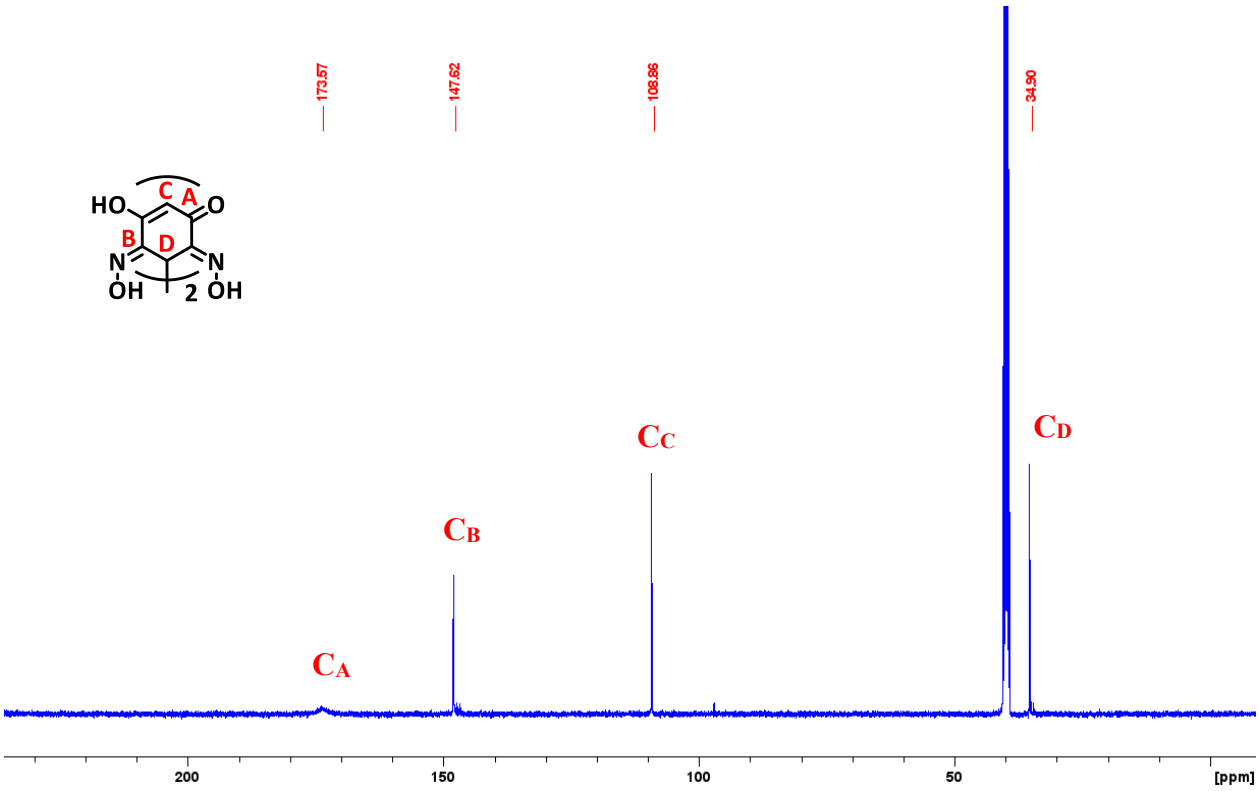

C

Figure 5.2 (**A**) Synthèse et maille cristalline du dimère **10** cristallisé dans le HCl dilué. Spectres RMN (**A**) ^{1}H (400 MHz, DMSO-d_6) et (**C**) ^{13}C (DMSO-D$_6$, 100 MHz) de **10**.

5.4. Conclusions

Nous sommes parvenus à élucider la structure du produit de condensation de l'hydroxylamine sur la dihydroxyquinone DHHQ-H_2 (**1**) dont des structures furent proposées à la fin du XIXe siècle. Ce dernier s'est révélé être une dioxime substituée en position 1,3 et capable de dimériser lorsque chauffée en solution. Ces deux composés ont été caractérisés par RMN ^{1}H, ^{13}C, HSQC ^{1}H-^{13}C, HRMS et SCXRD. Beaucoup de travail reste à faire concernant la caractérisation du potentiel équilibre entre les formes oximes et quinoïdes de ces composés, la régiosélectivité de la condensation dont ils sont issus ou encore le mécanisme de dimérisation. Nous avons également démontré que le dimère pouvait être réduit en DAR ·2 HCl, offrant ainsi une voie de synthèse de ce composé en condition plus douces que celles rapportées dans la littérature. En somme, ces travaux ouvrent l'accès à une nouvelle famille de composés aux propriétés inédites qui sont à la fois pertinentes à l'ingénierie cristalline et l'électronique organique.

5.5. Références

1. Nietzki, R.; Schmidt, F. Ueber Dioxychinon Und Tetroxybenzol. *Ber. Dtsch. Chem. Ges.* **1888**, *21* (2), 2374–2379.
2. Nietzki, R.; Schmidt, F. Ueber Dioxychinon Und Einige Derivate Desselben. *Ber. Dtsch. Chem. Ges.* **1889**, *22* (1), 1653–1662.
3. Kehrmann, Fr.; Tiesler, W. Ueber Die Einwirkung von Salzsaurem Hydroxylamin Auf Para-Dioxy-p-Chinone. *J. Prakt. Chem.* **1890**, *41* (1), 87–91.
4. Kehrmann, F.; Betsch, G. Ueber 1.4-Diaminochinon. *Ber. Dtsch. Chem. Ges.* **1897**, *30* (2), 2096–2103.
5. Typke, P. G. W. Ueber Nitroderivate Des Resorcins. *Ber. Dtsch. Chem. Ges.* **1883**, *16* (1), 551–557.
6. Pews, R. G.; Lysenko, Z.; Vosejpka, P. C. A Safe Cost-Efficient Synthesis of 4,6-Diaminoresorcinol. *J. Org. Chem.* **1997**, *62* (23), 8255–8256.
7. Mike, J. F.; Makowski, A. J.; Jeffries-EL, M. An Efficient Synthesis of 2,6-Disubstituted Benzobisoxazoles: New Building Blocks for Organic Semiconductors. *Org. Lett.* **2008**, *10* (21), 4915–4918.
8. Song, J.; Zhao, H.; Liu, Y.; Han, H.; Li, Z.; Chu, W.; Sun, Z. Efficient Symmetrical Bidentate Dioxime Ligand-Accelerated Homogeneous Palladium-Catalyzed Suzuki–Miyaura Coupling Reactions of Aryl Chlorides. *New J. Chem.* **2017**, *41* (1), 372–376.
9. Kotali, A.; Papageorgiou, V. P. The chemistry of 1,3-dioximes. A Brief Review. *Org. Prep. Proced. Int.* **1991**, *23* (5), 593–610.
10. Nietzki, R.; Benckiser, Th. Zur Kenntniss Der Krokonsäure Und Leukonsäure. *Ber. Dtsch. Chem. Ges.* **1886**, *19* (1), 293–309.
11. Nietzki, R.; Schmidt, L. Ueber Das Benachbarte Tetramidobenzol. *Ber. Dtsch. Chem. Ges.* **1889**, *22* (1), 1648–1653.
12. Taquet, J.; Siri, O.; Collin, J.-P.; Messaoudi, A.; Braunstein, P. One-Electron Oxidation-Induced Dimerising C–C Coupling of a 2,5-Diamino-1,4-Benzoquinonediimine: A Chemical and Electrochemical Investigation. *New J. Chem.* **2005**, *29* (1), 188–192.

13. Aslan, J. M.; Yousufuddin, M.; Boston, D. J.; MacDonnell, F. M. Quadruple Electron Storage Using Visible Light with Nitrogen-Heterocycles under Metal-Free Conditions. *Inorg. Chim. Acta* **2017**, *454*, 216–221.

Chapitre 6. Conclusions & perspectives

6.1. Conclusions générales

Le projet de recherche de cette thèse consiste à étudier la réactivité de l'isomère 1,2,4,5 de la benzènetétramine (1,2,4,5-BTA) et d'ultimement parvenir à bâtir des matériaux supramoléculaires pertinents au domaine des batteries. Bien que ce motif ait beaucoup été étudié pour la construction de matériaux covalents et de coordination en conditions solvothermales, la 1,2,4,5-BTA s'est révélée particulièrement réactive entre nos mains dans des conditions similaires à celles rapportées, et ce, même sous atmosphère inerte. Comme ce phénomène est délétère au contrôle de l'agrégation, nous nous sommes donc d'abord intéressés à sa réactivité en solutions aqueuses, peu étudiée depuis la fin du XIXe siècle, afin de pouvoir établir des stratégies fiables pour la construction de matériaux plus complexes. Nos travaux démontrent que :

- En milieu basique : 1,2,4,5-BTA est facilement oxydée par l'air pour former une diaminobenzoquinonediimine isolable (1,2,4,5-BTA-H_2). En absence d'air, un mélange de produits incluant la base libre et le sel 1,2,4,5-BTA · 2HCl précipitent.
- En milieu neutre : en présence ou en absence d'air, plusieurs processus simultanés sont en compétition (probablement d'hydrolyse et d'oxydation).
- En milieu acide dilué : 1,2,4,5-BTA demeure stable sur plusieurs heures autour de 20 °C mais est quantitativement hydrolysée en 2,5-diaminohydroquinone (DAHQ) et 4,6-diaminorésorcinol (DAR) à haute température. Ces derniers s'oxydent également en quinones relativement stables.

Parallèlement, nous avons caractérisé et/ou isolé l'ensemble des composés connexes à nos études dont les propriétés sont pertinentes à l'électronique organique. Se faisant, nous avons pu réaliser des contributions en chimie organique et supramoléculaire. L'étude expérimentale et théorique détaillée dans le Chapitre 2, nous a permis de collecter cinq structures cristallines jamais rapportées et des données de caractérisation permettant d'étudier l'arrangement solides de sels de 1,2,4,5 de BTA, de sa forme oxydée et des élusives bases libres de ces dernières. Une nouvelle méthode de synthèse de l'isomère 1,2,3,4 de BTA, sous-produit revalorisé de la préparation de l'isomère 1,2,4,5, a également été développée. Six nouvelles structures résolues de

bisulfates et de sels mixtes sulfates/bisulfates ont été décrites au Chapitre 3. L'étude de ces sels, à la composition inédite est prometteuse de générer des retombées à la fois pratique et théorique. En effet, nous proposons des méthodes de cristallisation de motifs rédox, jusqu'à maintenant étudiés séparément, mais maintenant cristallisés ensembles en un extensif réseau de ponts hydrogène peu soluble. Ce type de sel pourrait être utilisé comme matériaux cathodiques, de la même manière que les sels dérivés d'hydroxyde quinoïdes sont étudiés aujourd'hui. D'ailleurs, très peu de sulfate et encore moins de sels mixtes dérivés de phénylamines ont été étudiés. Dans le Chapitre 3, quatre nouvelles structures cristallines auxquelles vont vraisemblablement s'ajouter 3 produits actéylés jamais caractérisés auparavant ont été discutées. Elles apportent des informations sur les modes de connections de composés dérivés de l'unité DAR, précurseur de multiples matériaux optoélectroniques tels que les bisbenzoxazoles. L'étude mécanistique décrite est assez novatrice puisqu'elle traite d'un processus peu étudié dans des conditions plutôt récurrentes de préparation et d'utilisation du substrat. Le Chapitre 4 relate finalement de la caractérisation de deux nouveaux composés aux propriétés pertinentes à l'électronique et inédites en chimie organique. Ces résultats contribuent donc aux connaissances théoriques mais aussi pratiques car une voie de synthèse de DAR en conditions douces y est proposée.

6.2. Perspectives synthétiques

Plusieurs projets connexes intéressants ont été proposés dans les conclusions des différents chapitres. Pour ce qui a trait à l'utilisation de BTA pour la préparation de matériaux cristallin, nous aimerions nous tourner vers les composés de coordination. En effet ils représentent une classe de matériaux peu étudiés dans le domaine des batteries, bien qu'ils puissent être poreux, rédox-actifs et conducteurs. Parvenir à générer des matériaux monocristallins de coordination facilite d'ailleurs leur caractérisation structurale et physique. Notre approche ascendante proposée vers de tels matériaux est à deux volets. L'un d'eux repose sur l'utilisation directe des quinones étudiées dans la thèse, qui sont plus stables en solution que leurs composés parents et tout aussi capables de lier des cations (Schéma 6.1). D'ailleurs plusieurs études de ce genre ont déjà été publiées, notamment avec des centres métalliques Ni^{II}, mais seulement quelques composés monocristallins ont en effet été décrits.

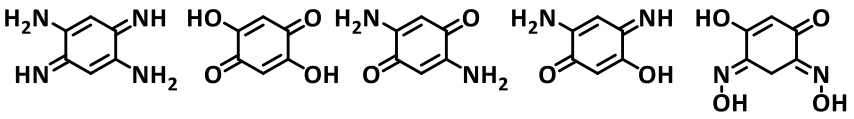

Schéma 6.1 Motifs quinoïdes utilisables pour générer des matériaux de coordination.

La seconde approche reposerait sur l'usage de 1,2,4,5-BTA comme précurseur de ligands ditopiques plus stables de type pyrazinoquinoxalines (Schéma 6.2). En effet, de telles structures sont moins réactives et arborent des fonctions rigides prédisposées à diriger des interactions ligand-métal et faciliter la cristallisation des assemblages. Nous préparerions également les complexes représentant les sous unités des matériaux étendus. Cette chimie s'inspirerait des complexes de phénanthroline de $Fe^{II/III}$ ou de Ru^{II}.

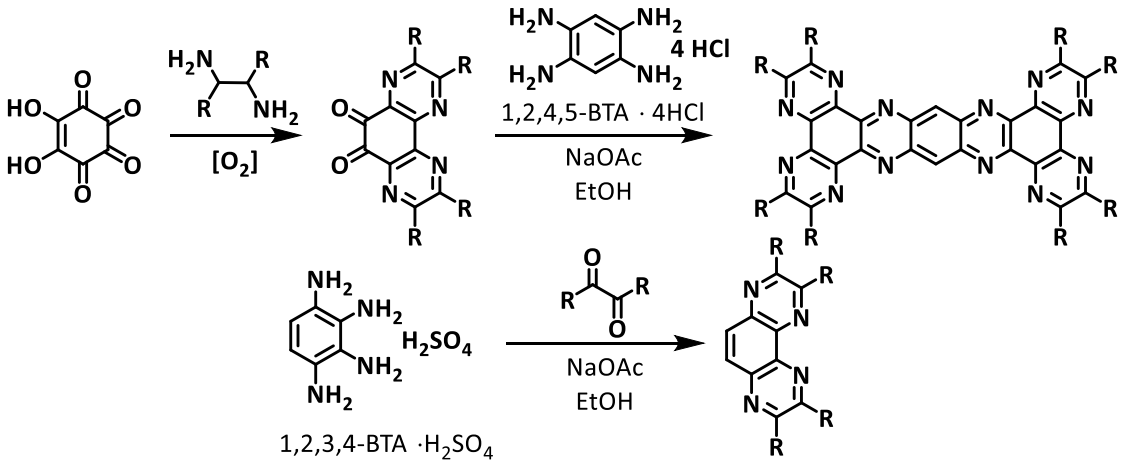

Schéma 6.2 Motifs quinoïdes utilisables pour générer des matériaux de coordination.

6.3. Études électrochimiques préliminaires

Note : l'ensemble des données présentées ont été collectées par A-Jay Khanmohamed avec des composés préparés par Johann Sosoe.

Comme peu d'études des processus rédox des composés du Schéma 6.1 ont été publiées jusqu'à maintenant, nous avons mené une série de mesures préliminaires de voltampérométrie

cyclique sur certains d'entre eux. Les voltampérogrammes de la 1,2,4,5-BTA · 4HCl (0.1 mM) dissoute dans du H_2SO_4 dilué (0.5 M, pH = 0.9) ont en l'occurrence pu être collectés à différentes vitesses de balayage (v) sous atmosphère d'argon (Figure 6.1.A). Des processus rédox *quasi*-réversibles dont les courants cathodiques (I_{pc}) et anodiques (I_{pa}) varient linéairement avec $v^{1/2}$ après 6 cycles y sont observés (Figure 6.1.B). L'élargissement des pics anodiques suggère une cinétique d'oxydation plus lente que les processus de réduction. Par ailleurs, l'hydrolyse de la BTA décrite au Chapitre 5 semble suffisamment lente pour ne pas compétitionner avec les processus rédox observés dans nos conditions expérimentales de voltampérométrie. Cela nous a d'ailleurs motivés à caractériser les processus rédox de BTA adsorbée sur un tissu de carbone utilisé comme électrode de travail dans ces mêmes conditions. Cette fois, le courant mesuré décroit rapidement vers zéro après 10 cycles probablement à cause de la dissolution progressive de l'espèce active adsorbée. Comme discuté au Chapitre 3, il est en effet possible que les sulfates de l'espèce oxydée BTA-H_2 soient plus solubles dans le H_2SO_4 que les sels de la forme réduite.

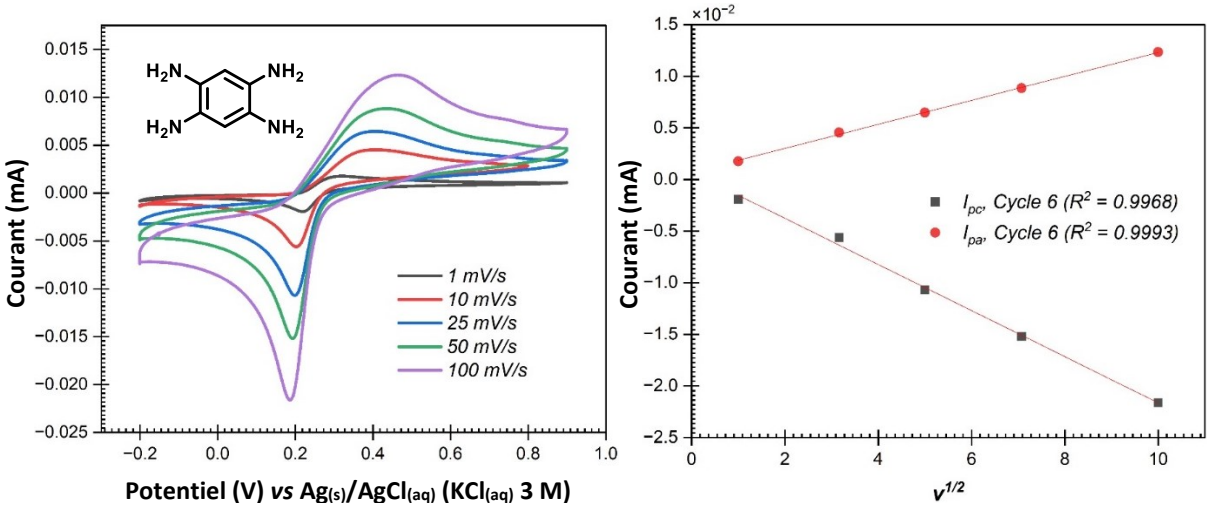

A **B**

Figure 6.1 (**A**) Voltampérogrammes cycliques (6^e cycle) de 1,2,4,5-BTA · 4HCl (0.1 mM) enregistrés à différentes vitesses de balayage (v) dans le H_2SO_4 0.5 M purgé à l'argon à 25 °C. Une électrode de carbone vitreux, d'Ag/AgCl immergée dans du $KCl_{(aq)}$ 3 M, ainsi qu'un fil de Pt furent respectivement utilisés comme électrodes de travail, de référence et contre-électrode. (**B**) Variation des courants de pics cathodiques (I_{pc}) et anodiques (I_{pa}) en fonction de $v^{1/2}$.

Dans le MeCN sec, la réponse de 1,2,4,5-BTA est nernstienne entre 50 et 1000 mV/s et le courant suit la relation de Randles-Ševčík (Figure 6.2.A & B), indiquant la réversibilité migration libre des espèces en solution. Il en est de même pour le composé DAR · 2HCl et sa forme oxydée DAR-H_2 (Figure 6.2.C à F) que l'hydrolyse de 1,2,4,5-BTA · 4HCl décrite au chapitre 5 nous a également amenés à étudier. Nous poursuivons d'ailleurs la caractérisation des autres motifs dérivés de 1,2,4,5-BTA en plus d'examiner les données quantitatives associées aux résultats préliminaires présentés ici. Un tel travail nous permettra de définir les conditions adaptées à l'application de l'ensemble de ces composés dans des dispositifs électrochimiques.

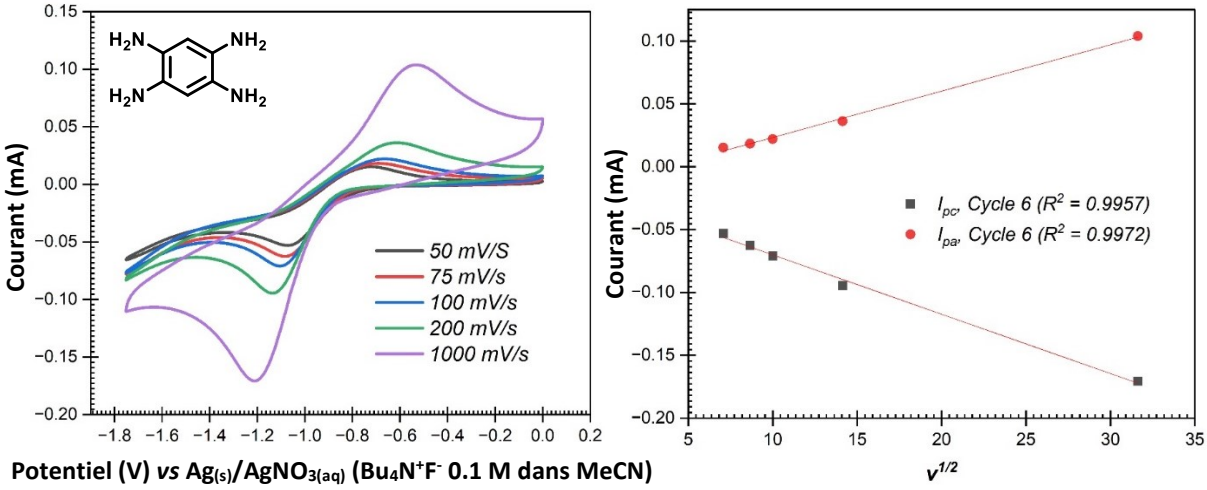

A **B**

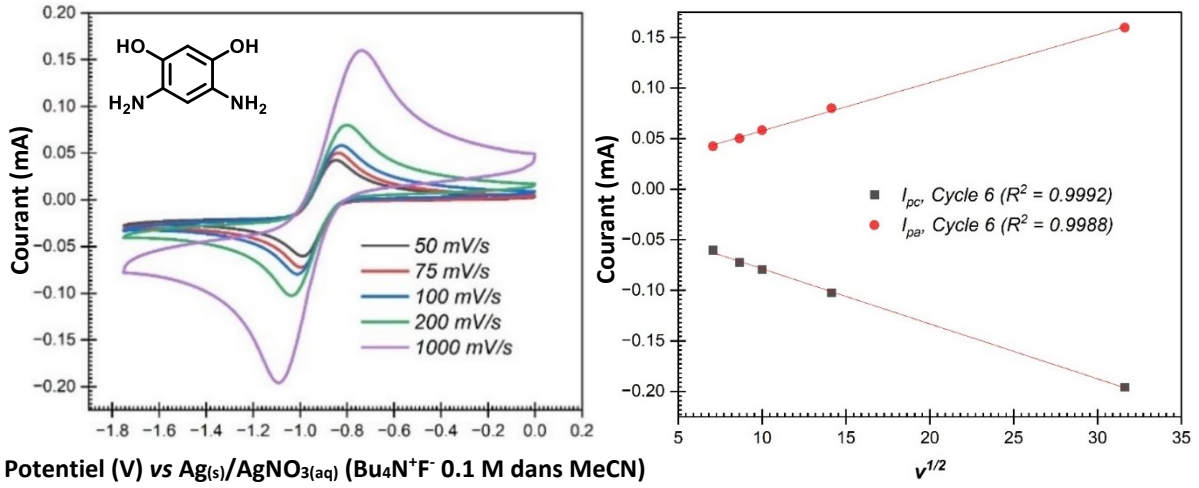

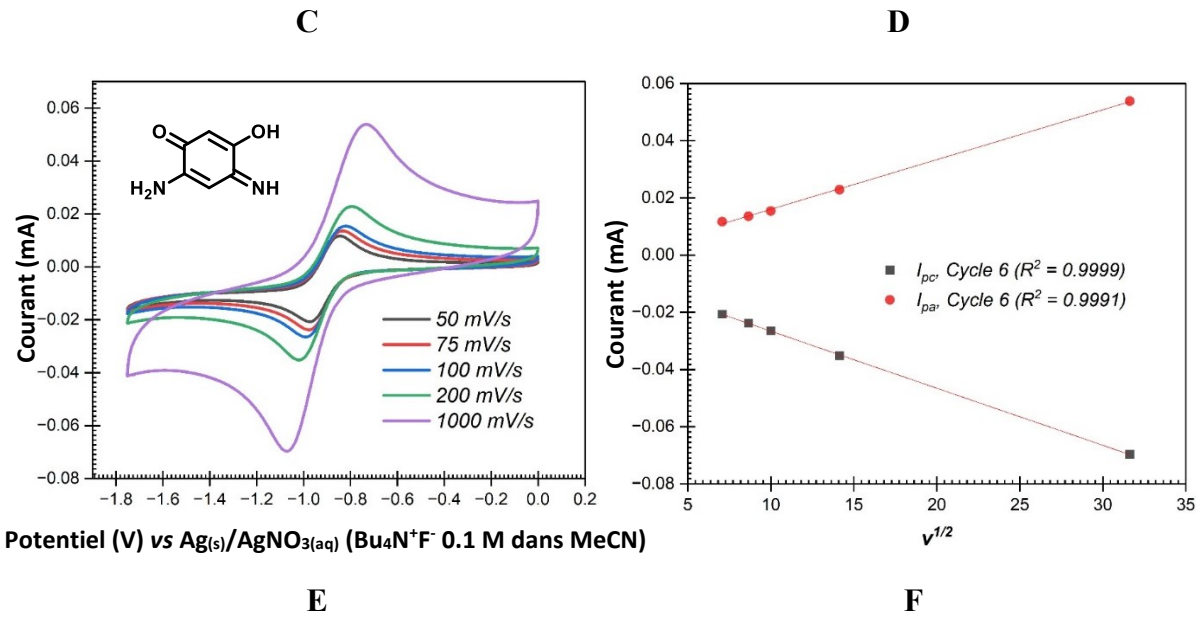

Figure 6.2 Voltampérogrammes cycliques (6^{e} cycle) de 1,2,4,5-BTA · 4HCl (**A**), DAR · 2HCl (**C**) et DAR-H_2 (**E**) enregistrés à différentes vitesses de balayage (v) et à 25 °C dans le MeCN sec purgé à l'argon avec $Bu_4N^+F^-$ utilisé comme électrolyte de support (0.1 M). Une électrode de travail en carbone vitreux, une électrode de référence d'Ag/$AgNO_3$, ainsi qu'un fil de Pt comme contre-électrode furent utilisés. Variation des courants de pics cathodiques (I_{pc}) et anodiques (I_{pa}) en fonction de $v^{½}$ de 1,2,4,5-BTA · 4HCl (**B**), DAR · 2HCl (**D**) et DAR-H_2 (**F**).

Annexe A

Informations supplémentaires

Chapitre 2

Redorer l'héritage de Rudolf Nietzki :

benzène-1,2,4,5-tétraamine et composés dérivés

Supporting Information

Refreshing the Legacy of Rudolf Nietzki:

Benzene-1,2,4,5-tetramine and Related Compounds

Johann O. E. Sosoe,* Cédric Malveau, Thierry Maris, Radu Iftimie, and James D. Wuest*

Département de Chimie, Université de Montréal, Montréal, Québec H2V 0B3 Canada

*Authors to whom correspondence may be addressed

Email: *johann.sosoe@umontreal.ca*; *james.d.wuest@umontreal.ca*

Annexe A

Contents **Page**

I. Additional Crystallographic Information

Single-crystal X-ray diffraction data for BTA (**1**), BTA (**1**) • 2HCl, BTA (**1**) • 4HCl, and BTA-H_2 (**2**) • 2HCl were collected on a Bruker Venture Kappa-geometry diffractometer equipped with a gallium liquid metal-jet source (GaKα radiation, λ = 1.34139 Å), a Photon III CMOS detector, and Helios MX mirror optics. Measurements for these compounds were carried out at 150 K using an Oxford Cryostream 700 low-temperature device. X-ray diffraction data for BTA-H_2 (**2**) were collected at 100 K on a 3-circle platform diffractometer equipped with an Incoatec Microfocus source (CuKα radiation, λ = 1.54179 Å) and an APEX2 CCD detector.

The unit-cell lattice parameters were determined by measurement of a limited set of frames using the *APEX4* suite of software.[1] Reflection data were integrated using *SAINT* V8.40B, and a multiscan absorption correction using *SADABS* was applied.[2] Structures were solved using the intrinsic phasing routine as implemented in *SHELXT*,[3] and cycles of refinement were performed by least-squares minimisation with *SHELXL*[4] within the graphical user interface of *OLEX2*.[5] All non-hydrogen atoms were refined using anisotropic thermal displacement parameters. For BTA (**1**), BTA (**1**) • 4HCl, and BTA-H_2 (**2**) • 2HCl, hydrogen atoms were located from Fourier difference maps and fully refined isotropically. For BTA (**1**) • 2HCl and BTA-H_2 (**2**), hydrogen atoms attached to carbon atoms were refined isotropically on calculated positions using standard riding models from *SHELXL*, with their U_{iso} constrained to 1.2 times the U_{eq} of their pivot, whereas hydrogen atoms attached to nitrogen were located from Fourier difference maps and fully refined isotropically.

II. Thermal Atomic Displacement Parameter Plots and Other Crystallographic Figures

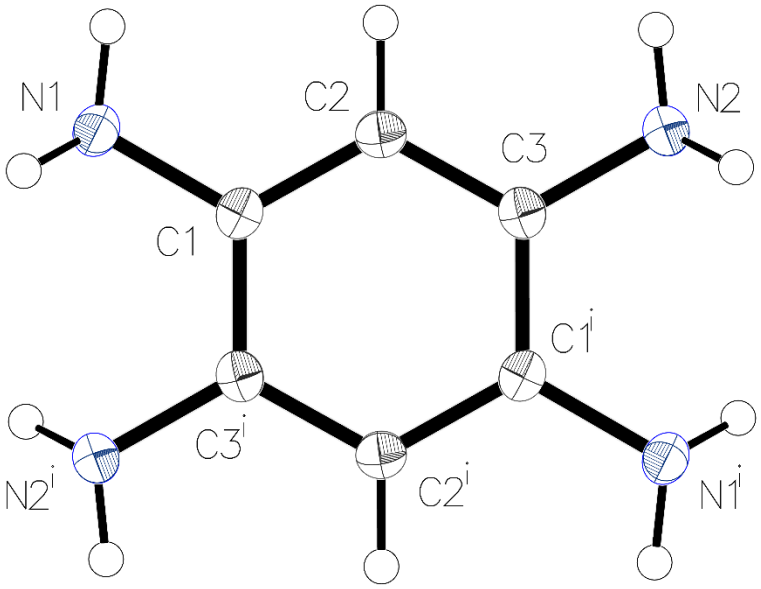

Figure A1. Thermal atomic displacement ellipsoid plot of the structure of BTA (**1**) with the atomic numbering scheme. The ellipsoids of non-hydrogen atoms are drawn at the 50% probability level, and hydrogen atoms are represented by a sphere of arbitrary size. Symmetry Codes (i): 1-x, 1-y, 1-z.

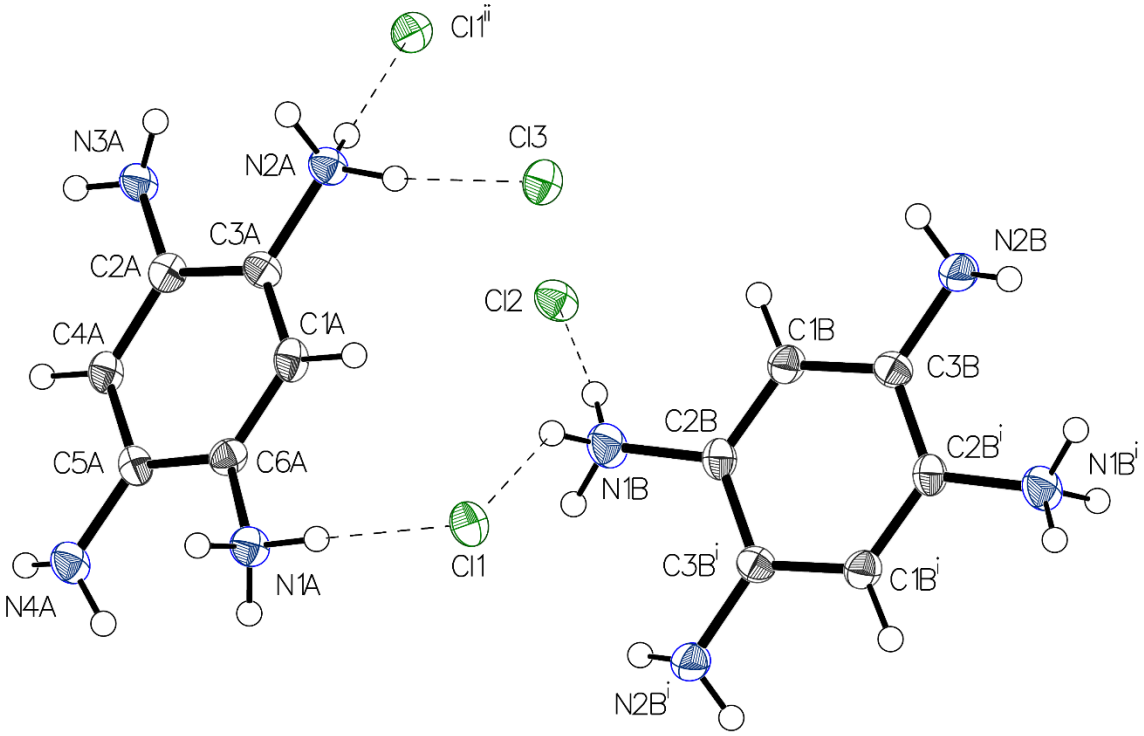

Figure A2. Thermal atomic displacement ellipsoid plot of the structure of BTA (**1**) • 2 HCl with the atomic numbering scheme. The ellipsoids of non-hydrogen atoms are drawn at the 50% probability level, and hydrogen atoms are represented by a sphere of arbitrary size. Symmetry Codes (i): 2-x, 1-y, 1-z.

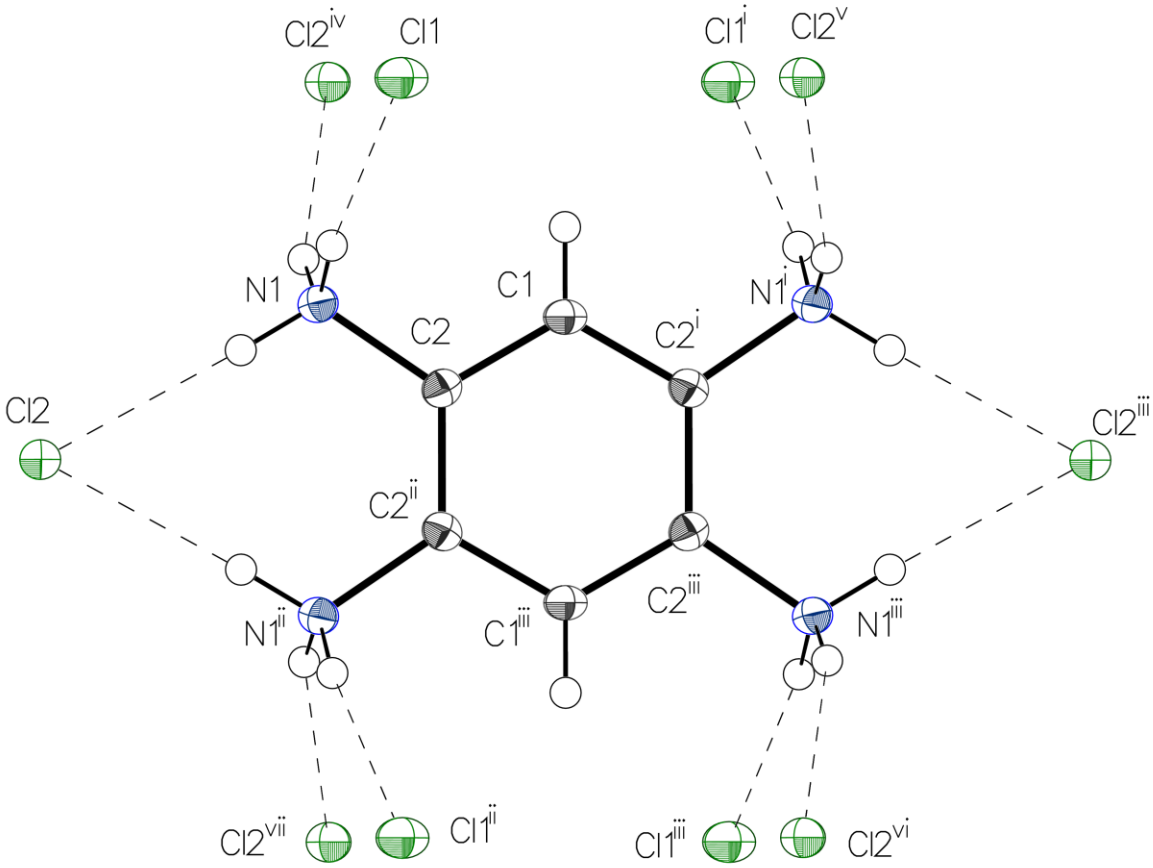

Figure A3. Thermal atomic displacement ellipsoid plot of the structure of BTA (**1**) • 4 HCl with the atomic numbering scheme. The ellipsoids of non-hydrogen atoms are drawn at the 50% probability level, and hydrogen atoms are represented by a sphere of arbitrary size. Symmetry Codes (i): 2-x, 1-y, z; (ii): x, y, -z; (iii): 2-x, 1-y, -z; (iv): 1/2+x, 3/2-y, 1/2-z; (v): 3/2-x, y-1/2, 1/2-z; (vi): 3/2-x, y-1/2, 1/2+z; (vii): 1/2+x, 3/2-y, z-1/2.

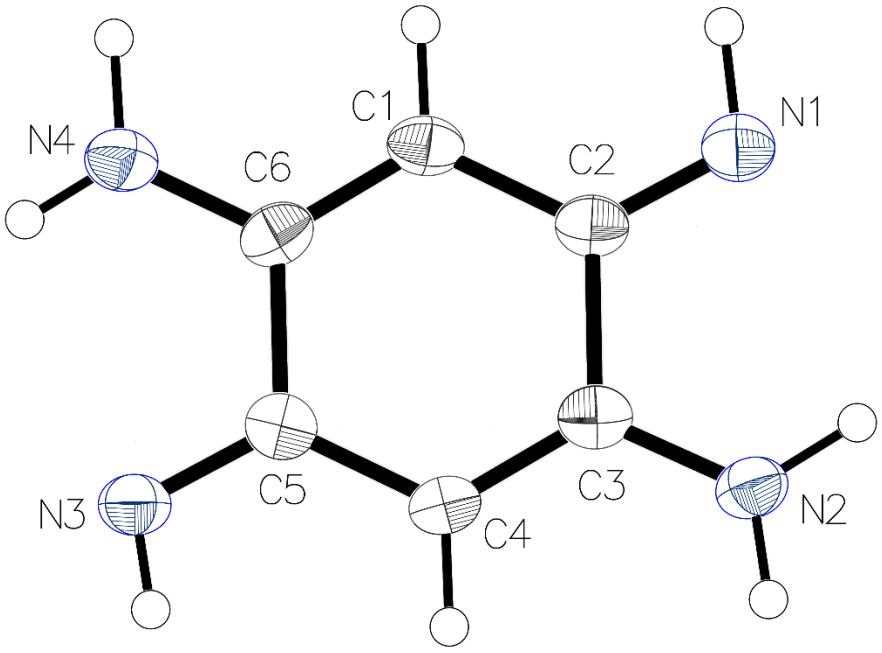

Figure A4. Thermal atomic displacement ellipsoid plot of the structure of BTA-H_2 (**2**) with the atomic numbering scheme. The ellipsoids of non-hydrogen atoms are drawn at the 50% probability level, and hydrogen atoms are represented by a sphere of arbitrary size.

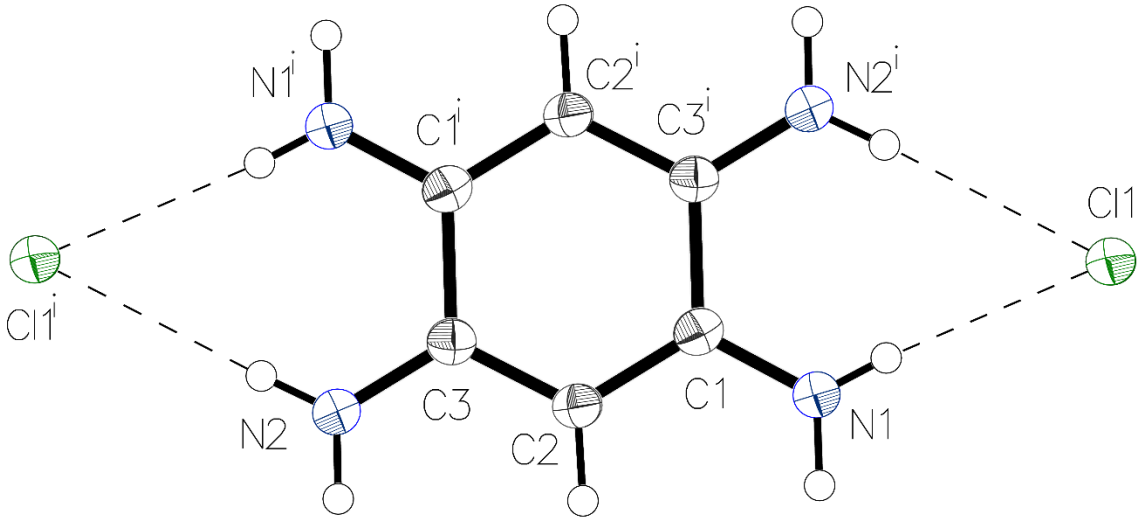

Figure A5. Thermal atomic displacement ellipsoid plot of the structure of BTA-H_2 (**2**) • 2 HCl with the atomic numbering scheme. The ellipsoids of non-hydrogen atoms are drawn at the 50% probability level, and hydrogen atoms are represented by a sphere of arbitrary size. Symmetry Codes (i): 1-x, 1-y, 1-z.

III. Additional Spectroscopic Data

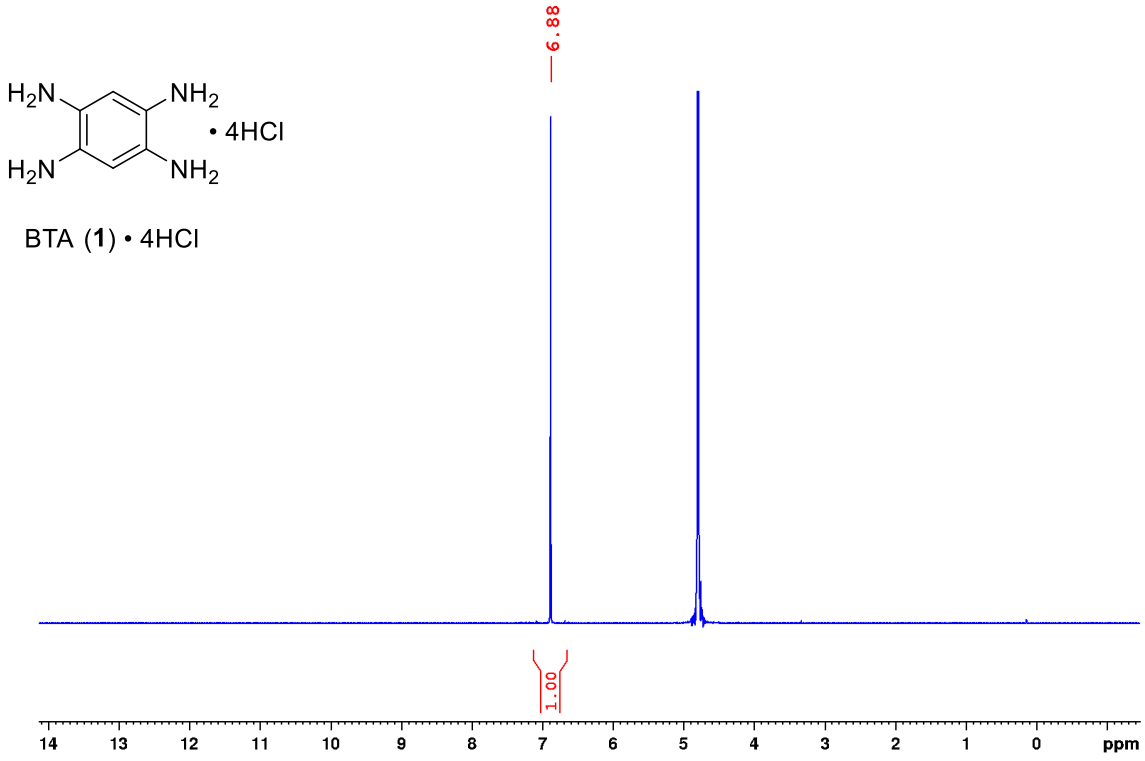

Figure A6. ^{1}H NMR spectrum of tetrahydrochloride salt BTA (**1**) • 4HCl (400 MHz, D_2O).

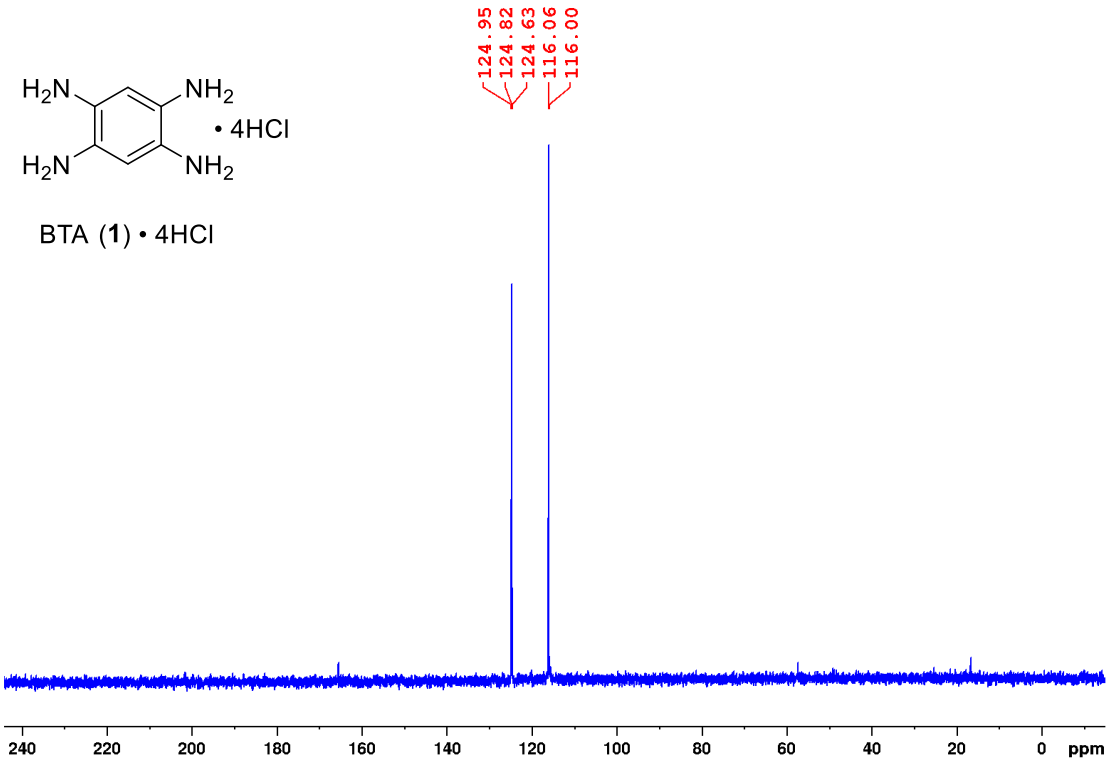

Figure A7. $^{13}C\{^{1}H\}$ NMR spectrum of tetrahydrochloride salt BTA (**1**) • 4HCl (101 MHz, D_2O).

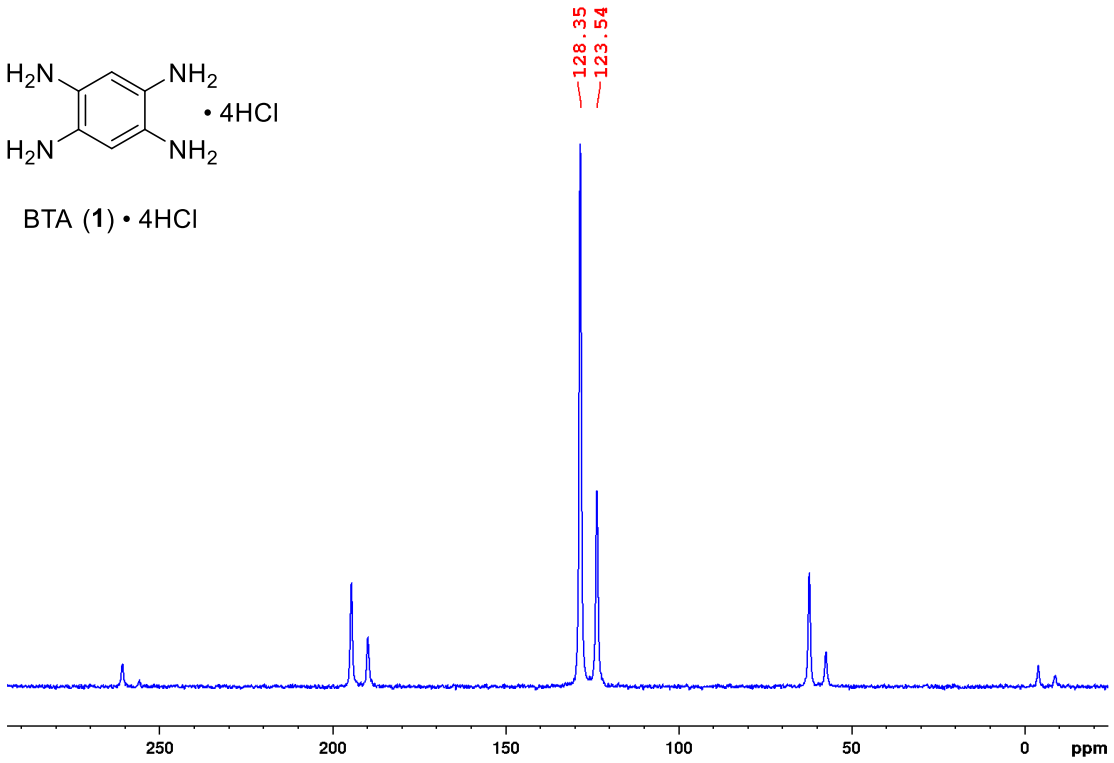

Figure A8. CP/MAS $^{13}C\{^{1}H\}$ NMR spectrum of tetrahydrochloride salt BTA (**1**) • 4HCl (151 MHz, 10 kHz).

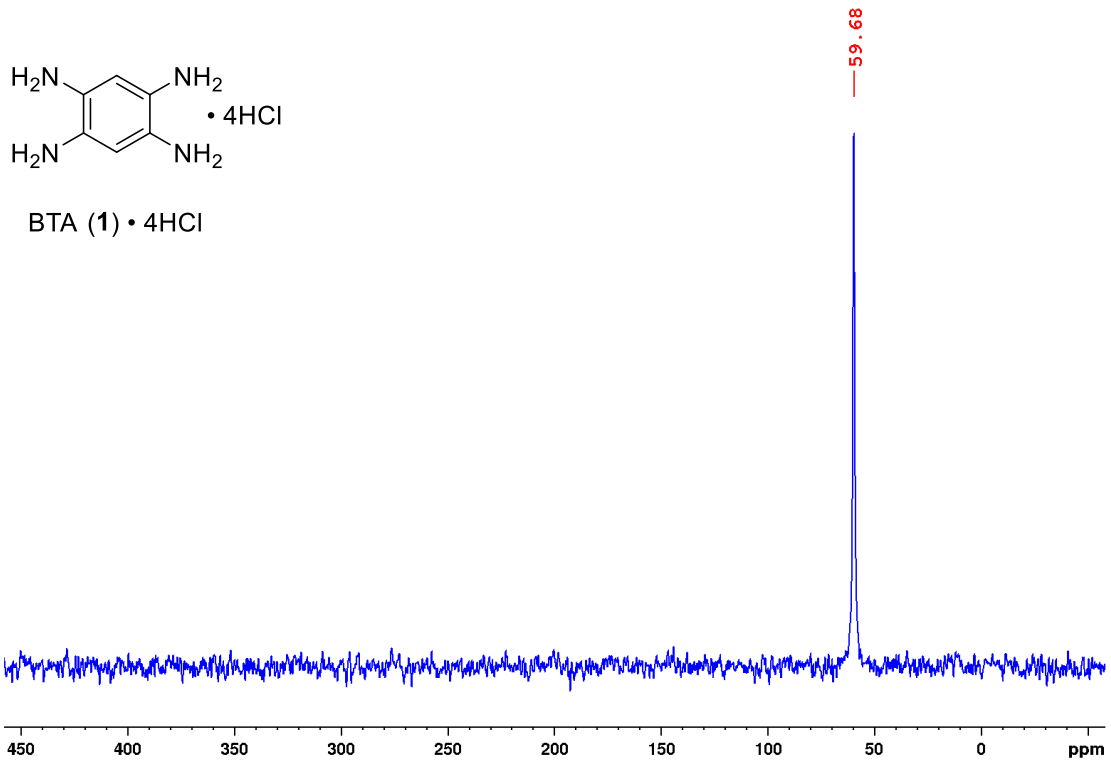

Figure A9. CP/MAS $^{15}N\{^{1}H\}$ NMR spectrum of tetrahydrochloride salt BTA (**1**) • 4HCl (61 MHz, 10 kHz).

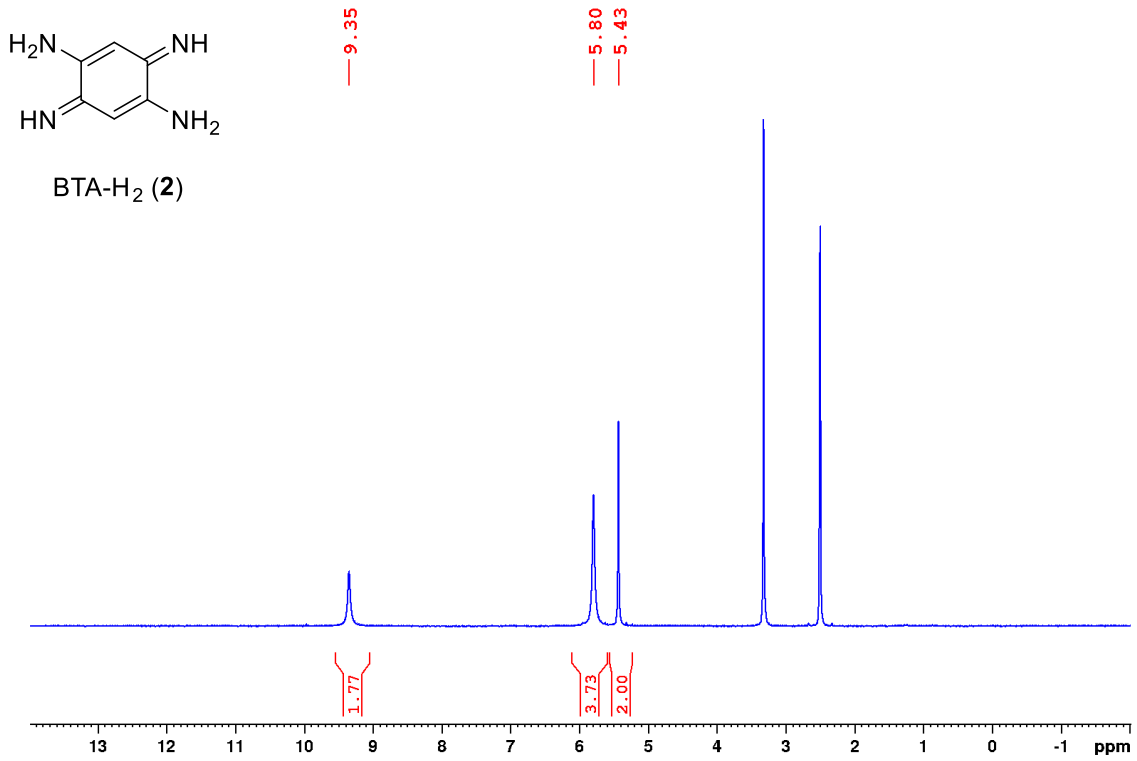

Figure A10. ^{1}H NMR spectrum of BTA-H_2 (**2**) (400 MHz, DMSO-d_6).

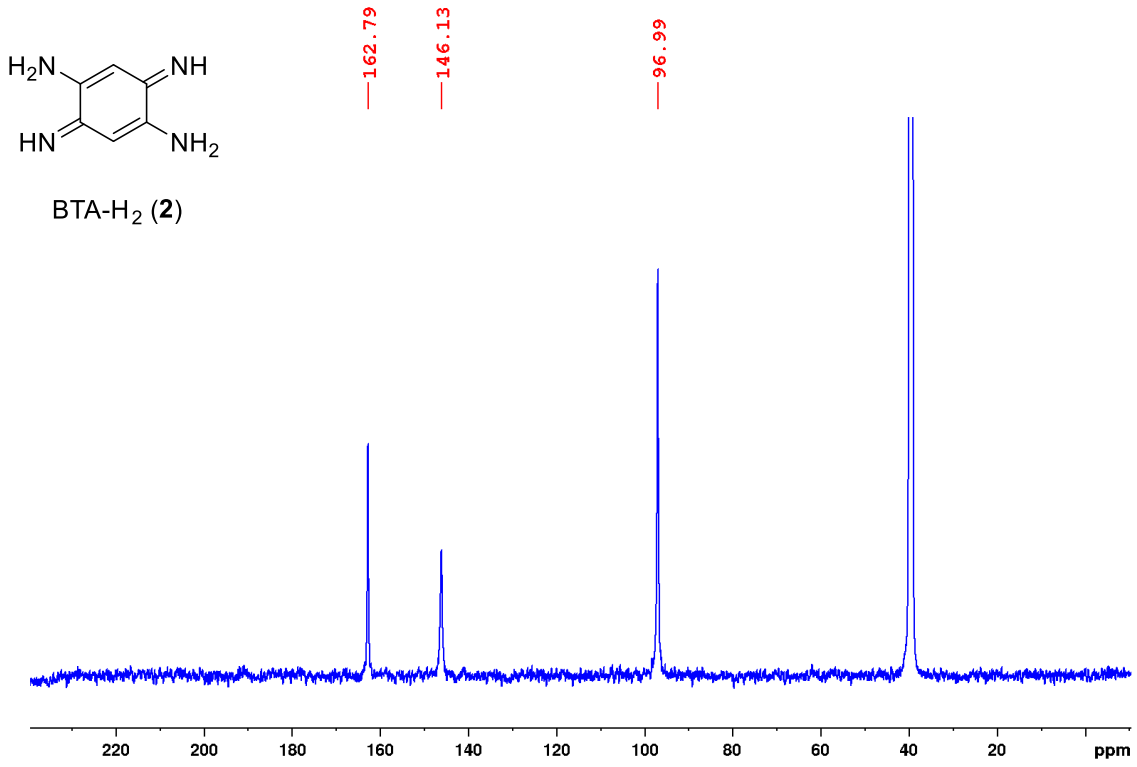

Figure A11. $^{13}C\{^{1}H\}$ NMR spectrum of BTA-H_2 (**2**) (101 MHz, DMSO-d_6).

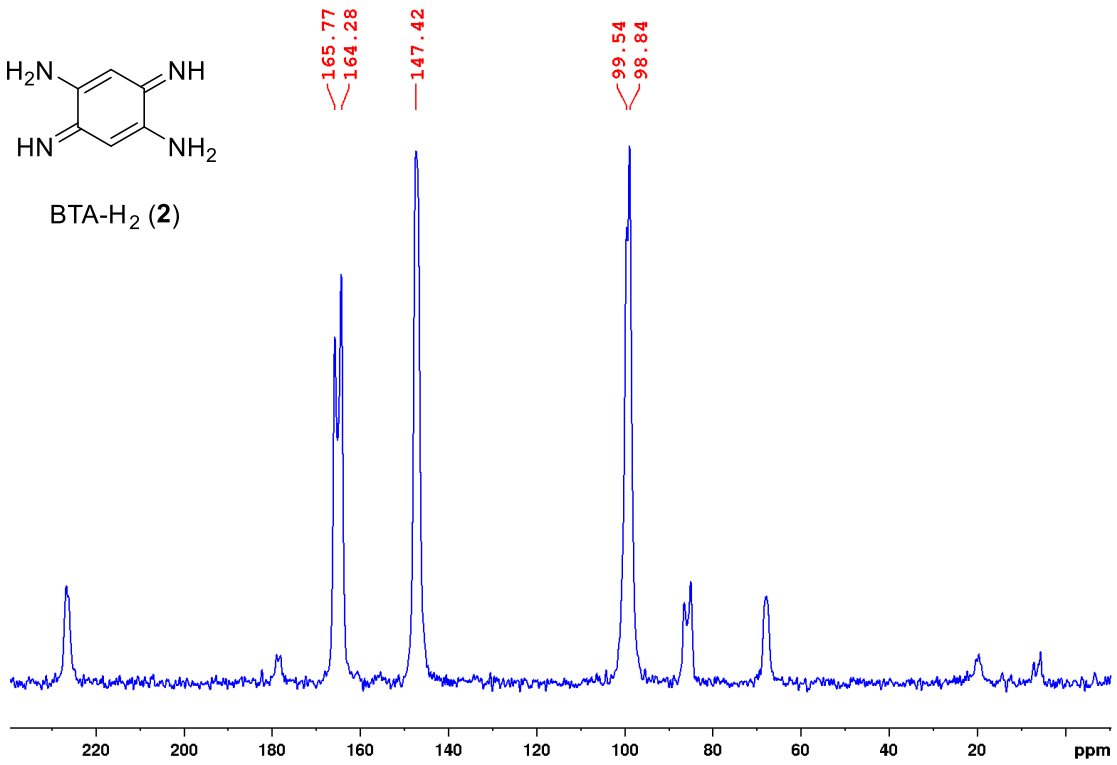

Figure A12. CP/MAS $^{13}C\{^{1}H\}$ NMR spectrum of BTA-H_2 (**2**) (151 MHz, 12 kHz).

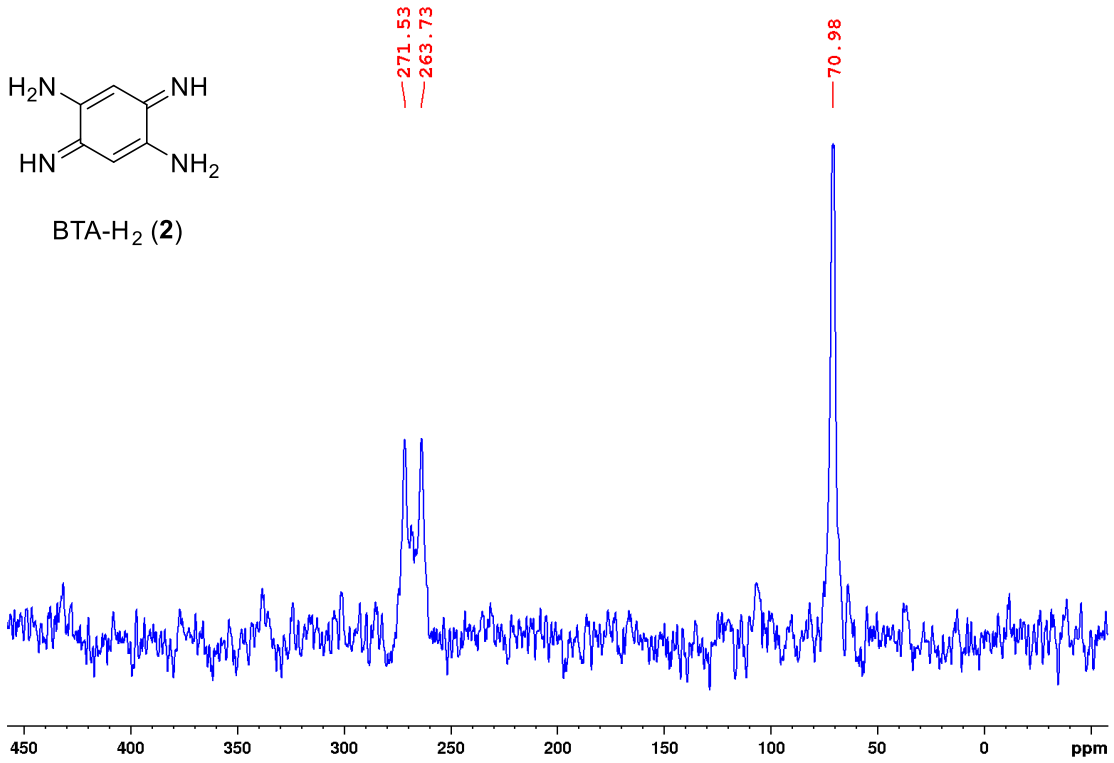

Figure A13. CP/MAS $^{15}N\{^{1}H\}$ NMR spectrum of BTA-H_2 (**2**) (61 MHz, 10 kHz).

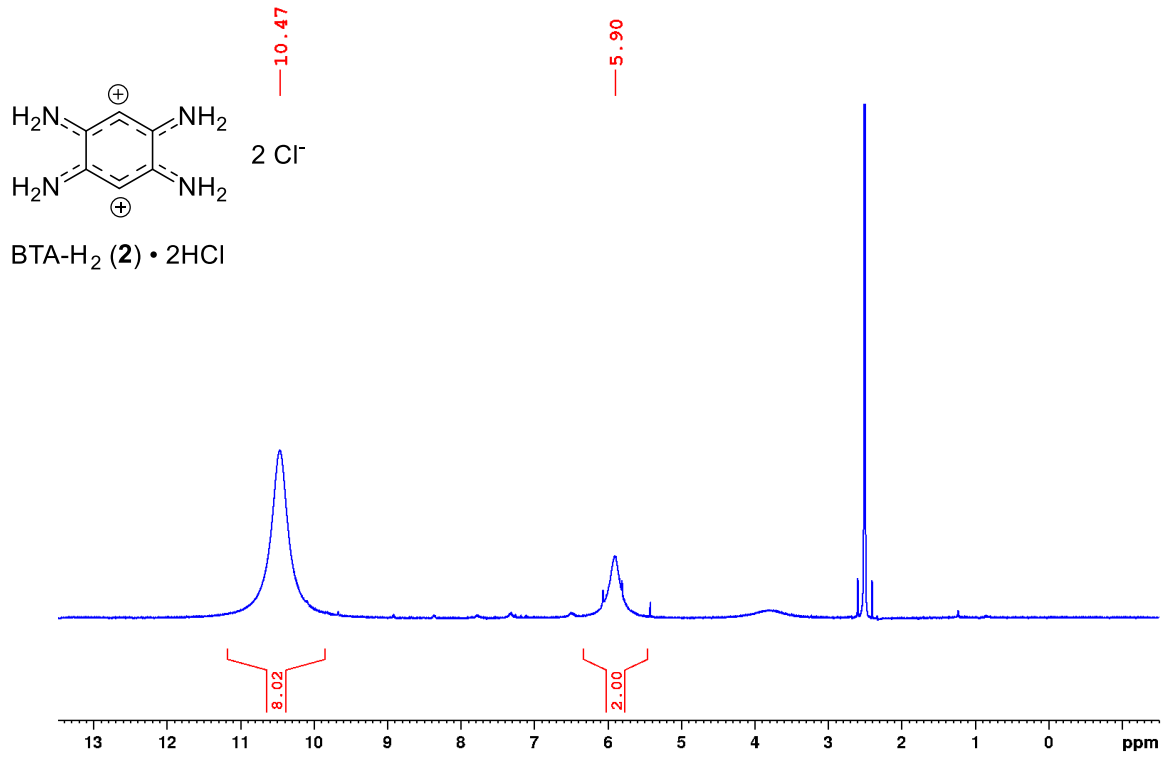

Figure A14. ^{1}H NMR spectrum of BTA-H_2 (**2**) • 2HCl (700 MHz, DMSO-d_6).

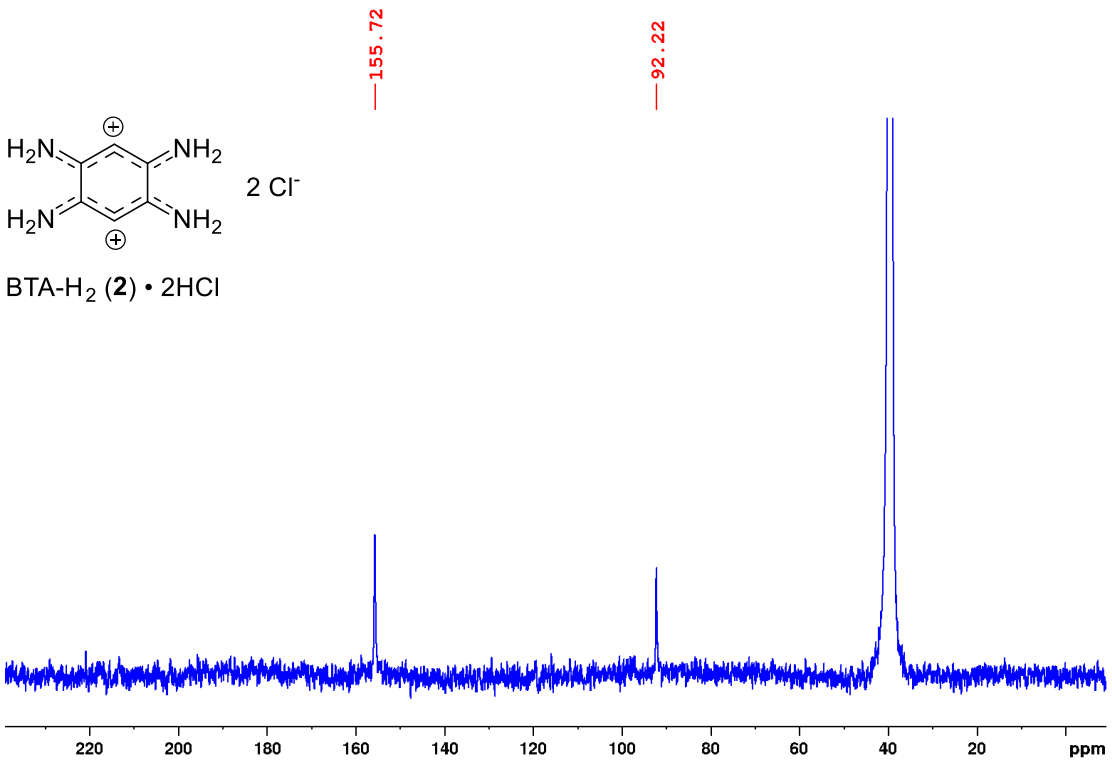

Figure A15. $^{13}C\{^{1}H\}$ NMR spectrum of BTA-H_2 (**2**) • 2HCl (176 MHz, DMSO-d_6).

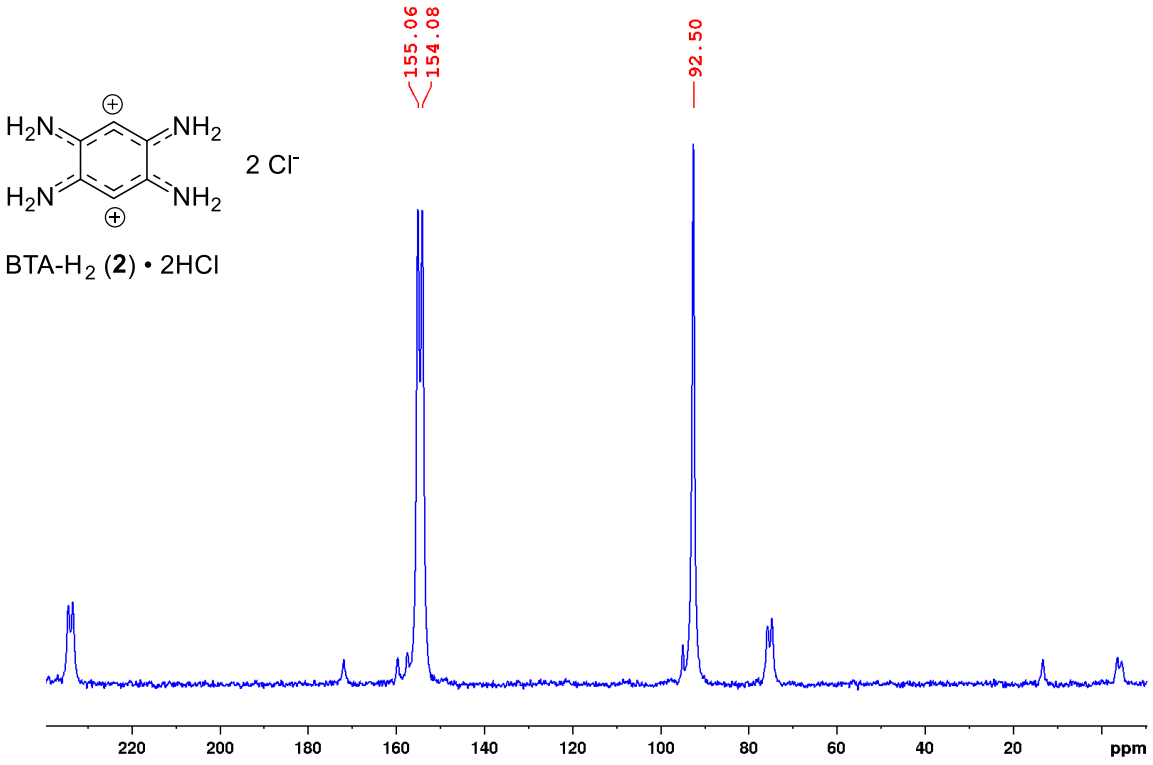

Figure A16. CP/MAS $^{13}C\{^{1}H\}$ NMR spectrum of BTA-H_2 (**2**) • 2HCl (151 MHz, 12 kHz).

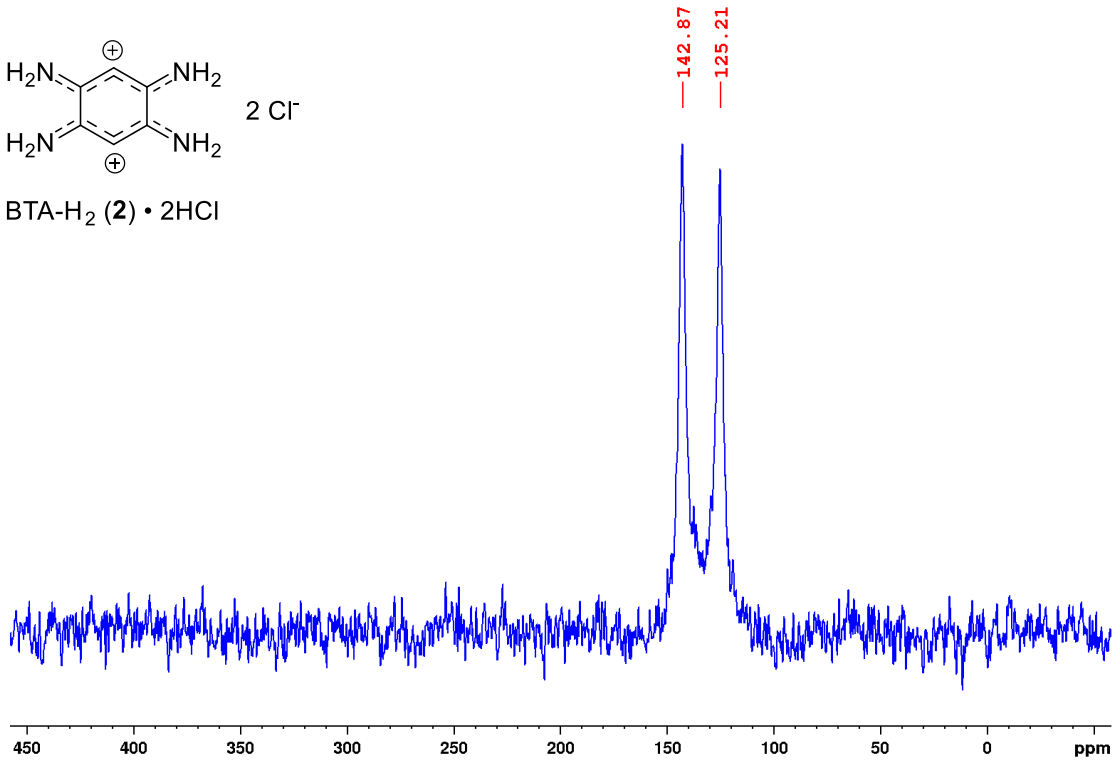

Figure A17. CP/MAS $^{15}N\{^{1}H\}$ NMR spectrum of BTA-H_2 (**2**) • 2HCl (61 MHz, 10 kHz).

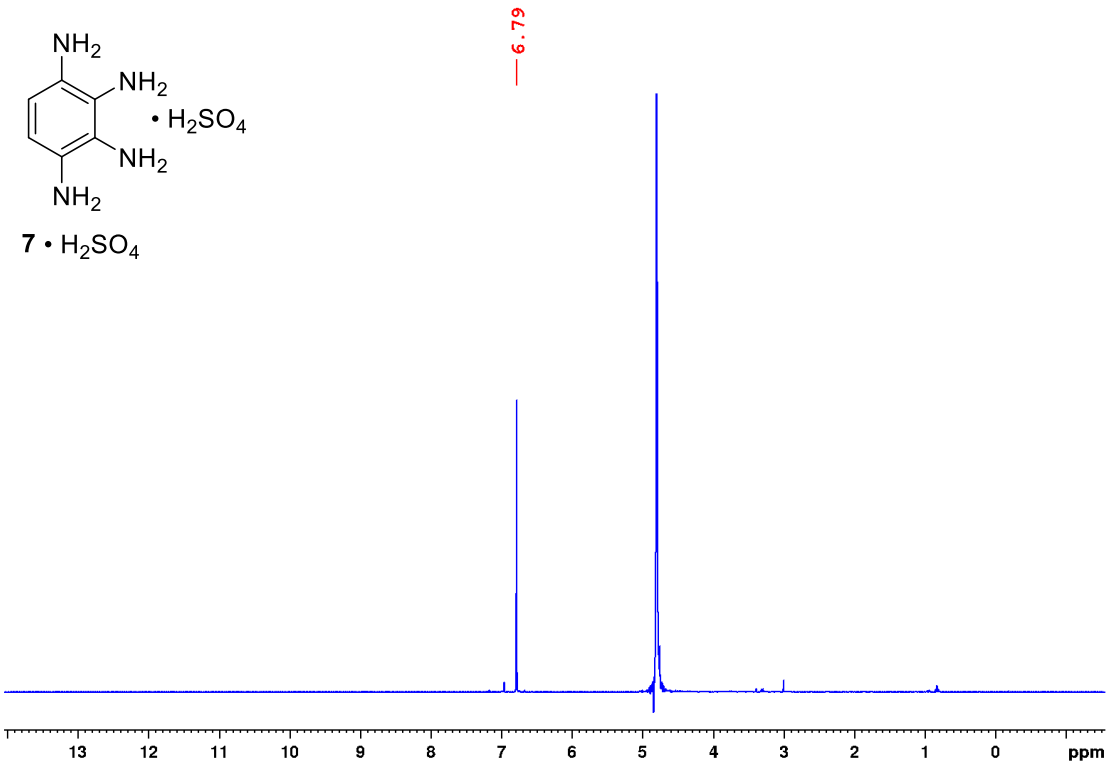

Figure A18. ^{1}H NMR spectrum (400 MHz, D_2O/DCl) of the sulfate salt of benzene-1,2,3,4-tetramine (**7** • H_2SO_4).

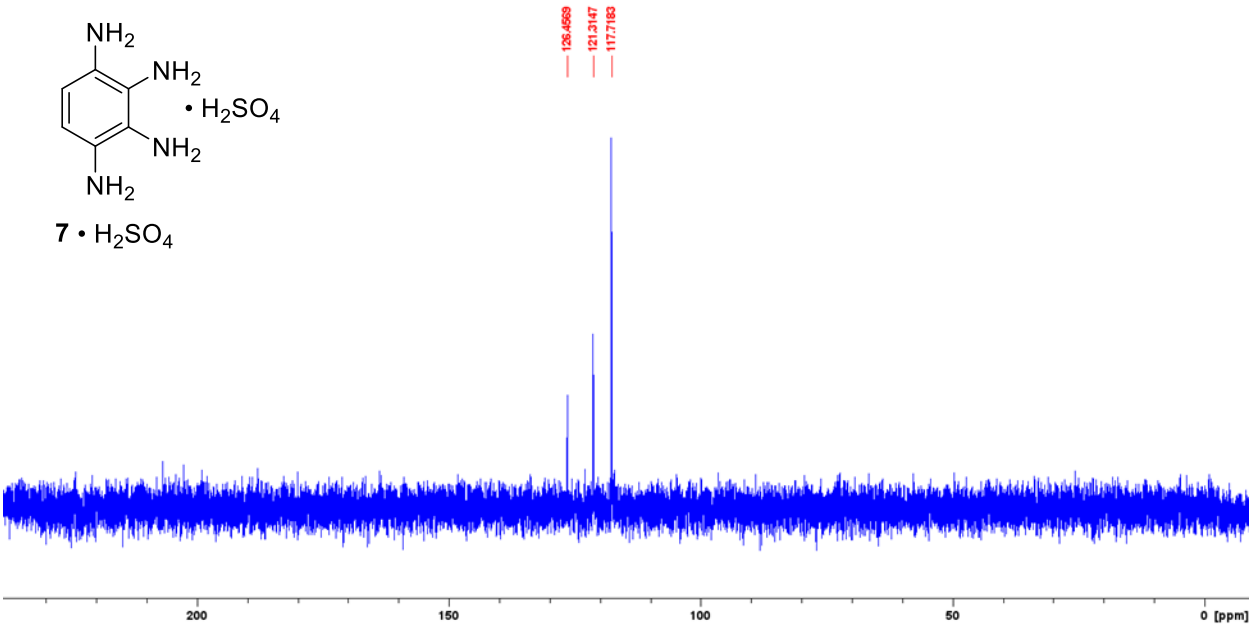

Figure A19. $^{13}C\{^{1}H\}$ NMR spectrum (101 MHz, D_2O/DCl) of the sulfate salt of benzene-1,2,3,4-tetramine (**7** • H_2SO_4).

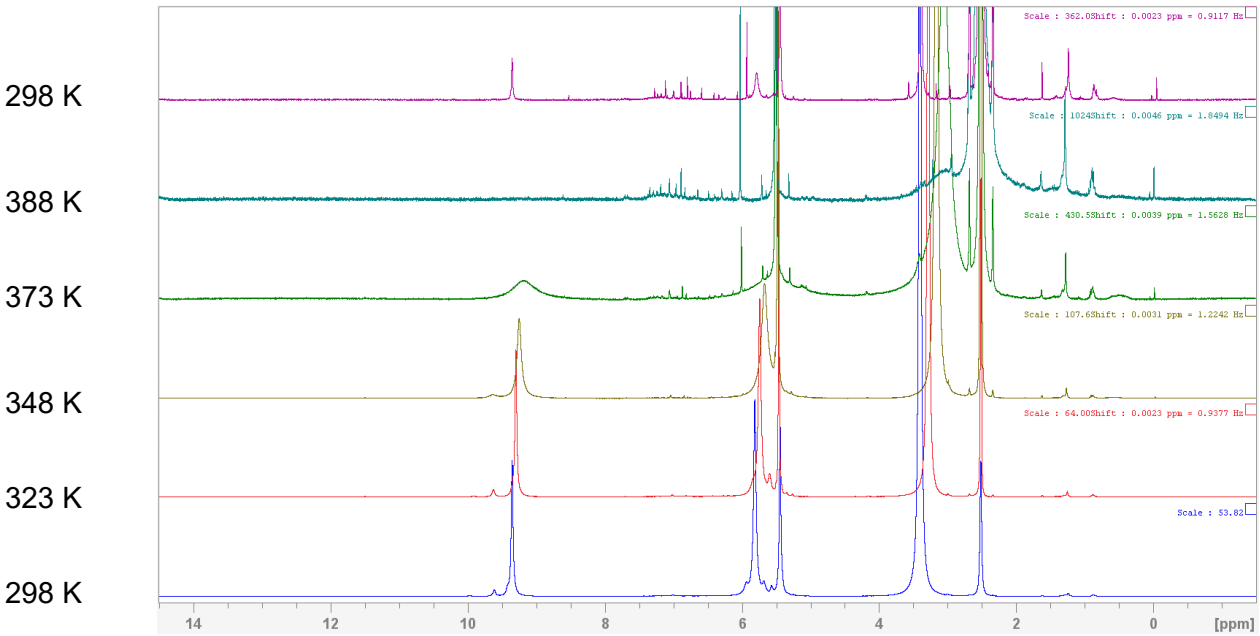

Figure A20. Variable-temperature ^{1}H NMR spectra (400 MHz) of a saturated solution of BTA-H_2 (**2**) in DMSO-d_6 containing a small amount of NaOH. An initial spectrum (blue) and a final spectrum (purple) were recorded at 25 °C before and after the sample was heated. Broadening, shifting, and coalescence of the two downfield signals are observed, but the final spectra show that decomposition of compound **2** occurs simultaneously.

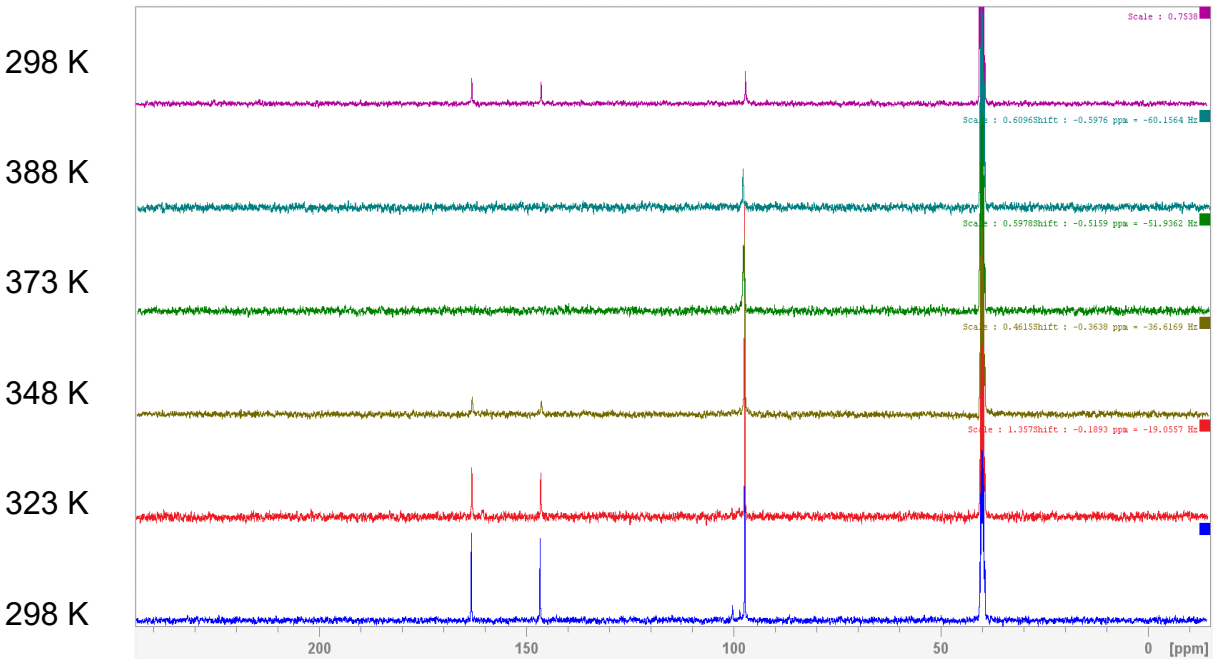

Figure A21. Variable-temperature $^{13}C\{^{1}H\}$ NMR spectra (101 MHz) of a saturated solution of BTA-H_2 (**2**) in DMSO-d_6 containing a small amount of NaOH. An initial spectrum (blue) and a final spectrum (purple) were recorded at 25 °C before and after the sample was heated. Broadening and coalescence of the two downfield signals are observed, but the final spectrum shows that decomposition of compound **2** occurs simultaneously.

IV. Supplementary Computational Information

A. This section provides the Cartesian coordinates and electronic potential energies (EE) for structures in Tables II - 3, 4, and 5 of the main paper. The data are presented in the following way:

- The number of the structure as it appears in the main paper is given first, followed by the density functional and basis set used to obtain the optimized structure. All geometric optimizations used RωB97X-D3/6-311+G(2df,2p), as stated in the main article.
- The next line describes the medium (gas phase or C-PCM), along with the energy value obtained at the geometric optimization level.
- Next, the single-point electronic energy value obtained at the RωB97M-V/QZVPPD level is provided, based on the geometry optimized at the RωB97X-D3/6-311+G(2df,2p) level.
- Finally the single-point electronic energy value obtained at the RωB97M(2)/QZVPPD level is given, as determined using electronic orbitals previously optimized at the RωB97M-V/QZVPPD level.

1) Structure **2** (BTA-H_2) Optimization level: RωB97X-D3/6-311+G(2df,2p)

1a) Medium: Gas phaseEE(RωB97X-D3/6-311+G(2df,2p)) = - 452.462466 a.u.0 imaginary frequencies
EE(RωB97M-V/QZVPPD) = -452.484553 a.u.
EE(RωB97M(2)/QZVPPD) = -452.786324 a.u.
0 1

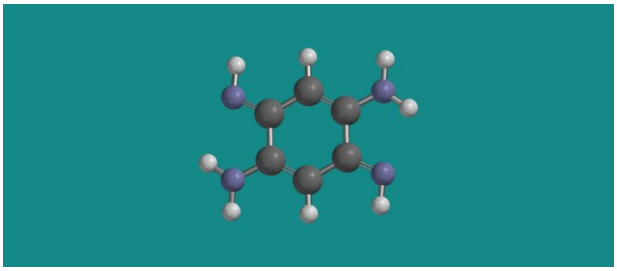

Standard Nuclear Orientation (Angstroms)

I	Atom	X	Y	Z
1	N	-1.5039068353	-0.0397411475	2.2581110907
2	H	-2.5061606982	-0.0035396378	2.0961538717
3	C	-1.4170831935	0.0608678007	-0.1690510612
4	H	-2.4973538985	0.0981623556	-0.2522802846
5	N	1.0950620201	-0.0985248036	2.5447494796
6	H	0.4020060461	-0.1571027990	3.2728879477
7	H	2.0651156977	-0.2316242210	2.7514352072
8	C	-0.8533701869	-0.0092763548	1.1569605622
9	N	1.5041236908	0.0400073139	-2.2580623635
10	H	2.5063932834	0.0038729570	-2.0961245001
11	C	0.6415588313	-0.0622435532	1.2769784975
12	N	-1.0952826665	0.0984688022	-2.5447136488
13	H	-2.0655120941	0.2306748908	-2.7512487866
14	H	-0.4026194338	0.1566469289	-3.2732443169
15	C	1.4173155624	-0.0606144982	0.1691417479
16	H	2.4975640602	-0.0979685896	0.2522069817
17	C	0.8535795706	0.0095458366	-1.1569136757
18	C	-0.6414297558	0.0623887191	-1.2769867486

1b) Medium: C-PCM, ε = 78.3EE(RωB97X-D3/6-311+G(2df,2p)) = - 452.481553 a.u.0 imaginary frequencies
EE(RωB97M-V/QZVPPD) = -452.502877 a.u.
EE(RωB97M(2)/QZVPPD) = -452.804488 a.u.
0 1

Standard Nuclear Orientation (Angstroms)

I	Atom	X	Y	Z
1	N	-1.5310205082	-0.0285875620	2.2454408660
2	H	-2.5287821289	0.0035728645	2.0494620214
3	C	-1.4152044815	0.0577231949	-0.1724227441
4	H	-2.4950484378	0.0939240400	-0.2606446070
5	N	1.1101879941	-0.0677473513	2.5436795281
6	H	0.4483030247	-0.1924289237	3.2908234986
7	H	2.0825645730	-0.2412479393	2.7242195844
8	C	-0.8567900830	-0.0041700133	1.1544233519
9	N	1.5313592009	0.0287459672	-2.2451419034
10	H	2.5291060868	-0.0041660027	-2.0491654728
11	C	0.6383220938	-0.0519850166	1.2828477515
12	N	-1.1100083521	0.0722120362	-2.5431657008
13	H	-2.0839772283	0.2349490556	-2.7249342397
14	H	-0.4487270719	0.1878204757	-3.2922007541
15	C	1.4154726825	-0.0560167271	0.1728118022
16	H	2.4953001771	-0.0923763134	0.2608539754
17	C	0.8570624631	0.0056030019	-1.1542013832
18	C	-0.6381200046	0.0541752134	-1.2826855744

2) Structure **11** Optimization level: RωB97X-D3/6-311+G(2df,2p)

2a) Medium: Gas phaseEE(RωB97X-D3/6-311+G(2df,2p)) = - 452.452210 a.u. 0 imaginary frequencies
EE(RωB97M-V/QZVPPD) = -452.475069 a.u.
EE(ωB97M(2)/QZVPPD) = -452.777421 a.u.

0 1

Standard Nuclear Orientation (Angstroms)

I	Atom	X	Y	Z
1	N	0.8103016001	-2.5093763142	0.5587697246
2	H	1.6424210301	-2.5158652611	1.1420781246
3	C	1.1291710787	-0.1054135027	0.6902713754
4	H	2.0680970365	-0.2230887198	1.2209875205
5	N	-1.2868336331	-2.3319248583	-1.0412296762
6	H	-0.9150222900	-3.1727270005	-0.6305391079
7	H	-2.2195817482	-2.3494613646	-1.4070608503
8	C	0.4475832345	-1.3187475574	0.2747359046
9	N	-1.2802258858	2.3815281968	-0.4211756223
10	H	-0.7983063867	3.1413510406	0.0505880388
11	C	-0.7704972349	-1.1665626357	-0.5749578133
12	N	1.2647811793	2.2776179455	0.8271523155
13	H	2.1964809836	2.1730860409	1.1903540866
14	H	1.1704650556	3.0738255783	0.2198300088
15	C	-1.2648621703	0.0611572754	-0.8270929299
16	H	-2.1688563400	0.1995487095	-1.4059099723
17	C	-0.6691776258	1.2662698782	-0.2887257732
18	C	0.6440621165	1.1187825495	0.4219246461

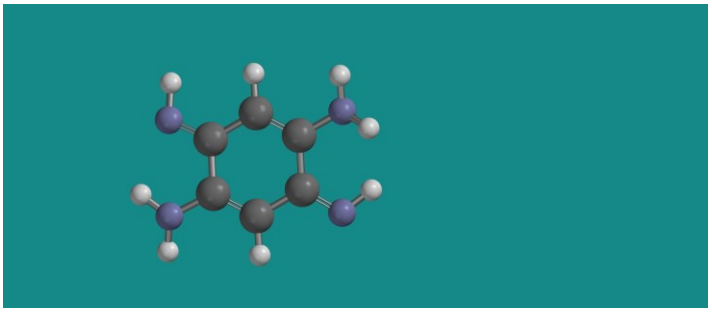

2b) Medium: C-PCM, ε = 78.3EE(RωB97X-D3/6-311+G(2df,2p)) = - 452.476234 a.u.0 imaginary frequencies
EE(RωB97M-V/QZVPPD) = -452.498017 a.u.
EE(ωB97M(2)/QZVPPD) = -452.800095 a.u.

0 1

Standard Nuclear Orientation (Angstroms)

I	Atom	X	Y	Z
1	N	0.8511933662	-2.5091705587	0.5388817923
2	H	1.6931856665	-2.4896644126	1.1098238228
3	C	1.1314801415	-0.1089452511	0.6869907461
4	H	2.0648505235	-0.2219178859	1.2274307427
5	N	-1.3040461329	-2.3315919655	-1.0347234460
6	H	-0.9718479265	-3.1853688925	-0.6178560003
7	H	-2.2407881913	-2.3299042244	-1.3990139501
8	C	0.4612274890	-1.3209236081	0.2659629026
9	N	-1.2616692752	2.3839261745	-0.4653737649
10	H	-0.7612552602	3.1541450044	-0.0322565693
11	C	-0.7732608068	-1.1770425745	-0.5662790225
12	N	1.2538615474	2.2658882550	0.8528226980
13	H	2.1866942679	2.1620811504	1.2186203253
14	H	1.1446619193	3.0988731257	0.2976905461
15	C	-1.2715494205	0.0534310230	-0.8154893945
16	H	-2.1832285374	0.1741611169	-1.3876393687
17	C	-0.6640207018	1.2612636768	-0.3025822258
18	C	0.6445113317	1.1207598473	0.4229901662

3) Structure **12** Optimization level: RωB97X-D3/6-311+G(2df,2p)

3a) Medium: Gas phaseEE(RωB97X-D3/6-311+G(2df,2p)) = - 452.445411 a.u. 0 imaginary frequencies
EE(RωB97M-V/QZVPPD) = -452.468481 a.u.
EE(ωB97M(2)/QZVPPD) = -452.770463 a.u.

0 1

Standard Nuclear Orientation (Angstroms)

I	Atom	X	Y	Z
1	C	-0.1369644040	-0.3125236014	-1.4836470517
2	C	0.1300830357	-0.2673491387	1.3528001581
3	C	-0.0593783555	0.8533886567	-0.8292418746
4	C	-0.0925819763	-1.5928256564	-0.7916649261
5	C	0.0993777298	-1.5685298263	0.7108360911
6	C	0.0325102365	0.8766035880	0.6480868561
7	H	-0.2102469202	-0.3496541751	-2.5634124376
8	H	0.2000229580	-0.2348369811	2.4345843217
9	N	-0.1326352884	2.1009156253	-1.4507771172
10	H	0.5718549971	2.7545191434	-1.1420161813
11	H	-0.1548157842	2.0461261197	-2.4564577442
12	N	0.0642148263	2.1306086129	1.2228365937
13	H	-0.0143834409	2.1510215093	2.2253175849
14	H	-0.5071180452	2.8240590035	0.7669663743
15	N	-0.1851748874	-2.6756579311	-1.4502677868
16	H	-0.1115506651	-3.4588172359	-0.7974972736
17	N	0.1930454616	-2.6953634273	1.3003688513
18	H	0.3137405221	-2.5816842856	2.3031855618

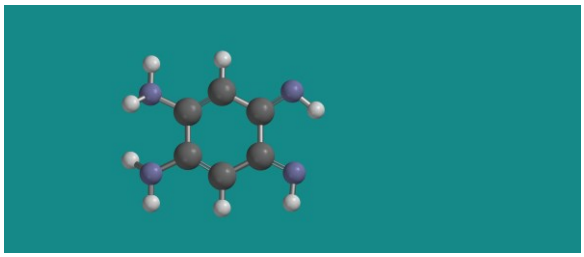

3b) Medium: C-PCM, ε = 78.3EE(RωB97X-D3/6-311+G(2df,2p)) = - 452.472296 a.u.0 imaginary frequencies
EE(RωB97M-V/QZVPPD) = -452.494049 a.u.
EE(ωB97M(2)/QZVPPD) = -452.795708 a.u.

0 1

Standard Nuclear Orientation (Angstroms)

I	Atom	X	Y	Z
1	C	-0.1451812509	-0.3245697617	-1.4921497920
2	C	0.1293450521	-0.2727041251	1.3448169004
3	C	-0.0658906189	0.8536520080	-0.8404145651
4	C	-0.0903060849	-1.5931721368	-0.8025849325
5	C	0.0898299467	-1.5642044943	0.7050804798
6	C	0.0323570752	0.8812400230	0.6442680835
7	H	-0.2191227735	-0.3448213554	-2.5725956975
8	H	0.2028051854	-0.2405720611	2.4258478160
9	N	-0.1347921265	2.0668251973	-1.4782019809
10	H	0.4199687869	2.8171306176	-1.0970687834
11	H	-0.0831959610	2.0293856038	-2.4841241760
12	N	0.0717387369	2.1105097441	1.2343362780
13	H	0.0114453078	2.1307543028	2.2395040652
14	H	-0.4233217836	2.8652040249	0.7881650558
15	N	-0.1643375552	-2.6955149913	-1.4463261198
16	H	-0.0849393001	-3.4647048275	-0.7793609151
17	N	0.1691651233	-2.6929881937	1.3043019268
18	H	0.2844322401	-2.5614495743	2.3065063568

4)Structure **13** Optimization level: RωB97X-D3/6-311+G(2df,2p)

4a) Medium: Gas phaseEE(RωB97X-D3/6-311+G(2df,2p)) = - 452.439655 a.u. 0 imaginary frequencies
EE(RωB97M-V/QZVPPD) = -452.461269 a.u.
EE(ωB97M(2)/QZVPPD) = -452.763253 a.u.

0 1

Standard Nuclear Orientation (Angstroms)

I	Atom	X	Y	Z
1	C	0.0004277265	0.0000000000	-1.3614609904
2	H	0.0004691229	0.0000000000	-2.4449127415
3	C	1.1922117735	0.0000000000	-0.6557815465
4	C	-1.1915613058	0.0000000000	-0.6559541273
5	C	-1.2323229624	0.0000000000	0.8561699114
6	C	1.2325439165	0.0000000000	0.8562551499
7	C	0.0000319506	0.0000000000	1.5255514538
8	H	-0.0002462686	0.0000000000	2.6087185067
9	N	2.3785000405	0.0000000000	-1.2254639926
10	H	2.5054532798	0.0000000000	-2.2199049135
11	N	-2.3782705839	0.0000000000	-1.2249742396
12	H	-2.5066059255	0.0000000000	-2.2192369192
13	N	2.4449425213	0.0000000000	1.3190465982
14	H	2.4526744908	0.0000000000	2.3327363332
15	N	-2.4450926458	0.0000000000	1.3183446230
16	H	-3.1570353239	0.0000000000	-0.5697807653
17	H	3.1579436025	0.0000000000	-0.5713613648
18	H	-2.4540634085	0.0000000000	2.3320090252

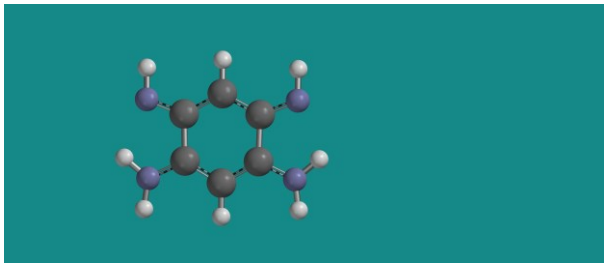

4b) Medium: C-PCM, ε = 78.3EE(RωB97X-D3/6-311+G(2df,2p)) = - 452.466538 a.u.0 imaginary frequencies
EE(RωB97M-V/QZVPPD) = -452.487299 a.u.
EE(ωB97M(2)/QZVPPD) = -452.788942 a.u.

0 1

Standard Nuclear Orientation (Angstroms)

I	Atom	X	Y	Z
1	C	0.0003952554	0.0000000000	-1.3436906662
2	H	0.0004338081	0.0000000000	-2.4263630732
3	C	1.1985624805	0.0000000000	-0.6478120030
4	C	-1.1979431631	0.0000000000	-0.6479677320
5	C	-1.2353915474	0.0000000000	0.8637918703
6	C	1.2356364710	0.0000000000	0.8638767661
7	C	0.0000588469	0.0000000000	1.5304220910
8	H	-0.0002010244	0.0000000000	2.6147001411
9	N	2.3678473061	0.0000000000	-1.2472881122
10	H	2.4567451877	0.0000000000	-2.2493907079
11	N	-2.3676702596	0.0000000000	-1.2468500140
12	H	-2.4578024137	0.0000000000	-2.2488373684
13	N	2.4348867005	0.0000000000	1.3702006027
14	H	2.3835229281	0.0000000000	2.3849721417
15	N	-2.4350155949	0.0000000000	1.3695561639
16	H	-3.1909528364	0.0000000000	-0.6612040243
17	H	3.1916048024	0.0000000000	-0.6624889732
18	H	-2.3847169462	0.0000000000	2.3843728980

5)Structure **14** Optimization level: RωB97X-D3/6-311+G(2df,2p)

5a) Medium: Gas phaseEE(RωB97X-D3/6-311+G(2df,2p)) = - 492.214166 a.u. 0 imaginary frequencies
EE(RωB97M-V/QZVPPD) = -492.256509 a.u.
EE(ωB97M(2)/QZVPPD) = -492.562184 a.u.

0 1

Standard Nuclear Orientation (Angstroms)

I	Atom	X	Y	Z
1	C	-0.0555188200	-0.0217047929	-1.7310758299
2	C	1.1777180012	-0.0830692141	0.4934978449
3	C	-1.2353316534	0.1017221528	0.4581789236
4	C	0.0110006820	0.0171718662	1.1708060675
5	C	-1.2041750640	0.0770412182	-1.0417437469
6	C	1.2023625209	-0.1083060197	-1.0285705794
7	H	-0.0385298147	-0.0392205302	-2.8111113318
8	H	-0.0135578127	0.0352159082	2.2539387679
9	O	2.2819272116	-0.2003774033	-1.5811139318
10	O	-2.3886857968	0.1598941263	-1.6196477546
11	H	-3.0310047805	0.2197419502	-0.8839514386
12	N	-2.4163773683	0.1988547178	0.9366266066
13	H	-2.4346635235	0.2151405192	1.9508850223
14	N	2.4047882041	-0.1703962927	1.0281940973
15	H	3.1791806538	-0.2374086909	0.3882517384
16	H	2.5608673608	-0.1642995151	2.0168355444

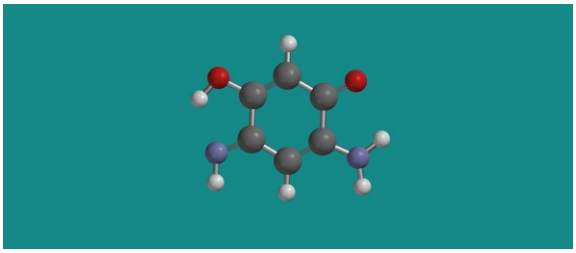

5b) Medium: C-PCM, ε = 78.3EE(RωB97X-D3/6-311+G(2df,2p)) = - 492.230758 a.u.0 imaginary frequencies
EE(RωB97M-V/QZVPPD) = -492.272446 a.u.
EE(ωB97M(2)/QZVPPD) = -492.577889 a.u.

0 1

Standard Nuclear Orientation (Angstroms)

I	Atom	X	Y	Z
1	C	-0.0596976793	-0.0205618124	-1.7354466277
2	C	1.1846648599	-0.0810877991	0.4836856290
3	C	-1.2326897065	0.1012617733	0.4576281043
4	C	0.0140435644	0.0175115098	1.1623583647
5	C	-1.2064998081	0.0778184949	-1.0418134744
6	C	1.1982844739	-0.1079847764	-1.0350314405
7	H	-0.0472458667	-0.0380449836	-2.8166622067
8	H	-0.0041410556	0.0351580342	2.2452351017
9	O	2.2730727716	-0.2032530658	-1.6082049101
10	O	-2.3913589082	0.1605731097	-1.6231810409
11	H	-3.0413930146	0.2208873278	-0.8932210793
12	N	-2.4118140830	0.1967641731	0.9461946256
13	H	-2.4110057683	0.2107112983	1.9621860309
14	N	2.4013938219	-0.1626548391	1.0343842065
15	H	3.2027712216	-0.2414960174	0.4318614812
16	H	2.5316151775	-0.1656024274	2.0300272358

6)Structure **15** Optimization level: RωB97X-D3/6-311+G(2df,2p)

6a) Medium: Gas phaseEE(RωB97X-D3/6-311+G(2df,2p)) = - 492.214284 a.u. 0 imaginary frequencies
EE(RωB97M-V/QZVPPD) = -492.254390 a.u.
EE(ωB97M(2)/QZVPPD) = -492.559980 a.u.

0 1

Standard Nuclear Orientation (Angstroms)

I	Atom	X	Y	Z
1	C	-0.3472326709	0.6191818330	-1.6721854991
2	C	0.0891290358	-1.2418902842	-0.0416193217
3	C	0.0628238214	0.9683091893	0.7818021498
4	C	0.2132214609	-0.3832327867	1.0359329864
5	C	-0.2302262998	1.5355130661	-0.6245555119
6	C	-0.2062684572	-0.7566902106	-1.4777988820
7	H	-0.5532343258	0.9868879655	-2.6666555535
8	O	-0.2883414034	-1.6573614064	-2.3156573670
9	O	-0.3332109231	2.7630807609	-0.6707153993
10	N	0.1493347098	1.9212767681	1.6787179920
11	H	0.3352667756	1.7544962200	2.6501478903
12	H	0.0116429913	2.8576027455	1.3062358990
13	N	0.2029786460	-2.5474077731	0.0119651901
14	H	0.0794261850	-3.0120613744	-0.8845938928
15	H	0.3946266033	-3.0550771050	0.8555482116
16	H	0.4200638573	-0.7526276192	2.0334311388

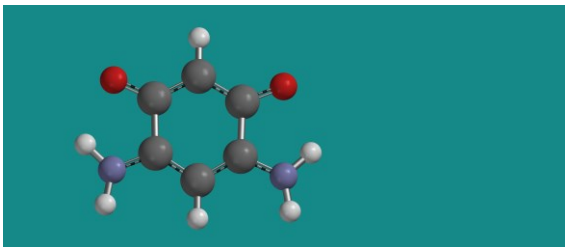

6b) Medium: C-PCM, ε = 78.3EE(RωB97X-D3/6-311+G(2df,2p)) = - 492.247649 a.u.0 imaginary frequencies
EE(RωB97M-V/QZVPPD) = -492.286633 a.u.
EE(ωB97M(2)/QZVPPD) = -492.591759 a.u.

0 1

Standard Nuclear Orientation (Angstroms)

I	Atom	X	Y	Z
1	C	-0.3494929045	0.6232859220	-1.6823488267
2	C	0.0853102549	-1.2436158077	-0.0658678620
3	C	0.0590714173	0.9848644016	0.7648935062
4	C	0.2065807615	-0.3708248715	1.0012350124
5	C	-0.2321989273	1.5422220719	-0.6353704064
6	C	-0.2094963358	-0.7544215251	-1.4905649546
7	H	-0.5571055901	0.9918108595	-2.6783652828
8	O	-0.3000164151	-1.6315803894	-2.3615246867
9	O	-0.3416051843	2.7737095641	-0.7214367479
10	N	0.1523349946	1.9067237461	1.6902270462
11	H	0.3382803720	1.6882216579	2.6550895997
12	H	0.0301793408	2.8691918481	1.4073828968
13	N	0.2063944936	-2.5440786970	0.0301889556
14	H	0.0999321942	-3.0887151231	-0.8145157627
15	H	0.3986172801	-3.0068023569	0.9032862317
16	H	0.4132142545	-0.7399913114	1.9976913118

7)Structure **16** Optimization level: RωB97X-D3/6-311+G(2df,2p)

7a) Medium: Gas phaseEE(RωB97X-D3/6-311+G(2df,2p)) = - 531.959110 a.u. 0 imaginary frequencies
EE(RωB97M-V/QZVPPD) = -532.022234 a.u.
EE(ωB97M(2)/QZVPPD) = -532.331892 a.u.

0 1

Standard Nuclear Orientation (Angstroms)

I	Atom	X	Y	Z
1	C	1.4543411276	-0.0092326923	-0.2402843049
2	C	-0.5983822368	0.0631278977	1.2735631398
3	C	-0.9115003313	-0.0585309290	-1.0927493040
4	C	-1.4540634187	0.0090784390	0.2403417826
5	C	0.5985664843	-0.0632050113	-1.2734768298
6	C	0.9117340290	0.0584229974	1.0928854462
7	H	2.5268422617	-0.0125702097	-0.3702531027
8	H	-2.5266511296	0.0125001511	0.3698207596
9	O	1.5677469318	0.1127010562	2.1165965913
10	O	-1.5676529984	-0.1126031152	-2.1164657217
11	O	-0.9676823250	0.1259019694	2.5358457935
12	H	-0.1408835815	0.1544238720	3.0533085137
13	O	0.9673279541	-0.1258233039	-2.5359898065
14	H	0.1402572329	-0.1541911214	-3.0531429572

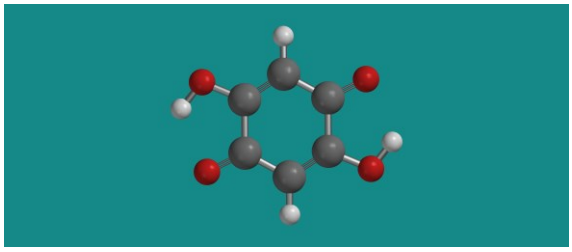

7b) Medium: C-PCM, ε = 78.3EE(RωB97X-D3/6-311+G(2df,2p)) = - 531.971550 a.u.0 imaginary frequencies
EE(RωB97M-V/QZVPPD) = -532.034030 a.u.
EE(ωB97M(2)/QZVPPD) = -532.343289 a.u.

0 1

Standard Nuclear Orientation (Angstroms)

I	Atom	X	Y	Z
1	C	1.4488935542	-0.0090489373	-0.2455743773
2	C	-0.5920951621	0.0636586692	1.2781844408
3	C	-0.9147831806	-0.0580716361	-1.0897918556
4	C	-1.4485750613	0.0088940647	0.2456170984
5	C	0.5923097106	-0.0637468614	-1.2781007724
6	C	0.9150557318	0.0580168846	1.0899241035
7	H	2.5214748520	-0.0127216297	-0.3815890373
8	H	-2.5212404176	0.0126343620	0.3811711524
9	O	1.5869664983	0.1117197123	2.1061810096
10	O	-1.5868064994	-0.1115708540	-2.1060766118
11	O	-0.9765165723	0.1264548119	2.5369977637
12	H	-0.1727007113	0.1559939736	3.0863713865
13	O	0.9761060682	-0.1264003114	-2.5371844412
14	H	0.1719111896	-0.1558122484	-3.0861298593

8)Structure **17** Optimization level: RωB97X-D3/6-311+G(2df,2p)

8a) Medium: Gas phaseEE(RωB97X-D3/6-311+G(2df,2p)) = - 531.931447 a.u. 0 imaginary frequencies
EE(RωB97M-V/QZVPPD) = -531.994701 a.u.
EE(ωB97M(2)/QZVPPD) = -532.303935 a.u.

0 1

Standard Nuclear Orientation (Angstroms)

I	Atom	X	Y	Z
1	C	1.3700164038	-0.1015480926	-0.2658295165
2	C	-0.7592642139	0.0299227916	-1.7194291702
3	C	-0.8978509132	0.0730880211	0.7096844892
4	C	-1.5195013471	0.1000639912	-0.4764528211
5	C	0.5768021370	-0.0293389479	0.8070748371
6	C	0.7905357679	-0.0794046975	-1.6108363064
7	H	2.4474853167	-0.1766907010	-0.1856178415
8	H	-2.5959786419	0.1752383869	-0.5370826231
9	O	1.4623335777	-0.1413634431	-2.6075057732
10	O	-1.2717784651	0.0525223608	-2.8095873813
11	O	0.9912141120	-0.0391046532	2.0898932541
12	H	1.9469323921	-0.1048854644	2.1446510738
13	O	-1.5763576787	0.1368294980	1.8591846747
14	H	-0.9645884472	0.1046709501	2.6018531043

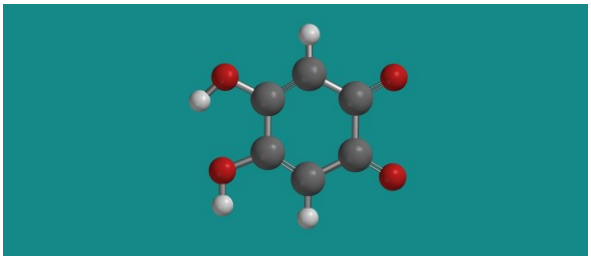

8b) Medium: C-PCM, ε = 78.3EE(RωB97X-D3/6-311+G(2df,2p)) = - 531.971550 a.u.0 imaginary frequencies
EE(RωB97M-V/QZVPPD) = -532.021419 a.u.
EE(ωB97M(2)/QZVPPD) = -532.330026 a.u.

0 1

Standard Nuclear Orientation (Angstroms)

I	Atom	X	Y	Z
1	C	1.3772361811	-0.1023462592	-0.2722469731
2	C	-0.7607336518	0.0305909706	-1.7038061923
3	C	-0.8949298228	0.0724029202	0.7082016268
4	C	-1.5229736942	0.1001402961	-0.4802529607
5	C	0.5857360903	-0.0296813043	0.8092115022
6	C	0.7901783600	-0.0793653515	-1.5947036302
7	H	2.4531902317	-0.1766033459	-0.1804211934
8	H	-2.6002826341	0.1747719573	-0.5364022895
9	O	1.4421669584	-0.1408197256	-2.6159621945
10	O	-1.2611257757	0.0525026588	-2.8102859438
11	O	0.9905803125	-0.0381810760	2.0750166828
12	H	1.9497272725	-0.1028992109	2.1516278927
13	O	-1.5735609702	0.1344980031	1.8455792098
14	H	-0.9752088573	0.1049894673	2.6044444634

9)Structure **18** Optimization level: RωB97X-D3/6-311+G(2df,2p)

9a) Medium: Gas phaseEE(RωB97X-D3/6-311+G(2df,2p)) = - 531.939109 a.u. 0 imaginary frequencies
EE(RωB97M-V/QZVPPD) = -532.002217 a.u.
EE(ωB97M(2)/QZVPPD) = -532.311766 a.u.

0 1

Standard Nuclear Orientation (Angstroms)

I	Atom	X	Y	Z
1	H	0.0513473624	0.0352784688	-2.6385775863
2	C	0.0303571896	0.0207235528	-1.5596781130
3	C	-0.0279688032	-0.0187784427	1.4418053548
4	C	-1.1805222462	0.0765049829	-0.8755293038
5	C	1.2138283033	-0.0532736214	-0.8307463734
6	C	1.1365205094	-0.0714880838	0.7107340962
7	C	-1.1633148543	0.0532022736	0.6677418820
8	H	-0.0491444913	-0.0334321674	2.5211850757
9	O	-2.3362613903	0.1455447856	-1.3079031777
10	O	2.3854292165	-0.1107645081	-1.2196793852
11	O	-2.3523349535	0.1105741327	1.1420904404
12	H	-2.9101479334	0.1527659131	0.3047549451
13	O	2.3059686234	-0.1434321708	1.2295841764
14	H	2.8962434675	-0.1634251155	0.4142179686

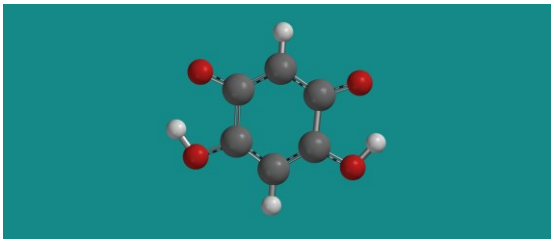

9b) Medium: C-PCM, ε = 78.3EE(RωB97X-D3/6-311+G(2df,2p)) = - 531.954815 a.u.0 imaginary frequencies
EE(RωB97M-V/QZVPPD) = -532.017068 a.u.
EE(ωB97M(2)/QZVPPD) = -532.326154 a.u.

0 1

Standard Nuclear Orientation (Angstroms)

I	Atom	X	Y	Z
1	H	0.0520730716	0.0352214156	-2.6455156615
2	C	0.0308125779	0.0207663630	-1.5651202864
3	C	-0.0276661547	-0.0189946475	1.4172840705
4	C	-1.1842586164	0.0778366789	-0.8868102600
5	C	1.2181171737	-0.0545159326	-0.8413866077
6	C	1.1412328289	-0.0711723926	0.6953166245
7	C	-1.1674737697	0.0528412645	0.6517743275
8	H	-0.0492209630	-0.0334122550	2.4972789866
9	O	-2.3308018652	0.1487133091	-1.3491175462
10	O	2.3822197036	-0.1129783730	-1.2596044487
11	O	-2.3450392457	0.1082094784	1.1608608388
12	H	-2.9599804694	0.1538976002	0.3845080617
13	O	2.2982775824	-0.1408840143	1.2474475939
14	H	2.9417081462	-0.1655284946	0.4930843066

B. This section provides the Cartesian coordinates, electronic potential energies (EE), enthalpies (H), entropies (S), and free energies (G) for structures in Table II - 6 of the main paper. The data are presented in the following way:

- The number of the structure as it appears in the main paper is given first, followed by the density functional and basis set used to obtain the optimized structure. All geometric optimizations used RωB97X-D3/6-311+G(2df,2p), as stated in the main article.
- The next line identifies the medium (gas phase or C-PCM) and provides the energy value obtained at the geometric optimization level. Enthalpy, entropy, and free energy values computed using the harmonic-oscillator/rigid-rotator model are also included.
- The following line provides the single-point electronic energy value obtained at the RωB97X-D3/6-311+G(2df,2p) level using the geometry optimized at the RωB97X-D3/6-311+G(2df,2p) level. No information about enthalpy, entropy, or free energy is included because vibrational frequencies were not computed at this level.
- The final line gives the single-point electronic energy value obtained at the RωB97M(2)/QZVPPD level using the electronic orbitals that were previously optimized at the RωB97M-V/QZVPPD level. No information about enthalpy, entropy, or free energy is included because vibrational frequencies were not computed at this level.

The values of enthalpy and free energy compiled in Table II - 6 of the main paper were computed as follows from the geometric optimization at the RωB97X-D3/6-311+G(2df,2p) level:

$$\Delta H^{\circ}(Table\ 6) = \Delta H^{\circ}\big(R\omega B97X - D3/6 - 311 + G(2df, 2p)\big) + \Delta\Delta E$$

The added correction $\Delta\Delta E$ corresponds to the electronic potential energy difference between single-point calculations at the RωB97M(2)/QZVPPD and RωB97X-D3/6-311+G(2df,2p) levels:

$$\Delta\Delta E = \Delta E(single\ point;\ R\omega B9M(2)/QZVPPD\ ) - \Delta E(single\ point;\ R\omega B97X - D3/6 - 311 + G(2df, 2p))$$

10) Structure **2** (BTA-H_2) Optimization level: RωB97X-D3/6-311+G(2df,2p)

10a) Medium: Gas phase*EE*(RωB97X-D3/6-311+G(2df,2p)) = - 452.462466 a.u.0 imaginary frequencies
H°(RωB97X-D3/6-311+G(2df,2p)) = - 452.306438 a.u
G°(RωB97X-D3/6-311+G(2df,2p)) = - 452.351005 a.u

EE(RωB97M-V/QZVPPD) = -452.484559 a.u.
EE(RωB97M(2)/QZVPPD) = - 452.786399 a.u.
0 1

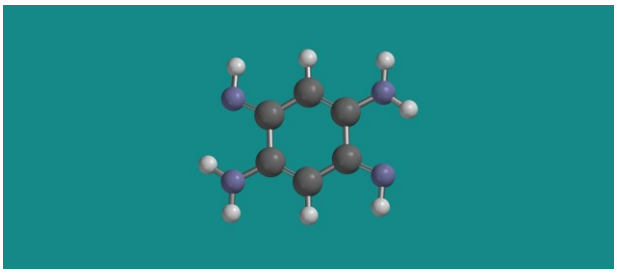

Standard Nuclear Orientation (Angstroms)

I	Atom	X	Y	Z
1	N	-1.5039068353	-0.0397411475	2.2581110907
2	H	-2.5061606982	-0.0035396378	2.0961538717
3	C	-1.4170831935	0.0608678007	-0.1690510612
4	H	-2.4973538985	0.0981623556	-0.2522802846
5	N	1.0950620201	-0.0985248036	2.5447494796
6	H	0.4020060461	-0.1571027990	3.2728879477
7	H	2.0651156977	-0.2316242210	2.7514352072
8	C	-0.8533701869	-0.0092763548	1.1569605622
9	N	1.5041236908	0.0400073139	-2.2580623635
10	H	2.5063932834	0.0038729570	-2.0961245001
11	C	0.6415588313	-0.0622435532	1.2769784975
12	N	-1.0952826665	0.0984688022	-2.5447136488
13	H	-2.0655120941	0.2306748908	-2.7512487866
14	H	-0.4026194338	0.1566469289	-3.2732443169
15	C	1.4173155624	-0.0606144982	0.1691417479
16	H	2.4975640602	-0.0979685896	0.2522069817
17	C	0.8535795706	0.0095458366	-1.1569136757
18	C	-0.6414297558	0.0623887191	-1.2769867486

10b) Medium: C-PCM, ε = 78.3*EE*(RωB97X-D3/6-311+G(2df,2p)) = - 452.481553 a.u.0 imaginary frequencies
H°(RωB97X-D3/6-311+G(2df,2p)) = - 452.326272 a.u
G°(RωB97X-D3/6-311+G(2df,2p)) = - 452.370572 a.u

EE(RωB97M-V/QZVPPD) = - 452.502910 a.u.
EE(RωB97M(2)/QZVPPD) = - 452.804637 a.u.
0 1

Standard Nuclear Orientation (Angstroms)

I	Atom	X	Y	Z
1	N	-1.5310205082	-0.0285875620	2.2454408660
2	H	-2.5287821289	0.0035728645	2.0494620214
3	C	-1.4152044815	0.0577231949	-0.1724227441
4	H	-2.4950484378	0.0939240400	-0.2606446070
5	N	1.1101879941	-0.0677473513	2.5436795281
6	H	0.4483030247	-0.1924289237	3.2908234986
7	H	2.0825645730	-0.2412479393	2.7242195844
8	C	-0.8567900830	-0.0041700133	1.1544233519
9	N	1.5313592009	0.0287459672	-2.2451419034
10	H	2.5291060868	-0.0041660027	-2.0491654728
11	C	0.6383220938	-0.0519850166	1.2828477515
12	N	-1.1100083521	0.0722120362	-2.5431657008
13	H	-2.0839772283	0.2349490556	-2.7249342397
14	H	-0.4487270719	0.1878204757	-3.2922007541
15	C	1.4154726825	-0.0560167271	0.1728118022
16	H	2.4953001771	-0.0923763134	0.2608539754
17	C	0.8570624631	0.0056030019	-1.1542013832
18	C	-0.6381200046	0.0541752134	-1.2826855744

11)Structure **20** (second-order saddle point) Optimization level: RωB97X-D3/6-311+G(2df,2p)

11a) Medium: Gas phase*EE*(RωB97X-D3/6-311+G(2df,2p)) = - 452.408636 a.u.**2 imaginary frequencies:**
H°(RωB97X-D3/6-311+G(2df,2p)) = - 452.277690 a.ui $\times 1719\ cm^{-1}$
G°(RωB97X-D3/6-311+G(2df,2p)) = - 452.319723 a.ui $\times 1402\ cm^{-1}$

EE(RωB97M-V/QZVPPD) = - 452.430233 a.u.
EE(RωB97M(2)/QZVPPD) = - 452.732175 a.u.
0 1

Standard Nuclear Orientation (Angstroms)

I	Atom	X	Y	Z
1	C	0.0003721171	-0.0027388671	1.4800328146
2	H	0.0003108102	-0.0016956437	2.5620433823
3	C	-1.1944693434	0.0019379286	0.7688609031
4	C	1.1951759766	-0.0072879209	0.7688094415
5	C	1.1949034728	-0.0003229363	-0.7684807845
6	C	-1.1948191810	-0.0064687821	-0.7684341577
7	C	0.0000405129	-0.0073562810	-1.4795268914
8	H	-0.0003083944	-0.0090888356	-2.5616153585
9	N	-2.4322810964	0.0137086341	1.1656190004
10	N	2.4328222753	-0.0143397343	1.1658639405
11	N	-2.4326319713	-0.0046281006	-1.1655243968
12	N	2.4325714297	0.0097233611	-1.1655707755
13	H	2.9779622837	0.0242278238	-0.0008761013
14	H	-2.9776882158	0.0002527781	-0.0002311770
15	H	-2.6490202807	-0.0084416191	-2.1478980378
16	H	2.6485134695	0.0136240975	-2.1483003272
17	H	2.6485025566	-0.0218330816	2.1483257897
18	H	-2.6499564214	0.0207271766	2.1469027355

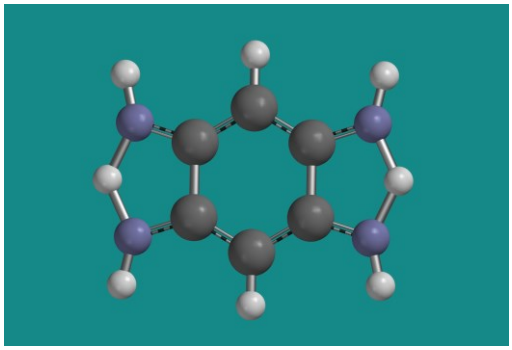

11b) Medium: C-PCM, ε = 78.3*EE*(RωB97X-D3/6-311+G(2df,2p)) = - 452.421091 a.u.**2 imaginary frequencies:**
H°(RωB97X-D3/6-311+G(2df,2p)) = - 452.276117 a.ui $\times 1770\ cm^{-1}$
G°(RωB97X-D3/6-311+G(2df,2p)) = - 452.317301 a.ui $\times 1587\ cm^{-1}$

EE(RωB97M-V/QZVPPD) = - 452.442302 a.u.
EE(RωB97M(2)/QZVPPD) = - 452.744224 a.u.
0 1

Standard Nuclear Orientation (Angstroms)

I	Atom	X	Y	Z
1	C	-0.0002761021	0.0099972634	1.4836393837
2	H	0.0000992782	0.0115944423	2.5659205009
3	C	-1.1958756916	-0.0093614110	0.7710518064
4	C	1.1953845839	0.0194131855	0.7706372672
5	C	1.1954996970	-0.0098780251	-0.7710367036
6	C	-1.1947758282	0.0172699828	-0.7707494546
7	C	0.0000464245	0.0163826467	-1.4843346205
8	H	-0.0004276072	0.0265646938	-2.5665527098
9	N	-2.4356732624	-0.0427032748	1.1699090387
10	N	2.4331708872	0.0396102461	1.1697454676
11	N	-2.4322340885	0.0347233450	-1.1707655701
12	N	2.4348256873	-0.0505059762	-1.1719716495
13	H	2.9761136760	-0.0153622950	-0.0008638363
14	H	-2.9766234379	-0.0156610561	0.0015932967
15	H	-2.6485341167	0.0496783473	-2.1547614764
16	H	2.6510964328	-0.0744591674	-2.1544709016
17	H	2.6464642253	0.0555131235	2.1555836007
18	H	-2.6482807578	-0.0628160721	2.1574265606

12) Structure **13** (zwitterionic intermediate)Optimization level: RωB97X-D3/6-311+G(2df,2p)

12a) Medium: Gas phase*EE*(RωB97X-D3/6-311+G(2df,2p)) = - 452.439657 a.u.0 imaginary frequencies
H°(RωB97X-D3/6-311+G(2df,2p)) = - 452.284225 a.u
G°(RωB97X-D3/6-311+G(2df,2p)) = - 452.326950 a.u

EE(RωB97M-V/QZVPPD) = - 452.461263 a.u.
EE(RωB97M(2)/QZVPPD) = - 452.763245 a.u.
0 1

Coordinates (Angstroms)

ATOM		X	Y	Z
1	C	-1.3619839101	0.0006627408	-0.0321768542
2	H	-2.4449894636	-0.0002664626	-0.0581495844
3	C	-0.6279670356	0.0009585558	-1.2067417881
4	C	-0.6851952338	0.0006166871	1.1760578776
5	C	0.8256078964	0.0002685419	1.2525464268
6	C	0.8851100620	0.0027205664	-1.2110886842
7	C	1.5246019137	0.0014215816	0.0367182194
8	H	2.6073238828	0.0016019392	0.0626188683
9	N	-1.1664582926	-0.0014251493	-2.4070747193
10	H	-2.1570778367	-0.0051724610	-2.5611353915
11	N	-1.2824202864	0.0012694621	2.3484367688
12	H	-2.2794916268	0.0001760968	2.4519446611
13	N	1.3760199988	0.0042752237	-2.4123359482
14	H	2.3894839551	0.0011337508	-2.3979230062
15	N	1.2590732460	-0.0026825807	2.4754853502
16	H	-0.6453249519	-0.0005361091	3.1426232882
17	H	-0.4884481701	-0.0008519946	-3.1677976161
18	H	2.2721358531	-0.0041703889	2.5079921321

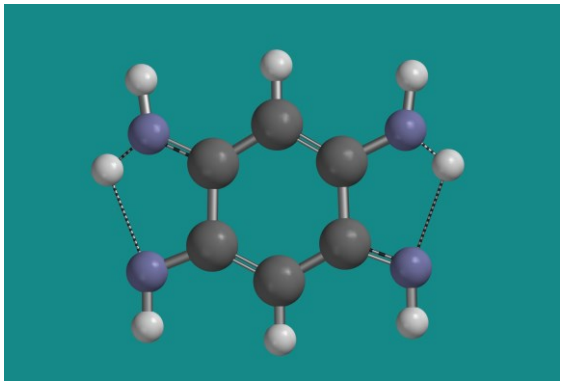

12b) Medium: C-PCM, ε = 78.3*EE*(RωB97X-D3/6-311+G(2df,2p)) = - 452.466551 a.u.0 imaginary frequencies
H°(RωB97X-D3/6-311+G(2df,2p)) = - 452.311089 a.u
G°(RωB97X-D3/6-311+G(2df,2p)) = - 452.353892 a.u

EE(RωB97M-V/QZVPPD) = - 452.487308 a.u.
EE(RωB97M(2)/QZVPPD) = - 452.788957 a.u.
0 1

Standard Nuclear Orientation (Angstroms)

I	Atom	X	Y	Z
1	C	-1.3440982993	-0.0003426658	-0.0319391022
2	H	-2.4264263818	-0.0006877820	-0.0580415318
3	C	-0.6192706581	-0.0000218835	-1.2129880097
4	C	-0.6771086567	-0.0003447423	1.1824435344
5	C	0.8331487014	-0.0000769832	1.2560053298
6	C	0.8929660039	0.0006164598	-1.2138932747
7	C	1.5297959528	0.0004056041	0.0370930192
8	H	2.6137269860	0.0007388596	0.0631323832
9	N	-1.1882523772	-0.0002493112	-2.3974016318
10	H	-2.1875702101	-0.0006726392	-2.5130401297
11	N	-1.3036941025	-0.0005989425	2.3373525626
12	H	-2.3075456446	-0.0007275065	2.4033937516
13	N	1.4265808178	0.0013022978	-2.4012654539
14	H	2.4399538638	0.0016972211	-2.3276912964
15	N	1.3098381306	-0.0002853155	2.4672167755
16	H	-0.7372772727	-0.0006436876	3.1736752727
17	H	-0.5803533131	-0.0000251944	-3.2047266898
18	H	2.3255864599	-0.0000837886	2.4406744911

13) Transition State Leading to Structure **13** (first-order saddle point)Optimization level: RωB97X-D3/6-311+G(2df,2p)

13a) Medium: Gas phase*EE*(RωB97X-D3/6-311+G(2df,2p)) = - 452.428787 a.u.**1 imaginary frequency:**
H°(RωB97X-D3/6-311+G(2df,2p)) = - 452.277690 a.u$i \times 1495\ cm^{-1}$
G°(RωB97X-D3/6-311+G(2df,2p)) = - 452.319723 a.u

EE(RωB97M-V/QZVPPD) = - 452.450536 a.u.
EE(RωB97M(2)/QZVPPD) = - 452.752461 a.u.
0 1

Standard Nuclear Orientation (Angstroms)

I	Atom	X	Y	Z
1	C	-1.4084347087	-0.0003281148	0.0117897774
2	H	-2.4911167462	-0.0006060522	-0.0069016840
3	C	-0.6783023762	0.0000535906	-1.1871875972
4	C	-0.7217781929	-0.0003665634	1.1979403985
5	C	0.7944592768	0.0000045094	1.2461425221
6	C	0.8439986112	0.0004409613	-1.1909524653
7	C	1.5056039037	0.0004104601	0.0137948217
8	H	2.5878058225	0.0006794184	0.0464157203
9	N	-1.0968788802	0.0001359914	-2.4098350789
10	H	-2.0767774788	-0.0000854215	-2.6355134191
11	N	-1.2995250583	-0.0007474525	2.3936505408
12	H	-2.2946326573	-0.0010490863	2.5073982560
13	N	1.2402467798	0.0007314381	-2.4413799873
14	H	2.2277149714	0.0010116036	-2.6323449181
15	N	1.2691452142	-0.0001294212	2.4422597535
16	H	-0.6708507727	-0.0007595259	3.1863588090
17	H	-0.0146010654	0.0005003582	-2.9761649461
18	H	2.2839233043	0.0001033068	2.4345294968

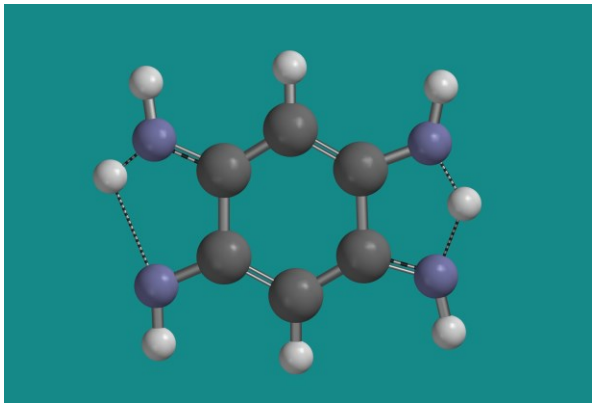

13b) Medium: C-PCM, ε = 78.3*EE*(RωB97X-D3/6-311+G(2df,2p)) = - 452.447019 a.u.**1 imaginary frequency:**
H°(RωB97X-D3/6-311+G(2df,2p)) = - 452.296908 a.u$i \times 1686\ cm^{-1}$
G°(RωB97X-D3/6-311+G(2df,2p)) = - 452.339187 a.u

EE(RωB97M-V/QZVPPD) = - 452.468175 a.u.
EE(RωB97M(2)/QZVPPD) = - 452.769965 a.u.
0 1

Standard Nuclear Orientation (Angstroms)

I	Atom	X	Y	Z
1	C	-1.4060712625	-0.0003292476	0.0184163444
2	H	-2.4884064211	-0.0005888468	0.0044090978
3	C	-0.6824855126	0.0000142503	-1.1846360354
4	C	-0.7202238950	-0.0003470900	1.2074495214
5	C	0.7969042454	-0.0000654354	1.2493266645
6	C	0.8402112113	0.0004838336	-1.1871326726
7	C	1.5075772602	0.0004000457	0.0130773983
8	H	2.5904150112	0.0006550307	0.0448646224
9	N	-1.1005272611	0.0000277571	-2.4064454005
10	H	-2.0857617205	-0.0002412972	-2.6209545139
11	N	-1.3164079713	-0.0006509860	2.3925201278
12	H	-2.3172941665	-0.0008477064	2.4816306222
13	N	1.2410109780	0.0008818846	-2.4399494847
14	H	2.2293922027	0.0011931690	-2.6346502144
15	N	1.3067952256	-0.0002789903	2.4337431565
16	H	-0.7357828438	-0.0006775443	3.2161345156
17	H	0.0186283045	0.0004267313	-2.9677545509
18	H	2.3220265627	-0.0000555582	2.3799508017

V. References

1. Bruker (2022). *APEX4* and *SAINT*, Bruker AXS Inc., Madison, Wisconsin, USA.
2. Krause, L.; Herbst-Irmer, R.; Sheldrick, G. M.; Stalke, D. Comparison of Silver and Molybdenum Microfocus X-Ray Sources for Single-Crystal Structure Determination. *J. Appl. Cryst*. **2015**, *48*, 3–10.
3. Sheldrick, G. M. *SHELXT* – Integrated Space-Group and Crystal-Structure Determination. *Acta Crystallogr*. **2015**, *A71*, 3–8.
4. Sheldrick, G. M. Crystal Structure Refinement with *SHELXL*. *Acta Crystallogr*. **2015**, *C71*, 3–8.
5. Dolomanov, O. V.; Bourhis, L. J.; Gildea, R. J.; Howard, J. A. K.; Puschmann, H. *OLEX2*: A Complete Structure Solution, Refinement and Analysis Program. *J. Appl. Crystallogr*. **2009**, *42*, 339–341.

Annexe B

Informations supplémentaires

Chapitre 3

Robustes réseaux de ponts-hydrogènes
formés par des sels de sulfate et bisulfate de benzènetétramines

Supporting Information

Strongly Hydrogen-Bonded Networks Formed by Sulfate and Bisulfate Salts of Benzenetetramines

Johann O. E. Sosoe,* Thierry Maris, and James D. Wuest*

Département de Chimie, Université de Montréal, Montréal, Québec H2V 0B3 Canada

*Authors to whom correspondence may be addressed

Email: *johann.sosoe@umontreal.ca*; *james.d.wuest@umontreal.ca*

Annexe B

Contents **Page**

Annexe B

I. Additional Crystallographic Information

Single-crystal X-ray diffraction data for H_4(1,2,4,5-BTA)$^{4+}$ SO_4^{2-} $2HSO_4^-$, H_3(1,2,4,5-BTA)$^{3+}$ SO_4^{2-} HSO_4^- (both $P\bar{1}$ and *Cc* forms), and H_2(1,2,3,4-BTA)$^{2+}$ SO_4^{2-} were collected on a Bruker Venture Kappa-geometry diffractometer equipped with a gallium liquid metal-jet source (GaKα radiation, λ = 1.34139 Å), a Photon III CMOS detector, and Helios MX mirror optics. Measurements for these compounds were carried out at 150 K using an Oxford Cryostream 700 low-temperature device. X-ray diffraction data for H_4(1,2,4,5-BTA)$^{4+}$ $4HSO_4^-$ were collected at 100 K on a 3-circle platform diffractometer equipped with an Incoatec Microfocus source (CuKα radiation, λ = 1.54179 Å) and an APEX2 CCD detector. The unit-cell lattice parameters were determined by measurement of a limited set of frames using the *APEX4* suite of software.[1] Reflection data were integrated using *SAINT* V8.40B, and a multiscan absorption correction using *SADABS* was applied.[2] Structures were solved using the intrinsic phasing routine as implemented in *SHELXT*,[3] and cycles of refinement were performed by least-squares minimisation with *SHELXL*[4] within the graphical user interface of *OLEX2*.[5] All non-hydrogen atoms were refined using anisotropic thermal displacement parameters. For H_4(1,2,4,5-BTA)$^{4+}$ $4HSO_4^-$, H_2(1,2,3,4-BTA)$^{2+}$ SO_4^{2-}, and the *Cc* polymorph of H_3(1,2,4,5-BTA)$^{3+}$ SO_4^{2-} HSO_4^-, all hydrogen atoms were first located in the difference Fourier map, then refined isotropically on calculated positions using standard riding models from *SHELXL* (AFIX 147 for sulfate OH groups, AFIX 137 for NH_3^+ groups, and AFIX 7 for NH_2 groups). For H_4(1,2,4,5-BTA)$^{4+}$ SO_4^{2-} $2HSO_4^-$, hydrogen atoms attached to carbon and nitrogen were freely refined isotropically, and the hydrogen atom from the bisulfate ion was refined with riding model AFIX 147 applied on the position located from difference Fourier map. For the $P\bar{1}$ polymorph of H_3(1,2,4,5-BTA)$^{3+}$ SO_4^{2-}

HSO_4^-, all the hydrogen atoms were refined using riding models, except the hydrogen atoms of the NH_2 group, which were freely refined isotropically.

II. Thermal Atomic Displacement Parameter Plots

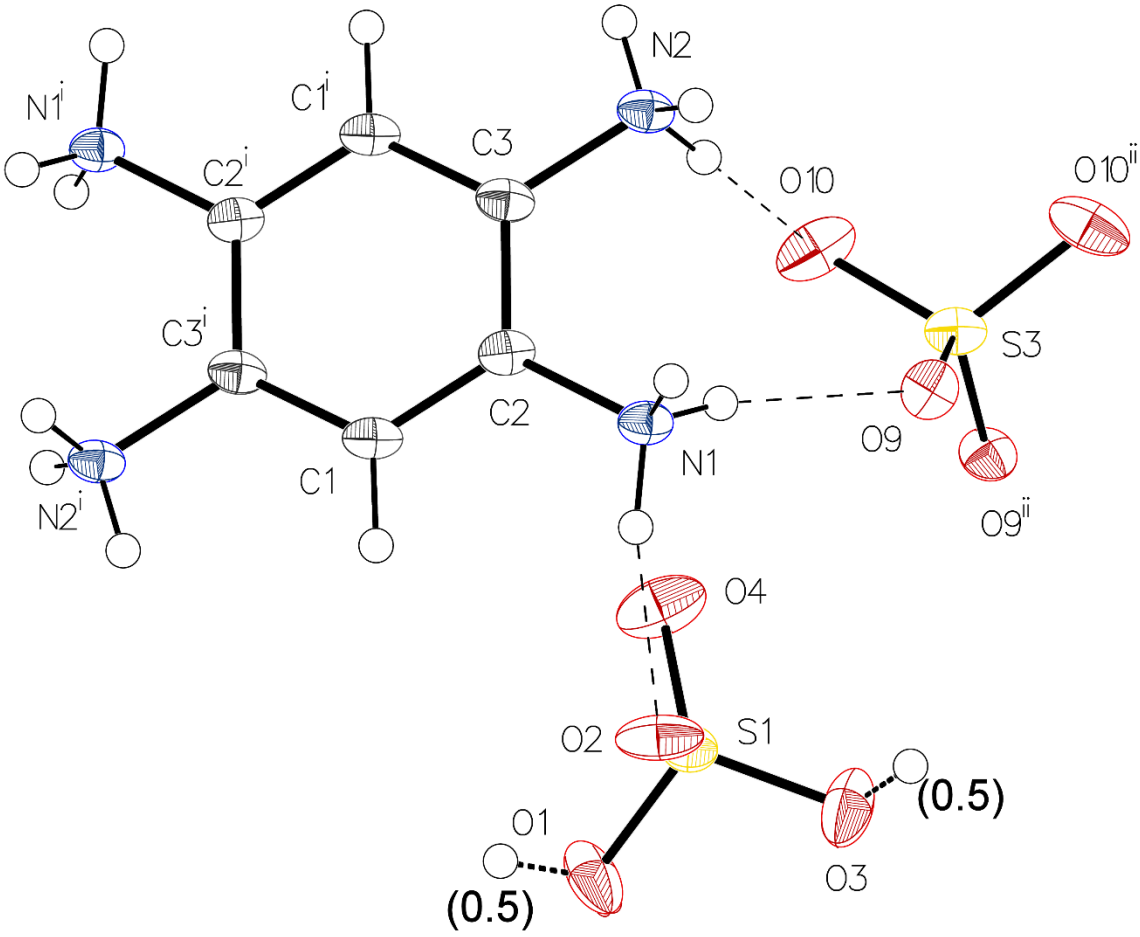

Figure B1. Thermal atomic displacement ellipsoid plot of the structure of *P*2/*c* crystals of salt H_4(1,2,4,5-BTA)$^{4+}$ SO_4^{2-} $2HSO_4^-$ grown from H_2SO_4 with the atomic numbering scheme. The ellipsoids of non-hydrogen atoms are drawn at the 50% probability level, and hydrogen atoms are represented by a sphere of arbitrary size. Symmetry Codes (i): 1-x, 1-y, 1-z.

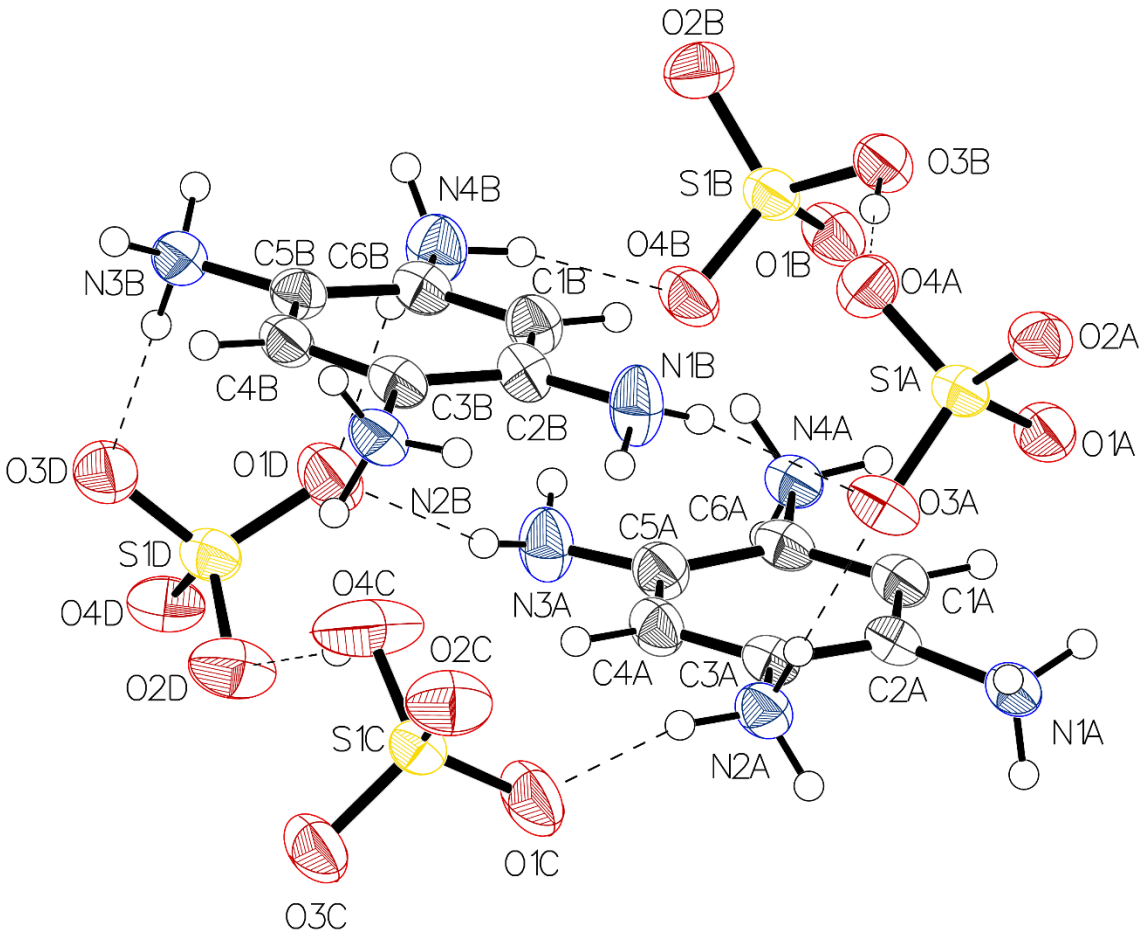

Figure B2. Thermal atomic displacement ellipsoid plot of the structure of $P\bar{1}$ crystals of salt H_3(1,2,4,5-BTA)$^{3+}$ SO_4^{2-} HSO_4^- grown from aqueous H_2SO_4 with the atomic numbering scheme. The ellipsoids of non-hydrogen atoms are drawn at the 50% probability level, and hydrogen atoms are represented by a sphere of arbitrary size.

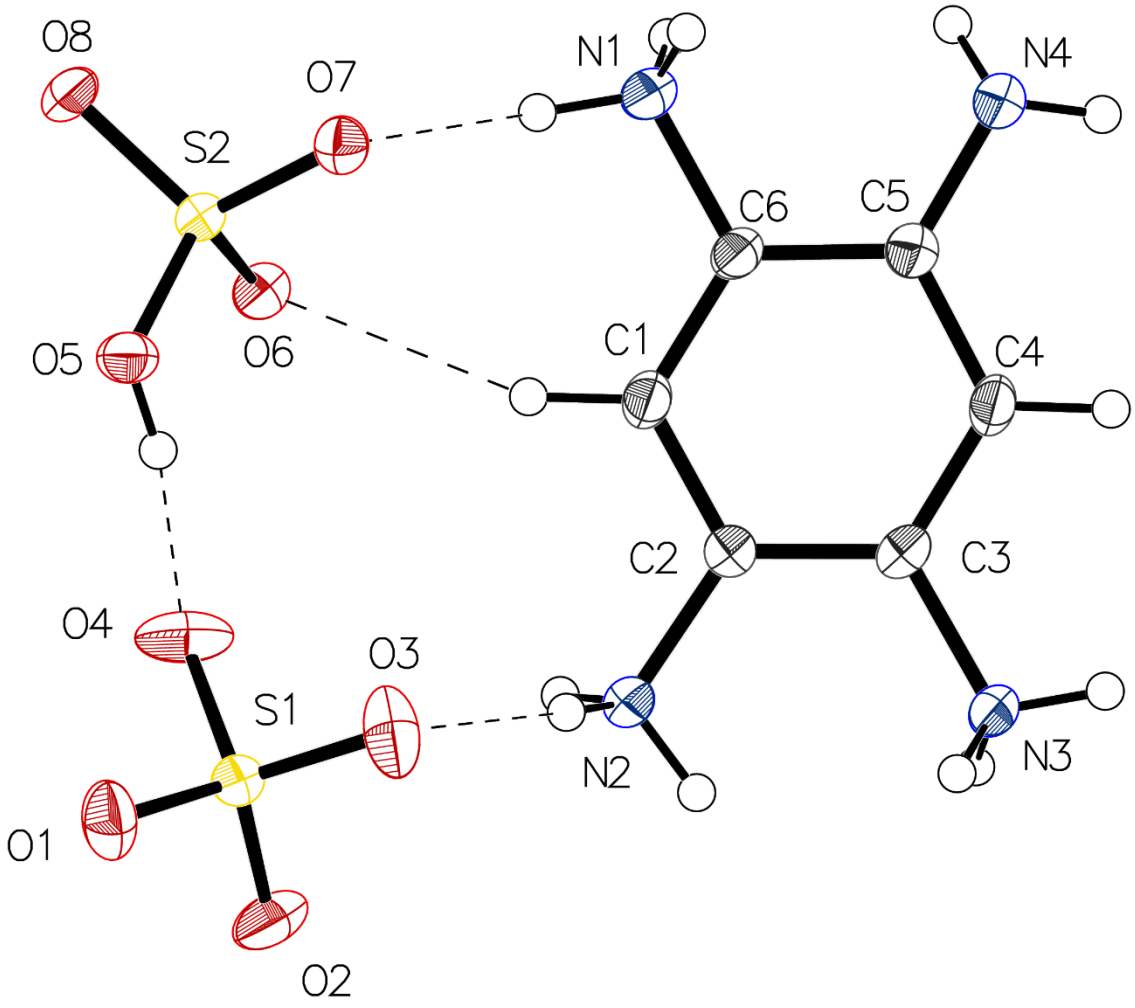

Figure B3. Thermal atomic displacement ellipsoid plot of the structure of *Cc* crystals of salt H_3(1,2,4,5-BTA)$^{3+}$ SO_4^{2-} HSO_4^- grown from aqueous H_2SO_4 with the atomic numbering scheme. The ellipsoids of non-hydrogen atoms are drawn at the 50% probability level, and hydrogen atoms are represented by a sphere of arbitrary size.

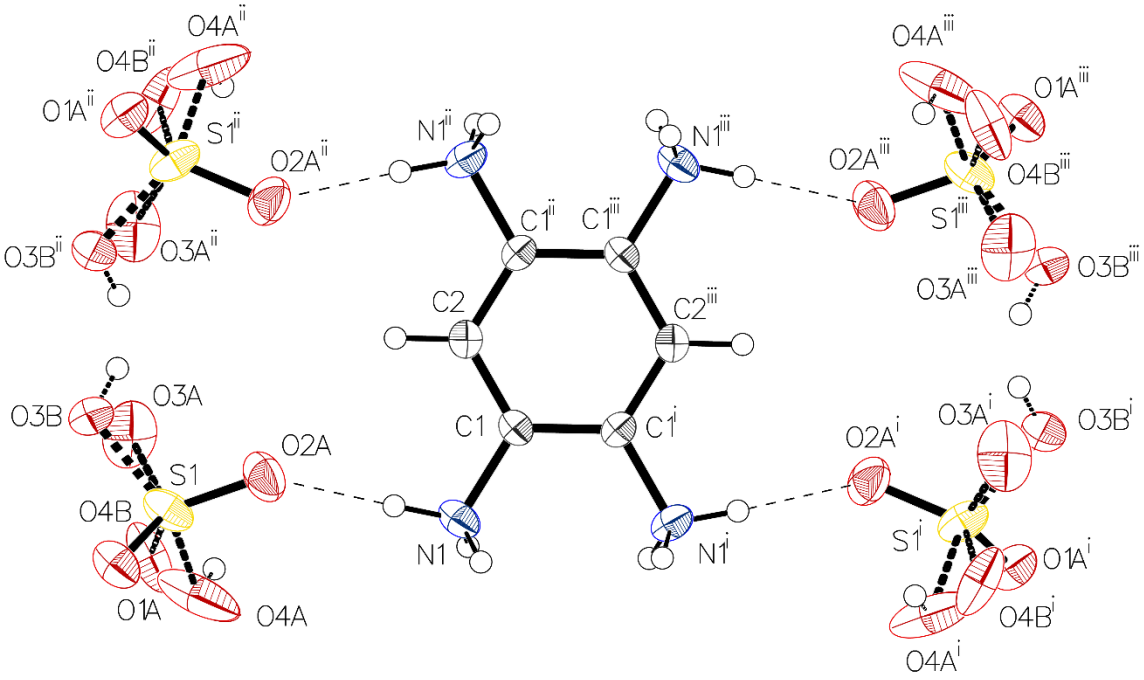

Figure B4. Thermal atomic displacement ellipsoid plot of the structure of *C*2/*m* crystals of salt H_4(1,2,4,5-BTA)$^{4+}$ 4HSO_4^- grown from concentrated H_2SO_4 with the atomic numbering scheme. The ellipsoids of non-hydrogen atoms are drawn at the 50% probability level, and hydrogen atoms are represented by a sphere of arbitrary size. Symmetry Codes (i): 2-x, y, 2-z ; (ii): x, 1-y, z ; (iii): 2-x, 1-y, 2-z.

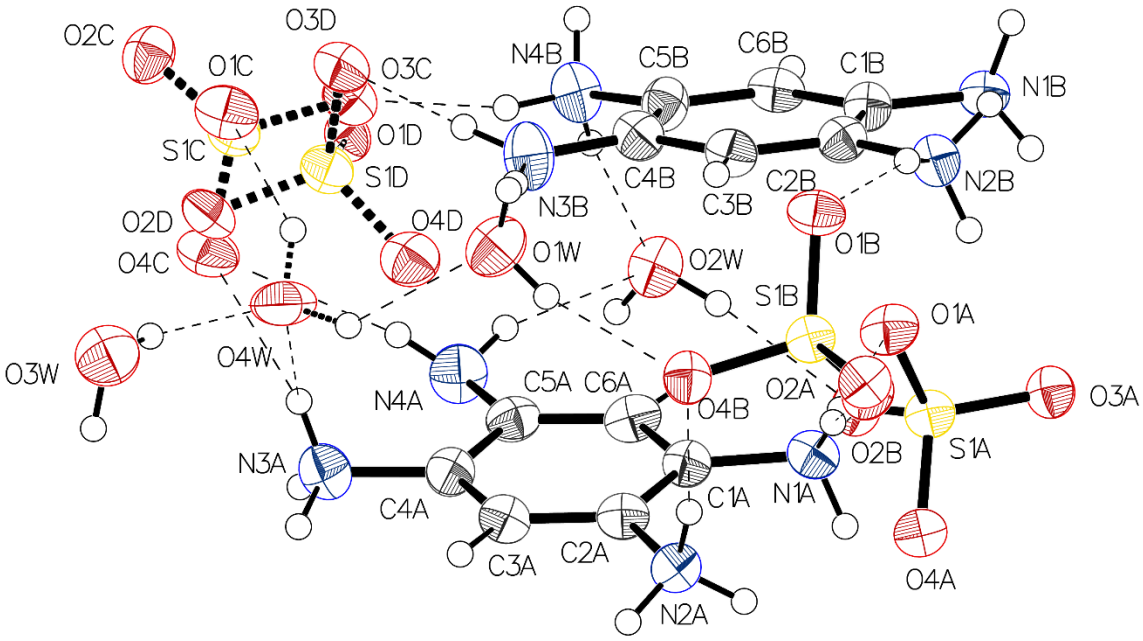

Figure B5. Thermal atomic displacement ellipsoid plot of the structure of *P*2$_1$/*n* crystals of salt H_3(1,2,4,5-BTA)$^{3+}$ 1.5SO_4^- • 2H_2O grown from 0.2 M aqueous H_2SO_4 with the atomic numbering scheme. The ellipsoids of non-hydrogen atoms are drawn at the 50% probability level, and hydrogen atoms are represented by a sphere of arbitrary size.

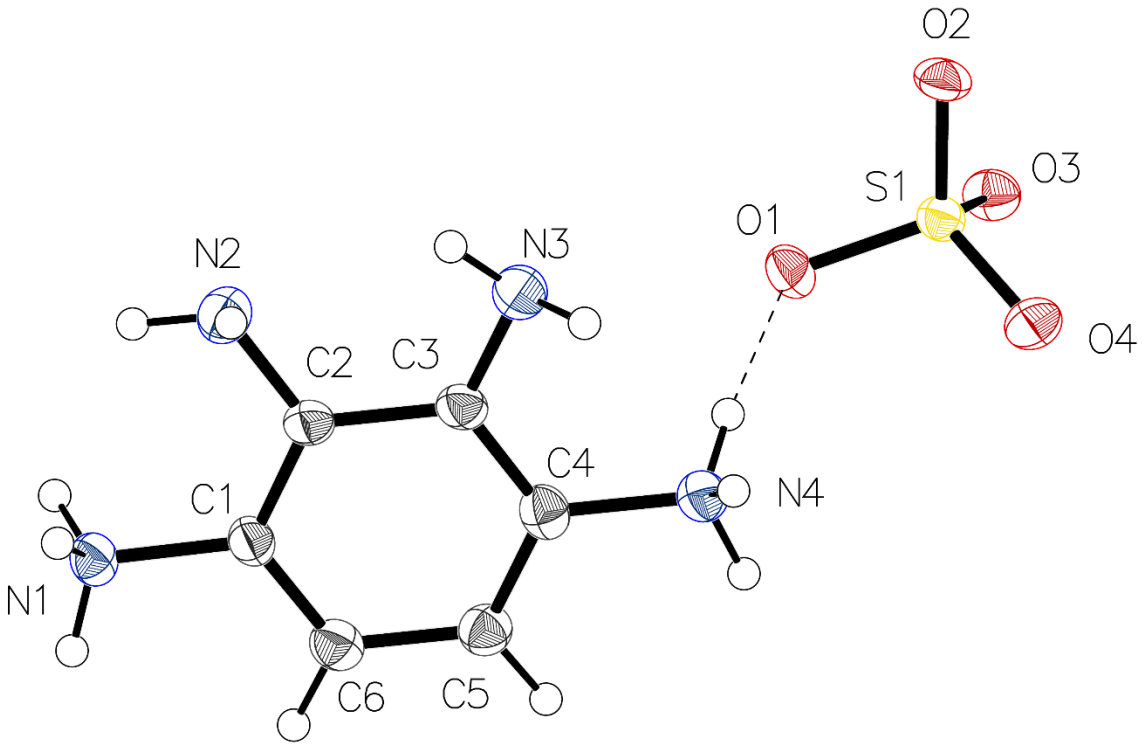

Figure B6. Thermal atomic displacement ellipsoid plot of the structure of *P*2$_1$/*c* crystals of salt H_2(1,2,3,4-BTA)$^{2+}$ SO_4^{2-} grown from EtOH/H_2O/H_2SO_4 with the atomic numbering scheme. The ellipsoids of non-hydrogen atoms are drawn at the 50% probability level, and hydrogen atoms are represented by a sphere of arbitrary size.

III. References

1. Bruker (2022). *APEX4* and *SAINT*, Bruker AXS Inc., Madison, Wisconsin, USA.
2. Krause, L.; Herbst-Irmer, R.; Sheldrick, G. M.; Stalke, D. Comparison of Silver and Molybdenum Microfocus X-Ray Sources for Single-Crystal Structure Determination. *J. Appl. Cryst*. **2015**, *48*, 3–10.
3. Sheldrick, G. M. *SHELXT* – Integrated Space-Group and Crystal-Structure Determination. *Acta Crystallogr*. **2015**, *A71*, 3–8.
4. Sheldrick, G. M. Crystal Structure Refinement with *SHELXL*. *Acta Crystallogr*. **2015**, *C71*, 3–8.
5. Dolomanov, O. V.; Bourhis, L. J.; Gildea, R. J.; Howard, J. A. K.; Puschmann, H. *OLEX2*: A Complete Structure Solution, Refinement and Analysis Program. *J. Appl. Crystallogr*. **2009**, *42*, 339–341.

Annexe C

Informations supplémentaires

Chapitre 4

Étude expérimentale et théorique

de l'hydrolyse de la benzène-1,2,4,5-tétramine et de composés analogues

Supporting Information

Experimental and Computational Study of the Hydrolysis of Benzene-1,2,4,5-tetramine and Related Compounds

Johann O. E. Sosoe,* Thierry Maris, Radu Iftimie, and James D. Wuest*

Département de Chimie, Université de Montréal, Montréal, Québec H2V 0B3 Canada

*Authors to whom correspondence may be addressed

Email: *johann.sosoe@umontreal.ca*; *james.d.wuest@umontreal.ca*

Annexe C

Contents **Page**

I. Additional Crystallographic Information

Single-crystal X-ray diffraction data were collected on a Bruker Venture Kappa-geometry diffractometer equipped with a gallium liquid metal-jet source (GaKα radiation, λ = 1.34139 Å), a Photon III detector, and Helios MX mirror optics. Measurements were carried out at 150 K using an Oxford Cryostream 700 low-temperature device. The unit-cell lattice parameters were determined by measurement of a limited set of frames using the *APEX3* suite of software.[1] Reflection data were integrated using *SAINT* V8.38A, and a multiscan absorption correction using *SADABS* was applied.[2] Structures were solved using the intrinsic phasing routine as implemented in *SHELXT*,[3] and cycles of refinement were performed by least-square minimization with *SHELXL*[4] within the graphical user interface of *OLEX2*.[5] All non-hydrogen atoms were refined using anisotropic thermal displacement parameters. Hydrogen atoms were located from Fourier difference maps and fully refined isotropically, except for hydrogen atoms linked to carbon atoms in DAR-H_2 (**5**) • HCl • H_2O, which were refined on calculated positions using standard riding models from *SHELXL*, with their U_{iso} constrained to 1.2 times the U_{eq} of the carbon atoms, and the hydrogen atoms of included H_2O were refined isotropically using constraints (DFIX) on O–H distances.

II. Thermal Atomic Displacement Parameter Plots

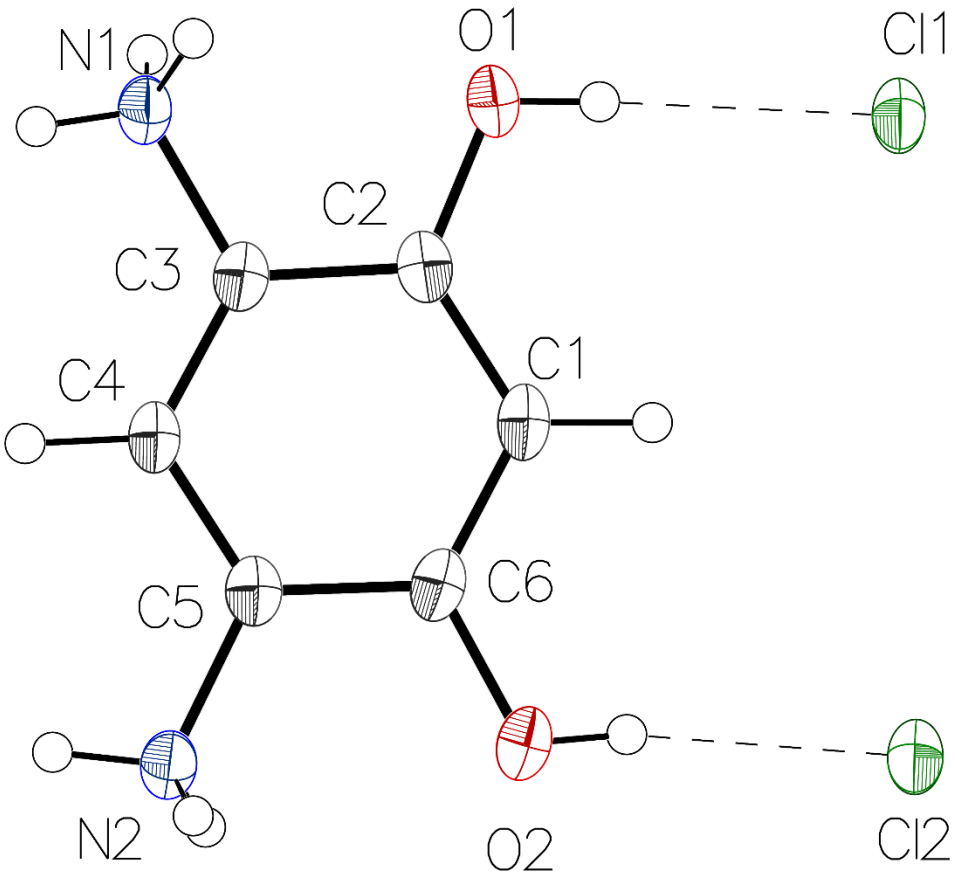

Figure C1. Thermal atomic displacement ellipsoid plot of the structure of $P2_1/n$ crystals of dihydrochloride salt DAR (**4**) • 2HCl grown from H_2O with the atomic numbering scheme. The ellipsoids of non-hydrogen atoms are drawn at the 50% probability level, and hydrogen atoms are represented by a sphere of arbitrary size.

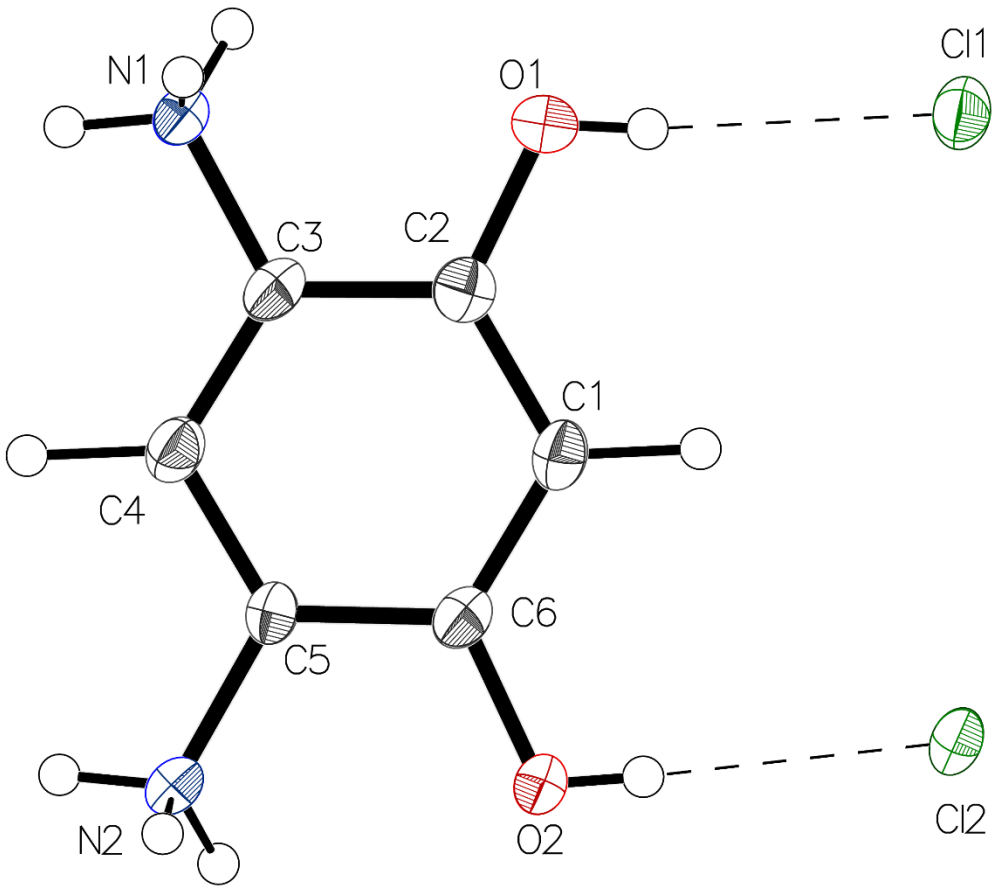

Figure C2. Thermal atomic displacement ellipsoid plot of the structure of $P\bar{1}$ crystals of dihydrochloride salt DAR (**4**) • 2HCl grown from H_2O with the atomic numbering scheme. The ellipsoids of non-hydrogen atoms are drawn at the 50% probability level, and hydrogen atoms are represented by a sphere of arbitrary size.

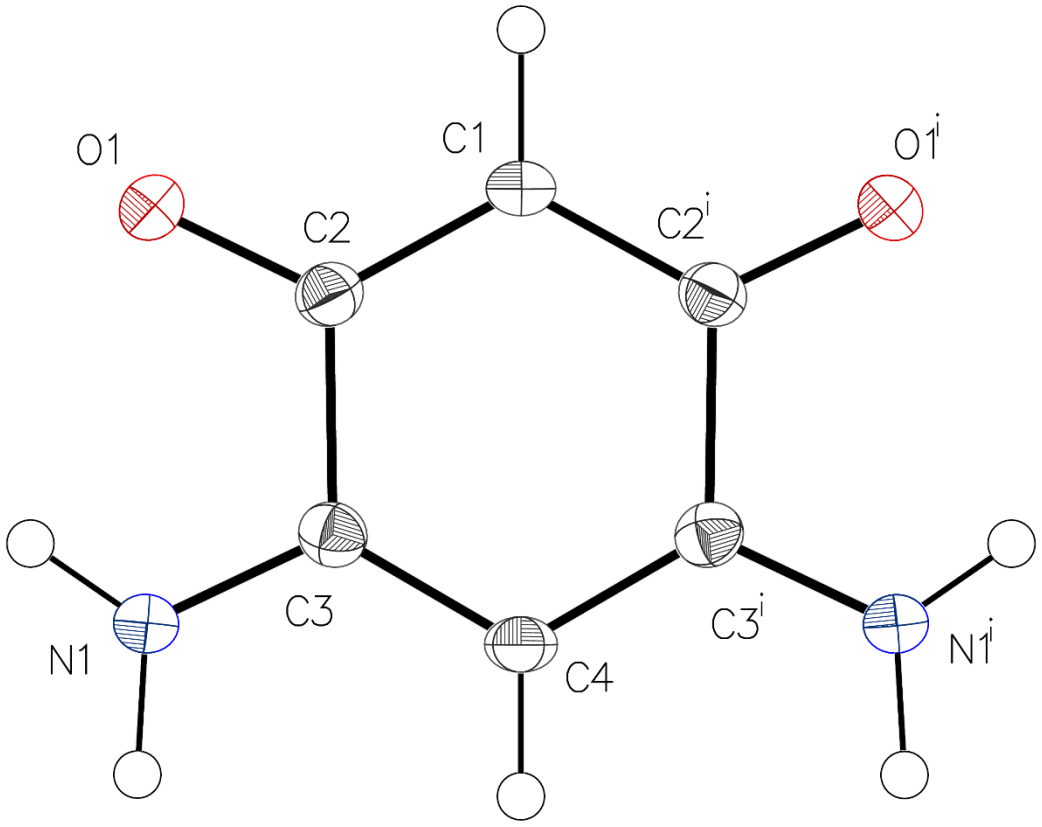

Figure C3. Thermal atomic displacement ellipsoid plot of the structure of *Pbcn* crystals of anhydrous zwitterion DAR-H_2 (**5**) grown from H_2O with the atomic numbering scheme. The ellipsoids of non-hydrogen atoms are drawn at the 50% probability level, and hydrogen atoms are represented by a sphere of arbitrary size. Symmetry Codes (i): 1-x, y, 0.5-z.

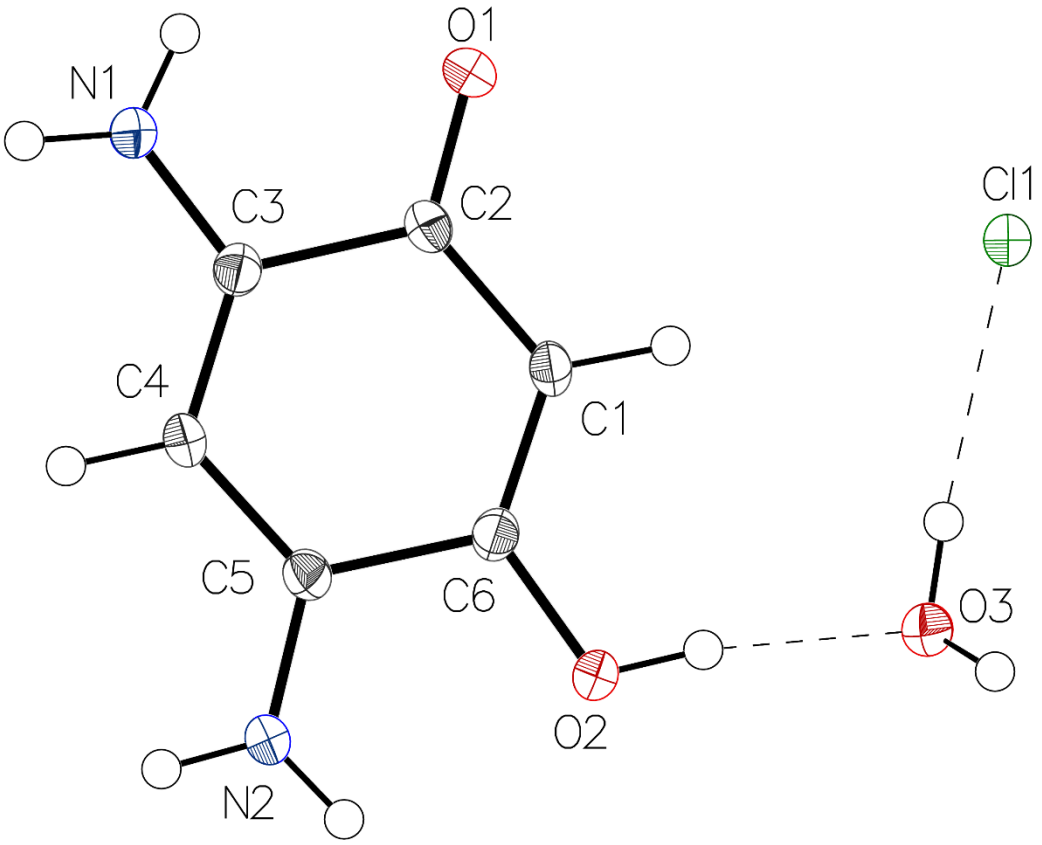

Figure C4. Thermal atomic displacement ellipsoid plot of the structure of $P\bar{1}$ crystals of hydrated monochloride salt DAR-H_2 (**5**) • HCl • H_2O grown from 1 M HCl with the atomic numbering scheme. The ellipsoids of non-hydrogen atoms are drawn at the 50% probability level, and hydrogen atoms are represented by a sphere of arbitrary size.

III. Additional Spectroscopic Data

IV. Supplementary Computational Information

This section provides the Cartesian coordinates, electronic potential energies (EE), and free energies (G) for structures involved in the reactions summarized in Table III - 1 of the main paper. Data are presented in the following way, with each reaction appearing on a different page:

- The reaction number entered in Table III - 1 appears at the top of the page. The next line identifies the density functional and basis set used to obtain the optimized structures. All geometric optimizations used RωB97X-D3/6-311+G(2df,2p), as stated in the main paper. On the same line. the medium in which the reaction takes place is specified (water, described at the C-PCM level).
- Data for the reactant are provided on the upper half of the page and data for the product on the lower half. The first line in the reactant/product sections provides the energy value in atomic units, obtained at the geometric optimization level. The next line gives the free energy in atomic units, obtained at the geometry optimization level. Finally, the single-point electronic energy value obtained at the RωB97M(2)/QZVPPD level is given, as determined using electronic orbitals previously optimized at the RωB97M-V/QZVPPD level. No information about enthalpy, entropy, or free energy is included because vibrational frequencies were not computed at this level.

The values of enthalpy and free energy compiled in Table III - 1 of the main paper were computed as follows from geometric optimization at the RωB97X-D3/6-311+G(2df,2p) level:

$$\Delta G^{\circ}(Table\ 1) = \Delta G^{\circ}\big(R\omega B97X - D3/6 - 311 + G(2df, 2p)\big) + \Delta\Delta E$$

The added correction $\Delta\Delta E$ corresponds to the electronic potential energy difference between single-point calculations at the RωB97M(2)/QZVPPD and RωB97X-D3/6-311+G(2df,2p) levels:

$$\Delta\Delta E = \Delta E(single\ point;\ R\omega B9M(2)/QZVPPD\ ) - \Delta E(single\ point;\ R\omega B97X - D3/6 - 311 + G(2df, 2p))$$

Annexe C

Reaction 1 in Table III - 1 from the main paper

Optimization level: RωB97X-D3/6-311+G(2df,2p)Medium: C-PCM, ε = 78.3

Reactant:

EE(RωB97X-D3/6-311+G(2df,2p)) = -288.071949 a.u.0 imaginary frequencies
G°(RωB97X-D3/6-311+G(2df,2p)) = -287.968675 a.u
EE(RωB97M(2)/QZVPPD) = -288.269736 a.u.

0 1

Standard Nuclear Orientation (Angstroms)

I	Atom	X	Y	Z
1	C	0.0005130101	-0.0114088528	-0.6946772251
2	C	0.0000142115	0.0046980477	2.0509955670
3	C	1.2108698305	-0.0082570739	-0.0278373508
4	C	-1.2098966253	-0.0075669924	-0.0281076606
5	C	-1.2032555607	0.0003004370	1.3588932755
6	C	1.2035645162	-0.0004174071	1.3592797216
7	H	2.1428397142	-0.0131042992	-0.5793554604
8	H	-2.1417570546	-0.0118771582	-0.5799401100
9	H	-2.1425708238	0.0013430246	1.8959653417
10	H	2.1424324372	0.0000513894	1.8970031512
11	H	-0.0004719239	0.0097634374	3.1332600765
12	N	-0.0002954872	0.0054677511	-2.1630838726
13	H	-0.0031900952	0.9585433879	-2.5287184913
14	H	-0.8190417433	-0.4658820737	-2.5462376987
15	H	0.8202455944	-0.4616536178	-2.5474393700

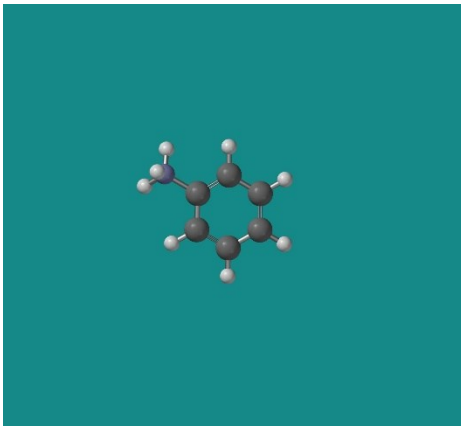

Product:

EE(RωB97X-D3/6-311+G(2df,2p)) = -288.046885 a.u.0 imaginary frequencies
G°(RωB97X-D3/6-311+G(2df,2p)) = -287.946406 a.u
EE(RωB97M(2)/QZVPPD) = -288.242121 a.u.
0 1

Standard Nuclear Orientation (Angstroms)

I	Atom	X	Y	Z
1	C	-0.1124374773	0.0000106622	-0.9266568665
2	C	-0.0859654560	-0.0000136947	1.9169672265
3	C	-1.3383707622	0.0000267524	-0.2010553910
4	C	1.1836799603	0.0000214217	-0.1970649999
5	C	1.0901356186	-0.0000040109	1.2839221136
6	C	-1.3096500857	0.0000093645	1.1508763490
7	H	-2.2723679569	0.0000346031	-0.7471860736
8	H	2.0249618723	-0.0000212526	1.8293318964
9	H	-2.2497996501	0.0000062017	1.6894079392
10	H	-0.1451017988	-0.0000401865	2.9962393451
11	N	-0.1080686782	-0.0000224772	-2.2283897511
12	H	0.7528266299	-0.0000493053	-2.7548452384
13	H	-0.9699176859	-0.0000323965	-2.7534257856
14	H	1.7700533505	-0.8645602098	-0.5290733865
15	H	1.7700220664	0.8646345279	-0.5290473772

Reaction 2 in Table III - 1 from the main paper
Optimization level: RωB97X-D3/6-311+G(2df,2p)Medium: C-PCM, ε = 78.3

Reactant:
EE(RωB97X-D3/6-311+G(2df,2p)) = -343.884608 a.u.0 imaginary frequencies
G°(RωB97X-D3/6-311+G(2df,2p)) = -343.750903 a.u
EE(RωB97M(2)/QZVPPD) = -344.118269 a.u.
0 1

Standard Nuclear Orientation (Angstroms)

I	Atom	X	Y	Z
1	C	-1.1776350237	0.0061972644	0.1335464710
2	C	1.2025179580	-0.0551851647	-1.2486419199
3	C	-1.2017381370	-0.0353441250	-1.2474450070
4	C	0.0018138176	0.0201407588	0.8495831932
5	C	1.1809192715	-0.0128351339	0.1307379711
6	C	-0.0009977992	-0.0663512251	-1.9367053521
7	H	-2.1454696186	-0.0470578489	-1.7778185704
8	H	0.0045991241	0.0529309915	1.9321134829
9	H	-0.0021851600	-0.1023747327	-3.0171886984
10	H	2.1443311417	-0.0820581996	-1.7816800156
11	N	-2.4510202973	0.0440133440	0.8564042170
12	H	-2.9388620918	0.9291103788	0.7085816750
13	H	-2.3265723461	-0.0660140338	1.8626723051
14	H	-3.0770421322	-0.7008541590	0.5478981981
15	N	2.4508483110	0.0210926281	0.8579950321
16	H	2.8122358665	0.9735633492	0.9329313954
17	H	3.1652791045	-0.5371364896	0.3903259101
18	H	2.3589779050	-0.3418376025	1.8066897122

Product:
EE(RωB97X-D3/6-311+G(2df,2p)) = -343.857067 a.u.0 imaginary frequencies
G°(RωB97X-D3/6-311+G(2df,2p)) = -343.725594 a.u
EE(RωB97M(2)/QZVPPD) = -344.088708 a.u.
0 1

Standard Nuclear Orientation (Angstroms)

I	Atom	X	Y	Z
1	C	-0.1916279159	0.0425268365	-1.4055489161
2	C	1.2691425723	-0.1051508558	1.0304558717
3	C	1.2366863983	-0.0523047341	-1.4259953394
4	C	-0.9268318146	0.0651953429	-0.1106730505
5	C	-0.0523837706	-0.0178432915	1.0840963109
6	C	1.9164585144	-0.1213934443	-0.2672111782
7	H	1.7428894392	-0.0656255625	-2.3817403724
8	H	2.9961147481	-0.1924693642	-0.2890512788
9	H	1.8725215476	-0.1652916838	1.9260894010
10	N	-0.8651619778	0.1102192007	-2.5090516034
11	H	-1.8733638580	0.1776428728	-2.5163504185
12	H	-0.3984886848	0.0983151267	-3.4049533509
13	H	-1.5327019726	0.9782311710	-0.0692507035
14	H	-1.6503900396	-0.7589561057	-0.1047201611
15	N	-0.7484594911	-0.0011274313	2.3632764970
16	H	-1.3776436400	-0.8020544543	2.4606176960
17	H	-1.3201951843	0.8401045297	2.4718745672
18	H	-0.0965648706	-0.0300180469	3.1481361348

Reaction 3 in Table III - 1 from the main paper
Optimization level: RωB97X-D3/6-311+G(2df,2p)Medium: C-PCM, ε = 78.3

Reactant:
EE(RωB97X-D3/6-311+G(2df,2p)) = -343.445045 a.u.0 imaginary frequencies
G°(RωB97X-D3/6-311+G(2df,2p)) = -343.326093 a.u
EE(RωB97M(2)/QZVPPD) = -343.681299 a.u.
0 1

Standard Nuclear Orientation (Angstroms)

I	Atom	X	Y	Z
1	C	-0.0581382678	-0.4819482306	-1.3055604776
2	C	0.2625091946	-0.5224487213	1.4920512847
3	C	0.1685399209	-1.6841526332	-0.6213438252
4	C	-0.1239894741	0.7025551165	-0.5685005239
5	C	0.0374922784	0.6491761839	0.8012322714
6	C	0.3248255853	-1.6978174811	0.7505970170
7	H	0.2197486151	-2.6090716288	-1.1832024559
8	H	-0.2989953336	1.6489348513	-1.0665311692
9	H	0.4969485978	-2.6385343009	1.2576525201
10	H	0.3829734428	-0.5253018029	2.5672400917
11	N	-0.0373725068	1.9115858194	1.5475598079
12	H	0.0727658788	1.7620295158	2.5495451240
13	H	-0.9335623183	2.3784682072	1.4081510657
14	H	0.6914346296	2.5633272203	1.2566102290
15	N	-0.1614225020	-0.4616026146	-2.6811138609
16	H	-0.6252873280	0.3354702978	-3.0848003038
17	H	-0.4184704127	-1.3306697458	-3.1195869012

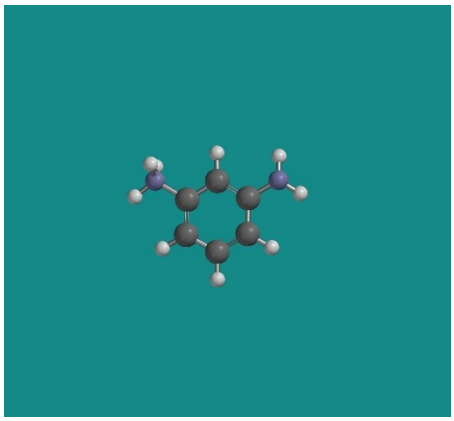

Product:
EE(RωB97X-D3/6-311+G(2df,2p)) = -343.436085 a.u.0 imaginary frequencies
G°(RωB97X-D3/6-311+G(2df,2p)) = -343.320842 a.u
EE(RωB97M(2)/QZVPPD) = -343.66886 a.u.
0 1

Standard Nuclear Orientation (Angstroms)

I	Atom	X	Y	Z
1	C	-1.2713349815	-0.0000215548	0.1710114846
2	C	1.2332579157	0.0001095036	-1.2136286681
3	C	-1.2329507143	0.0000670746	-1.2134751217
4	C	0.0000313423	0.0003019931	0.9583175815
5	C	1.2714386042	-0.0000119840	0.1709004455
6	C	0.0001228778	0.0001692901	-1.8539089367
7	H	-2.1520641095	-0.0000310982	-1.7825623892
8	H	-0.0001629461	0.0002157349	-2.9383973741
9	H	2.1522464143	0.0000453093	-1.7828454330
10	N	-2.4001548417	-0.0002873059	0.8613101230
11	H	-2.4047363525	-0.0004079861	1.8674045705
12	H	-3.2904078572	-0.0004046480	0.3919075598
13	H	-0.0001022252	0.8709394466	1.6211914211
14	H	-0.0000967199	-0.8694948151	1.6222665611
15	N	2.4001052629	-0.0003074783	0.8612777482
16	H	2.4044656510	-0.0004660743	1.8673583082
17	H	3.2903426266	-0.0004154604	0.3918721196

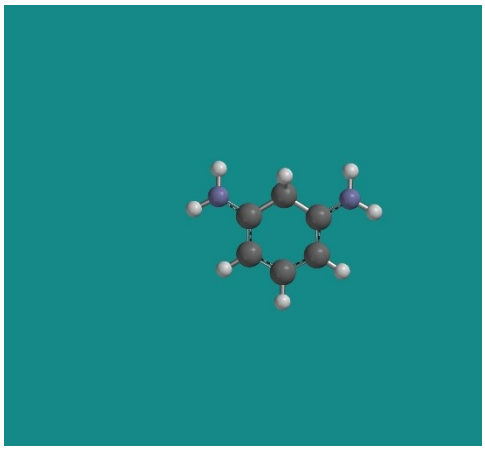

Reaction 4 in Table III - 1 from the main paper
Optimization level: RωB97X-D3/6-311+G(2df,2p)Medium: C-PCM, ε = 78.3

Reactant:

EE(RωB97X-D3/6-311+G(2df,2p)) = -399.690612 a.u.0 imaginary frequencies
G°(RωB97X-D3/6-311+G(2df,2p)) = -399.526551 a.u
EE(RωB97M(2)/QZVPPD) = -399.960038 a.u.

0 1

Standard Nuclear Orientation (Angstroms)

I	Atom	X	Y	Z
1	C	0.0010344270	0.0020114213	1.3617750508
2	C	0.0010333984	-0.0257753178	-1.3977406688
3	C	-1.2069273198	-0.0032586948	0.6946305099
4	C	1.2095032075	-0.0048534784	0.6951579723
5	C	1.1822134337	-0.0204297754	-0.6845526302
6	C	-1.1802355258	-0.0188058000	-0.6848961514
7	H	-2.1458495280	-0.0000350194	1.2348864756
8	H	2.1481910742	-0.0027980899	1.2355880928
9	H	0.0009137897	-0.0406321127	-2.4806801705
10	N	-0.0013997163	0.0365380687	2.8228700762
11	H	-0.0109025629	0.9970342022	3.1731871554
12	H	0.8218444040	-0.4207362929	3.2162531226
13	H	-0.8181481843	-0.4352690482	3.2129669758
14	N	2.4493329047	-0.0121468845	-1.4110185599
15	H	2.8488437622	0.9279158734	-1.4519534647
16	H	2.3409622468	-0.3355129201	-2.3728865013
17	H	3.1430106987	-0.6168608961	-0.9686430523
18	N	-2.4489705719	-0.0096352647	-1.4092989016
19	H	-2.8538552008	0.9285470278	-1.4401263279
20	H	-3.1387589393	-0.6219248236	-0.9710463411
21	H	-2.3418356920	-0.3233721749	-2.3744727677

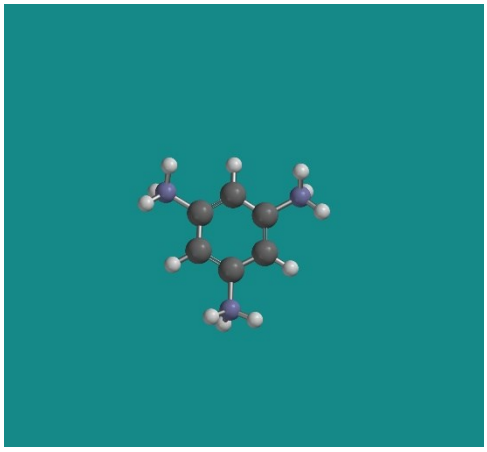

Product:

EE(RωB97X-D3/6-311+G(2df,2p)) = -399.657233 a.u.0 imaginary frequencies
G°(RωB97X-D3/6-311+G(2df,2p)) = -399.495448 a.u
EE(RωB97M(2)/QZVPPD) = -399.924823 a.u.

0 1

Standard Nuclear Orientation (Angstroms)

I	Atom	X	Y	Z
1	C	-0.9839617817	0.0360824876	0.9468028084
2	C	1.2558361045	-0.0592096038	-0.7870000795
3	C	-1.2038624008	0.0532335621	-0.4819926837
4	C	0.2187842014	-0.0155514302	1.5304593193
5	C	1.3876221124	-0.0560848910	0.6953772467
6	C	-0.1416307683	0.0078243573	-1.2734101088
7	H	-2.2122580511	0.0979957561	-0.8727747940
8	H	0.3331829796	-0.0237409884	2.6068425527
9	N	-2.1675057200	0.0843504210	1.7999106780
10	H	-2.1823049626	0.9397313598	2.3621438153
11	H	-2.1875491603	-0.7052702815	2.4505480710
12	H	-3.0393498361	0.0596441670	1.2691147205
13	N	2.5600345653	-0.0916109185	1.2294014525
14	H	2.6798038145	-0.0919393364	2.2336422256
15	H	3.4012067267	-0.1181286001	0.6680602858
16	N	-0.2975162050	0.0156701619	-2.7184538604
17	H	-1.2779733289	0.0719969083	-2.9972797418
18	H	0.0927938685	-0.8301094064	-3.1429714992
19	H	0.1876851524	0.8097012754	-3.1451198440
20	H	1.8357142891	0.7771738967	-1.1947716236
21	H	1.7412484534	-0.9617588967	-1.1785288351

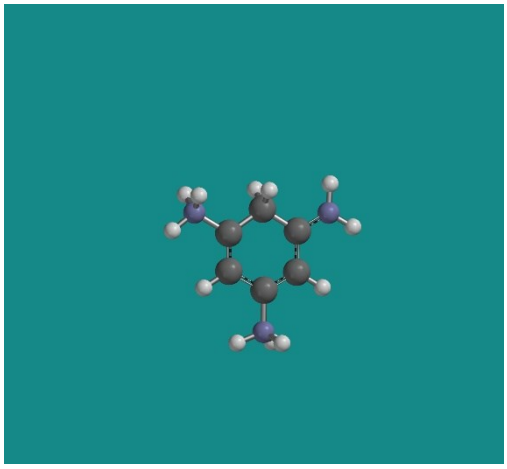

Reaction 5 in Table III - 1 from the main paper
Optimization level: RωB97X-D3/6-311+G(2df,2p)Medium: C-PCM, ε = 78.3

Reactant:

EE(RωB97X-D3/6-311+G(2df,2p)) = -399.259526 a.u.0 imaginary frequencies
G°(RωB97X-D3/6-311+G(2df,2p)) = -399.110869 a.u
EE(RωB97M(2)/QZVPPD) = -399.531547 a.u.

0 1

Standard Nuclear Orientation (Angstroms)

I	Atom	X	Y	Z
1	C	-1.1703691075	0.0161516299	0.5312504713
2	C	1.2040518644	0.0153603112	-0.8440823865
3	C	-1.2021903036	0.0158414728	-0.8435247959
4	C	0.0008054951	0.0178804481	1.2641153675
5	C	1.1718008195	0.0157137464	0.5308912018
6	C	0.0006609894	0.0175560614	-1.5613453710
7	H	-2.1487064447	0.0135588659	-1.3704067864
8	H	0.0006521428	0.0189737676	2.3458240470
9	H	2.1502981318	0.0128073864	-1.3712036610
10	N	-2.4503607300	0.0200162605	1.2456804631
11	H	-2.9650270610	0.8871948017	1.0854300888
12	H	-2.3268576065	-0.0755994787	2.2531779448
13	H	-3.0501473420	-0.7475985892	0.9413085390
14	N	2.4505100157	0.0198010369	1.2468157531
15	H	2.9629132839	0.8890631703	1.0909816117
16	H	3.0524172812	-0.7452497673	0.9404285918
17	H	2.3250210509	-0.0801170827	2.2536534564
18	N	-0.0010443345	0.0647699579	-2.9264073630
19	H	-0.8490848703	-0.1870281135	-3.4048533160
20	H	0.8446566194	-0.1890958326	-3.4077338565

Product:

EE(RωB97X-D3/6-311+G(2df,2p)) = -399.248008 a.u.0 imaginary frequencies
G°(RωB97X-D3/6-311+G(2df,2p)) = -399.102837 a.u
EE(RωB97M(2)/QZVPPD) = -399.51712 a.u.

0 1

Standard Nuclear Orientation (Angstroms)

I	Atom	X	Y	Z
1	C	0.0008088399	-0.0148621182	-1.2585264581
2	C	0.0001845849	0.0003261705	1.5311036691
3	C	1.2379097448	-0.0123145620	-0.6450238501
4	C	-1.2362750719	-0.0117108113	-0.6449344427
5	C	-1.2711175262	-0.0035838290	0.7445870542
6	C	1.2718131306	-0.0043052609	0.7447595984
7	H	2.1516304698	-0.0153448649	-1.2226813313
8	H	-2.1498860413	-0.0142813603	-1.2228704474
9	N	-0.0005618765	0.0051357153	-2.7230936134
10	H	-0.0076217298	0.9672291798	-3.0710007525
11	H	-0.8214539173	-0.4618418192	-3.1096937801
12	H	0.8251162500	-0.4511698875	-3.1119492658
13	N	-2.3982304753	0.0007454100	1.4220143870
14	H	-3.2872445189	-0.0010890331	0.9483560024
15	H	-2.4090756364	0.0066610817	2.4290252790
16	N	2.3983206935	-0.0006876257	1.4229095868
17	H	3.2876669874	-0.0030049483	0.9499095934
18	H	2.4081865303	0.0051702947	2.4299330727
19	H	0.0001672157	0.8753197280	2.1881870845
20	H	-0.0003376535	-0.8663915126	2.1989886134

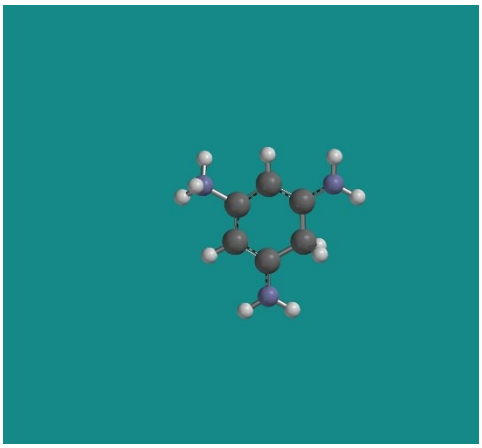

Reaction 6 in Table III - 1 from the main paper
Optimization level: RωB97X-D3/6-311+G(2df,2p)Medium: C-PCM, ε = 78.3

Reactant:

EE(RωB97X-D3/6-311+G(2df,2p)) = -455.473639 a.u.0 imaginary frequencies
G°(RωB97X-D3/6-311+G(2df,2p)) = -455.275944 a.u
EE(RωB97M(2)/QZVPPD) = -455.778526 a.u.

0 1

Standard Nuclear Orientation (Angstroms)

I	Atom	X	Y	Z
1	H	0.0011080772	0.0001123950	-2.4586510330
2	C	0.0009957984	0.0000985312	-1.3756309798
3	C	0.0003366032	-0.0000035502	1.3790778720
4	C	-1.1962017926	0.0008760390	-0.6919756336
5	C	1.1977863889	-0.0007450111	-0.6914640438
6	C	1.1975148315	0.0007872373	0.6946748583
7	C	-1.1965929388	-0.0007344158	0.6941246202
8	H	-0.0003234311	-0.0000588337	2.4620587767
9	N	-2.4281578709	0.0153180613	-1.4727817492
10	H	-3.0506973251	-0.7668095912	-1.2523159073
11	H	-2.2296749363	-0.0536772066	-2.4729494040
12	H	-2.9589032880	0.8821954873	-1.3442502813
13	N	-2.4305082098	-0.0152154241	1.4714167515
14	H	-2.9608879250	-0.8819781774	1.3404570877
15	H	-3.0521505300	0.7669756384	1.2485547758
16	H	-2.2353627563	0.0535898425	2.4721872586
17	N	2.4299085575	0.0152078335	1.4735095634
18	H	3.0512057647	-0.7674933026	1.2517719670
19	H	2.2327230171	-0.0529357567	2.4739119823
20	H	2.9604300886	0.8818172774	1.3426582945
21	N	2.4286733759	-0.0153449709	-1.4731420104
22	H	2.9592902351	-0.8822218914	-1.3446364508
23	H	3.0509553530	0.7671579674	-1.2535884441
24	H	2.2285329129	0.0530818215	-2.4730178705

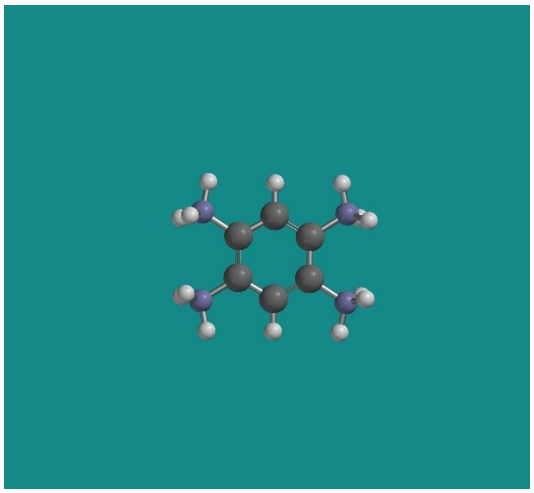

Product:

EE(RωB97X-D3/6-311+G(2df,2p)) = -455.437725 a.u.0 imaginary frequencies
G°(RωB97X-D3/6-311+G(2df,2p)) = -455.24357 a.u
EE(RωB97M(2)/QZVPPD) = -455.740589 a.u.

0 1

Standard Nuclear Orientation (Angstroms)

I	Atom	X	Y	Z
1	C	-1.4774146135	0.0063869705	0.0669447444
2	C	1.3446242484	-0.0111052178	0.1866409582
3	C	-0.6432063659	0.0014526619	-1.1549598000
4	C	-0.7591499682	0.0053209092	1.3689630359
5	C	0.6813323818	-0.0039857639	1.3495601464
6	C	0.6862219952	-0.0047736019	-1.0978967671
7	H	2.4293222686	-0.0212858514	0.1948973713
8	N	-1.3911106015	0.0156164588	-2.4036557181
9	H	-1.2703678456	0.8985736433	-2.9130786010
10	H	-2.3966915501	-0.0872275574	-2.2433150318
11	H	-1.1255321237	-0.7465660789	-3.0353158206
12	N	1.5414314292	-0.0157212273	-2.2768773136
13	H	1.3358683214	0.7515410230	-2.9223045882
14	H	1.4658138860	-0.8933604181	-2.7999449519
15	H	2.5280284759	0.0834675149	-2.0286842997
16	N	1.4225610531	-0.0058121811	2.6001481283
17	H	2.4312322225	-0.0094283667	2.4320006610
18	H	1.2261638175	-0.8334681293	3.1717735349
19	H	1.2322710621	0.8247019949	3.1697430444
20	N	-1.4533513660	0.0096642702	2.4521976160
21	H	-2.4662838125	0.0154380932	2.4188427814
22	H	-1.0520779619	0.0070795773	3.3805579002
23	H	-2.1455817360	-0.8653297140	0.0435432711
24	H	-2.1441032173	0.8788209905	0.0402196985

Reaction 7 in Table III - 1 from the main paper
Optimization level: RωB97X-D3/6-311+G(2df,2p)Medium: C-PCM, ε = 78.3

Reactant:

EE(RωB97X-D3/6-311+G(2df,2p)) = -455.058094 a.u.0 imaginary frequencies
G°(RωB97X-D3/6-311+G(2df,2p)) = -454.876164 a.u
EE(RωB97M(2)/QZVPPD) = -455.365549 a.u.

0 1

Standard Nuclear Orientation (Angstroms)

I	Atom	X	Y	Z
1	H	0.0927273309	-0.2561732236	-2.5164685736
2	C	0.1054788844	-0.1522298481	-1.4388082613
3	C	0.1160815760	0.1140079400	1.3041385691
4	C	1.3441566766	-0.1616923750	-0.7757353153
5	C	-1.0723690714	-0.0138714770	-0.7541724349
6	C	-1.0851032151	0.1254712988	0.6313748935
7	C	1.3017499731	-0.0291677214	0.6174145600
8	H	0.1296093124	0.2147874351	2.3829805492
9	N	-2.3102097831	-0.0156362488	-1.5341373007
10	H	-2.8365491984	0.8560383035	-1.4400645471
11	H	-2.9352356711	-0.7847434204	-1.2805815949
12	H	-2.1099078802	-0.1226548870	-2.5294506342
13	N	-2.3195587525	0.2766201883	1.3990644476
14	H	-2.8534349501	1.1104156172	1.1424177165
15	H	-2.1135226701	0.3673943088	2.3946212569
16	H	-2.9422464575	-0.5294169001	1.3109784528
17	N	2.5488597036	-0.0508083648	1.3761524383
18	H	2.3748249342	-0.0088658516	2.3807289978
19	H	3.1554688566	0.7425094337	1.1550434842
20	H	3.0858516146	-0.9057423131	1.2115584829
21	N	2.4875294351	-0.3317170059	-1.4759917119
22	H	2.4456743642	-0.3068694420	-2.4802934321
23	H	3.3901249879	-0.1376554466	-1.0807700428

Product:

EE(RωB97X-D3/6-311+G(2df,2p)) = -455.047185 a.u.0 imaginary frequencies
G°(RωB97X-D3/6-311+G(2df,2p)) = -454.869083 a.u
EE(RωB97M(2)/QZVPPD) = -455.351578 a.u.

0 1

Standard Nuclear Orientation (Angstroms)

I	Atom	X	Y	Z
1	C	0.0000588540	0.0001355973	-1.5384321143
2	C	0.0005673993	0.0000959250	1.2676867973
3	C	1.2813289600	-0.0000012067	-0.7698175387
4	C	-1.2808481312	0.0000458279	-0.7695424506
5	C	-1.2192357400	0.0000574481	0.6221325479
6	C	1.2201485283	0.0000929264	0.6219622020
7	H	0.0003854032	0.0000899020	2.3532814263
8	N	-2.3878202023	-0.0000295991	-1.4698838677
9	H	-3.3061755032	-0.0000544557	-1.0555442154
10	H	-2.3589184199	-0.0000696726	-2.4782722283
11	N	-2.4456886353	-0.0000660594	1.4127486458
12	H	-3.0241129767	0.8260991386	1.2421530491
13	H	-2.2412041554	-0.0001211109	2.4127999077
14	H	-3.0240017280	-0.8262894356	1.2420516922
15	N	2.4457831175	0.0000652436	1.4133995329
16	H	2.2399364899	0.0000748168	2.4131847999
17	H	3.0241119066	0.8263458960	1.2433340639
18	H	3.0240804423	-0.8262413017	1.2433548818
19	N	2.3878043005	-0.0001967035	-1.4706723816
20	H	2.3581562686	-0.0003001657	-2.4790342443
21	H	3.3062823770	-0.0002738330	-1.0566404860
22	H	-0.0002994523	0.8721527862	-2.1999506409
23	H	-0.0003391030	-0.8716119638	-2.2002993792

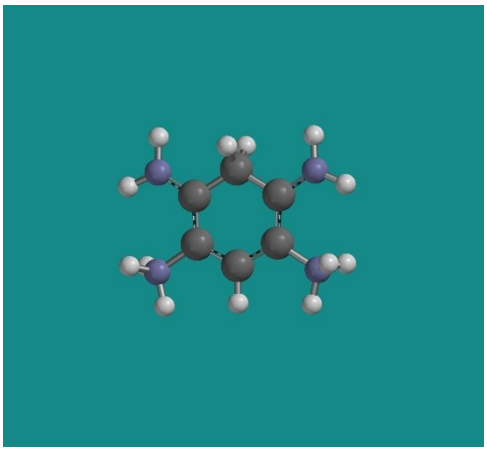

Reaction 8 in Table III - 1 from the main paper
Optimization level: RωB97X-D3/6-311+G(2df,2p)Medium: C-PCM, ε = 78.3

Reactant:

EE(RωB97X-D3/6-311+G(2df,2p)) = -454.629699 a.u.0 imaginary frequencies
G°(RωB97X-D3/6-311+G(2df,2p)) = -454.463404 a.u
EE(RωB97M(2)/QZVPPD) = -454.940196 a.u.

0 1

Standard Nuclear Orientation (Angstroms)

I	Atom	X	Y	Z
1	H	0.0005864064	0.1171508899	-2.5981949277
2	C	0.0006137762	0.0842479971	-1.5155095715
3	C	0.0005062910	-0.0238355517	1.2414597408
4	C	1.2213194055	0.0589133131	-0.8467008402
5	C	-1.2202734361	0.0587573556	-0.8467409369
6	C	-1.1910385205	0.0054011338	0.5533924916
7	C	1.1920528790	0.0056397977	0.5533933951
8	H	0.0001815178	-0.0595298714	2.3248854127
9	N	-2.4019003978	0.1443668687	-1.5427864820
10	H	-3.2211814443	-0.3006865780	-1.1628743042
11	H	-2.3313555533	0.0204963009	-2.5397016850
12	N	-2.4476290323	0.0008822598	1.3009412392
13	H	-3.0626785768	0.7677910370	1.0216267743
14	H	-2.2825973441	0.1122143520	2.3009837079
15	H	-2.9720757009	-0.8688643756	1.1888143726
16	N	2.4475947868	0.0014107200	1.3018558190
17	H	2.2810892153	0.1131651975	2.3015969536
18	H	3.0626517239	0.7682989398	1.0227466469
19	H	2.9718178882	-0.8684958752	1.1905370045
20	N	2.4021682599	0.1446538518	-1.5438244081
21	H	2.3293215373	0.0206346306	-2.5405919949
22	H	3.2208263185	-0.3026123936	-1.1653084071

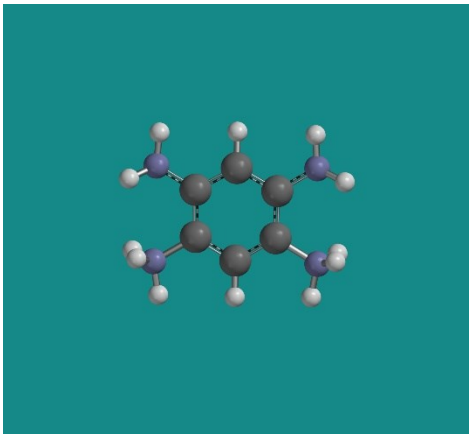

Product:

EE(RωB97X-D3/6-311+G(2df,2p)) = -454.608843 a.u.0 imaginary frequencies
G°(RωB97X-D3/6-311+G(2df,2p)) = -454.446328 a.u
EE(RωB97M(2)/QZVPPD) = -454.917139 a.u.

0 1

Standard Nuclear Orientation (Angstroms)

I	Atom	X	Y	Z
1	C	-1.4718747055	0.0654401609	0.1822553344
2	C	1.3308991179	0.0315460365	0.1004205230
3	C	-0.6448445826	-0.0641262640	1.4137920455
4	C	-0.7581859744	0.0063146316	-1.1290267931
5	C	0.6128964078	0.0005463457	-1.1096344485
6	C	0.7624186356	0.0007830879	1.3453881511
7	H	2.4148528139	0.0589886987	0.0419285965
8	N	-1.5180484031	-0.0069644795	-2.2184747743
9	H	-1.1439703527	0.0199899601	-3.1514428001
10	H	-2.5212226472	-0.0113016391	-2.1399802199
11	N	1.3626947616	-0.0310143478	-2.3649067065
12	H	1.1423450183	-0.8514061849	-2.9334738136
13	H	2.3673330720	-0.0685043090	-2.1931994956
14	H	1.2015618911	0.7970127659	-2.9421349004
15	N	1.4930733651	-0.0772192916	2.5485465453
16	H	2.4801351009	-0.2181203490	2.3897581130
17	H	1.3760007275	0.7444953814	3.1290585698
18	N	-1.2577201011	-0.2039849599	2.5618249666
19	H	-2.2614281333	-0.2668686565	2.6264588600
20	H	-0.7230750339	-0.2954829161	3.4124389113
21	H	-2.2764546840	-0.6728786563	0.1982983033
22	H	-1.9673862939	1.0427549851	0.2321050321

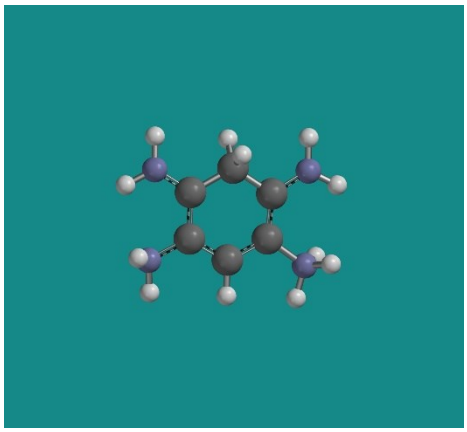

Reaction 9 in Table III - 1 from the main paper
Optimization level: RωB97X-D3/6-311+G(2df,2p)Medium: C-PCM, ε = 78.3

Reactant:

EE(RωB97X-D3/6-311+G(2df,2p)) = -454.182208 a.u.0 imaginary frequencies
G°(RωB97X-D3/6-311+G(2df,2p)) = -454.031256 a.u
EE(RωB97M(2)/QZVPPD) = -454.496805 a.u.

0 1

Standard Nuclear Orientation (Angstroms)

I	Atom	X	Y	Z
1	H	0.1272060255	0.1225246220	-2.5245944236
2	C	0.1257184344	0.0842661352	-1.4410328842
3	C	0.1452560322	-0.0513418797	1.3147784544
4	C	1.3377138057	0.0621975855	-0.7645626990
5	C	-1.0939464880	0.0371501968	-0.7699127524
6	C	-1.0507357941	-0.0272673029	0.6139661012
7	C	1.3519784193	-0.0027498909	0.6436080483
8	H	0.1330387404	-0.0896693160	2.3982924621
9	N	-2.3205296260	0.1208959099	-1.4462804297
10	H	-2.9798283029	-0.6085863890	-1.2129746421
11	H	-2.2109542754	0.1544026674	-2.4488035266
12	N	-2.3151887674	-0.0313233949	1.3506684979
13	H	-2.9861116492	0.6091367292	0.9210924770
14	H	-2.1880364121	0.2681846449	2.3160147116
15	H	-2.7560348408	-0.9515028352	1.3777697522
16	N	2.5855718010	-0.0719838734	1.3113886193
17	H	2.4990163277	0.0367105106	2.3109452792
18	H	3.2653593871	0.5895258319	0.9606530335
19	N	2.5457339334	0.1504398455	-1.4465722517
20	H	2.4814526404	-0.0314344410	-2.4359982592
21	H	3.3033206087	-0.3695753556	-1.0284455685

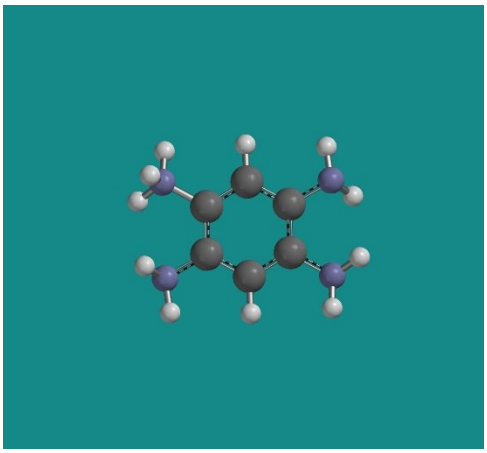

Product:

EE(RωB97X-D3/6-311+G(2df,2p)) = -454.161775 a.u.0 imaginary frequencies
G°(RωB97X-D3/6-311+G(2df,2p)) = -454.015923 a.u
EE(RωB97M(2)/QZVPPD) = -454.473562 a.u.

0 1

Standard Nuclear Orientation (Angstroms)

I	Atom	X	Y	Z
1	H	0.0008860903	-0.1379029383	-2.4533242894
2	C	0.0007168255	-0.0645873278	-1.3690736705
3	C	0.0000382139	0.0015100038	1.4193675861
4	C	1.2416534624	-0.0008898773	-0.7409143798
5	C	-1.2405532453	-0.0010539311	-0.7413626422
6	C	-1.2684238663	0.0780558474	0.6424893271
7	C	1.2689555482	0.0780710363	0.6429699770
8	N	-2.4653275894	0.0489700072	-1.4556532342
9	H	-3.0172725024	-0.7916551261	-1.3338512281
10	H	-2.3193239886	0.1840206786	-2.4457423356
11	N	-2.4085084271	0.1746112638	1.3183046464
12	H	-3.2830041899	0.2368502454	0.8241740441
13	H	-2.4223450218	0.2732018802	2.3187756840
14	N	2.4085164160	0.1747200558	1.3193334898
15	H	2.4216817991	0.2736221860	2.3197654835
16	H	3.2830766872	0.2367566466	0.8253036352
17	N	2.4661821502	0.0490193744	-1.4556149059
18	H	2.3190398658	0.1892828318	-2.4448531530
19	H	3.0147276792	-0.7945139332	-1.3389023468
20	H	-0.0003497542	-0.9642610474	1.9397802851
21	H	-0.0003661528	0.7561721238	2.2090280274

Reaction 10 in Table III - 1 from the main paper
Optimization level: RωB97X-D3/6-311+G(2df,2p)Medium: C-PCM, ε = 78.3

Reactant:

EE(RωB97X-D3/6-311+G(2df,2p)) = -474.920606 a.u.0 imaginary frequencies
G°(RωB97X-D3/6-311+G(2df,2p)) = -474.751044 a.u
EE(RωB97M(2)/QZVPPD) = -475.240849 a.u.

0 1

Standard Nuclear Orientation (Angstroms)

I	Atom	X	Y	Z
1	H	-0.3604279894	0.2197422632	-2.5655381514
2	C	-0.3180927084	0.1296906945	-1.4871807929
3	C	-0.2127411365	-0.0969624266	1.2741284751
4	C	-1.4992681190	0.1163376566	-0.7552374438
5	C	0.8932346832	0.0299616759	-0.8416452749
6	C	0.9566403687	-0.0873863155	0.5416476108
7	C	-1.4224064380	0.0058420578	0.6276222738
8	H	-0.1786007892	-0.1841008778	2.3532870894
9	O	-2.7154914838	0.2057877816	-1.2937182838
10	H	-2.6846457495	0.2761452839	-2.2541165501
11	N	-2.6701054305	0.0048535139	1.3783860404
12	H	-3.2015304939	0.8651295617	1.2258304490
13	H	-2.5114424153	-0.0770017040	2.3829378347
14	H	-3.2755880218	-0.7717260012	1.1029560581
15	N	2.2234911800	-0.1985147543	1.2602347657
16	H	2.8211463291	0.6223670569	1.1385195222
17	H	2.7666440453	-1.0220310018	0.9894139440
18	H	2.0605621642	-0.2850637425	2.2644535247
19	N	2.1002538818	0.0559120906	-1.6647251496
20	H	2.6499057626	-0.8031020035	-1.5859509373
21	H	2.7154335850	0.8414884376	-1.4381450970
22	H	1.8630287754	0.1526307530	-2.6531599072

Product:

EE(RωB97X-D3/6-311+G(2df,2p)) = -474.898038 a.u.0 imaginary frequencies
G°(RωB97X-D3/6-311+G(2df,2p)) = -474.732672 a.u
EE(RωB97M(2)/QZVPPD) = -475.215415 a.u.

0 1

Standard Nuclear Orientation (Angstroms)

I	Atom	X	Y	Z
1	C	-1.5933346401	0.0001698448	-0.1483436225
2	C	1.2268638369	0.0000944882	-0.1308418953
3	C	-0.8059955252	0.0000666329	-1.4046014450
4	C	-0.8257029013	-0.0000065669	1.1320472161
5	C	0.5901038449	0.0001113015	1.0699676839
6	C	0.5494944201	0.0000386636	-1.3647992542
7	H	2.3123158052	0.0000808063	-0.1526566498
8	O	-1.4193954062	0.0000197657	-2.5600701103
9	H	-2.3834000848	-0.0000310920	-2.4943847318
10	N	1.3117012673	-0.0001174352	-2.6045970837
11	H	1.9090162684	0.8248606704	-2.6880597875
12	H	0.6899017546	-0.0001943260	-3.4160972697
13	H	1.9089603708	-0.8251565398	-2.6878711416
14	N	1.3730365874	0.0000982895	2.2989652567
15	H	1.2000684513	0.8275602794	2.8759949051
16	H	2.3742405743	0.0002011443	2.0966061062
17	H	1.2002214782	-0.8274689267	2.8758892118
18	N	-1.5055842220	-0.0002586253	2.2379685603
19	H	-2.5163506784	-0.0003911420	2.2233876205
20	H	-1.0824689749	-0.0003512160	3.1541033977
21	H	-2.2570608562	-0.8726159963	-0.1563347326
22	H	-2.2566313704	0.8732899797	-0.1562722340

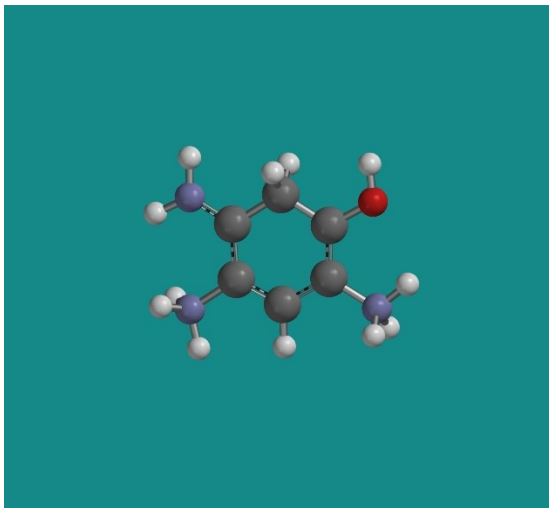

Reaction 11 in Table III - 1 from the main paper
Optimization level: RωB97X-D3/6-311+G(2df,2p)Medium: C-PCM, ε = 78.3

Reactant:

EE(RωB97X-D3/6-311+G(2df,2p)) = -474.920606 a.u.0 imaginary frequencies
G°(RωB97X-D3/6-311+G(2df,2p)) = -474.751044 a.u
EE(RωB97M(2)/QZVPPD) = -475.240849 a.u.

0 1

Standard Nuclear Orientation (Angstroms)

I	Atom	X	Y	Z
1	H	-0.3604279894	0.2197422632	-2.5655381514
2	C	-0.3180927084	0.1296906945	-1.4871807929
3	C	-0.2127411365	-0.0969624266	1.2741284751
4	C	-1.4992681190	0.1163376566	-0.7552374438
5	C	0.8932346832	0.0299616759	-0.8416452749
6	C	0.9566403687	-0.0873863155	0.5416476108
7	C	-1.4224064380	0.0058420578	0.6276222738
8	H	-0.1786007892	-0.1841008778	2.3532870894
9	O	-2.7154914838	0.2057877816	-1.2937182838
10	H	-2.6846457495	0.2761452839	-2.2541165501
11	N	-2.6701054305	0.0048535139	1.3783860404
12	H	-3.2015304939	0.8651295617	1.2258304490
13	H	-2.5114424153	-0.0770017040	2.3829378347
14	H	-3.2755880218	-0.7717260012	1.1029560581
15	N	2.2234911800	-0.1985147543	1.2602347657
16	H	2.8211463291	0.6223670569	1.1385195222
17	H	2.7666440453	-1.0220310018	0.9894139440
18	H	2.0605621642	-0.2850637425	2.2644535247
19	N	2.1002538818	0.0559120906	-1.6647251496
20	H	2.6499057626	-0.8031020035	-1.5859509373
21	H	2.7154335850	0.8414884376	-1.4381450970
22	H	1.8630287754	0.1526307530	-2.6531599072

Product:

EE(RωB97X-D3/6-311+G(2df,2p)) = -474.885225 a.u.0 imaginary frequencies
G°(RωB97X-D3/6-311+G(2df,2p)) = -474.720104 a.u
EE(RωB97M(2)/QZVPPD) = -475.203671 a.u.

0 1

Standard Nuclear Orientation (Angstroms)

I	Atom	X	Y	Z
1	H	-2.5561406840	-0.0966580532	0.0920890644
2	C	-1.4739489095	-0.0572889616	0.0148633953
3	C	1.3475378273	0.0623618339	-0.2686978251
4	C	-0.8992884801	-0.0546940960	-1.3131333094
5	C	-0.7357448654	-0.0123991775	1.1340134034
6	C	0.7014317708	0.0394194437	1.0704175817
7	C	0.4294522043	-0.0022665125	-1.4257577967
8	O	-1.6743709117	-0.0946463664	-2.4030935325
9	H	-2.6110020822	-0.1765927167	-2.1964136295
10	N	1.0360432878	0.0036471375	-2.7431608768
11	H	1.5233086692	0.8825421916	-2.9369406063
12	H	0.3268467986	-0.1188695959	-3.4697565641
13	H	1.7180220540	-0.7508472315	-2.8554068972
14	N	-1.4027916971	-0.0158165019	2.4290991361
15	H	-1.2113139995	0.8315959814	2.9719047161
16	H	-1.1473344299	-0.8239704317	3.0042969043
17	H	-2.4177501961	-0.0581882854	2.3175402552
18	N	1.4542805526	0.0688655033	2.1181341042
19	H	1.1085380521	0.0636198484	3.0677014329
20	H	2.4618746860	0.1020565602	2.0249625492
21	H	1.9564083738	0.9739698616	-0.3242475913
22	H	2.0659419788	-0.7658404315	-0.3084139135

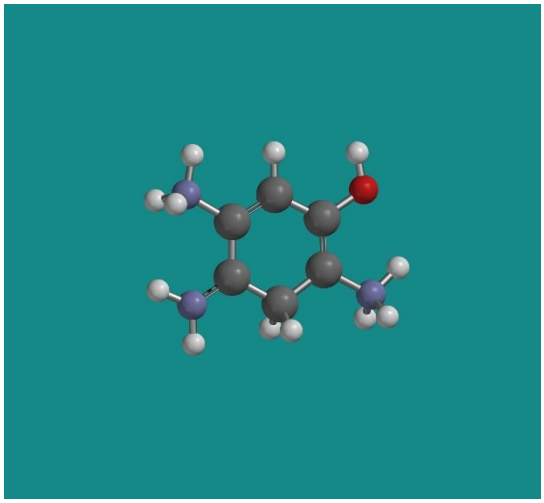

Reaction 12 in Table III - 1 from the main paper
Optimization level: RωB97X-D3/6-311+G(2df,2p)Medium: C-PCM, ε = 78.3

Reactant:

EE(RωB97X-D3/6-311+G(2df,2p)) = -474.495232 a.u.0 imaginary frequencies
G°(RωB97X-D3/6-311+G(2df,2p)) = -474.342424 a.u
EE(RωB97M(2)/QZVPPD) = -474.818111 a.u.

0 1

Standard Nuclear Orientation (Angstroms)

I	Atom	X	Y	Z
1	H	0.0678220344	-0.1877720250	-2.6621735409
2	C	0.0963075901	-0.1202870235	-1.5815118208
3	C	0.1912020795	0.0657982198	1.1833617261
4	C	1.3163632147	-0.0897454495	-0.9342460908
5	C	-1.1033219798	-0.0598670614	-0.8678065823
6	C	-1.0207011171	0.0294114055	0.5295337058
7	C	1.3559440816	0.0071141282	0.4541221126
8	H	0.2300154578	0.1360277464	2.2640519063
9	O	2.4990662286	-0.1414867069	-1.5728550198
10	H	2.3848571218	-0.2018657415	-2.5264579326
11	N	-2.2509204955	0.0725959381	1.3190506735
12	H	-2.8764128377	-0.7057366205	1.1007199791
13	H	-2.7780563679	0.9376258813	1.1830841025
14	H	-2.0502478525	0.0101084115	2.3168978845
15	N	2.6549871179	0.0373427821	1.1177786255
16	H	3.4065022491	0.0566560980	0.4258063123
17	H	2.8059593927	-0.7830077860	1.7054539998
18	H	2.7650087544	0.8628931119	1.7067466028
19	N	-2.3026344819	-0.1491976784	-1.5218856758
20	H	-3.1194843218	0.2756027770	-1.1162060077
21	H	-2.2722558683	-0.0522104072	-2.5234649599

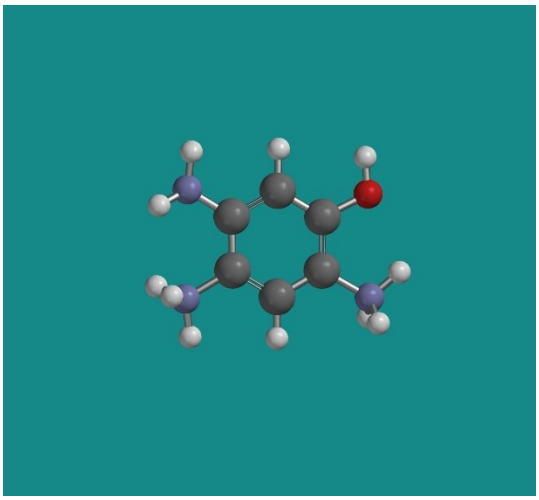

Product:

EE(RωB97X-D3/6-311+G(2df,2p)) = -474.473893 a.u.0 imaginary frequencies
G°(RωB97X-D3/6-311+G(2df,2p)) = -474.325234 a.u
EE(RωB97M(2)/QZVPPD) = -474.794232 a.u.

0 1

Standard Nuclear Orientation (Angstroms)

I	Atom	X	Y	Z
1	C	-1.4090299996	0.0600762416	-0.2341140088
2	C	1.4004897293	-0.0525484516	-0.3407293553
3	C	-0.8355739953	0.0616088015	-1.4718327344
4	C	-0.6796173263	0.0086368321	0.9689021896
5	C	0.6908273300	-0.0443422675	0.9753096944
6	C	0.5650254191	0.0070493239	-1.5711055862
7	O	-1.5094847069	0.1109547582	-2.6518361397
8	H	-2.4593347114	0.1593198306	-2.5112920718
9	N	1.1515114031	0.0057375621	-2.7406626688
10	H	0.6005002001	0.0420425156	-3.5847795551
11	H	2.1543163568	-0.0333441965	-2.8333560348
12	H	-2.4925193368	0.1015137287	-0.1729339241
13	N	-1.4214134288	0.0127675761	2.2286737985
14	H	-1.2639157477	-0.8330896736	2.7807491166
15	H	-2.4270734361	0.0606034771	2.0649732225
16	H	-1.1919515565	0.8153622555	2.8187580436
17	N	1.4569398467	-0.0913539218	2.0596125156
18	H	1.0885084748	-0.0964100751	2.9951654126
19	H	2.4589182968	-0.1267419423	1.9744379378
20	H	2.1034634432	0.7859805892	-0.3615950418
21	H	2.0194137452	-0.9538229636	-0.3923448103

Reaction 13 in Table III - 1 from the main paper
Optimization level: RωB97X-D3/6-311+G(2df,2p)Medium: C-PCM, ε = 78.3

Reactant:

EE(RωB97X-D3/6-311+G(2df,2p)) = -474.495232 a.u.0 imaginary frequencies
G°(RωB97X-D3/6-311+G(2df,2p)) = -474.342424 a.u
EE(RωB97M(2)/QZVPPD) = -474.818111 a.u.

0 1

Standard Nuclear Orientation (Angstroms)

I	Atom	X	Y	Z
1	H	0.0678220344	-0.1877720250	-2.6621735409
2	C	0.0963075901	-0.1202870235	-1.5815118208
3	C	0.1912020795	0.0657982198	1.1833617261
4	C	1.3163632147	-0.0897454495	-0.9342460908
5	C	-1.1033219798	-0.0598670614	-0.8678065823
6	C	-1.0207011171	0.0294114055	0.5295337058
7	C	1.3559440816	0.0071141282	0.4541221126
8	H	0.2300154578	0.1360277464	2.2640519063
9	O	2.4990662286	-0.1414867069	-1.5728550198
10	H	2.3848571218	-0.2018657415	-2.5264579326
11	N	-2.2509204955	0.0725959381	1.3190506735
12	H	-2.8764128377	-0.7057366205	1.1007199791
13	H	-2.7780563679	0.9376258813	1.1830841025
14	H	-2.0502478525	0.0101084115	2.3168978845
15	N	2.6549871179	0.0373427821	1.1177786255
16	H	3.4065022491	0.0566560980	0.4258063123
17	H	2.8059593927	-0.7830077860	1.7054539998
18	H	2.7650087544	0.8628931119	1.7067466028
19	N	-2.3026344819	-0.1491976784	-1.5218856758
20	H	-3.1194843218	0.2756027770	-1.1162060077
21	H	-2.2722558683	-0.0522104072	-2.5234649599

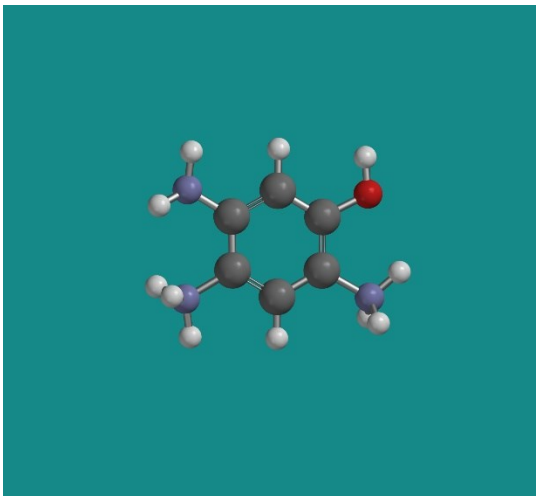

Product:

EE(RωB97X-D3/6-311+G(2df,2p)) = -474.462824 a.u.0 imaginary frequencies
G°(RωB97X-D3/6-311+G(2df,2p)) = -474.312548 a.u
EE(RωB97M(2)/QZVPPD) = -474.783744 a.u.

0 1

Standard Nuclear Orientation (Angstroms)

I	Atom	X	Y	Z
1	C	0.0349554670	-0.2349888525	-1.6176746395
2	C	-0.0453431134	-0.2824126338	1.1970366347
3	C	-0.0279425964	-1.4902808554	-0.8405557516
4	C	0.0566818230	1.0313033394	-0.8281870928
5	C	0.0130851708	0.9402423009	0.5706130076
6	C	-0.0667067101	-1.5135127209	0.5273240713
7	H	-0.0769618242	-0.3060108898	2.2820519838
8	O	-0.0447752575	-2.5930244972	-1.5423788517
9	H	-0.0880550746	-3.3307561210	-0.9009969419
10	N	-0.1241062498	-2.7905263035	1.1477988058
11	H	-0.9614206339	-2.9132148194	1.7014781665
12	H	0.6789991172	-2.9697449728	1.7357591781
13	N	0.0348843379	2.1557007520	1.3801778219
14	H	0.8903428436	2.7009077839	1.2499669734
15	H	-0.0100838660	1.9312014146	2.3748215792
16	H	-0.7601637006	2.7707794286	1.1920881764
17	N	0.1151821233	2.1542572216	-1.4972903294
18	H	0.1329273158	3.0623603818	-1.0615025280
19	H	0.1446605935	2.1494087580	-2.5057855901
20	H	0.9214874130	-0.2652890958	-2.2600333756
21	H	-0.8176471785	-0.2063996189	-2.3047112981

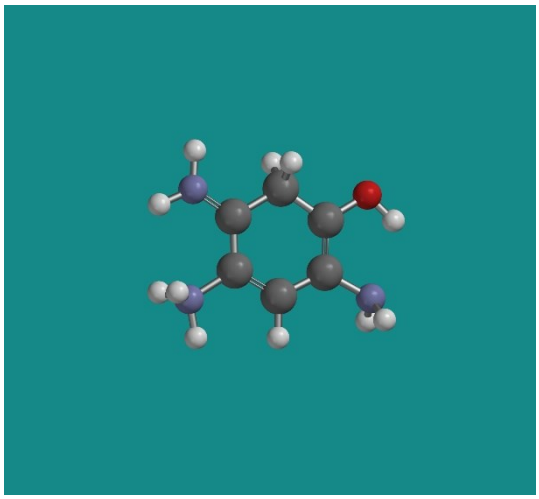

V. References

1. Bruker (2020). *APEX3* and *SAINT*, Bruker AXS Inc., Madison, Wisconsin, USA.
2. Krause, L.; Herbst-Irmer, R.; Sheldrick, G. M.; Stalke, D. Comparison of Silver and Molybdenum Microfocus X-Ray Sources for Single-Crystal Structure Determination. *J. Appl. Cryst*. **2015**, *48*, 3–10.
3. Sheldrick, G. M. *SHELXT* – Integrated Space-Group and Crystal-Structure Determination. *Acta Crystallogr*. **2015**, *A71*, 3–8.
4. Sheldrick, G. M. Crystal Structure Refinement with *SHELXL*. *Acta Crystallogr*. **2015**, *C71*, 3–8.
5. Dolomanov, O. V.; Bourhis, L. J.; Gildea, R. J.; Howard, J. A. K.; Puschmann, H. *OLEX2*: A Complete Structure Solution, Refinement and Analysis Program. *J. Appl. Crystallogr*. **2009**, *42*, 339–341.

Annexe D

Informations supplémentaires

Chapitre 5

Des composés inattendus

Partie expérimentale

Tableau D - 1 Optimisation de la synthèse de la dioxime 4.

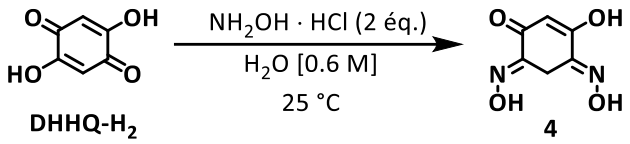

Entrée	Atmosphère	Temps (h)	NaOH (éq.)	R%
1	Air	24	0	49
2	Air	24	1.0	52
3	Air	24	1.9	60
4	N_2	24	0	76
5*	N_2	48	0	93

Rendements (R%) déterminés à partir de la masse du produit brut collecté.

*4.0 éq. de $NH_2OH{\cdot}HCl$

Synthèse de la dioxime 4. Dans un vial de 10 mL, DHHBQ-H_2 (200 mg, 1.43 mmol) recristallisée et broyée finement ainsi que $NH_2OH \cdot HCl$ (397 mg, 5.71 mmol) sont suspendus dans de l'eau (2.5 mL). La solution est purgée 15 min à l'azote et agitée 40 h à 25 °C sous atmosphère inerte. Le précipité ainsi formé est filtré sous vide, lavé à l'eau froide (4 °C) et séché à l'étuve à 60 °C. Le produit brut est alors isolé sous forme d'une poudre blanc cassé (299 mg, 93%) pouvant être recristallisé dans l'eau chaude et collecté sous forme de plaquettes incolores (Recristallisation = 86%). RMN ^{1}H (400 MHz, DMSO-d_6) δ: 12.34 (s, 2H), 11.17 (s, 0.83H), 5.79 (s, 1H), 3.67 (s, 2H). RMN ^{13}C (100 MHz, DMSO-d_6) δ: 147.00, 110.75, 23.91. HRMS (ESI) : m/z calculé pour $C_6H_6N_2O_4$ [M+] 171.04003; trouvé 171.04076.

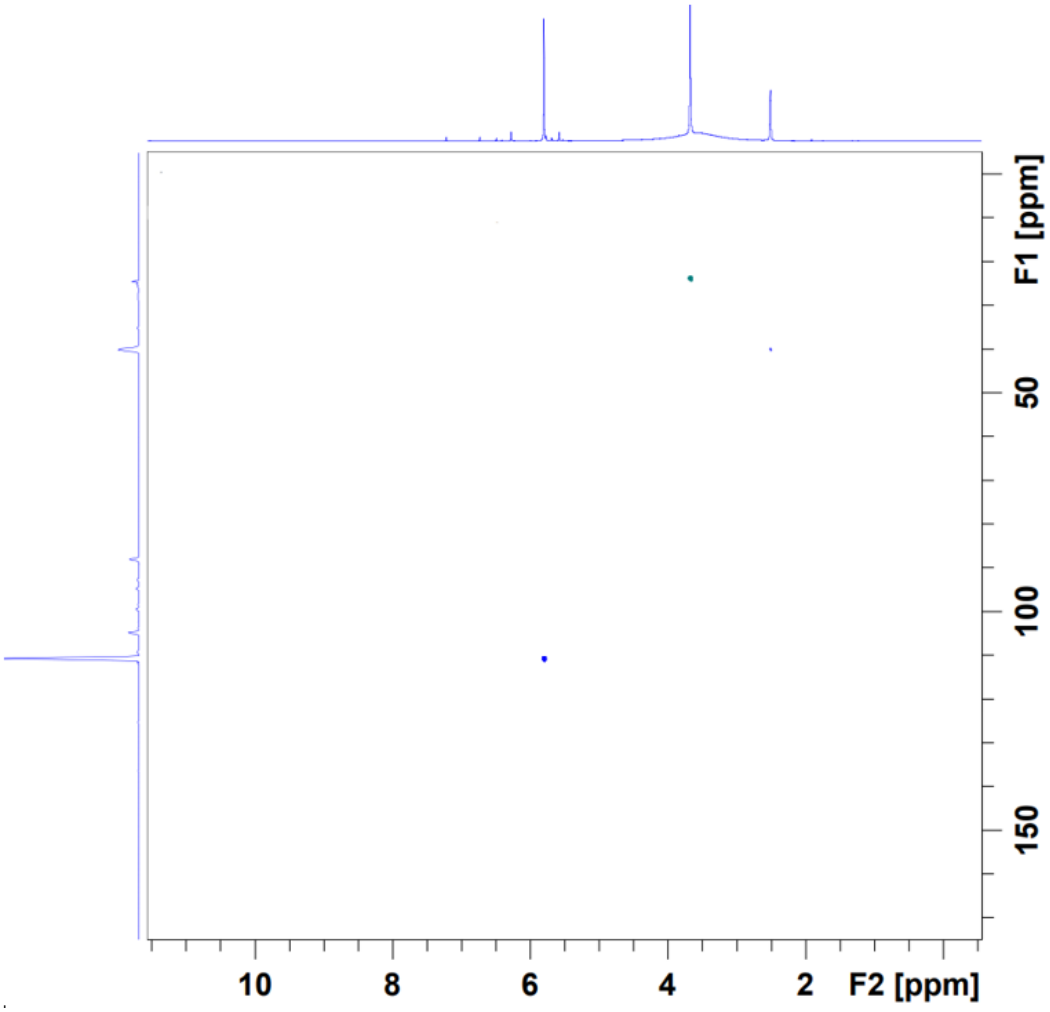

Figure D1. Spectre RMN HSQC ^{1}H-^{13}C (DMSO-D_6, 400 MHz) de la dioxime **10**.

Synthèse du dimère 10. Dans un vial de 10 mL, DHHBQ-H_2 (200 mg, 1.43 mmol) recristallisée et broyée finement ainsi que $NH_2OH \cdot HCl$ (198 mg, 2.86 mmol) sont mis en suspension dans l'eau (2.5 mL). Le mélange est alors agité 24 h au contact de l'air à 50 °C. Le précipité ainsi formé est filtré, lavé à l'eau et séché sous vide. Le produit désiré est isolé sous la forme d'une poudre brune (188 mg, 77 %). RMN ^{1}H (400 MHz, DMSO-d_6) δ: 12.19 (s, 4H), 11.17 (s, 2H), 5.66 (s, 2H), 5.51 (s, 2H). RMN ^{13}C (100 MHz, DMSO-d_6) δ: 173.56, 148.01, 109.25, 35.28. HRMS (ESI) : m/z calculé pour $C_{12}H_{10}N_4O_8$ [M+] 339.0571 ; trouvé 339.0564.

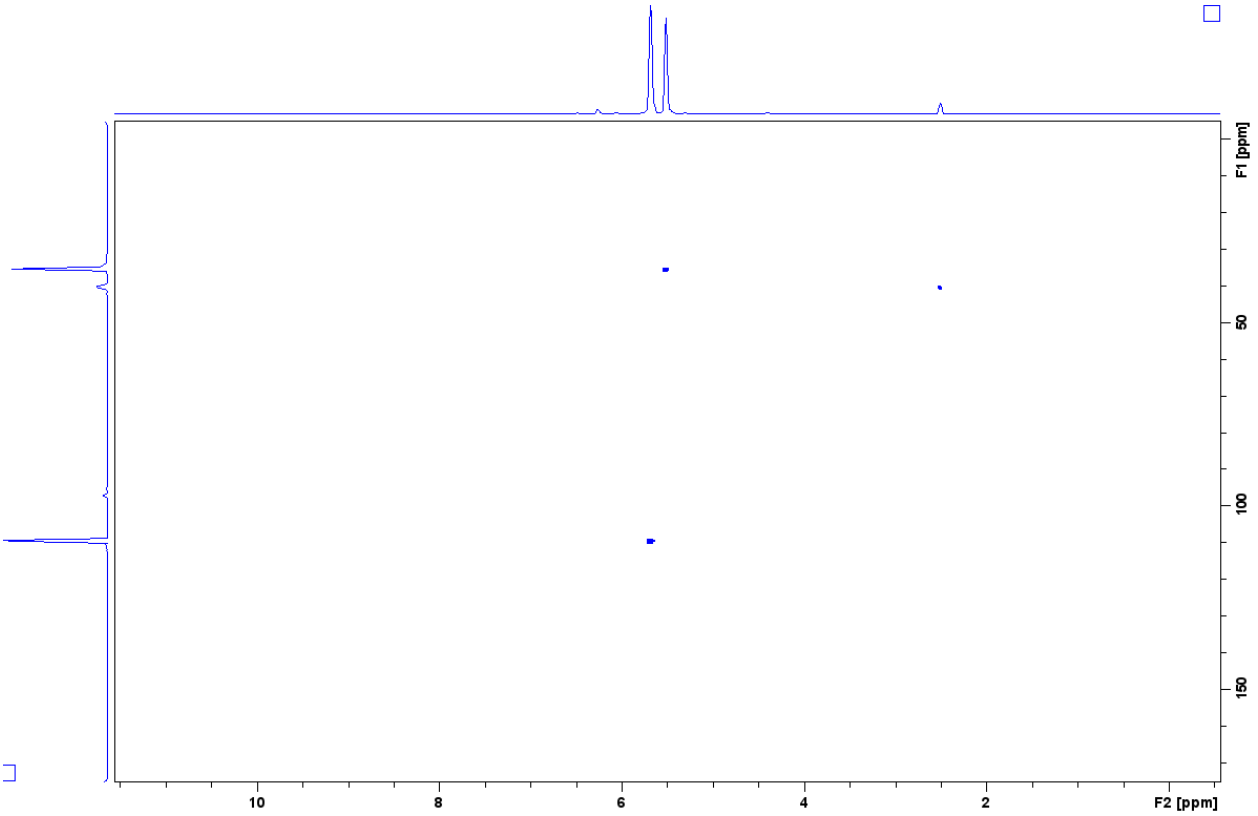

Figure D2. Spectre RMN HSQC ^{1}H-^{13}C (DMSO-d_6, 400 MHz) du dimère **10**.

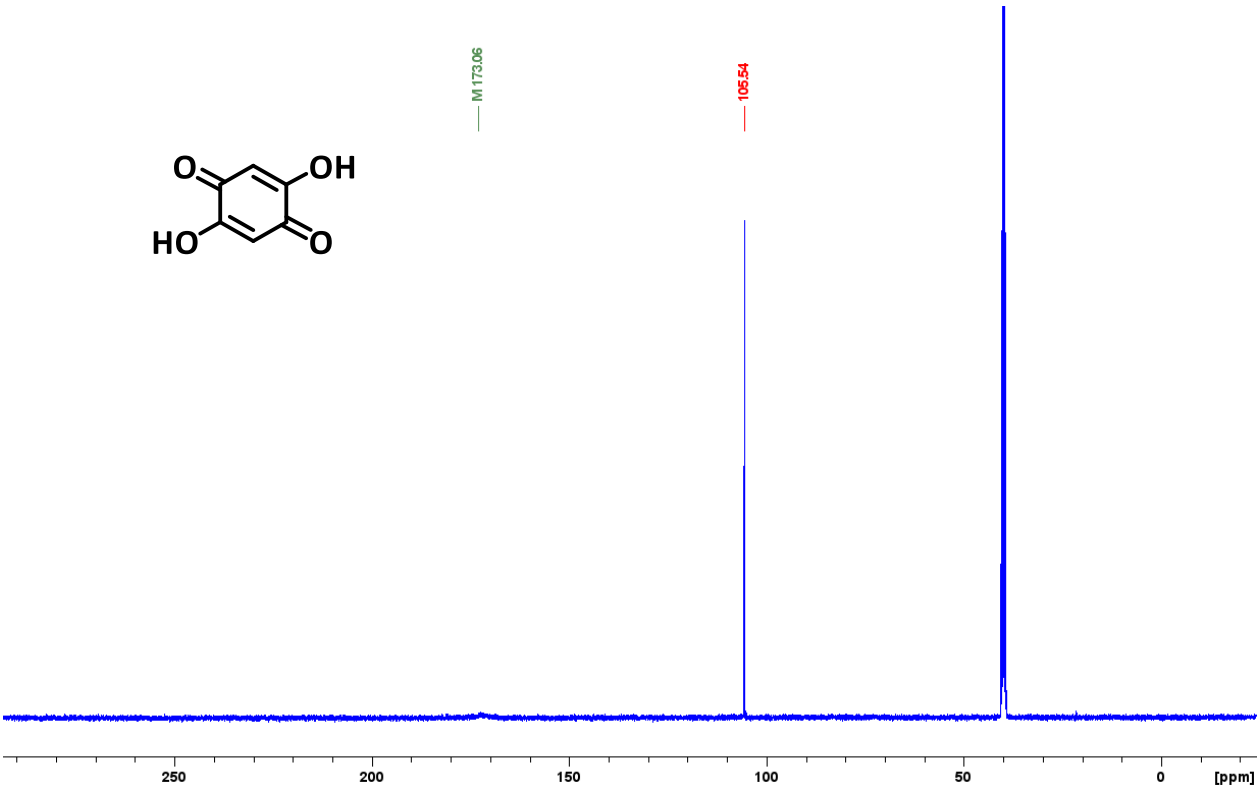

Figure D3. Spectre RMN ^{13}C (DMSO-d_6, 100 MHz) de DHHQ-H_2.